TECHNISCHE UNIVERSITÄT MÜNCHEN
Lehrstuhl für Computation in Engineering

Non-reflecting Boundary Conditions for the Lattice Boltzmann Method

Martin B. Schlaffer

Vollständiger Abdruck der von der Ingenieurfakultät Bau Geo Umwelt der Technischen Universität München zur Erlangung des akademischen Grades eines

Doktor-Ingenieurs

genehmigten Dissertation.

Vorsitzender: Univ.-Prof. Dr.-Ing. habil. Michael Manhart

Prüfer der Dissertation:

1. Univ.-Prof. Dr.rer.nat. Ernst Rank
2. Univ.-Prof. Dr.-Ing. habil. Manfred Krafczyk
   Technische Universität Braunschweig
3. Univ.-Prof. Dr.-Ing. habil. Gerhard H. Müller

Die Dissertation wurde am 06.02.2013 bei der Technischen Universität München eingereicht und durch die Ingenieurfakultät Bau Geo Umwelt am 28.05.2013 angenommen.

Zusammenfassung

Die vorliegende Arbeit behandelt eine Methode für nichtreflektierende Randbedingungen für das Lattice Boltzmann Verfahren zur Simulation von Fluidströmungen. Sie basiert auf integraler Impulserhaltung mit einem analytischen Zeitintegrationsmodel. Die daraus resultierende Unabhängigkeit von räumlichen Gradienten und zeitlichen Ableitungen ermöglicht eine stabile Umsetzung für beliebige Einfallsrichtungen von Druckwellen. Dabei weist sie eine Genauigkeit bezüglich der Restreflektion für alle Richtungen auf, die bei charakteristikenbasierten Ansätzen nur im Fall eines senkrechten Einfalls erreicht wird. In der Arbeit wird eine Methode erläutert, die eine Randwertanpassung erlaubt (Druck, Geschwindigkeit) unter Berücksichtigung eines vorgegebenen maximalen Restreflektionsgrads. Darüber hinaus wird die Anwendung bei einem Flachwassergleichungsmodel gezeigt.

Abstract

This thesis presents an approach for non-reflecting boundary conditions for the Lattice Boltzmann Method for the simulation of fluid flows. It is based on integral momentum conservation with an analytical time integration model. The resulting independence of spatial gradients and time derivatives provides a stable implementation for arbitrary directions of incidence of the pressure waves. The residual reflection is for any direction of the same order as achieved by characteristic based approaches only in case of a normal incidence. In this work, a method is described which allows for a boundary state adaption (pressure, velocity) based on a predetermined maximum residual reflection rate. Additionally, its applicability is shown for a nonlinear shallow water equation model.

Acknowledgments

First of all I would like to express my gratitude to Prof. Ernst Rank, my principle supervisor during my time at the Chair for Computation in Engineering at the Technische Universität München. Mr. Rank gave me permission to work on a self-selected topic. This is particularly remarkable as it took considerable time to lead to first presentable results. I thank Mr. Rank very much for his generous support, his great faith, and for his remarkable patience.

Mr. Rank allowed me to visit Prof. Manfred Krafczyk and his staff of the IRMB at the Technische Universität Braunschweig. Without these stays, I would not have been able to complete my work in this form, as it is quite impossible to learn a new innovative approach like the Lattice Boltzmann Method merely from journal articles. In particular, I would like to thank Mr. Krafcyk for his work as a member of the dissertation committee. In this context, I wish to thank also his staff, especially Dr. Martin Geier and Dr. Christian Janßen, from which I certainly have learned the most about the Lattice Boltzmann Method. I definitely had a marvelous time in Braunschweig and I am thankful for their great hospitality.

During my work on this thesis, there were several problems from the field of technical acoustics, which kept me busy for weeks or even months without developing significant advance. Often a discussion with Prof. Gerhard Müller from the Chair of Structural Mechanics at the Technische Universität München solved the problem in no time. I thank Mr. Müller sincerely for taking his time for the discussions and also for his efforts as a member of the committee.

A considerable proportion of the work on my thesis consisted of elaborating and testing numerous approaches. Fortunately, I had an excellent motivator with my group leader Dr. Stefan Kollmannsberger. I can say that I discussed by far most of the resulting issues with him, and he has greatly contributed to my success with his expertise and his sincere helpfulness, for which I am truly grateful.

Finally, I would like to thank Dr. Maximilian Emans of the Austrian Academy of Sciences, Institut RICAM, Linz. In numerous discussions, I learned a lot from his outstanding knowledge about fluid mechanics and numerical analysis. In particular, I would like to thank him for taking so much time for the proofreading of my theses.

Contents

Table of Symbols

Notation

$\underline{v}$	vector v
$\underline{\underline{M}}$	matrix M
$a^{(n)}$	quantity a at time step $t = n \cdot \Delta t$
ϵ	formal expansion parameter
$\underline{e}_i$	Cartesian unit vector in direction i
$(\nabla y)_i := \frac{\partial}{\partial x_i} y$	gradient of a scalar
$(\nabla \underline{v})_{(i,j)} := \frac{\partial}{\partial x_j} v_i$	gradient of a vector
$\nabla \cdot \underline{v} := \frac{\partial}{\partial x_i} v_i$	divergence of a vector
$(\nabla \cdot \underline{\underline{M}})_i := \frac{\partial}{\partial x_j} M_{(i,j)}$	divergence of a matrix
$((\underline{v} \cdot \nabla)\underline{v})_i := v_j \cdot \frac{\partial v_i}{\partial x_j}$	common abbreviation in vector analysis
$\Delta := \nabla \cdot \nabla$	nabla operator
$\delta_{\alpha\beta} := \begin{cases} 1 & \text{if } \alpha \equiv \beta \\ 0 & \text{else} \end{cases}$	Kronecker delta

(summation convention is used for repeated indices)

Macroscopic Quantities

t	[s]	time
x_i	[m]	space coordinate along direction of unit vector $\underline{e}_i$
r	[m]	radius length
L	[m]	characteristic length
A	[m^2]	general area
V	[m^3]	general volume
$\underline{v}$	[m s^{-1}]	bulk velocity

ϱ	[kg m^{-3}]	bulk mass density
ϱ_0	[kg m^{-3}]	hydrostatic or ambient density
j, J	[kg m s^{-1}]	momentum
p	[N m^{-2}]	isotropic pressure
p_0	[N m^{-2}]	hydrostatic or ambient pressure
T	[K]	temperature
μ	[kg m^{-1} s^{-1}]	dynamic shear viscosity
ν	[m^2 s^{-1}]	kinematic shear viscosity, $\nu = \mu/\varrho$
μ'	[kg m^{-1} s^{-1}]	dynamic bulk or volume viscosity
$\underline{\underline{\sigma}}$	[N m^{-2}]	stress tensor
$\underline{\underline{\tau}}$	[N m^{-2}]	viscous shear stress tensor
E	[N kg^{-1} m^2]	total energy per unit density
e	[N kg^{-1} m^2]	inner energy per unit density
R	[N m mol^{-1} K^{-1}]	universal gas constant ($R = 8.31$ N m mol^{-1} K^{-1})
Q	[m^3 s^{-1}]	volume flow
z	[N m^{-3} s]	acoustic impedance
c_s	[m s^{-1}]	speed of sound
Re	[1]	Reynolds number (Re $= (\varrho \cdot v \cdot L)/\mu$)
Ma	[1]	Mach number (Ma $= v/c_s$)
γ	[1]	specific heat ratio

Mesoscopic Quantities

f	[kg m^{-3} (m/s)$^{-3}$]	density distribution in phase space
f^{eq}	[kg m^{-3} (m/s)$^{-3}$]	equilibrium density distribution
$\underline{c}$	[m s^{-1}]	molecular propagation speed
$\underline{\xi}$	[1]	normalized molecular propagation speed
τ	[s]	mean relaxation time
ω	[s^{-1}]	relaxation frequency
l_f	[m]	mean free path length
c_0	[m s^{-1}]	mean thermal molecular propagation speed
Kn	[1]	Knudsen number (Kn $= l_f/L$)

Chapter 1

Introduction

The Lattice Boltzmann Method

The Lattice Boltzmann Method (LBM) emerged in the early nineties from research on Lattice Gas Cellular Automata (LGCA). It was a breakthrough in terms of efficiency, compared to the predecessor method, and made it competitive with classical Navier-Stokes approaches (cf. Krafczyk [35]). Since then, the method evolved and is already well established in industry (cf. Exa Corp. [1]).

There are fundamental advantages of the LBM compared to classical Navier-Stokes approaches. The simplicity of the underlying explicit evolution scheme allows a very efficient implementation. Basically the core of the algorithm is a plain shift operation, involving directly neighboring grid points, and a strictly local collision operation. Due to this property, the method is readily implemented on parallel computers, even if a fine-grained parallelism is required. The commonly used equidistant square lattices allow for a most efficient grid generation (cf. Wenisch et al. [61]), excellent memory efficiency and permit to implement algorithms for complex or even moving geometries in a way that the computational cost is effectively reduced to a minimum (cf. Kollmannsberger et al. [34], Geller [18]).

Another field of application where the LBM proves to be applicable in a favorable manner is the field of multiphase flow. Demonstrating the efficiency of the LB method, Tölke et al. solved a multiphase flow problem of industrial relevance [58]. The article additionally describes the potential of implementing LBM on conventional graphics hardware (Graphic Processing Units, GPUs). As shown already by Tölke and Krafczyk ([57], [59]), this architecture is particularly well suited for the LBM and seems to have revolutionized its application: It is easily possible to utilize about 60% of a GPU's peak performance. This opens up whole new perspectives to real-time steering applications (cf. Linxweiler et al. [40]).

Of course there are also inherent restrictions to the LBM. First, there is the restriction to low Mach number flow ($\mathrm{Ma} \lesssim 0.3$). Current research is conducted in order to overcome this problem (cf. Nie et al. [49]). Second, the LBM covers only isothermal flow, although coupled schemes with the Boussinesq approximation can be used (cf. Guo et al. [21]). An extension to thermal multispeed models seems to lack stability (cf. McNamara et al. [42]).

Furthermore, the time integration is limited to first order. Dellar presents progress towards ways to obtain second order accurate schemes [11]. Moreover, turbulence modeling has not yet reached the level of maturity that characterizes implementations of classical Navier-Stokes

based methods.

LBM and Aeroacoustics

As will be shown in chapter 3, the so-called incompressible LBM unifies the advantages of a weakly compressible continuity and Navier-Stokes equation paired with a pressure scale relative to an ambient pressure instead of an absolute one. This has an important implication for the field of aeroacoustics. Classically, such problems are tackled either by using incompressible Navier-Stokes equations with a coupled transport equation for the acoustic field or by using fully compressible Navier-Stokes equations. Both demand a huge computational effort, the latter also covers only the absolute pressure. An acoustical phenomenon in the range of 10^{-5} Pa added to an ambient pressure of 10^5 Pa would cause a significant loss of accuracy for numerical computation. The IEEE 754 single precision floating point number format would not even be adequate to cover that range.

The incompressible LBM is not affected by both problems, which makes it especially useful for aeroacoustics (cf. Wilde [62], Neuhierl [48]). The recent development of commercial products (e.g. Exa PowerACOUSTICS [1]) reflects this fact. Prof. Peter Zeller, Director of Acoustics and Vibration at BMW AG, wrote about the Lattice Boltzmann Method in 2009: "It can be predicted that for numerical aeroacoustics a similar wide range of application opens similar as it emerged ten years ago in the field of aerodynamics." (translated from German [63]).

Non-reflecting Boundary Conditions

For aeroacoustics, an important problem are spurious pressure waves reflected from the boundary of the domain. Even for conventional flow problems, the LBM is known to suffer from spurious pressure waves, usually caused by poor initialization. Both require the use of non-reflecting boundary conditions.

In general one has to clarify what part of the flow should not be reflected, i.e. what part of the flow should not interact with the domain. Naturally this would be the interaction which is not influencing the flow itself, but is superimposed and distracts the significant signals. The part of the flow which is not interacting with the flow itself are reflected sound pressure waves, provided it is in the regime of linear acoustics. On the other hand, also pressure changes propagate with speed of sound. Prohibiting reflection of sound in general will result possibly in a wrong boundary state. The remedy is to allow a certain rate of reflection.

The next issue is to clarify what sound actually means under the condition that it is not influencing the flow. Although this might seem trivial, this is not unambiguous at all. In acoustics, sound is usually defined by a frequency range of a pressure fluctuation, which then can be isolated and treated separately. This could be done with a high-pass filter, as described in section 5.1. An alternative definition is that sound is a pressure change propagating with speed of sound, provided that the flow itself is of low Mach numbers. This includes also infrasound. For a general fluid flow, a pressure change will in general not be propagating with speed of sound, e.g. in the case of transported vortices.

The key issue is how to "remove" the unwanted sound component on the boundary. If the sound pressure respectively sound density can be separated, a first approach would be to

simply remove it by low-pass filtering. Unfortunately sound does not only appear in pressure or density, but particle velocity and even temperature as well. To retain the velocity results inevitably in a wrong momentum and a reflection in consequence. In fact, both have to be adapted, according to the well known physical concept of their proper ratio, the impedance.

A requirement for a boundary which even exceeds non-reflection is to create one which appears to be not existing, as if a free field would continue. A free field boundary condition of course has to fulfill much more than simply not to reflect sound pressure waves, it has to recover the correct fluid state of a free field. As the system is under-determined on the boundary (information is virtually cut away), simulation of a proper free field is theoretically impossible. Consequently, certain assumptions have to be made to close the problem.

There exist numerous approaches which re-determine the state on the boundary, so that a non-reflecting boundary condition can be installed. A survey is e.g. provided by Kam et al. [31]. As there will always be an assumption having contradicting conditions and consequently resulting in an error, it is simply not possible to have a perfectly non-reflecting boundary condition. The challenge is to chose the one with the least deficiencies for the problem of interest.

An approach implemented for the LBM by Kim et. al. [33] and by Izquierdo and Fueyo [28], based on the work of Thompson [56] respectively Poinsot and Lele [51], is the characteristics-based boundary condition, which solves the Euler equations in normal direction to the boundary. While the assumption of zero viscosity might not cause a significant error (an extension covering viscous interaction is offered), the perpendicular approximation, involving finite differences in space, does: For transversely incoming sound pressure waves, there will be a significant reflection.

The crucial assumption of the boundary condition presented in chapter 6 is different. The prerequisite is that every pressure change propagates with speed of sound. For an inflow boundary condition this might be without consequences, because emerging turbulence will not reach the inflow boundary. On an outflow boundary, convected vortices will contradict the assumption. This will result in a slight over-adaption of pressure and velocity.

As a second prerequisite in chapter 6, a viscous pressure loss is not considered. Actually this is not a necessary condition: With a proper velocity gradient information on the boundary node, it might be possible to include also viscid flow. Anyhow, a viscous extension like the one offered by Poinsot and Lele [51] for proper boundary state adaption (velocity or pressure) is included, although in a different way.

Overview

To clarify the terminology and introduce important derivations used throughout the thesis, chapter 2 will sketch the governing equations in fluid mechanics from a classical, macroscopic point of view. Chapter 3 will then illustrate the Lattice Boltzmann Method and its analysis, i.e. the formal link to the macroscopic equations of chapter 2. Chapter 4 follows with a discussion of different approaches for boundary conditions used in the subsequent sections. Chapter 5 introduces both already mentioned approaches to non-reflecting boundary conditions. The first part of the chapter is about low-pass filtering, probably the most intuitive approach, and includes the theory of discrete low-pass filter design from scratch, with application to LBM as well as its implementation. The second part discusses in detail the involved Navier-Stokes

characteristic boundary conditions, which are widely used. It will be illustrated that this approach is closely related to the boundary conditions of the subsequent chapter 6, which, as the core of this thesis, describes an integral approach with isotropic behavior and increasing stability, compared to schemes which rely on explicit numerical time integration. Chapter 7 then shows an extension that allows to set a specific pressure or velocity on the boundary while using the free field boundary conditions of chapter 6. Chapter 7 also includes an extensive benchmark simulation of the boundary condition introduced in chapter 6 and 7. In chapter 8, their application is demonstrated for a specific LBM shallow water equation model. The conclusion and outlook in chapter 9 sums up the essential results of the work and addresses some issues which could be interesting in continuation of the described matter. In appendix A, various code examples of the discussed non-reflecting boundary conditions are given in 1D and 2D, as implemented for the simulation of the test cases.

Chapter 2

Governing Equations in Fluid Mechanics

2.1 Conservation Properties

For a system invariant under Galilean transformations, certain quantities are conserved. For a thermodynamic system in fluid mechanics, this implies the conservation of mass, momentum and energy. The governing equations in fluid mechanics are derived from these conservation laws. The illustration throughout this chapter is based on the description by Hirsch [26].

2.1.1 Scalar Conservation Law

Let U be a scalar quantity per unit volume in an arbitrary control volume Ω with surface S. The change of the total amount of U in the control volume is according to the Reynolds' Transport Theorem

$$\frac{D}{Dt}\int\limits_{\Omega} U \; d\Omega \; = \int\limits_{\Omega} \frac{\partial}{\partial t} U \; d\Omega \; + \; \oint\limits_{S} \underline{F} \cdot d\underline{s} \tag{2.1}$$

with the flux vector $\underline{F}$ of U per unit surface and unit time. On the other hand, the change itself is caused by sources Q_v in the volume and Q_s on the surface of the volume

$$\frac{D}{Dt}\int\limits_{\Omega} U \; d\Omega \; = \int\limits_{\Omega} Q_v \; d\Omega \; + \; \oint\limits_{S} \underline{Q_s} \cdot d\underline{s}. \tag{2.2}$$

In the integral formulation, the scalar conservation law therefore results in

$$\int\limits_{\Omega} \frac{\partial}{\partial t} U \; d\Omega \; = \int\limits_{\Omega} Q_v \; d\Omega \; + \; \oint\limits_{S} \underline{Q_s} \cdot d\underline{s} \; - \; \oint\limits_{S} \underline{F} \cdot d\underline{s}. \tag{2.3}$$

According to the divergence theorem, the surface integrals can be transformed to volume integrals under the condition that $\underline{F}$ and $\underline{Q_s}$ are C^1-continuous. Equation 2.3 then turns into the differential form

$$\frac{\partial}{\partial t}U \;+\; \nabla \cdot (\underline{F} \;-\; \underline{Q_s}) \;=\; Q_v \tag{2.4}$$

The flux $\underline{F}$ can be split into

$$\underline{F} = \underline{F_c} + \underline{F_d}, \tag{2.5}$$

with the convective flux of the center of gravity's velocity $\underline{v}$

$$\underline{F_c} = U \cdot \underline{v} \tag{2.6}$$

and $\underline{F_d}$ describing the movement relative to the center of gravity, according to Fick's laws of diffusion

$$\underline{F_d} = -\kappa \; \varrho \; \nabla u \quad \text{with} \quad U = \varrho \cdot u, \tag{2.7}$$

with mass density ϱ and the diffusion coefficient κ. u marks the scalar value per unit mass. Using this, equation 2.4 turns it into the convection-diffusion equation

$$\frac{\partial}{\partial t}\varrho u \;+\; \nabla \cdot (\varrho \; \underline{v} \; u) \;=\; \nabla \cdot (\kappa \; \varrho \; \nabla u) \;+\; Q_v \;+\; \nabla \cdot \underline{Q_s} \tag{2.8}$$

2.1.2 Vector Conservation Law

For a vector quantity $\underline{U}$ per unit volume, the Reynolds' Transport Theorem holds as well, and F turns into a flux tensor $\underline{\underline{F}}$:

$$\frac{D}{Dt}\int\limits_{\Omega} \underline{U} \; d\Omega \;=\; \int\limits_{\Omega} \frac{\partial}{\partial t}\underline{U} \; d\Omega \;+\; \oint\limits_{S} \underline{\underline{F}} \cdot d\underline{s}. \tag{2.9}$$

The total change in time is caused by volume and surface sources:

$$\frac{D}{Dt}\int\limits_{\Omega} \underline{U} \; d\Omega \;=\; \int\limits_{\Omega} \underline{Q_v} \; d\Omega \;+\; \oint\limits_{S} \underline{\underline{Q_s}} \cdot d\underline{s}. \tag{2.10}$$

The integral formulation of the vector conservation law reads

$$\int\limits_{\Omega} \frac{\partial}{\partial t}\underline{U} \; d\Omega \;=\; \int\limits_{\Omega} \underline{Q_u} \; d\Omega \;+\; \oint\limits_{S} \underline{\underline{Q_s}} \cdot d\underline{s} \;-\; \oint\limits_{S} \underline{\underline{F}} \cdot d\underline{s}, \tag{2.11}$$

or, with the divergence theorem, in the differential form

$$\frac{\partial}{\partial t}\underline{U} \;+\; \nabla\cdot(\underline{\underline{F}} - \underline{\underline{Q_s}}) \;=\; \underline{Q_v}. \tag{2.12}$$

The flux tensor again can be split into a convective and a diffusive part

$$\underline{\underline{F}} \;=\; \underline{\underline{F_c}} \;+\; \underline{\underline{F_d}} \tag{2.13}$$

with

$$\underline{\underline{F_c}} = \underline{U}\otimes\underline{v} \tag{2.14}$$

and, according to Fick's law

$$\left(\underline{\underline{F_d}}\right)_{i,j} = -\kappa\;\varrho\;\frac{\partial u_i}{\partial x_j} \quad \text{and} \quad U_i = \varrho\;u_i. \tag{2.15}$$

This results in the vector convection-diffusion equation

$$\frac{\partial}{\partial t}\varrho\underline{u} \;+\; \nabla\cdot(\varrho\;\underline{v}\otimes\underline{u}) \;=\; \nabla\cdot(\kappa\;\varrho\;\nabla\underline{u}) \;+\; \underline{Q_v} \;+\; \nabla\cdot\underline{\underline{Q_s}}. \tag{2.16}$$

2.2 Continuity Equation

For $U = \varrho$, equation 2.8 becomes

$$\frac{\partial}{\partial t}\varrho \;+\; \nabla\cdot(\varrho\;\underline{v}) \;=\; Q_v \;+\; \nabla\cdot\underline{Q_s}. \tag{2.17}$$

The diffusive term vanishes, as overall mass diffusion is a part of transport and would therefore result in convection. For a closed system, in absence of a source term, the continuity equation is derived as:

$$\frac{\partial}{\partial t}\varrho \;+\; \nabla\cdot(\varrho\;\underline{v}) \;=\; 0. \tag{2.18}$$

The non-conservative formulation

$$\frac{D}{Dt}\varrho \;+\; \varrho\nabla\cdot\underline{v} \;=\; 0 \tag{2.19}$$

is mathematically equivalent, although not numerically in the discretized case (cf. [38]).

The strict definition for incompressibility refers to a constant size V of the control volume Ω:

$$\frac{dV}{dt} = \int_{\Omega} \nabla \cdot \underline{v} \; dx \; dy \; dz \equiv 0. \tag{2.20}$$

As equation 2.20 is valid for an arbitrary volume, the integrand must be zero. This results in the incompressible continuum equation

$$\nabla \cdot \underline{v} = 0. \tag{2.21}$$

From equation 2.21 and the non-conservative continuum equation 2.19 follows for the incompressible case:

$$\frac{d}{dt}\varrho = 0. \tag{2.22}$$

2.3 Navier-Stokes Equation

If $\underline{U}$ is set to the momentum density $\varrho\underline{v}$, the volume source term becomes an external volume force $\varrho\underline{f_e}$ and the convective flux tensor reads

$$\underline{\underline{F_c}} = \varrho\underline{v} \otimes \underline{v}. \tag{2.23}$$

Momentum diffusion is expressed by the stress tensor $\underline{\underline{\sigma}}$, additionally including the surface source term,

$$\underline{\underline{F_d}} + \underline{\underline{Q_s}} = -\underline{\underline{\sigma}} = p\underline{\underline{I}} - \underline{\underline{\tau}}. \tag{2.24}$$

Equation 2.12 becomes

$$\int_{\Omega} \frac{\partial}{\partial t}\varrho\underline{v} \; d\Omega + \oint_{S} \varrho\underline{v} \otimes \underline{v} \cdot d\underline{s} = \int_{\Omega} \varrho\underline{f_e} \; d\Omega - \oint_{S} p \cdot ds + \oint_{S} \underline{\underline{\tau}} \cdot d\underline{s} \tag{2.25}$$

or, in differential form:

$$\frac{\partial}{\partial t}(\varrho\underline{v}) + \nabla \cdot (\varrho\underline{v} \otimes \underline{v} + p\underline{\underline{I}} - \underline{\underline{\tau}}) = \varrho\underline{f_e}. \tag{2.26}$$

With

$$\nabla \cdot (\varrho\underline{v} \otimes \underline{v}) \equiv \underline{v} \cdot \nabla \cdot (\varrho\underline{v}) + \varrho(\underline{v} \cdot \nabla)\underline{v} \tag{2.27}$$

and the continuum equation 2.18, the non-conservative formulation reads

$$\varrho \frac{d\underline{v}}{dt} \;=\; \varrho \frac{\partial \underline{v}}{\partial t} \;+\; \varrho(\underline{v}\cdot\nabla)\underline{v} \;=\; -\nabla p \;+\; \nabla\cdot\underline{\underline{\tau}} \;+\; \varrho\underline{f_e}. \tag{2.28}$$

For the derivation of the Navier-Stokes equation, a material law is introduced assuming Newtonian fluids, i.e. stress and strain rate are linearly dependent. The viscous shear stress tensor is hereby given as

$$\tau_{i,j} \;=\; \mu\left[\left(\frac{\partial v_j}{\partial x_i}+\frac{\partial v_i}{\partial x_j}\right) \;-\; \frac{2}{3}(\nabla\cdot\underline{v})\;\delta_{i,j}\right] + \mu'(\nabla\cdot\underline{v})\;\delta_{i,j} \tag{2.29}$$

with the dynamic shear viscosity μ and the dynamic bulk or volume viscosity μ'. The latter is in most practical applications negligible. However, for some widely used Lattice Boltzmann collision schemes it becomes numerically significant (c.f. section 3.4) or is even set on purpose to gain a damping of sound pressure waves.

Now the divergence of the material law 2.29 can be simplified for spatially constant viscosity:

$$\begin{aligned}(\nabla\cdot\underline{\underline{\tau}})_i \;&=\; \left[\mu\left(\frac{\partial^2 v_j}{\partial x_i \partial x_j} \;+\; \frac{\partial^2 v_i}{\partial x_j^2} \;-\; \frac{2}{3}\frac{\partial^2 v_j}{\partial x_i \partial x_j}\right)\right] + \mu'\left[\nabla(\nabla\cdot\underline{v})\right]_i = \\ &=\; \mu\left[\Delta\underline{v}+\frac{1}{3}\nabla(\nabla\cdot\underline{v})\right]_i + \mu'\left[\nabla(\nabla\cdot\underline{v})\right]_i\end{aligned} \tag{2.30}$$

Using equation 2.28, the Navier-Stokes equation is derived:

$$\varrho\frac{\partial\underline{v}}{\partial t} \;+\; \varrho(\underline{v}\cdot\nabla)\underline{v} \;=\; -\nabla p \;+\; \mu\left[\Delta\underline{v}+\frac{1}{3}\nabla(\nabla\cdot\underline{v})\right] \;+\; \mu'\nabla(\nabla\cdot\underline{v}) \;+\; \varrho\underline{f_e}. \tag{2.31}$$

For incompressible flow with a divergence free velocity field, equation 2.31 turns into the incompressible Navier-Stokes equation:

$$\varrho\frac{\partial\underline{v}}{\partial t} \;+\; \varrho(\underline{v}\cdot\nabla)\underline{v} \;=\; -\nabla p \;+\; \mu\Delta\underline{v} \;+\; \varrho\underline{f_e}. \tag{2.32}$$

For inviscid flow, it becomes the Euler equation:

$$\varrho\frac{\partial\underline{v}}{\partial t} \;+\; \varrho(\underline{v}\cdot\nabla)\underline{v} \;=\; -\nabla p \;+\; \varrho\underline{f_e}. \tag{2.33}$$

2.4 Energy Equation

Next, the scalar quantity $U = \varrho E$ per unit volume is considered, with E being the energy per unit density. E consists of the inner energy e and, regarding the movement of the center of gravity itself, the kinetic energy $\underline{v}^2/2$:

$$E = e + \frac{\underline{v}^2}{2}. \tag{2.34}$$

The convective flux is according to equation 2.6

$$\underline{F_c} \;=\; \varrho E \underline{v} = \varrho \underline{v}(e + \frac{\underline{v}^2}{2}). \tag{2.35}$$

The diffusive term can be expressed by Fourier's law:

$$\underline{F_d} \;=\; -\kappa \nabla T. \tag{2.36}$$

The volume sources for energy are split into those by external force $\underline{f_e}$ and those by general heat sources q_h, e.g. by radiation or chemical reaction:

$$Q_v \;=\; \varrho \; \underline{f_e} \; \underline{v} + q_h. \tag{2.37}$$

For the surface sources, the work dues to stress is remaining:

$$\underline{Q_s} \;=\; \underline{\underline{\sigma}} \cdot \underline{v} \;=\; -p\underline{v} \;+\; \underline{\underline{\tau}} \cdot \underline{v}. \tag{2.38}$$

Inserting all these terms into the scalar conservation equation 2.3 result in the integral form of the energy equation:

$$\int_\Omega \frac{\partial}{\partial t}(\varrho E)\; d\Omega \;+\; \oint_S \varrho E \underline{v} \cdot d\underline{s} \;=\; \oint_S \kappa \cdot \nabla T \cdot d\underline{s} \;+\; \int_\Omega (\varrho \; \underline{f_e} \; \underline{v} + q_h)\; d\Omega \;+\; \oint_S \underline{\underline{\sigma}} \cdot \underline{v} \cdot d\underline{s}. \tag{2.39}$$

Applying the divergence theorem, again subject to the condition of C^1-continuity, leads to the differential formulation of the energy equation:

$$\frac{\partial}{\partial t}(\varrho E) \;+\; \nabla \cdot (\varrho E \underline{v}) \;= \nabla \cdot (\kappa \cdot \nabla T) \;+\; (\varrho \; \underline{f_e} \; \underline{v} + q_h) \;+\; \nabla \cdot (\underline{\underline{\sigma}} \cdot \underline{v}). \tag{2.40}$$

Chapter 3

Lattice Boltzmann Method

3.1 Boltzmann Equation

By using the classical Navier-Stokes equations for a flow problem, the inquired state variables are themselves directly part of the constitutive equations, defined on a time and space domain, as it has been seen in the previous chapter.

The Lattice Boltzmann Method (LBM) is a different approach. The domain is extended virtually with a molecular propagation speed. Now, as the degree of freedom of the domain is increasing, fluid flow can be described by a single quantity, namely the so-called density distribution function f. This implies that the evolution of a fluid can be broken down to a single evolution equation. The inquired state variables are computed indirectly by moments of the distribution function.

With the density distribution function, the LBM uses an average of the molecular state and becomes therefore basically a statistical method. The analogies to statistical concepts are immanent and will be pointed out below.

The benefit of the LBM is described by the fact that the underlying evolution equation becomes compact in a way that allows for an efficient implementation. This comes for the price of an involved theoretical analysis of the scheme. The following description of the fundamentals of the LBM is based on the work by Hänel [23], Krafczyk [35] and Succi [54].

3.1.1 Density Distribution Function

The physical domain of the LBM, the so-called phase-space, consists of position $\underline{x}$ and propagation speed $\underline{c}$. The distribution function of a fluid at a certain point in time t specifies the mass density in phase-space

$$f(t, \underline{x}, \underline{c}) = \frac{dm(t, \underline{x}, \underline{c})}{dx\ dy\ dz\ dc_x\ dc_y\ dc_z}. \tag{3.1}$$

Descriptively, f consists of the distinctive part of molecules in a control volume at a certain spot $\underline{x}$ propagating all with a velocity within an interval $[\underline{c}, \underline{c} + d\underline{c}]$.

3.1.2 Moments of the Density Distribution Function

The moments of the density distribution function are defined as in stochastics, based on the domain of propagation speed $\underline{c}$. A moment therefore represents an average state within a control volume. In order to have physical significance, the number of molecules in that volume has to be sufficient, i.e. the average state must not be influenced by statistical noise of specific molecules. This is equivalent with the prerequisite of continuum.

Raw moments are defined as

$$M_{x^l y^m z^n} = \int_{\underline{c}} c_x^l \; c_y^m \; c_z^n \; f \; d\underline{c}, \tag{3.2}$$

central moments relative to the bulk velocity $\underline{v}$

$$K_{x^l y^m z^n} = \int_{\underline{c}} (c_x - v_x)^l \; (c_y - v_y)^m \; (c_z - v_z)^n \; f \; d\underline{c}. \tag{3.3}$$

The sum of $l + m + n$ designates the order of the moment. Common moments are:

$$\varrho = \int_{\underline{c}} f \; d\underline{c} \qquad \text{mass density} \tag{3.4}$$

$$\varrho \underline{v} = \int_{\underline{c}} \underline{c} \; f \; d\underline{c} \qquad \text{momentum density} \tag{3.5}$$

$$\varrho v_\alpha v_\beta + p\delta_{\alpha\beta} - \tau_{\alpha\beta} = \int_{\underline{c}} c_\alpha c_\beta \; f \; d\underline{c} \qquad \text{momentum flux tensor} \tag{3.6}$$

$$p\delta_{\alpha\beta} - \tau_{\alpha\beta} = \int_{\underline{c}} (c_\alpha - v_\alpha) \; (c_\beta - v_\beta) \; f \; d\underline{c} \qquad \text{stress tensor} \tag{3.7}$$

The derivation of equation 3.6 and 3.7 is shown in detail in section 3.4 for the discrete lattice Boltzmann equation.

3.1.3 Boltzmann Equation

In a moving reference system, changes of the density distribution of a fluid can physically only be caused by collision of molecules. Let $\Omega(f(t, \underline{x}, \underline{c}))$ be a general expression of a change of f by collision. A simplified form of the Boltzmann equation reads accordingly:

$$\frac{Df}{Dt} = \frac{\partial f}{\partial t} + \frac{\partial x_i}{\partial t} \cdot \frac{\partial f}{\partial x_i} + \frac{\partial c_i}{\partial t} \cdot \frac{\partial f}{\partial c_i} = \Omega(f). \tag{3.8}$$

The third term of partial derivatives represents the influence of external forces $\underline{F}$ on the mass m in the control volume. An equivalent formulation with all source terms on the right hand side is

$$\frac{\partial f}{\partial t} + \underline{c} \cdot \nabla_{\underline{x}} f = \Omega(f) - \frac{\underline{F}}{m} \cdot \nabla_{\underline{c}} f. \tag{3.9}$$

The collision term $\Omega(f)$ consists of a complex integral functional of the distribution function itself, involving differential cross sections and a specific atomar model (cf. Hänel [23], Chapman and Cowling [9]). For the LBM, a linear approximation will be used, which is described later on in section 3.2.3.

3.1.4 From Boltzmann Equation to Continuity Equation

The zeroth moment of the Boltzmann equation 3.9 for a physical system without an external source term results in

$$\int_{\underline{c}} \left[\frac{\partial f}{\partial t} + \underline{c} \cdot \nabla_{\underline{x}} f \right] d\underline{c} = \int_{\underline{c}} \Omega(f) \, d\underline{c} \tag{3.10}$$

$$\Longrightarrow \frac{\partial}{\partial t} \int_{\underline{c}} f \, d\underline{c} + \int_{\underline{c}} \nabla_{\underline{x}} \cdot (\underline{c} \cdot f) \, d\underline{c} = \int_{\underline{c}} \Omega(f) \, d\underline{c}. \tag{3.11}$$

Collision does not change the total mass of the fluid in a certain moving reference volume:

$$\frac{\partial}{\partial t} \int_{\underline{c}} f \, d\underline{c} \; + \; \nabla \cdot \int_{\underline{c}} \underline{c} \cdot f \, d\underline{c} = 0 \tag{3.12}$$

Provided the collision of gas molecules was fully elastic, the collision term would change the total momentum neither. The continuity equation 2.18 results directly from the zeroth moment of the Boltzmann equation:

$$\frac{\partial}{\partial t} \varrho \; + \; \nabla \cdot (\varrho \underline{v}) = 0 \tag{3.13}$$

The Navier-Stokes equation 2.31 can be derived by the first moment of equation 3.9. However, this analysis will be more involved due to the consideration of non-equilibrium terms being not conserved during collision. The appropriate method will be discussed in chapter 3.4.

3.2 Solution of the Boltzmann Equation

3.2.1 General Solution of Simplified Boltzmann Equation

The Boltzmann equation 3.9 is now further examined without the force term:

$$\frac{\partial f}{\partial t} + \underline{c} \cdot \nabla_{\underline{x}} f = \Omega(f). \tag{3.14}$$

Details on implementing external forcing with LBM can be found e.g. in Guo et al. [22]. Suppose the collision term of equation 3.14 was simplified so that it depends only on the initial condition. Equation 3.14 then turns into an inhomogeneous linear transport equation with constant coefficients. Its unique solution is obtained by (cf. Evans [15]):

$$f(t, \underline{x}, \underline{c}) = f(0, \underline{x} - \underline{c}t, \underline{c}) + \int_{s=0}^{t} \Omega\left(f(s, \underline{x} - \underline{c} \cdot (t - s))\right)\ ds \tag{3.15}$$

The integral on the right hand side of equation 3.15 is the sum of all collision events along the trajectory of the moving volume. Eventually, equation 3.15 shows already the two distinctive algorithmic steps of the LBM: First, the propagation of the distribution function along its characteristic, i.e. the solution of the homogeneous transport equation,

$$f(t, \underline{x}, \underline{c}) = f(0, \underline{x} - \underline{c}t, \underline{c}), \tag{3.16}$$

second, the change of the distribution function by collision,

$$\Delta f_{\text{collision}} = \int_{s=0}^{t} \Omega\left(f(s, \underline{x} - \underline{c} \cdot (t - s))\right)\ ds. \tag{3.17}$$

For a discrete time stepping, the collision integral over time reduces to a single collision event. In that case, the sequence of the solution steps can be turned around: First the impact of collision, leading to a post-collision state f^*:

$$f^*(t, \underline{x}, \underline{c}) = f(t, \underline{x}, \underline{c}) + \Delta f_{\text{collision}}(t, \underline{x}, \underline{c}), \tag{3.18}$$

second, the streaming step:

$$f(t + \Delta t, \underline{x} + \Delta t \cdot \underline{c}, \underline{c}) = f^*(t, \underline{x}, \underline{c}). \tag{3.19}$$

3.2.2 Equilibrium Distribution Function

A control volume with a constant density distribution function over time represents an equilibrium state. The mathematical formulation is accordingly

$$\frac{Df}{Dt} = \Omega(f) \equiv 0. \tag{3.20}$$

For this case, the analytical equilibrium solution of the collision integral in an ideal gas is given by the Maxwell distribution (cf. Hänel [23]):

$$f(\varrho, \underline{c}, \underline{v})^{eq} = \frac{\varrho}{(2\pi RT)^{3/2}} \exp\left(-\frac{(\underline{c}-\underline{v})^2}{2RT}\right). \tag{3.21}$$

R denotes the universal gas constant, T the temperature. The square root of their product is proportional to the mean thermal molecular speed c_0 (cf. Hänel [23]):

$$c_0 = \sqrt{3RT} \tag{3.22}$$

Equation 3.21 represents a scaled three dimensional normal distribution with arithmetic mean $\underline{v}$ and speed of sound as standard deviation $c_s = \sqrt{RT}$. In the same way the normal distribution in stochastics emerges from random variables of independent events, a prerequisite for the Maxwell distribution is as well that the single collisions are independent, i.e. binary.

3.2.3 Collision Modeling

The evaluation of the collision term of the Boltzmann equation 3.8 for the LBM requires a numerical approximation of the rather complex integral function. The term is simplified by its effective impact of conditioning the control volume towards an equilibrium state. This simplification gives rise to the solution of equation 3.15. $\Omega(f)$ is linearized to a function subtracting the non-equilibrium of the density distribution $f^{(neq)}$ by a certain rate ω per unit time, namely the collision frequency, e.g. with the frequently used Bhatnagar-Gross-Krook (BGK) model [5]:

$$\Omega(f) = -\omega \cdot (f - f^{(eq)}) =: -\omega \cdot f^{(neq)} \tag{3.23}$$

The advanced collision transformation into moment space is described later in section 3.5.2. The modeling of collision by non-equilibrium relaxation is valid only for the collision dominated case, i.e. the mean free path length of the molecules is small compared to the macroscopic length scale of the problem (corresponding to a small Knudsen number, cf. section 3.2.4).

The collision frequency ω is the reverse of the mean collision time τ, also known as relaxation time. The relaxation time equals the mean time between two molecular collisions. With the mean free path length l_f between two collisions, equation 3.23 can be expressed as

$$\Omega(f) = -\frac{c_0}{l_f} \cdot (f - f^{(eq)}) \tag{3.24}$$

However, as shown later, the collision frequency for the LBM is computed from the analysis regarding the viscous properties of the fluid and does not resemble a physical one. The distance between two collisions in an actual implementation is a property of the grid, and not a physical mean free path.

3.2.4 Nondimensionalization of the BGK Boltzmann Equation

Applying the BGK scheme 3.24 to the Boltzmann equation 3.14 without external forces results in

$$\frac{\partial f}{\partial t} + \underline{c} \cdot \nabla\ f = -\frac{c_0}{l_f} \cdot (f - f^{(eq)}). \tag{3.25}$$

For further examination, equation 3.25 is transformed according to the Buckingham Π theorem to a characteristic, non-dimensional equation (cf. Buckingham [8]). Including the variables of equation 3.21 and a characteristic macroscopic length L, there is a set of 9 relevant variables, t, $\underline{x}$, l_f, L, c_0, $\underline{v}$, $\underline{c}$, ϱ and f. A specific set of repeating variables L, c_0 and ϱ will lead to the following Π groups:

$$\pi_1 = \frac{t \cdot c_0}{L} =: \hat{t} \tag{3.26}$$

$$\pi_2 = \frac{\underline{x}}{L} =: \underline{\hat{x}} \tag{3.27}$$

$$\pi_3 = \frac{l_f}{L} =: \mathrm{Kn} \quad \text{(Knudsen number)} \tag{3.28}$$

$$\pi_4 = \frac{\underline{v}}{c_0} =: \mathrm{Ma} \quad \text{(local Mach number)} \tag{3.29}$$

$$\pi_5 = \frac{\underline{c}}{c_0} =: \underline{\xi} \tag{3.30}$$

$$\pi_6 = \frac{f \cdot c_0^3}{\varrho^3} =: \hat{f} \tag{3.31}$$

This results in the non-dimensional formulation of the BGK Boltzmann equation

$$\frac{\partial \hat{f}}{\partial \hat{t}} + \underline{\xi} \cdot \nabla_{\underline{\hat{x}}}\ \hat{f} = -\frac{1}{\mathrm{Kn}} \cdot (\hat{f} - \hat{f}^{(eq)}) = \Omega(\hat{f}). \tag{3.32}$$

The hat on top of non-dimensional quantities will be omitted below in case that it is obviously the non-dimensional formulation, e.g. if ξ appears to be the propagation speed.

3.2.5 Lattice Unit Set

For computation, the time and grid scale is further reduced by units of time and grid spacing, marked by double hats. The magnitude of the propagation speed ξ changes appropriately to 1.

$$\hat{\hat{t}} = \frac{\hat{t}}{\Delta\hat{t}} \quad , \quad \hat{\hat{x}} = \frac{\hat{x}}{\Delta\hat{x}} \tag{3.33}$$

$$\hat{\hat{\xi}} = \frac{\Delta\hat{\hat{x}}}{\Delta\hat{\hat{t}}} \equiv 1 \tag{3.34}$$

This has the important implication that some of the raw moments 3.2 are no longer independent due to an aliasing effect (cf. section 3.3).

3.3 Lattice Boltzmann Equation

For the numerical treatment of the Boltzmann equation, a finite difference discretization is applied in time and phase space. The discretization in phase space is performed on an equidistant square lattice with uniform grid spacing $\Delta x = \Delta y = \Delta z$. Position and propagation speed are discretized on the same grid.

Figure 3.1 shows the finite discrete velocity models (FDVMs) commonly used with the LBM. Its labeling follows the notation D<*dim*>Q<*num*>, where <*dim*> indicates the dimension of the model and <*num*> the number of discrete velocities. The zero velocity is also member of the set, indexed by 0.

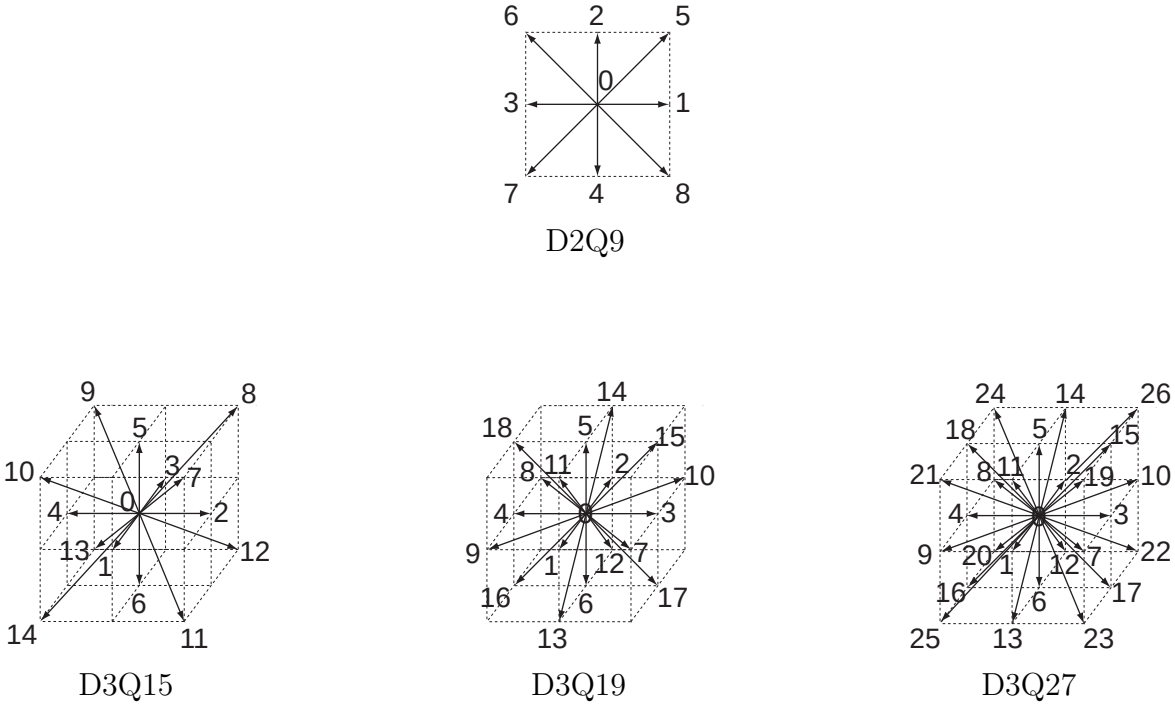

Figure 3.1: FDVM schemes

The continuous propagation speed $\underline{\xi}$ in equation 3.30 turns into a set of discrete velocities $\underline{\xi}_i$. The arbitrary numbering of the directions used in figure 3.1 is often replaced by the index $l_x, m_y, n_z \in [-1, 0, 1], [-1, 0, 1], [-1, 0, 1]$. Commonly and also throughout this thesis, the 1D and 2D models are specified as follows, for D1Q3:

$$\underline{\xi}_i = \begin{cases} 0 & \text{for } i = 0 \\ 1 \cdot c_0 & \text{for } i = 1 \\ -1 \cdot c_0 & \text{for } i = 2, \end{cases} \tag{3.35}$$

and D2Q9:

$$\underline{\xi}_i = \begin{cases} (0,0) & \text{for } i = 0 \\ \left(\cos\left[\frac{\pi}{2}(i-1)\right],\ \sin\left[\frac{\pi}{2}(i-1)\right]\right) \cdot c_0 & \text{for } i \in 1-4 \\ \left(\cos\left[\frac{\pi}{4}(2i-9)\right], \sin\left[\frac{\pi}{4}(2i-9)\right]\right) \cdot \sqrt{2} \cdot c_0 & \text{for } i \in 5-9. \end{cases} \tag{3.36}$$

The continuous distribution function $f(t, \underline{x}, \underline{\xi})$ turns into a vector

$$f(t, \underline{x}, \underline{\xi}_i) = \widetilde{f}_i(t, \underline{x}). \tag{3.37}$$

A constant time step Δt, first order finite differences and a forward time stepping applied on equation 3.32 results in

$$\frac{\widetilde{f}_i(t+\Delta t, \underline{x}) - \widetilde{f}_i(t, \underline{x})}{\Delta t} + c_0 \frac{\widetilde{f}_i(t+\Delta t, \underline{x} + \underline{\xi}_i \Delta t) - \widetilde{f}_i(t+\Delta t, \vec{x})}{\Delta x} = \Omega. \tag{3.38}$$

With the propagation speed $c_0 = \Delta x / \Delta t$, this becomes the so-called Lattice Boltzmann Equation (LBE)

$$\widetilde{f}_i(t+\Delta t, \underline{x} + \underline{\xi}_i \Delta t) = \widetilde{f}_i(t, \underline{x}) + \Delta t \cdot \Omega. \tag{3.39}$$

According to equation 3.22, this entails that the LBM as shown does only cover isothermal flow. For the calculation of moments, the integral of equation 3.2 has to be treated numerically:

$$M_{x^l y^m z^n} = \int_{\underline{\xi}} \xi_x^l\ \xi_y^m\ \xi_z^n\ f(t, \underline{x}, \underline{\xi})\ d\underline{\xi} = \sum_i \gamma_i \cdot \xi_{i,x}^l\ \xi_{i,y}^m\ \xi_{i,z}^n\ \widetilde{f}_i(t, \underline{x}), \tag{3.40}$$

with specific integration weights γ_i, which are merged with $\widetilde{f}_i$ to a discrete distribution function f_i:

$$f_i(t, \underline{x}) := \gamma_i \cdot \widetilde{f}_i(t, \underline{x}). \tag{3.41}$$

In the lattice unit set, all even powers of the components of the vector $\underline{\xi}$ become one respectively zero, so some of the higher moments become linear dependent on lower ones:

$$\begin{aligned} \hat{\hat{M}}_{x^l y^m z^n} &= \sum_i \hat{\hat{\xi}}_{i,x}^l\ \hat{\hat{\xi}}_{i,y}^m\ \hat{\hat{\xi}}_{i,z}^n\ f_i(\hat{\hat{t}}, \hat{\hat{\underline{x}}}) = \\ &= \sum_i \hat{\hat{\xi}}_{i,x}^{(l+2j_l)}\ \hat{\hat{\xi}}_{i,y}^{(m+2j_m)}\ \hat{\hat{\xi}}_{i,z}^{(n+2j_n)}\ f_i(\hat{\hat{t}}, \hat{\hat{\underline{x}}}) = \\ &= \hat{\hat{M}}_{x^{(l+2j_l)} y^{(m+2j_m)} z^{(n+2j_n)}} \quad \forall l, m, n \in \mathbb{N} \text{ and } \forall j_l, j_m, j_n \in \mathbb{N}_0 \end{aligned} \tag{3.42}$$

This aliasing effect is important for the selection of a proper basis for transformation from distribution into moment space, as seen later in section 3.4.2.

The equilibrium distribution 3.21, as part of the linear model of the collision operator, has to be discretized, too. For numerical integration the exponential function 3.21 is approximated by a polynomial. This is done by a Taylor series expansion for the Mach number truncated after the second order term:

$$\widetilde{f}^{eq} = \varrho \cdot \underbrace{\frac{1}{(2\pi c_s^2)^{3/2}} \cdot \exp\left(-\frac{1}{2}\frac{\underline{\xi}^2}{c_s^2}\right)}_{:=t_i/\gamma_i} \cdot \left(1 + \frac{\underline{\xi}\cdot\underline{v}}{c_s^2} - \frac{1}{2}\left(\frac{\underline{v}^2}{c_s^2} - \frac{(\underline{\xi}\cdot\underline{v})^2}{c_s^4}\right)\right) + O(\mathrm{Ma}^3). \tag{3.43}$$

Due to the resulting error of $O(\mathrm{Ma}^3)$, the application of LBM is restricted to low mach number flow. Two sampling points per space dimension would be enough to integrate the second order polynomial 3.43 accurately, if the reference points could be chosen arbitrarily (cf. Karniadakis [32]). However, the grid stencil has to be space filling, symmetric and able to offer the possibility to recover shear forces (cf. section 3.4.2). The smallest suitable model has to have seven velocities (including the zero velocity), the smallest on a Cartesian grid would be a nine velocity model. The coefficients have to be determined by additional requirements.

Let f_i^{eq} be defined as:

$$f_i^{eq} := \widetilde{f}^{eq}(\underline{\xi}_i) \cdot \gamma_i. \tag{3.44}$$

The symmetry of the FDVM arrangement results in

$$\sum_i t_i \prod_k \xi_{i,\alpha}^{2n_\alpha+1} \equiv 0 \quad \forall\ n_\alpha \in \mathbb{N}_0 \text{ and } \alpha \in x, y, z. \tag{3.45}$$

The moments 3.4, 3.5 and 3.6 applied on f_i^{eq} together with 3.45 result in (cf. Hänel [23]):

$$\varrho = \sum_i f_i^{eq} = \varrho \sum_i t_i + \frac{\varrho v_\alpha v_\beta}{2\ c_s^2}\left(\frac{1}{c_s^2}\sum_i t_i \xi_{i,\alpha}\xi_{i,\beta} - \delta_{\alpha\beta}\sum_i t_i\right) \tag{3.46}$$

$$\varrho v_\alpha = \sum_i \xi_{i,\alpha} f_i^{eq} = \frac{\varrho v_\alpha}{c_s^2}\sum_i t_i \xi_{i,\alpha}\xi_{i,\beta}\delta_{\alpha\beta} \tag{3.47}$$

$$\begin{aligned}\varrho v_\alpha v_\beta + p\delta_{\alpha\beta} &= \sum_i \xi_{i,\alpha}\xi_{i,\beta} f_i^{eq} = \varrho \sum_i t_i \xi_{i,\alpha}\xi_{i,\beta} \\ &+ \frac{\varrho v_\alpha v_\beta}{2\ c_s^2}\left(\frac{1}{c_s^2}\sum_i t_i \xi_{i,\alpha}\xi_{i,\beta}\xi_{i,\gamma}\xi_{i,\delta} - \delta_{\alpha\beta}\sum_i t_i \xi_{i,\gamma}\xi_{i,\delta}\right)\end{aligned} \tag{3.48}$$

The shear stress tensor, being derived in the next section, has to vanishes in equation 3.48 for equilibrium. From those equations, insertion of a zero velocity and subsequent variation of indices lead to:

$$\begin{aligned}
\sum_i t_i &= 1 \\
\sum_i t_i \xi_{i,\alpha} \xi_{i,\beta} &= c_s^2 \delta_{\alpha\beta} \\
\sum_i t_i \xi_{i,\alpha} \xi_{i,\beta} \xi_{i,\gamma} \xi_{i,\delta} &= c_s^4 (\delta_{\alpha\beta}\delta_{\gamma\delta} + \delta_{\alpha\gamma}\delta_{\beta\delta} + \delta_{\alpha\delta}\delta_{\beta\gamma})
\end{aligned}$$

Together with the equations 3.45, this leads to a total hierarchy:

$$\sum_i t_i = 1 \tag{3.49}$$

$$\sum_i t_i \xi_{i,\alpha} = 0 \tag{3.50}$$

$$\sum_i t_i \xi_{i,\alpha} \xi_{i,\beta} = c_s^2 \delta_{\alpha\beta} \tag{3.51}$$

$$\sum_i t_i \xi_{i,\alpha} \xi_{i,\beta} \xi_{i,\gamma} = 0 \tag{3.52}$$

$$\sum_i t_i \xi_{i,\alpha} \xi_{i,\beta} \xi_{i,\gamma} \xi_{i,\delta} = c_s^4 (\delta_{\alpha\beta}\delta_{\gamma\delta} + \delta_{\alpha\gamma}\delta_{\beta\delta} + \delta_{\alpha\delta}\delta_{\beta\gamma}) \tag{3.53}$$

By variation of α, β and the other indices of the Kronecker symbols indices, the t_is can be calculated for every FDVM (cf. Hänel [23]). The weighting factors are listed in table 3.1 with

$$p(i) = \xi_i^2 \tag{3.54}$$

for the models of figure 3.1 and the one dimensional D1Q3 discretization.

Model	$p = \xi_i^2$	$t_{p\equiv 0}$	$t_{p\equiv 1}$	$t_{p\equiv 2}$	$t_{p\equiv 3}$
D1Q3	0, 1	2/3	1/6	-	-
D2Q9	0, 1, 2	4/9	1/9	1/36	-
D3Q15	0, 1, 3	2/9	1/9	-	1/72
D3Q19	0, 1, 2	1/3	1/18	1/36	-
D3Q27	0, 1, 2, 3	8/27	2/27	1/54	1/216

Table 3.1: Weighting factors for FDVM equilibrium distribution

It can be seen directly from equation 3.51 with $\alpha = \beta$ that for all the discretized models there is a constant speed of sound with

$$c_s \equiv \sqrt{1/3} \cdot c_0. \tag{3.55}$$

The discretized Maxwell equilibrium distribution is accordingly given by:

$$f_i^{(eq)}(\varrho, \underline{v}) = t_i \varrho \left[1 + \frac{\underline{\xi}_i \cdot \underline{v}}{c_s^2} + \frac{1}{2} \left(\left(\frac{\underline{\xi}_i \cdot \underline{v}}{c_s^2} \right)^2 - \frac{\underline{v}^2}{c_s^2} \right) \right] \tag{3.56}$$

or, by substituting equation 3.55:

$$f_i^{(eq)}(\varrho, \underline{v}) = t_i \varrho \left[1 + 3\frac{\underline{\xi}_i \cdot \underline{v}}{c_0^2} + \frac{9}{2} \left(\frac{\underline{\xi}_i \cdot \underline{v}}{c_0^2} \right)^2 - \frac{3}{2} \frac{\underline{v}^2}{c_0^2} \right] \tag{3.57}$$

The Lattice Boltzmann equation 3.39 with the BGK collision model from equation 3.24 is referred to as the Lattice BGK (LBGK) equation:

$$f_i(t + \Delta t, \underline{x} + \Delta t \cdot \underline{\xi}_i) = f_i(t, \underline{x}) - \Delta t \cdot \omega \cdot (f_i(t, \underline{x}) - f_i^{(eq)}(\varrho, \underline{v})). \tag{3.58}$$

3.4 Analysis of the LBGK Equation

The Boltzmann equation, as described in section 3.1, emerges from kinetic theory, and it is primarily unclear how it is related to the macroscopic equations of chapter 2. Although the link to the macroscopic quantities by computation of moments of the distribution function is provided, it is not yet shown whether the moments are solving the Navier-Stokes equations. In this section an analytical method is described showing the relation of the LBM to the Navier-Stokes equations. The analysis is done for the LBGK equation, which is the relevant equation for the implementation.

From equation 3.32, it can be seen that the LBE constitutes of a perturbative partial differential equation, where a well known analytical solution is disturbed by a nonlinear term with a leading smallness parameter, in that case the Knudsen number Kn. In equation 3.58, this perturbation parameter is $\tau = 1/\omega$, and the partial differential equation is obtained from a Taylor series expansion of the left-hand side of equation 3.58. A general approach for solving those problems is to expand the solution in this parameter. However, other parameters might depend on even multiple scales of it, and an approximate solution might diverge. The remedy is to introduce multiple time scales (cf. Bender and Orszag [2]).

For the LBE, two time scales are relevant with regard to the macroscopic behavior of the fluid: While the first one determines fast, acoustic effects, the second one governs the slow, diffusive scale (cf. Junk et al. [30]). To cover both effects at the same time, it is necessary to resolve also the time scale as a perturbation expansion, leading to a multiple-scale analysis. The Chapman-Enskog procedure does this for the LBE. The sketch of its principle in section 3.4.1 is based on Hou et al. [27].

Practically, only one of the two time scales can be used. Therefore it is reasonable to consider both scalings separately. This is essentially done by the asymptotic analysis, which is not covered here. Details can be found e.g. in the article by Junk et al. [30].

3.4.1 Chapman-Enskog Analysis

For the Chapman-Enskog expansion, τ, respectively the Knudsen number, cannot simply be used as a perturbation parameter in the LBGK equation 3.58, because a scaling of τ would have to be applied also on other time scales. Therefore τ and all other times variables are scaled by a formal perturbation parameter ϵ:

$$f_i(t + \epsilon\Delta t, \underline{x} + \epsilon\Delta t \cdot \underline{\xi}_i) = f_i(t, \underline{x}) - \epsilon\Delta t \cdot \frac{1}{\epsilon\tau} \cdot (f_i(t, \underline{x}) - f_i^{(eq)}(\varrho, \underline{v})). \tag{3.59}$$

Δx is scaled as Δt by ϵ, resulting in a constant speed of sound $c_s = 1/\sqrt{3} \cdot \Delta x/\Delta t$. The propagation speed $\underline{\xi}$ therefore also stays constant, which is referred to as the acoustic scaling (cf. Junk et al. [30], for diffusive scaling $\Delta x \sim \epsilon^2$).

The left hand side of equation 3.59 can now be Taylor series expanded in ϵ:

$$f_i(t + \epsilon\Delta t, \underline{x} + \epsilon\Delta t \cdot \underline{\xi}_i) = \sum_{n=0}^{\infty} \frac{\epsilon^n}{n!} (\Delta t \frac{\partial}{\partial t} + \Delta t \xi_{i,\alpha} \frac{\partial}{\partial x_\alpha})^n f_i(t, \underline{x}). \tag{3.60}$$

This, substituted into equation 3.59, results in:

$$\epsilon(\Delta t\frac{\partial}{\partial t}+\Delta t\xi_{i,\alpha}\frac{\partial}{\partial x_\alpha})f_i(t,\underline{x})+\frac{\epsilon^2}{2}(\Delta t\frac{\partial}{\partial t}+\Delta t\xi_{i,\alpha}\frac{\partial}{\partial x_\alpha})^2 f_i(t,\underline{x})+\frac{\Delta t}{\tau}(f_i-f_i^{(eq)})+O(\epsilon^3)=0. \quad (3.61)$$

As already motivated, f is subsequently expanded as power series of the formal perturbation parameter ϵ:

$$f_i(t,\underline{x})=\sum_{n=0}^{\infty}\epsilon^n f_i^{(n)}. \quad (3.62)$$

In order to separate the time scales and thus gain a convergent approximate solution, those time scales are established in orders of ϵ:

$$t_n := \epsilon^n \cdot t. \quad (3.63)$$

If t is substituted by a summation of all different time scales,

$$t \to \sum_{n=0}^{\infty} t_n, \quad (3.64)$$

the derivative with respect to t changes to

$$\frac{\partial}{\partial t} \to \sum_{n=0}^{\infty}\frac{\partial t_n}{\partial t}\frac{\partial}{\partial t_n}=\sum_{n=0}^{\infty}\epsilon^n\frac{\partial}{\partial t_n}. \quad (3.65)$$

Equations 3.62 and 3.65 are finally substituted into equation 3.61 and sorted by orders of ϵ. All terms of different orders have to be zero for any $\epsilon \geq 0$:

For $O(\epsilon^0)$:

$$f_i^{(0)} = f_i^{(eq)} \quad (3.66)$$

From equation 3.66 and the perturbative approach of equation 3.62, a power series around an equilibrium solution, can be concluded:

$$\sum_i f_i^{(n)} = \begin{cases}\varrho & \text{if } n=0\\ 0 & \text{if } n\neq 0\end{cases} \quad (3.67)$$

$$\sum_i \underline{\xi}_i f_i^{(n)} = \begin{cases}\varrho\underline{v} & \text{if } n=0\\ 0 & \text{if } n\neq 0\end{cases} \quad (3.68)$$

For $O(\epsilon^1)$:

$$\frac{\partial}{\partial t_0} f_i^{(0)} + \xi_{i,\alpha} \frac{\partial}{\partial x_\alpha} f_i^{(0)} + \frac{1}{\tau} f_i^{(1)} = 0 \tag{3.69}$$

The zeroth moment of equation 3.69 together with equation 3.67 is used to derive the continuum equation 2.18 for order $O(\epsilon)$:

$$\frac{\partial}{\partial t_0} \varrho \; + \; \nabla \cdot (\varrho \; \underline{v}) \; = \; 0. \tag{3.70}$$

Let $\underline{\underline{\Pi}}$ be the momentum flux tensor

$$\Pi_{\alpha,\beta}^{(n)} = \sum_i \xi_{i,\alpha} \xi_{i,\beta} f_i^{(n)} \tag{3.71}$$

The first moment of equation 3.69 together with equation 3.68 results in:

$$\frac{\partial}{\partial t_0} \varrho \; \underline{v} \; + \; \nabla \cdot \underline{\underline{\Pi}}^{(0)} \; = \; 0. \tag{3.72}$$

According to equation 3.66, the momentum flux tensor of the zeroth order equals that of the equilibrium distribution 3.56. Using equations 3.51 to 3.53, this results in:

$$\Pi_{\alpha,\beta}^{(0)} = \varrho c_s^2 \delta_{\alpha\beta} + \varrho v_\alpha v_\beta \tag{3.73}$$

Equation 3.72 resembles therefore the Euler equation 2.33 for order one of ϵ:

$$\frac{\partial}{\partial t_0} \varrho v_\alpha \; + \; \frac{\partial}{\partial x_\beta} (\varrho c_s^2 \delta_{\alpha\beta} + \varrho v_\alpha v_\beta) \; = \; 0, \tag{3.74}$$

Applying equations 2.27, 3.70 and the ideal gas law $\gamma \cdot p = \varrho c_s^2$ with specific heat ratio $\gamma \equiv 1$ for the LBM, one obtains:

$$\varrho \frac{\partial \underline{v}}{\partial t_0} \; + \; \varrho (\underline{v} \cdot \nabla) \underline{v} \; = \; -\nabla p. \tag{3.75}$$

For $O(\epsilon^2)$:

$$\frac{\partial}{\partial t_1} f_i^{(0)} + \left(\frac{\partial}{\partial t_0} + \xi_{i,\alpha} \frac{\partial}{\partial x_\alpha} \right) f_i^{(1)} + \frac{\Delta t}{2} \left(\frac{\partial}{\partial t_0} + \xi_{i,\alpha} \frac{\partial}{\partial x_\alpha} \right)^2 f_i^{(0)} + \frac{1}{\tau} f_i^{(2)} = 0 \tag{3.76}$$

Using equation 3.69 yields:

$$\frac{\partial}{\partial t_1} f_i^{(0)} + \left(1 - \frac{\Delta t}{2\tau} \right) \left(\frac{\partial}{\partial t_0} + \xi_{i,\alpha} \frac{\partial}{\partial x_\alpha} \right) f_i^{(1)} + \frac{1}{\tau} f_i^{(2)} = 0 \tag{3.77}$$

The zeroth moment results in:

$$\frac{\partial}{\partial t_1}\varrho = 0. \tag{3.78}$$

According to equation 3.70 and 3.65, this provides the total continuum equation from the first and second order of ϵ:

$$\boxed{\frac{\partial}{\partial t}\varrho \; + \; \nabla \cdot (\varrho \; \underline{v}) + O(\epsilon^2) \; = \; 0.} \tag{3.79}$$

With the first moment of equation 3.77 one obtains:

$$\frac{\partial}{\partial t_1}\varrho \; \underline{v} \; + \; \left(1 - \frac{\Delta t}{2\tau}\right) \nabla \cdot \underline{\underline{\Pi}}^{(1)} \; = \; 0. \tag{3.80}$$

The momentum flux tensor of order 1 can be expressed by 3.69 as:

$$\begin{aligned}
\Pi^{(1)}_{\alpha,\beta} &= \sum_i \xi_{i,\alpha}\xi_{i,\beta} f_i^{(1)} = -\tau \sum_i \xi_{i,\alpha}\xi_{i,\beta}\left(\frac{\partial}{\partial t_0} + \xi_{i,\gamma}\frac{\partial}{\partial x_\gamma}\right) f_i^{(0)} = \\
&= -\tau\left[\frac{\partial}{\partial t_0}\Pi^{(0)}_{\alpha,\beta} + \frac{\partial}{\partial x_\gamma}\sum_i \xi_{i,\alpha}\xi_{i,\beta}\xi_{i,\gamma} f_i^{(eq)}\right] \overset{(3.53)}{=} \\
&= -\tau\left[\frac{\partial}{\partial t_0}(\varrho c_s^2\delta_{\alpha\beta} + \varrho v_\alpha v_\beta) + \frac{\partial}{\partial x_\gamma}\varrho c_s^2 v_\delta(\delta_{\alpha\beta}\delta_{\gamma\delta} + \delta_{\alpha\gamma}\delta_{\beta\delta} + \delta_{\alpha\delta}\delta_{\beta\gamma})\right] = \\
&= -\tau\Bigg[c_s^2\delta_{\alpha\beta}\underbrace{\left(\frac{\partial}{\partial t_0}\varrho \; + \; \nabla\cdot(\varrho \; \underline{v})\right)}_{=0} + \frac{\partial}{\partial t_0}(\varrho v_\alpha v_\beta) + c_s^2\left(v_\beta\frac{\partial \varrho}{\partial x_\alpha} + v_\alpha\frac{\partial \varrho}{\partial x_\beta}\right) \\
&\qquad + \varrho c_s^2\left(\frac{\partial v_\beta}{\partial x_\alpha} + \frac{\partial v_\alpha}{\partial x_\beta}\right)\Bigg]
\end{aligned} \tag{3.81}$$

Hou et al. prove [27]:

$$\frac{\partial}{\partial t_0}(\varrho v_\alpha v_\beta) + c_s^2\left(v_\beta\frac{\partial \varrho}{\partial x_\alpha} + v_\alpha\frac{\partial \varrho}{\partial x_\beta}\right) = O(\mathrm{Ma}^3) \tag{3.82}$$

The error reflects the approximation of the equilibrium distribution 3.43. This leads to:

$$\Pi^{(1)}_{\alpha,\beta} = -\tau\varrho c_s^2\left(\frac{\partial v_\beta}{\partial x_\alpha} + \frac{\partial v_\alpha}{\partial x_\beta}\right) + O(\mathrm{Ma}^3) \tag{3.83}$$

Equation 3.80 and 3.83 result in:

$$\frac{\partial}{\partial t_1}\varrho v_\alpha \;-\; \frac{\partial}{\partial x_\beta}\varrho c_s^2\left(\tau-\frac{\Delta t}{2}\right)\left(\frac{\partial v_\beta}{\partial x_\alpha}+\frac{\partial v_\alpha}{\partial x_\beta}\right)+O(\mathrm{Ma}^3) \;=\; 0. \tag{3.84}$$

The total first moment for the first and second order of ϵ is finally derived with equation 3.74, 3.65 and 3.84:

$$\frac{\partial}{\partial t}\varrho v_\alpha+\frac{\partial}{\partial x_\beta}(\varrho v_\alpha v_\beta) \;=\; -\frac{\partial p}{\partial x_\alpha}+\frac{\partial}{\partial x_\beta}\epsilon\varrho c_s^2\left(\tau-\frac{\Delta t}{2}\right)\left(\frac{\partial v_\beta}{\partial x_\alpha}+\frac{\partial v_\alpha}{\partial x_\beta}\right)+O(\mathrm{Ma}^3)+O(\epsilon^2) \tag{3.85}$$

With equations 2.27, 3.79 and 2.30, this can be reformulated to (omitting the error term):

$$\boxed{\varrho\frac{\partial \underline{v}}{\partial t} \;+\; \varrho(\underline{v}\cdot\nabla)\underline{v} \;=\; -\nabla p \;+\; \left[\epsilon\varrho c_s^2\left(\tau-\frac{\Delta t}{2}\right)\right]\left[\left(\Delta\underline{v}+\frac{1}{3}\nabla(\nabla\cdot\underline{v})\right) \;+\; \frac{2}{3}\nabla(\nabla\cdot\underline{v})\right]} \tag{3.86}$$

The comparison with equation 2.31 shows that the appropriate moments of the solution of the LBGK equation provide a solution (within the specified error) to the compressible Navier-Stokes equation with a shear viscosity of

$$\mu=\left[\epsilon\varrho c_s^2\left(\tau-\frac{\Delta t}{2}\right)\right] \tag{3.87}$$

and a bulk viscosity of $\mu'=\frac{2}{3}\cdot\mu$. Equation 3.87 shows that the shear viscosity depends on the scaling parameter ϵ. Inferring from equations 3.79 and 3.85, the error with acoustic scaling is of the order $O(\Delta t^2)+O(\Delta x^2)$ per time step, with an additional error $O(\mathrm{Ma}^3)$ in the Navier-Stokes equation. For $n=(t_{\mathrm{end}}-t_0)/\Delta t$ time steps, the total error in time increases consequently to $O(\Delta t)$.

However, this is only valid for isothermal compressible systems. The given errors reflect neither a fully compressible system nor the error by the persistent divergence terms if used as approximation for incompressible flow.

3.4.2 Moment Basis

For the LBM, it is in some cases more adequate to use the representation of the problem in moment space. This refers especially to collision modeling (cf. section 3.5.2) or analysis of boundary conditions (cf. Bennet [3]). Basically every set of linear independent moments can be used. Due to the aliasing effect (cf. equation 3.42), some of the higher order moments loose their independence in lattice unit representation. For D2Q9, the only possible moment basis representation, apart from linear combined moments, would be:

$$\mathbb{B} := \{M_0, M_x, M_y, M_{x^2}, M_{xy}, M_{y^2}, M_{x^2y}, M_{xy^2}, M_{x^2y^2}\} \tag{3.88}$$

The solution of the corresponding linear system of equations results in:

$$\begin{aligned}
f_0 &= \phantom{\frac{1}{2}} \quad M_0 \; -M_{x^2} \; -M_{y^2} \; -M_{x^2y^2} \\
f_1 &= \frac{1}{2} \quad (M_x \; +M_{x^2} \; -M_{xy^2} - M_{x^2y^2}) \\
f_2 &= \frac{1}{2} \quad (M_y \; +M_{y^2} \; -M_{x^2y} - M_{x^2y^2}) \\
f_3 &= \frac{1}{2} \; (-M_x \; +M_{x^2} \; +M_{xy^2} - M_{x^2y^2}) \\
f_4 &= \frac{1}{2} \; (-M_y \; +M_{y^2} \; +M_{x^2y} - M_{x^2y^2}) \\
f_5 &= \frac{1}{4} \quad (M_{xy} + M_{x^2y} + M_{xy^2} + M_{x^2y^2}) \\
f_6 &= \frac{1}{4} \; (-M_{xy} + M_{x^2y} - M_{xy^2} + M_{x^2y^2}) \\
f_7 &= \frac{1}{4} \quad (M_{xy} - M_{x^2y} - M_{xy^2} + M_{x^2y^2}) \\
f_8 &= \frac{1}{4} \; (-M_{xy} - M_{x^2y} + M_{xy^2} + M_{x^2y^2})
\end{aligned} \tag{3.89}$$

Trivially one could see e.g. that shear forces could not be recovered with an orthogonal velocity model. In section 4.3.1, the moment decomposition will be used for the derivation of the accuracy of the Zou and He boundary conditions.

3.5 Incompressible LBM

3.5.1 SRT

As seen in section 3.4.1, the equilibrium equation 3.56 recovers the compressible continuity and Navier-Stokes equations. He and Luo [24] propose an alternative formulation for the single relaxation time (SRT) scheme of equation 3.59 to recover the incompressible Navier-Stokes equation with a constant hydrostatic density ϱ_0:

$$f_i^{(eq)}(\varrho, \underline{v}) = t_i \left[\varrho + \varrho_0 \left(\frac{\underline{\xi}_i \cdot \underline{v}}{c_s^2} + \frac{1}{2} \left[\left(\frac{\underline{\xi}_i \cdot \underline{v}}{c_s^2} \right)^2 - \frac{\underline{v}^2}{c_s^2} \right] \right) \right] \tag{3.90}$$

From equations 3.49 to 3.53, it can easily be derived:

$$\varrho = \sum_i f_i^{(eq)} \tag{3.91}$$

$$\underline{v}\varrho_0 = \sum_i \underline{\xi}_i f_i^{(eq)} \tag{3.92}$$

In the Chapman-Enskog derivation of section 3.4.1 with acoustic scaling, the zeroth moment of equation 3.69 results in:

$$\frac{\partial}{\partial t_0}\varrho + \nabla \cdot (\varrho_0 \, \underline{v}) = 0. \tag{3.93}$$

With the zeroth moment of equation 3.77, one obtains:

$$\frac{\partial}{\partial t_1}\varrho = 0. \tag{3.94}$$

Both combined yield:

$$\nabla \cdot \underline{v} + \frac{1}{\varrho_0}\frac{\partial}{\partial t}\varrho + O(\epsilon^2) = 0. \tag{3.95}$$

With equations 3.49 to 3.53, the first moment of equation 3.69 equals:

$$\varrho_0 \frac{\partial}{\partial t_0} v_\alpha + \frac{\partial}{\partial x_\beta}(\varrho c_s^2 \delta_{\alpha\beta} + \varrho_0 v_\alpha v_\beta) = 0, \tag{3.96}$$

A derivation similar to equation 3.81 for the first moment of equation 3.77 leads to:

$$\varrho_0 \frac{\partial}{\partial t_1} v_\alpha - \frac{\partial}{\partial x_\beta} \varrho_0 c_s^2 \left(\tau - \frac{\Delta t}{2} \right) \left(\frac{\partial v_\beta}{\partial x_\alpha} + \frac{\partial v_\alpha}{\partial x_\beta} \right) + O(\mathrm{Ma}^3) = 0. \tag{3.97}$$

Combining equation 3.96 and 3.97 results in:

$$\begin{aligned}\varrho_0\frac{\partial}{\partial t}v_\alpha \;+\; \varrho_0\frac{\partial}{\partial x_\beta}(v_\alpha v_\beta) \;&=\\ =\; -c_s^2\frac{\partial \varrho}{\partial x_\alpha} + \frac{\partial}{\partial x_\beta}\epsilon\varrho_0 c_s^2\left(\tau-\frac{\Delta t}{2}\right)\left(\frac{\partial v_\beta}{\partial x_\alpha}+\frac{\partial v_\alpha}{\partial x_\beta}\right) &+ O(\mathrm{Ma}^3)+O(\epsilon^2),\end{aligned} \tag{3.98}$$

alternatively with $p = \varrho \cdot c_s^2$:

$$\begin{aligned}\varrho_0\frac{\partial \underline{v}}{\partial t} \;+\; \varrho_0(\underline{v}\cdot\nabla)\underline{v} \;+\; \varrho_0\underline{v}\,\nabla\cdot\underline{v} \;&=\\ -\;\nabla p \;+\; \left[\epsilon\varrho_0 c_s^2\left(\tau-\frac{\Delta t}{2}\right)\right]\left[\left(\Delta\underline{v}+\frac{1}{3}\nabla(\nabla\cdot\underline{v})\right) \;+\; \frac{2}{3}\nabla(\nabla\cdot\underline{v})\right] \;&+\\ +\;\; O(\mathrm{Ma}^3)+O(\epsilon^2)\end{aligned} \tag{3.99}$$

Equation 3.95 and 3.99 form a weakly compressible counterpart to the compressible continuity and Navier-Stokes equation, with a dominating constant base density and an additional error term in equation 3.99. For the stationary case

$$\frac{\partial}{\partial t}\varrho \;\equiv\; 0, \tag{3.100}$$

equation 3.95 turns into the incompressible continuity equation 2.21

$$\boxed{\nabla\cdot\underline{v}+O(\epsilon^2) \;=\; 0} \tag{3.101}$$

and equation 3.99 into the incompressible Navier-Stokes equation 2.32:

$$\boxed{\varrho_0\frac{\partial \underline{v}}{\partial t} \;+\; \varrho_0(\underline{v}\cdot\nabla)\underline{v} \;=\; -\nabla p \;+\; \mu\Delta\underline{v}+O(\mathrm{Ma}^3)+O(\epsilon^2)} \tag{3.102}$$

with a shear viscosity same as in section 3.4.1:

$$\mu = \left[\epsilon\varrho_0 c_s^2\left(\tau-\frac{\Delta t}{2}\right)\right]. \tag{3.103}$$

The overall error once again is of the order $O(\Delta t)$, $O(\Delta x^2)$ and $O(\mathrm{Ma}^3)$ with acoustic scaling (cf. section 3.4.1).

He and Luo illustrate with a nondimensionalization of equation 3.95 that in the transient case, the non-vanishing divergence term is negligible if $T \gg L/c_s$ with T as the time for a macroscopic change and L the range of distance of it.

3.5.2 MRT

Instead of relaxing all distributions f_i with a single relaxation time, a full set of multiple relaxation times (MRT) could be used, equaling the number of finite discrete velocities. This full parameter space provides means to tune additional physical properties and numerical stability. In contrary to the BGK collision, the relaxation is advantageously conducted in moment space (cf. section 3.4.2): The requirements of a collision operator are primarily on the moments, e.g. conservation or vanishing of certain moments, rather than on the distribution function. With the mutual spaces, MRT offers the possibility to have specific representations for propagation and collision control. Moreover, the equilibria can be tuned as well (cf. Lallemand and Luo [37]).

The evolution equation 3.58 turns for MRT into:

$$f_i(t + \Delta t, \underline{x} + \Delta t \cdot \underline{\xi}_i) = f_i(t, \underline{x}) - \Delta t \cdot [M^{-1} \cdot S \cdot (\underline{\rho}(t, \underline{x}) - \underline{\rho}^{(eq)})]_i. \tag{3.104}$$

M defines the transformation matrix from distribution to moment space and $S = \mathrm{diag}(\underline{s})$ a diagonal matrix of relaxation frequencies s_j for the specific moments ρ_j. $\rho_j^{(eq)}$ is the associated equilibrium of the js moment.

For the D2Q9 model, Lallemand and Luo [37] take the following basic setup of moments:

$$\begin{bmatrix} \varrho \\ e \\ \epsilon \\ j_x \\ q_x \\ j_y \\ q_y \\ p_{xx} \\ p_{xy} \end{bmatrix} = \begin{bmatrix} \text{mass density} \\ \text{kinetic energy} \\ \text{energy square} \\ \text{x-momentum} \\ \text{x-energy flux} \\ \text{y-momentum} \\ \text{y-energy flux} \\ \text{normal stresses} \\ \text{tangential stresses} \end{bmatrix} = \begin{bmatrix} 1 & 1 & 1 & 1 & 1 & 1 & 1 & 1 & 1 \\ 0 & 1 & 1 & 1 & 1 & 2 & 2 & 2 & 2 \\ 0 & 1 & 1 & 1 & 1 & 4 & 4 & 4 & 4 \\ 0 & 1 & 0 & -1 & 0 & 1 & -1 & -1 & 1 \\ 0 & 1 & 0 & -1 & 0 & 2 & -2 & -2 & 2 \\ 0 & 0 & 1 & 0 & -1 & 1 & 1 & -1 & -1 \\ 0 & 0 & 1 & 0 & -1 & 2 & 2 & -2 & -2 \\ 0 & 1 & 0 & 1 & 0 & 0 & 0 & 0 & 0 \\ 0 & 0 & 0 & 0 & 0 & 1 & -1 & 1 & -1 \end{bmatrix} \cdot \underline{f} =$$

$$=: \quad M' \cdot \underline{f} \tag{3.105}$$

This is equivalent to a linear combination of the moment base referred to in chapter 3.4.2:

$$\begin{aligned} M \cdot f \quad = \quad & [M_0,\ M_{x^2} + M_{y^2},\ M_{x^2} + M_{y^2} + M_{x^2y^2},\ M_x,\ M_x + M_{xy^2}, \\ & M_y,\ M_y + M_{x^2y},\ M_{xx},\ M_{xy}] \end{aligned} \tag{3.106}$$

Obviously the transformation is not orthogonal. For linear independent moments, a Gram-

Schmidt procedure is applied on M', resulting in:

$$M := \begin{bmatrix} 1 & 1 & 1 & 1 & 1 & 1 & 1 & 1 & 1 \\ -4 & -1 & -1 & -1 & -1 & 2 & 2 & 2 & 2 \\ 4 & -2 & -2 & -2 & -2 & 1 & 1 & 1 & 1 \\ 0 & 1 & 0 & -1 & 0 & 1 & -1 & -1 & 1 \\ 0 & -2 & 0 & 2 & 0 & 1 & -1 & -1 & 1 \\ 0 & 0 & 1 & 0 & -1 & 1 & 1 & -1 & -1 \\ 0 & 0 & -2 & 0 & 2 & 1 & 1 & -1 & -1 \\ 0 & 1 & -1 & 1 & -1 & 1 & 1 & 1 & 1 \\ 0 & 0 & 0 & 0 & 0 & 1 & -1 & 1 & -1 \end{bmatrix} \tag{3.107}$$

The relaxation frequencies for mass density and both momenta can be arbitrarily set to zero due to conservation, $s_1 = s_4 = s_6 \equiv 0$. The equilibria of the other moments and their relaxation frequencies used below are taken from the involved derivation by Lallemand and Luo [37]:

$$e^{(eq)} := -2\varrho + 3(j_x^2 + j_y^2) \tag{3.108}$$
$$\epsilon^{(eq)} := \varrho - 3(j_x^2 + j_y^2) \tag{3.109}$$
$$q_x^{(eq)} := -j_x \tag{3.110}$$
$$q_y^{(eq)} := -j_y \tag{3.111}$$
$$p_{xx}^{(eq)} := j_x^2 - j_y^2 \tag{3.112}$$
$$p_{xy}^{(eq)} := j_x \cdot j_y \tag{3.113}$$

The quantities are given in lattice unit description. Their respective relaxation frequencies are:

$$s_2 := 1/(2\mu' + 0.5) \tag{3.114}$$
$$s_3 := s_2 \tag{3.115}$$
$$s_5 := 8(2 - s_8)/(8 - s_8) \tag{3.116}$$
$$s_7 := s_5 \tag{3.117}$$
$$s_8 := 1/(2\mu + 0.5) \tag{3.118}$$
$$s_9 := s_8 \tag{3.119}$$

The given equilibria recover the incompressible formulation of equation 3.90 (cf. Lallemand and Luo [37]). However, also the compressible formulation could be derived by defining appropriate equilibria. Contrary to the SRT scheme, the bulk viscosity μ' can now be set separately. Frequencies s_5 and s_7 are set according to the "magic" collision number described by d'Humières and Ginzburg [12], reducing the slip velocity error for bounce-back boundary conditions.

A D3Q19 implementation of the MRT scheme is described by d'Humières et al. [13].

Chapter 4

Boundary Conditions for LBM

4.1 General Classification

Problems in fluid mechanics are initial-boundary value problems. They depend in a natural way not only on the governing equations, but also on the modeling of the initial state, and on the boundary conditions. Latter can be classified into four categories [26]:

1. Dirchlet boundary conditions
2. Neumann boundary conditions
3. Cauchy (Robin) boundary conditions
4. Periodic boundary conditions

Dirichlet boundary conditions set the flow quantity U on a specific boundary location $\underline{x}_{\mathrm{BC}}$ to a fixed value a:

$$U\left(\underline{x}_{\mathrm{BC}}\right) = a. \tag{4.1}$$

A specific case is the No-Slip boundary condition, modeling a fixed border with zero velocity $\underline{v}(\underline{x}_{\mathrm{BC}}) \equiv 0$. The Neumann type, however, sets the derivative of U to a value b,

$$\frac{\partial U\left(\underline{x}_{\mathrm{BC}}\right)}{\partial x_i} = b, \tag{4.2}$$

usually by using difference equations, involving certain stability conditions. The Cauchy or Robin type is a mixture of both Dirichlet and Neumann boundary conditions. An example for a Cauchy type is the Free Slip boundary condition, which models a fixed boundary, where the velocity normal to the wall equals zero, $v_{\perp} \equiv 0$, but for the tangential components $v_{\parallel}$ the gradient is set to zero:

$$\frac{\partial v_{\parallel}\left(\underline{x}_{\mathrm{BC}}\right)}{\partial x_{\parallel}} \equiv 0. \tag{4.3}$$

The forth type, periodic boundary conditions, repeat the flow quantity from one boundary on the opposing side. This is usually used for modeling an entity out of a bigger, homogenous or periodic problem.

A special feature of the LBM is that boundary values at a node do not to be determined entirely. After the streaming step, those distributions are already known that have been streamed from the domain onto the boundary node. Defining the boundary condition can therefore be done in a manner which considers the knowledge about the known distributions. Information can be derived, such as the estimate of the tangential velocity, which is e.g. essential for the isotropic boundary conditions in section 6.3. Furthermore, other calculations are possible, such as the estimation of the direction of an incident sound pressure wave from the first moment of the low-pass filtered, known distributions. The assumption is justified that a pressure wave affects only those distributions at all.

In this chapter, all boundary conditions used throughout this work will shortly be introduced. A particular emphasis is put on the analysis of the error of the non-equilibrium bounce-back relation, which is used among others by the boundary condition of Zou and He [65], but is also applied several times in this work.

4.2 Bounce-Back Boundary Conditions

As an advantage of the LBM, fixed No-Slip boundaries along the Cartesian directions of the grid can be implemented in a simple and efficient manner with the same accuracy as the LBM itself. The simplest type of implementation, the so-called bounce-back method, is possible if the boundary lies exactly between the grid nodes. It is used e.g. in chapter 7 and shall therefore be shortly introduced.

The principle is illustrated in figure 4.1(a) and can be motivated by a particle point of view: If an adjacent grid node was located already within the solid boundary, i.e. $\underline{x}_F + \Delta t \cdot \underline{\xi}_{i,b} = \underline{x}_{B,n}$ for directions $\underline{\xi}_{i,b}$ towards the boundary, a propagating particle would virtually "bounce back" to its origin. For a rough surface, the particle would even be reflected in the transverse direction, i.e. directing to a transverse node $\underline{x}_{B,tr}$.

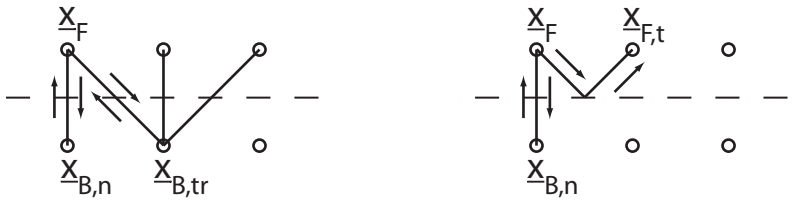

(a) No-Slip (b) Free Slip

Figure 4.1: Bounce-back boundary conditions

This motivates the bounce-back rule for no-slip boundaries, where $f_{\overline{i,b}}$ is the opposite distribution to $f_{i,b}$ and the superscript * marks the post-collision state:

$$f_{\overline{i,b}}(t + \Delta t, \underline{x}_F) = f^*_{i,b}(t, \underline{x}_F). \tag{4.4}$$

A free slip boundary is motivated by a perfectly reflecting wall, illustrated in figure 4.1(b). Transverse directions towards a boundary are set differently and affect the adjacent fluid node $\underline{x}_{F,t}$ in tangential direction:

$$f_{\overline{i,b}}(t + \Delta t, \underline{x}_{F,t}) = f^*_{i,b}(t, \underline{x}_F). \tag{4.5}$$

Quite often, a "2 time step" scheme is implemented, where distributions are shifted towards the boundary node, turned around and shifted back without collision in the next time step. However, unlike the original bounce-back scheme, this approach is not mass conservative.

As shown by Ginzburg and Adler, bounce-back is second order accurate in space [19]. Bennet points out that the simple bounce-back scheme includes a slight error in the slip velocity [3]. d'Humières and Ginzburg offer a remedy to this issue by introducing a scheme which removes the non-equilibrium error during the collision cycle [12] (so-called "magic" collision number for MRT collision, also used with the incompressible LBM simulations in this work). The boundary conditions by Bouzidi et al. [6] are a generalization of bounce-back boundary conditions, allowing among others to place the boundary not only half way, but in an arbitrary distance between two grid layers.

4.3 Zou-He Boundary Conditions

For the boundary conditions in Chapter 6, the relationship between density and velocity has been calculated in the same way as by Zou and He for their boundary conditions [65]. Also the non-equilibrium bounce-back relation is used in this work. Moreover, the boundary conditions of Zou and He are used in the reference implementations in section 7.4. Therefore those boundary conditions are briefly described below.

The basic idea of the boundary conditions by Zou and He is to calculate the unknown state basically from mass and momentum conservation. However, as the resulting number of equations is not sufficient to determine the state of the boundary node, the boundary conditions use the additional assumption that in the normal direction of the boundary, i.e. for the link $f_1 - f_3$ for a boundary normal to the $\underline{e}_x$ direction, the non-equilibrium part of both distributions is symmetric (cf. equation 4.9). This assumption includes an error of $O(\Delta t)$, as it will be derived in section 4.3.1. The error becomes not significant, as the relation does not reuse one of the involved distributions, but rather includes the streamed-in post-collision state of the neighboring node. By this approach, the error does not sum up and stays in the corresponding limit of the LB method itself. The boundary conditions of section 6 use the same relation, but there the error becomes indeed significant. Section 6.5 shows a possible remedy for this issue.

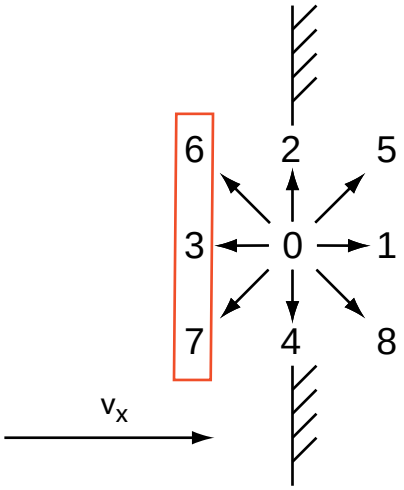

Figure 4.2: Unknown pre-collision distributions on a right boundary

The boundary conditions are without loss of generality described for a left boundary normal to the direction $\underline{e}_x$. For a grid node, mass and momentum conservation hold as well as the non-equilibrium bounce-back rule as discussed in detail in section 4.3.1:

$$\varrho = \sum_i f_i, \tag{4.6}$$

$$v_x \cdot \varrho = \sum_i f_i \xi_{i,x}, \tag{4.7}$$

$$v_y \cdot \varrho = \sum_i f_i \xi_{i,y}, \tag{4.8}$$

$$f_1 = f_3 + \frac{2}{3}\varrho v_x. \tag{4.9}$$

For a velocity boundary condition, Zou and He prescribe both velocities v_x and v_y. For a pressure boundary condition, they set the tangential velocity $v_y \equiv 0$ and prescribe the density. Equation 4.6 and 4.7 result in

$$\varrho = \frac{f_0 + f_2 + f_4 + 2\,(f_3 + f_6 + f_7)}{1 - v_x} \tag{4.10}$$

for the velocity boundary condition and

$$v_x = 1 - \frac{f_0 + f_2 + f_4 + 2\,(f_3 + f_6 + f_7)}{\varrho} \tag{4.11}$$

for the pressure boundary condition. It has to be stated that even the macroscopic state is not completely predetermined, but follows eventually from equation 4.10 or 4.11. This kind of boundary condition can therefore not be strictly classified as a Dirichlet boundary condition in

the sense it has for a classical Navier-Stokes approach, although it is refereed to be a Dirichlet type in the subsequent chapters.

The unknown distributions are set by solving equation 4.7, 4.8 and 4.9:

$$f_1 = f_3 + \frac{2}{3}\varrho v_x, \tag{4.12}$$
$$f_5 = f_7 + \frac{1}{2}(f_4 - f_2) + \frac{1}{6}\varrho v_x + \frac{1}{2}\varrho v_y, \tag{4.13}$$
$$f_8 = f_6 - \frac{1}{2}(f_4 - f_2) + \frac{1}{6}\varrho v_x - \frac{1}{2}\varrho v_y. \tag{4.14}$$

The derivation for the incompressible LBM model is similarly done by replacing equation 4.6 to 4.9 by

$$\varrho = \sum_i f_i, \tag{4.15}$$
$$v_x \cdot \varrho_0 = \sum_i f_i \xi_{i,x}, \tag{4.16}$$
$$v_y \cdot \varrho_0 = \sum_i f_i \xi_{i,y}, \tag{4.17}$$
$$f_1 = f_3 + \frac{2}{3}\varrho_0 v_x. \tag{4.18}$$

ϱ specifies in this case the density deviation relative to ϱ_0.

4.3.1 Error of the Non-Equilibrium Bounce-Back Relation

Below, the error of the non-equilibrium bounce-back relation is derived for the compressible D2Q9 model with BGK collision. The derivation for incompressible LBM can be carried out in the same way and is not done separately. The procedure below follows the recommendations by Geier [17], emerging from his procedure for the asymptotic error analysis.

The error of the assumption that the non-equilibrium of a distribution equals to that of the corresponding opposite will be shown for a perpendicular and a transverse FDVM link, without loss of generality for the direction along f_1 and f_5:

$$f_1 - f_1^{(eq)} = f_3 - f_3^{(eq)} \iff f_1 - f_3 = f_1^{(eq)} - f_3^{(eq)} \equiv \frac{2}{3}\varrho v_x \tag{4.19}$$
$$f_5 - f_5^{(eq)} = f_7 - f_7^{(eq)} \iff f_5 - f_7 = f_5^{(eq)} - f_7^{(eq)} \equiv \frac{1}{2}\varrho\,(v_x + v_y) \tag{4.20}$$

The difference of the equilibria follow from their definition by equation 3.57. On the other hand, the moment decomposition of section 3.4.2 shows:

$$f_1 - f_1^{(eq)} = M_x - M_{xy^2} \tag{4.21}$$
$$f_5 - f_5^{(eq)} = \frac{1}{2}\,(M_{x^2y} + M_{xy^2}) \tag{4.22}$$

The error of equation 4.19 and 4.20 can be derived from equation 4.21 and 4.22. This is equivalent to an error analysis of the moments M_x and, without loss of generality, M_{xy^2}, which is done below with the Chapman-Enskog procedure, as described in section 3.4.1. The left hand side of equation 3.59 is Taylor expanded by equation 3.60, which leads to:

$$f_i(t, \underline{x}) = f_i^{(eq)}(t, \underline{x}) - \epsilon \ \tau \ (\frac{\partial}{\partial t} + \xi_{i,\alpha} \frac{\partial}{\partial x_\alpha}) f_i(t, \underline{x}) + O(\epsilon^2) \tag{4.23}$$

Now f_i is expanded as a power series of ϵ, and multiple time scales are introduced:

$$f_i(t, \underline{x}) = \sum_{n=0}^{\infty} \epsilon^n f_i^{(n)}, \quad t_n := \epsilon^n \cdot t, \quad t \to \sum_{n=0}^{\infty} t_n. \tag{4.24}$$

Next, the analysis of equation 4.23 can be conducted for the different orders of ϵ:

For $O(\epsilon^0)$:

The zeroth order of equation 4.23 reduces to:

$$f_i(t, \underline{x})^{(0)} = f_i^{(eq)}(t, \underline{x}). \tag{4.25}$$

Calculating the moments M_x and M_{xy^2} of equation 4.25 by using the equilibrium distribution from equation 3.57 gains:

$$M_x^{(0)} = \sum_i \xi_{i,x} \ f_i^{(eq)} = \varrho v_x, \tag{4.26}$$

$$M_{xy^2}^{(0)} = \sum_i \xi_{i,x} \ \xi_{i,y}^2 \ f_i^{(eq)} = \frac{1}{3} \varrho v_x. \tag{4.27}$$

For $O(\epsilon^1)$:

The first order of equation 4.23 reads:

$$f_i(t, \underline{x})^{(1)} = -\tau \ (\frac{\partial}{\partial t_0} + \xi_{i,\alpha} \frac{\partial}{\partial x_\alpha}) f_i^{(0)}. \tag{4.28}$$

The moment M_x of equation 4.28 results in

$$M_x^{(1)} = -\tau \ \sum_i \xi_{i,x} \ (\frac{\partial}{\partial t_0} + \xi_{i,\alpha} \frac{\partial}{\partial x_\alpha}) f_i^{(0)} = -\tau \ \left(\frac{\partial}{\partial t_0} \varrho \ \underline{v} \ + \ \nabla \cdot \underline{\underline{\Pi}}^{(0)} \right) = 0, \tag{4.29}$$

which is proven by equation 3.72. On the other hand, the moment M_{xy^2} of equation 4.28,

$$M_{xy^2}^{(1)} = -\tau \ \sum_i \xi_{i,x} \ \xi_{i,y}^2 \ (\frac{\partial}{\partial t_0} + \xi_{i,\alpha} \frac{\partial}{\partial x_\alpha}) f_i^{(0)}, \tag{4.30}$$

will not generally vanish. Reassembling the different orders gains in total:

$$M_x = \varrho v_x + O(\epsilon^2), \tag{4.31}$$

$$M_{xy^2} = \frac{1}{3}\varrho v_x + O(\epsilon). \tag{4.32}$$

This is equivalent to an error of $O(\epsilon) \equiv O(\Delta t)$ and $O(\epsilon^2) \equiv O(\Delta t^2)$, respectively (cf. section 3.4.1, valid for both acoustic and diffusive scaling). Consequently, equation 4.21 and 4.22 indicate a first order error in time for the non-equilibrium bounce-back relation:

$$f_1 - f_1^{(eq)} = M_x - M_{xy^2} = \frac{2}{3}\varrho v_x + O(\Delta t), \tag{4.33}$$

$$f_5 - f_5^{(eq)} = \frac{1}{2}\left(M_{x^2y} + M_{xy^2}\right) = \frac{1}{2}\varrho\left(v_x + v_y\right) + O(\Delta t). \tag{4.34}$$

Chapter 5

Non-reflecting Boundary Conditions

As a boundary condition is supposed to install a desired state, e.g. a specific velocity or pressure, it usually has to reflect, respectively interact with the fluid. Also a boundary which is not processing the incoming fluid, e.g. by setting a constant equilibrium distribution, would indeed lead to a certain reflection of an incoming pressure wave, although the pressure change itself would never be processed (chapter 6 will show that a dynamic reaction is mandatory). This means that a reflection is intentional and has to react in a way that cancels spurious signals. It is rather a matter of what has to be reacted on. A non-reflecting boundary condition should set a desired state for the fluid and at the same time intercept undesired reflection effects. It will be clearly shown in section 5.2.1 and in chapter 6 that it is not possible to fulfill both requirements in a strict manner at the same time.

These undesired effects are e.g. for acoustic applications the reflection of sound pressure waves inside a certain frequency bandwidth. For other applications, this might not be sufficient: For instance an absolute drag or lift force on an object might be significantly distracted even by low-frequent spurious pressure waves in the context of an LBM simulation. To consider the whole frequency range, a proper way would be to solve the constitutive equations on the boundary. However, this is not possible, as on a boundary node the system of equations naturally will always be under-determined. Certain assumptions then have to be made to remedy the lack of information on a boundary node. It will be seen that all non-reflecting boundary conditions rely on various assumptions.

This chapter covers as an introduction to the topic two approaches for the implementation of non-reflecting boundary conditions. The first approach is a low-pass filtering method, which will turn out not to produce results of acceptable quality. The second approach is based on the method of the characteristics, gains excellent results and is widely used in the context of computational fluid dynamics.

5.1 Filtering Methods

The most obvious approach for non-reflecting boundary conditions is applying a low-pass filter to the density distribution function on the boundary. A corner frequency ω_c defines hereby a relevant frequency range for the distribution function. However, this range can be defined completely arbitrarily and is depending probably in most cases on the range of human perception. The next section will give a short introduction to the field of continuous low-pass

filtering, followed by the transition to discrete filters in a brief "how-to" approach. Finally, an implementation for the LBM will show its practical use.

5.1.1 Continuous Low-pass Filter

For a continuous complex frequency s, the general transfer function of a low-pass filter of order n is given by (cf. Kugelstadt [36])

$$H(s) = \frac{H_0}{\prod_{i=1}^{n}(1+\alpha_i s)} =: \frac{H_0}{\prod_i (1 + a_i s + b_i s^2)}. \tag{5.1}$$

The structure as a product of broken second order complex polynomials represents the combination of basic electronic filter circuits and is maintained for practical reasons. There are three ranges defined for the transfer function: A pass-band from the lowest to a frequency with an attenuation down to -3 dB, a transition band from -3 dB to -80 dB (depending on application) and the stop-band below that interval. The order of the filter will determine the steepness within the transition band (known as roll-off). The magnitude of the transfer function $H(s)$ with a complex frequency $s = i\omega$ is illustrated in figure 5.1 for different orders, all for a corner frequency of 1 Hz. The corner frequency specifies hereby a drop of -3 dB respectively 50% in amplitude. The coefficients a_i, b_i for stable filter design are practically taken from tables, see Kugelstadt [36].

There are three main filter characteristics used for low-pass filters: Butterworth, Tschebyscheff and Bessel (cf. Kugelstadt [36]). Their difference is illustrated in figures 5.2, 5.3 and 5.4. The Butterworth type provides the best possible flatness in the pass-band (cf. figure 5.2), Tschebyscheff filters are designed to provide the best possible roll-off from pass-band to transition band. However, both suffer from a non-linear group delay, resulting in undesirable dispersion (cf. figure 5.4). The group delay is hereby given by the derivative of the phase shift (figure 5.3) with respect to time (cf. Maheshwari and Anand [41]):

$$\tau_{gr} = -\frac{d\phi}{d\omega}. \tag{5.2}$$

The total time delay of a filter is then computed by a convolution of the signal with the group delay. The focus for the choice of a low-pass filter in this work was set on a minimum dispersion, therefore the Bessel type was chosen.

5.1.2 Discrete Low-pass Filter

The continuous signal $f(t)$ can be represented by a series of Dirac's delta functions, with $f_k = f(k \cdot T_s)$ and a sampling rate of $1/T_s$:

$$f(t) = \sum_{k=0}^{\infty} f_k \cdot (\delta(t - k \cdot T_s)\,. \tag{5.3}$$

The Laplace transformation

$$\mathcal{L}(f(t)) := \int_{t=0}^{\infty} f(t)e^{-st}dt = \int_{t=0}^{\infty} \left[\sum_{k=0}^{\infty} f_k \cdot (\delta(t - k \cdot T_s)\right] e^{-st}dt \tag{5.4}$$

from time to frequency domain accordingly results in the z-transformation $Z(f_k)$ (cf. Müller [45])

$$\mathcal{L}(f(t)) = \sum_{k=0}^{\infty} f_k e^{s \cdot {T_s}^{-k}} =: \sum_{k=0}^{\infty} f_k z^{-k} =: Z(f_k). \tag{5.5}$$

It can be seen from equation 5.5 that a multiplication in the z-space with z^{-k} equals a time shift of the signal by $k \cdot T_s$. For designing a discrete filter from a continuous one, the bilinear transformation

$$s = \frac{2}{T_s}\left(\frac{z-1}{z+1}\right) \tag{5.6}$$

can be used to map the s-space to the z-space. For a stable filter, that means with complex poles in the left half of the s-space (as provided by appropriate tables), stability will be maintained by the bilinear transformation due to the mapping of the poles inside the unit circle (cf. Shenoi [53]). The ordinate of the s-space, describing the undamped frequency space, is mapped consistently onto the unit circle ($s = i\omega$ is transformed to $z = e^{i\omega T_s}$). The approach for designing a discrete low-pass filter is therefore:

1. Choose filter type and order
2. Pick filter coefficients from table (e.g. by Kugelstadt [36]) for $\omega_c = 1$ Hz
3. Transform filter to new corner frequency $s \rightarrow p/\omega_c$
4. Apply bilinear transformation to the continuous transfer function $p = \frac{2}{T_s}\left(\frac{z-1}{z+1}\right)$
5. Write the filter convolution as $f_{\text{lpf}}(z) = H(z) * f(z)$
6. Reformulate as polynomial of z^{-1}

According to the remark below equation 5.5, the polynomial can be directly used to implement the filter (addition and time shift).

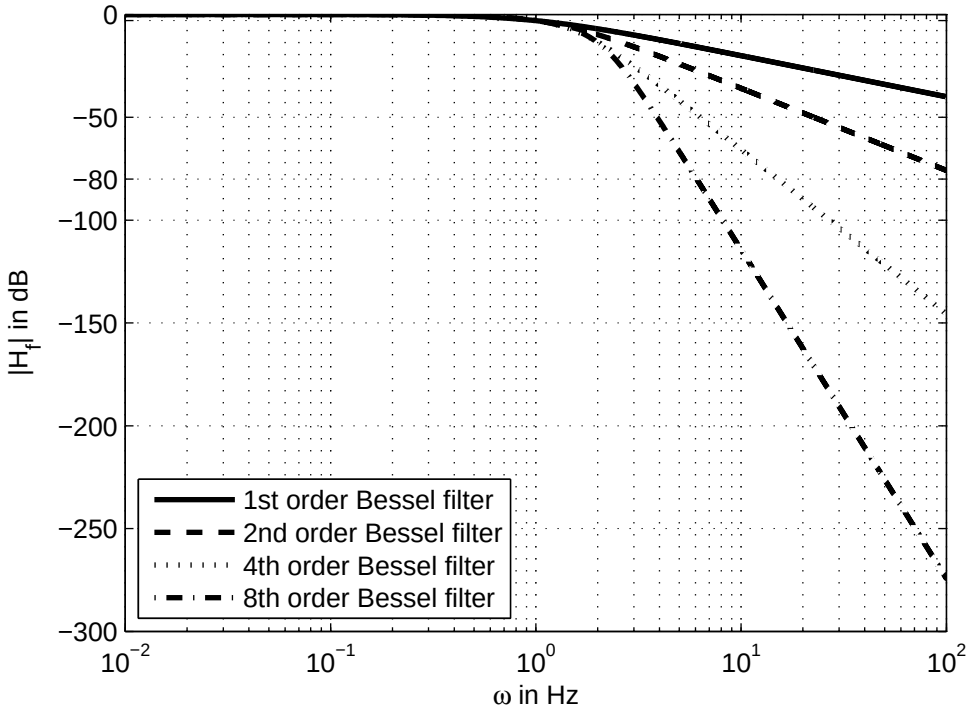

Figure 5.1: Bessel filter characteristic of different orders with corner frequency of 1 Hz

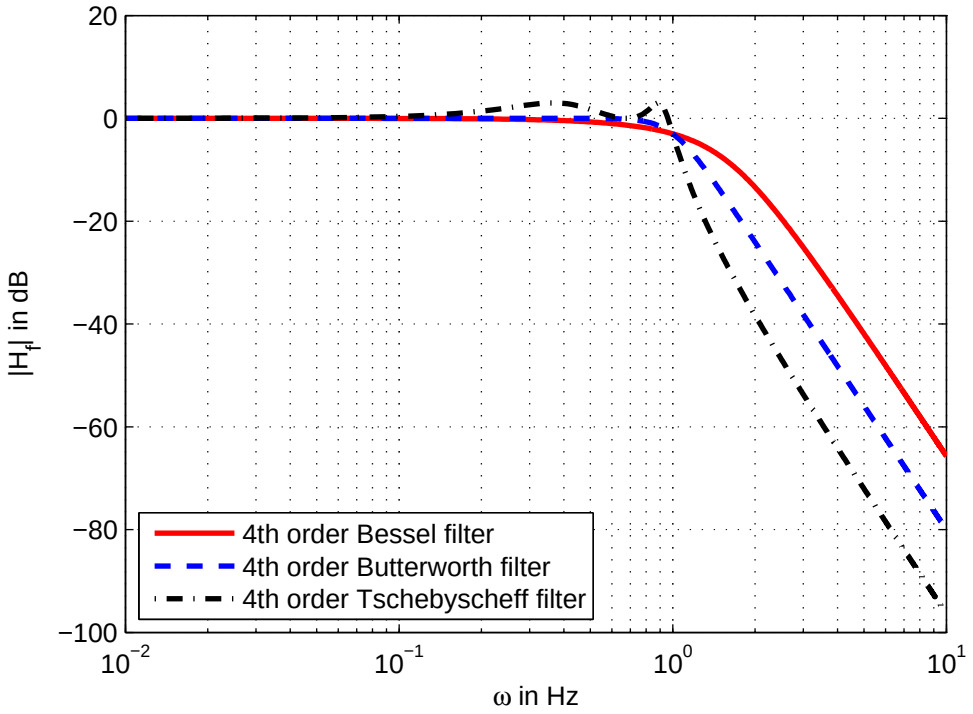

Figure 5.2: Filter characteristic of different types with corner frequency of 1 Hz

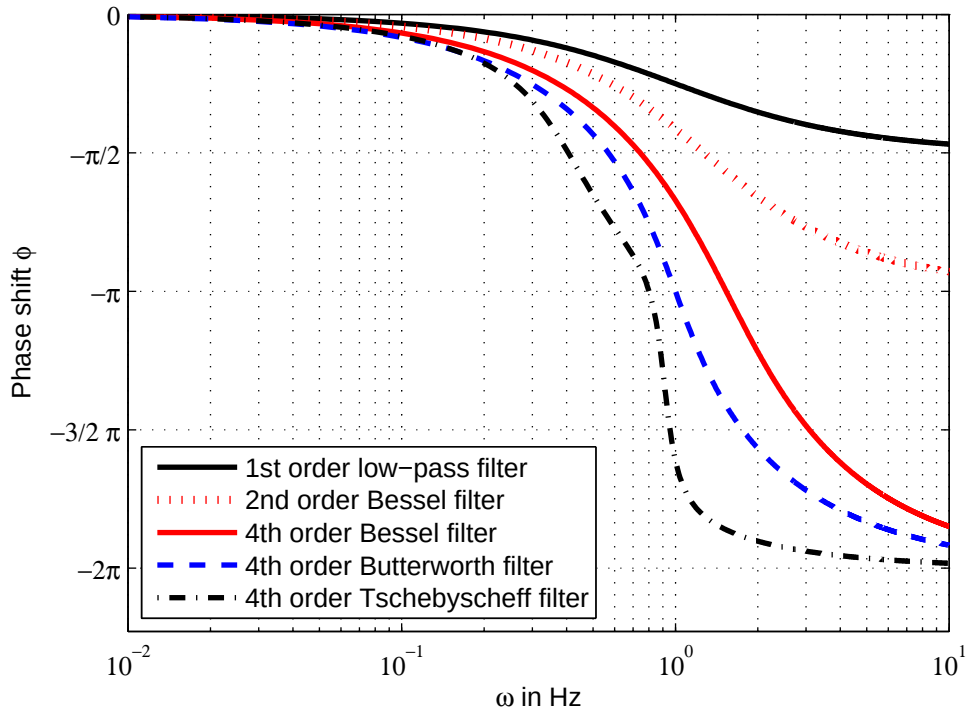

Figure 5.3: Phase shift of different types with corner frequency of 1 Hz

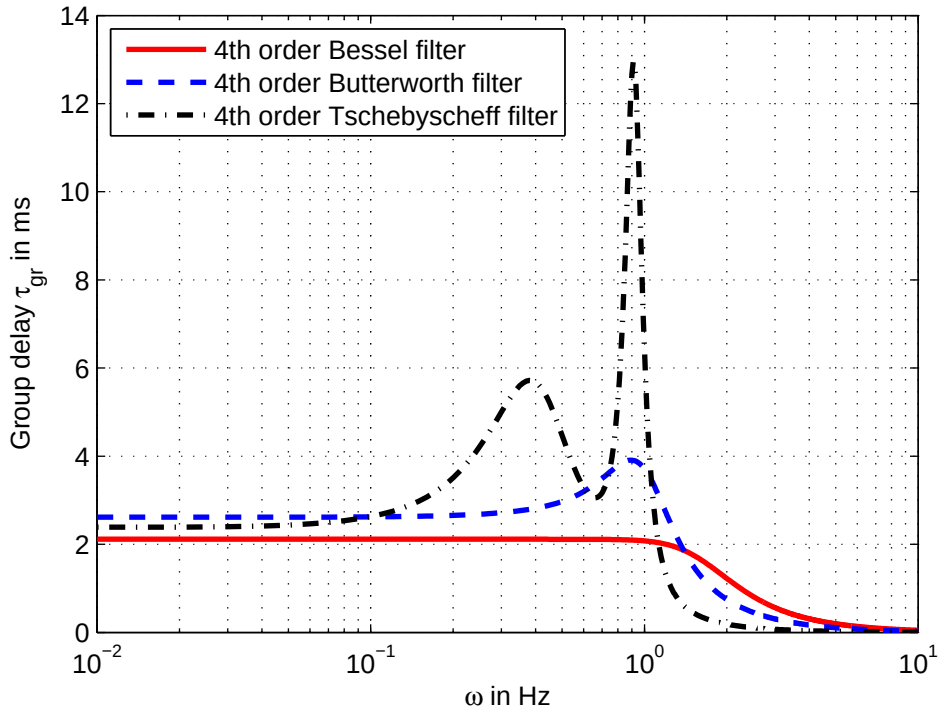

Figure 5.4: Group delay of different types with corner frequency of 1 Hz

5.1.3 Low-pass Filter Boundary Condition for LBM

A simple low-pass filter boundary condition for LBM can be set up by applying the filter on the incoming density distributions f_i previous to further processing with conventional boundary conditions. All filters are applied in time rather than in space to gain a full local data consistency and a corresponding isotropy. A second order low-pass filter with

$$H(s) = \frac{1}{1 + a_i s + b_i s^2} \tag{5.7}$$

and with a normalized time step $\Delta t := 1$ results according to section 5.1.2 in a discrete low-pass filter

$$f_{i,\mathrm{lpf}} = C_1 \cdot \left[f_i + 2 \left(f_i + (C_3 - 1)\, f_{i,\mathrm{lpf}} \right) z^{-1} + \left(f_i + (C_2 - C_3 - 1)\, f_{i,\mathrm{lpf}} \right) z^{-2} \right]. \tag{5.8}$$

Let the superscript (n) mark the corresponding time step $n \cdot \Delta t$. The filter function in time can be read directely from the z-polynomial of equation 5.8:

Second order Bessel filter:

$$f_{\mathrm{lpf}}^{(n)} = C_1 \cdot \left[f^{(n)} + 2 \left(f^{(n-1)} + (C_3 - 1)\, f_{\mathrm{lpf}}^{(n-1)} \right) + \left(f^{(n-2)} + (C_2 - C_3 - 1)\, f_{\mathrm{lpf}}^{(n-2)} \right) \right] \tag{5.9}$$

with

$$C_1 := \frac{1}{1 + C_2 + C_3}, \qquad C_2 := \frac{2a_1}{\omega_c}, \qquad C_3 := \frac{4b_1}{\omega_c^2},$$
$$a_1 := 1.3617, \qquad b_1 := 0.6180$$

Correspondingly, f and the filtered f_{lpf} have to be recorded for the two last time steps. The filter coefficients a_1 and b_1 were selected from Kugelstadt [36] and form a stable second order Bessel filter. The corner frequency could be practically tuned to the latest possible reflection, e.g. at the outflow boundary. For an inflow boundary condition, ω_c has accordingly to be tuned to a propagation over twice the domain length:

$$\omega_c := \frac{1}{2 \cdot L \cdot c_s^{-1}} = \frac{1}{2 \cdot L \cdot \sqrt{3}}. \tag{5.10}$$

With the same procedure as above, all other Bessel filters up to 4th order can be set up:

First order low-pass filter:

$$f_{\mathrm{lpf}}^{(n)} = C_1 \cdot \left[f^{(n)} + f^{(n-1)} + (C_2 - 1) \cdot f_{\mathrm{lpf}}^{(n-1)} \right] \tag{5.11}$$

with

$$C_1 := \frac{1}{1+C_2}, \qquad C_2 := \frac{2}{\omega_c}.$$

Third order Bessel filter:

$$\begin{aligned} f_{\text{lpf}}^{(n)} = C_1 \cdot \big[& f^{(n)} \\ & + \left(3f^{(n-1)} + (C_3 - C_2 + C_4 - 3)\, f_{\text{lpf}}^{(n-1)}\right) \\ & + \left(3f^{(n-2)} + (C_2 + C_3 - C_4 - 3)\, f_{\text{lpf}}^{(n-2)}\right) \\ & + \left(\; f^{(n-3)} + (C_2 - C_3 + C_4 - 1)\, f_{\text{lpf}}^{(n-3)}\right)\big] \end{aligned} \tag{5.12}$$

with

$$\begin{aligned} C_1 &:= \frac{1}{1+C_2+C_3+C_4}, & C_2 &:= \frac{2(a_1+a_2)}{\omega_c}, \\ C_3 &:= \frac{4(a_1a_2+b_2)}{\omega_c^2}, & C_4 &:= \frac{8a_1b_2}{\omega_c^3}, \\ a_1 &:= 0.7560, & a_2 &:= 0.9996, & b_2 &:= 0.4772 \end{aligned}$$

Forth order Bessel filter:

$$\begin{aligned} f_{\text{lpf}}^{(n)} = C_1 \cdot \big[& f^{(n)} \\ & + 2\left(2f^{(n-1)} + (C_4 - C_2 + 2C_5 - 2)\, f_{\text{lpf}}^{(n-1)}\right) \\ & + 2\left(3f^{(n-2)} + (C_3 - 3C_5 - 3)\, f_{\text{lpf}}^{(n-2)}\right) \\ & + 2\left(2f^{(n-3)} + (C_2 - C_4 + 2C_5 - 2)\, f_{\text{lpf}}^{(n-3)}\right) \\ & + \left(\; f^{(n-4)} + (C_2 - C_3 + C_4 - C_5 - 1)\, f_{\text{lpf}}^{(n-4)}\right)\big] \end{aligned} \tag{5.13}$$

with

$$\begin{aligned} C_1 &:= \frac{1}{1+C_2+C_3+C_4+C_5}, & C_2 &:= \frac{2(a_1+a_2)}{\omega_c}, & C_3 &:= \frac{4(a_1a_2+b_1+b_2)}{\omega_c^2}, \\ C_4 &:= \frac{8(a_1b_2+a_2b_1)}{\omega_c^3}, & C_5 &:= \frac{16b_1b_2}{\omega_c^4}, & a_1 &:= 1.3397, \\ a_2 &:= 0.7743, & b_1 &:= 0.4889, & b_2 &:= 0.3890 \end{aligned}$$

5.1.4 1D Pressure Wave Test Case

For the discussion of the implemented LBM filtering boundary condition, the D1Q3 compressible LBM model of section 3.1 is set up on a domain of $L = 1000$ grid nodes. On the left-hand side, a Dirichlet velocity boundary condition with $v_0 = 0.1$ is installed, correspondingly on the right hand side a Dirichlet pressure boundary condition with $p_0 = c_s^2 \cdot \varrho_0$ and $\varrho_0 \equiv 1$. The Dirichlet boundary conditions can be simply computed by solving mass and momentum conservation on the boundary, which gains

$$f_1 = \frac{1}{1 - v_0} \cdot (f_2 + v_0 \cdot (f_0 + f_2)) \tag{5.14}$$

for the velocity boundary and

$$f_2 = \varrho_0 - f_0 - f_1 \tag{5.15}$$

for the pressure boundary. It is stressed that for the velocity boundary condition, the pressure is not fixed, but is a function of the conservation properties. The same is valid vice versa for the pressure boundary condition.

Initially, a constant velocity of $v_0 \equiv 0.1$ was set over the whole domain. For the density, a Gauss peak with a maximum value of $\varrho_p = 2$ and $\sigma = 50$ was placed at position $x_c = 100 \cdot \Delta x$:

$$\varrho(x) = \varrho_0 + (\varrho_p - \varrho_0) \cdot e^{-\frac{1}{2}\left(\frac{(x - x_c)\cdot\sigma}{L}\right)^2}. \tag{5.16}$$

Figure 5.5 shows how the density in the domain evolves over time. The Reynolds number was set to $Re = \frac{v_0 \cdot L}{\nu} = 100$.

Figure 5.6 and 5.7 show density and velocity for a free field simulation, where the domain size was increased by $\Delta L = 1000$ on the left hand side. The extended domain is cut off for the plots to show how a perfectly non-reflecting free field boundary would have to respond. The peak displayed at $x \approx 500 \cdot \Delta x$ is the one splitting from the initial pressure peak and being convected to the right hand side (cf. 5.5). Being geometrically damped (i.e. in this case by viscous loss), it will be used below as reference for the reflection level of the boundary conditions. The left partial peak (cf. 5.5) propagated out of the left bound.

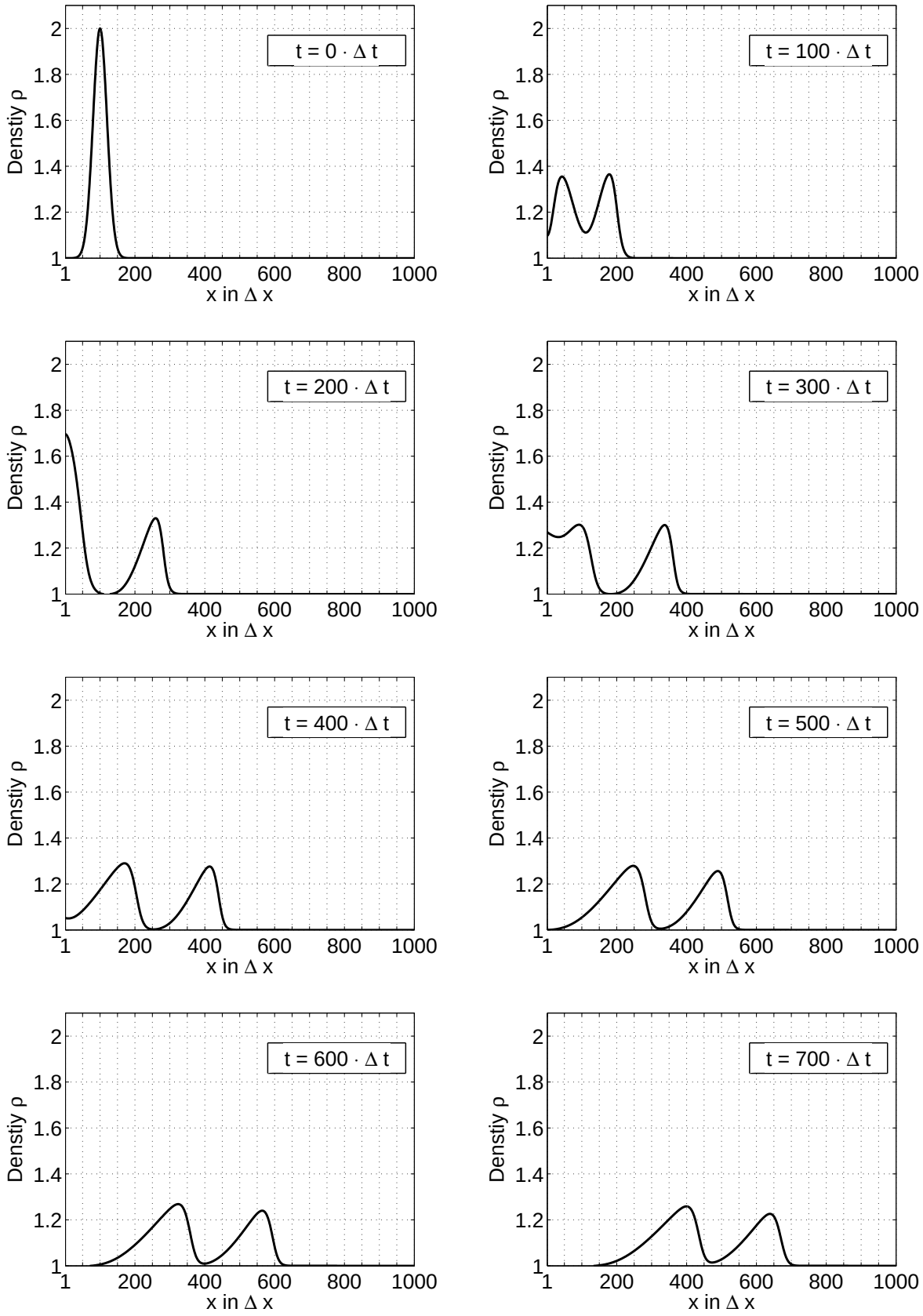

Figure 5.5: Initial pressure peak evolving over time, Dirichlet velocity BC at left inlet

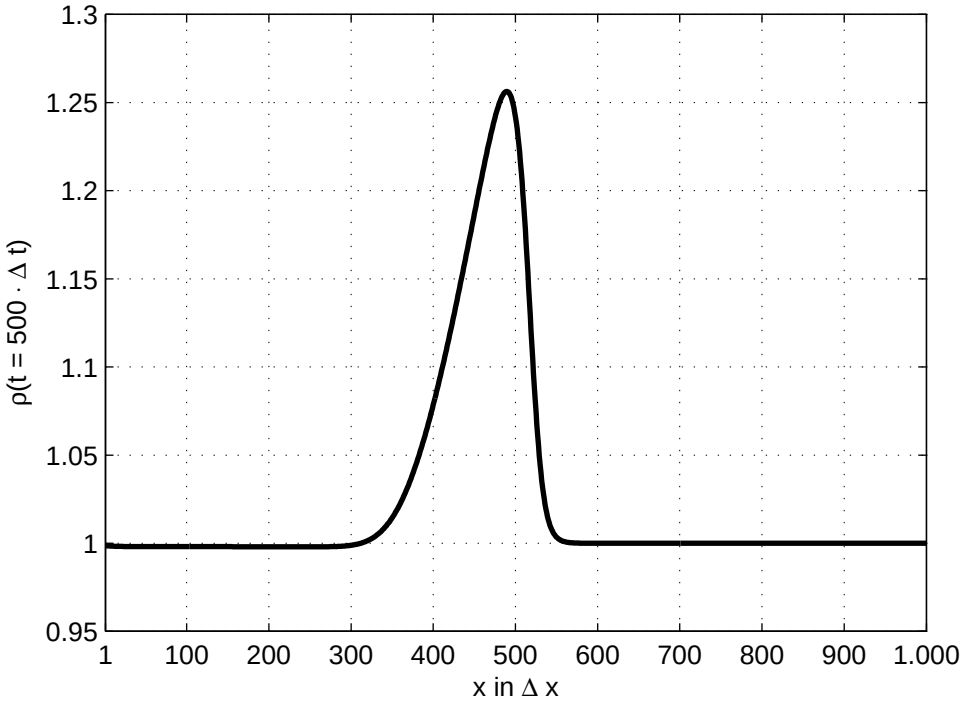

Figure 5.6: Free field density after 500 time steps

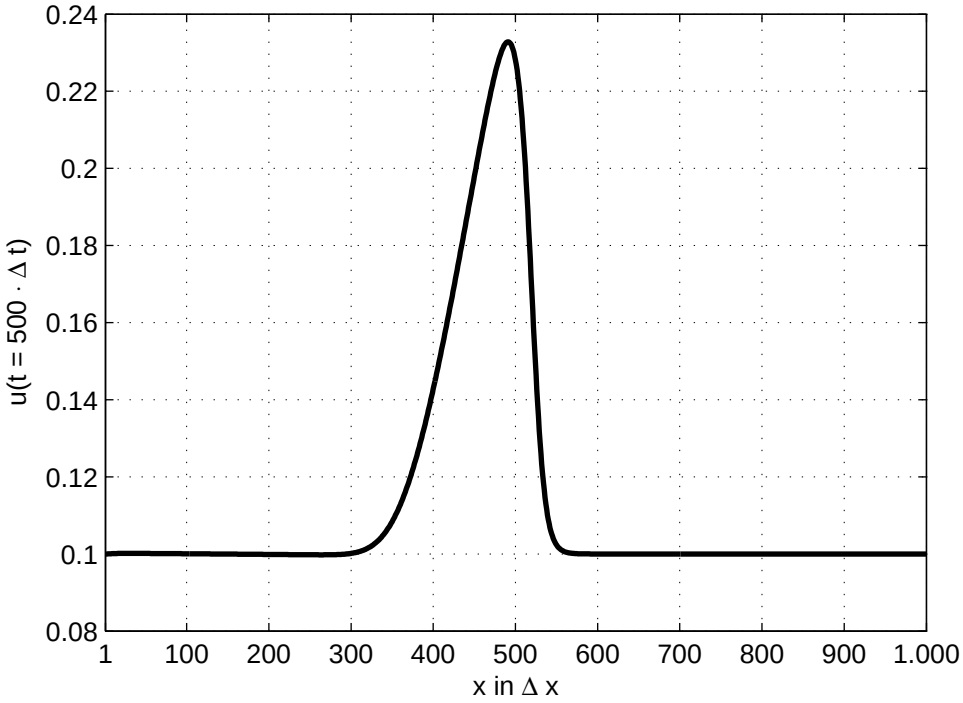

Figure 5.7: Free field velocity after 500 time steps

5.1.5 Discussion of 1D Pressure Wave Test Case

For the filtering boundary conditions, the filter was applied prior to the use of the Dirichlet velocity boundary condition on the known part of the distribution function:

$$f_0 \xrightarrow[\text{pass filter}]{n\text{-th order low}} f_{0,\text{lpf}}, \qquad f_2 \xrightarrow[\text{pass filter}]{n\text{-th order low}} f_{2,\text{lpf}},$$

$$f_1 = \frac{1}{1-v_0} \cdot \left(f_{2,\text{lpf}} + v_0 \cdot \left(f_{0,\text{lpf}} + f_{2,\text{lpf}}\right)\right),$$

$$f_0 = f_{0,\text{lpf}}, \qquad f_2 = f_{2,\text{lpf}}.$$

Its extension to the 2D and 3D case is straight forward and shall not be discussed. The implications can be seen on figures 5.8 to 5.11, which is summarized:

1. A significant reduction of the reflected sound pressure wave can be achieved.
2. Due to the local application of the filter, a major jump is observable both in density and velocity.
3. This jump causes a wrongly set inflow velocity.
4. The group delay of the filter can clearly be noticed.

To 1: With a Dirichlet velocity boundary condition, the reflected density accounts for 109 % of the geometrically damped wave at $x \approx 500$. The reflection with the filter boundary condition ranges from 24 % for the first order filter to 22 % for third and forth order (cf. figure 5.8).

To 2 and 3: A filter applied locally to node 1 causes a jump regarding node 2. This manifests itself in a jump of density (cf. figure 5.9) and, for a fixed velocity even more severe, a jump in velocity (cf. figure 5.11). The boundary velocity will therefore be slightly wrong (cf. figure 5.11: 5 % at the specific time step). Depending on the corner frequency, this offset will be equalized over time, as the low-pass property damps the adaption correspondingly. In the specific case, the adaption in density for the first order filter will be in the range of 0.002 per 1000 timesteps. A velocity of 0.1 at node 2 will therefore be reached approximately at timestep $t = 6000 \cdot \Delta t$, if no other disturbances are encountered.

To 4: In figure 5.8, a group delay of the reflected pressure peak of approximately 30 nodes can be observed. This equals an equivalent shift of the inflow boundary towards outside.

In consequence, the filtering boundary condition as discussed does not gain sufficiently accurate results. A simple approach to "remove" the sound pressure wave is not possible.

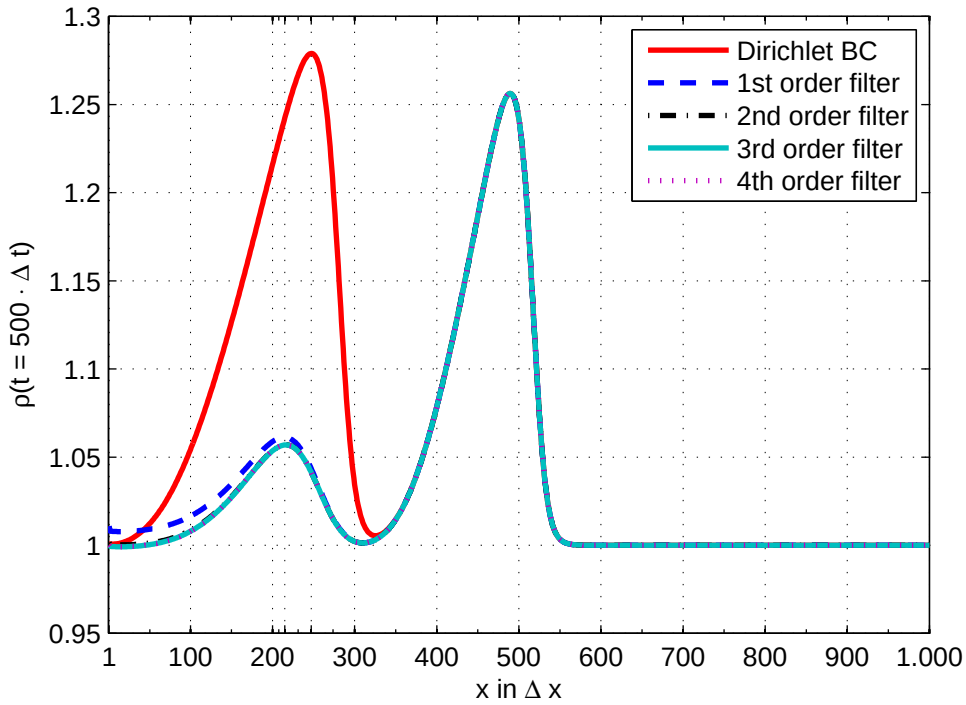

Figure 5.8: Reflection of pressure peak for density, group delay can clearly be seen. (2nd order masked by 3rd order, cf. figure 5.9)

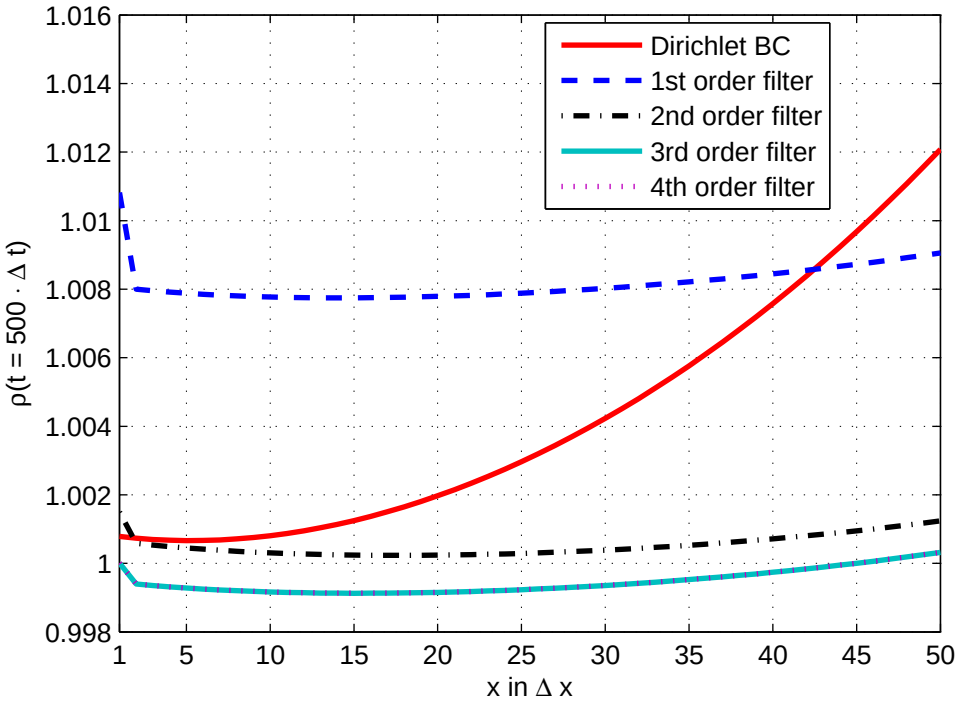

Figure 5.9: Density on first 50 grid nodes. Jump can clearly be seen.

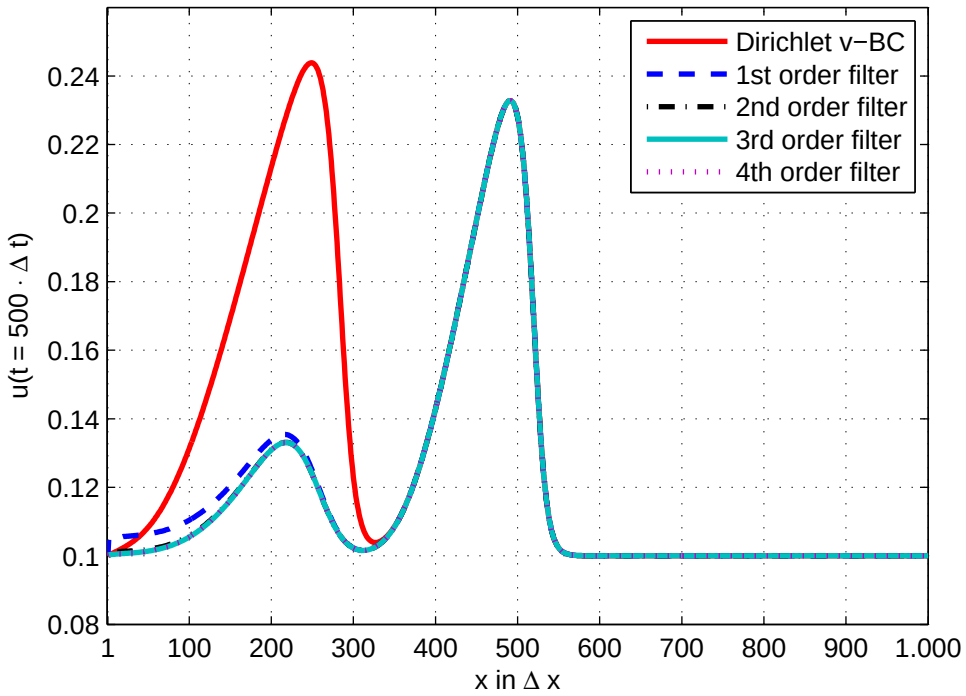

Figure 5.10: Reflection of pressure peak on left hand side for velocity (2nd order masked by 3rd order, cf. figure 5.11)

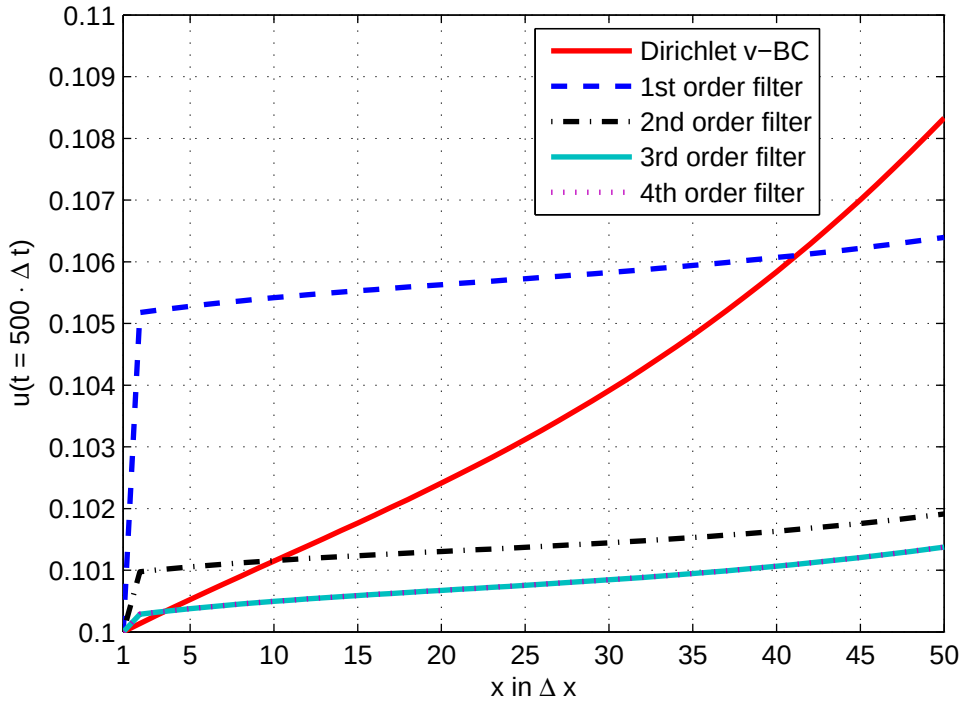

Figure 5.11: Velocity on first 50 grid nodes. Jump can clearly be seen.

5.2 Characteristic Based Methods

The basic idea of characteristic based boundary condition for hyperbolic systems of equations dates back to at least the 1970s (cf. Chen [10], Lindman [39], Engquist and Majda [14], Hedstrom [25], Thompson [56]) and is probably the most widely used non-reflecting type. An implementation for the LBM was introduced by Kim et. al. [33] and Izquierdo and Fueyo [28].

In contrast to the filtering method of the previous section, the approach of characteristic based methods is to actually solve a set of simplified constitutive equations on the boundary, combined with an assumption for the adjacent region outside the domain. More specific, the amplitude of acoustic waves propagating into the domain is deliberately set to zero. The boundary node is hereby basically modeled by a system of inviscid conservation equations, namely the continuity equation 2.18, the Euler equation 2.33 and the energy equation 2.40 without viscous shear stress term. The derivatives normal to the boundary are then neglected, which leads to the LODI (Linear One Dimensional Inviscid) system of equations. The restriction to the normal direction of incoming pressure waves represents the most important one to this type of boundary conditions. The resulting hyperbolic system of equations can be transformed into its characteristic form, describing the propagation of partial waves. Acoustic waves propagating into the domain can then be set to zero. The components referring to waves directing towards the boundary from the inside of the domain are computed by use of finite difference stencils and a forward Euler scheme.

Although this procedure is designed only for inviscid flow, it can be adapted for the Navier-Stokes equations, as they also include wave propagation. By adding viscous effects to the boundary condition, it is able to interact with the fluid and set a desired boundary state. The boundary conditions by Poinsot and Lele [51] split diffusive effects and include viscous conditions separately, leading to a small pressure wave propagation towards the fluid. This indicates on the other hand that a perfectly non-reflecting boundary condition for viscous flow is contradicting physical reasoning.

5.2.1 Principle of the LODI Method

The principle of the LODI method introduced by Poinsot and Lele [51] is sketched roughly for the two-dimensional case, as it is extensively described in the referred article or by Izquierdo and Fueyo [28]. The aforementioned system of inviscid constitutive equations 2.18, 2.33 and 2.40 without viscous term, heat diffusion and external sources is cut down by setting derivatives parallel to the specific boundary to zero. For a boundary with normal $\underline{e}_x$ on the left hand side of a domain with length L, i.e. at position $x_b = 0$ with $0 \leq x \leq L$, all derivatives parallel to the boundary are canceled for an arbitrary variable of state Φ:

$$\frac{\partial \Phi}{\partial y} \equiv 0. \tag{5.17}$$

The equations can be cast to a four-dimensional system of equations

$$\frac{\partial}{\partial t}\underline{U} + \underline{\underline{A}} \cdot \frac{\partial}{\partial x}\underline{U} = 0 \tag{5.18}$$

with a state vector

$$\underline{U} := [\varrho, v_x, v_y, E]^T \tag{5.19}$$

and

$$\underline{\underline{A}} := \begin{bmatrix} v_x & \varrho & 0 & 0 \\ c_s^2/\varrho & v_x & 0 & 0 \\ 0 & 0 & v_x & 0 \\ c_s v_x/\varrho & c_s^2 & 0 & v_x \end{bmatrix}. \tag{5.20}$$

It is assumed consistently to the LBM that speed of sound is constant and the heat capacity ratio equals one. Now $\underline{\underline{A}}$ can be decomposed into $\underline{\underline{A}} = \underline{\underline{S}}^{-1}\underline{\underline{\Lambda}}\underline{\underline{S}}$, which bases on an eigenvector decomposition given by the row vectors of $\underline{\underline{V_e}}$:

$$\underline{\underline{V_e}} := \begin{bmatrix} -c_s/\varrho & 1 & 0 & 0 \\ 0 & 0 & 1 & 0 \\ -c_s^2/\varrho & -v_x & 0 & 1 \\ c_s/\varrho & 1 & 0 & 0 \end{bmatrix} \tag{5.21}$$

$\underline{\underline{V_e}}$ is now multiplied by $D := \mathrm{diag}(-\varrho c_s, 1, -\varrho, \varrho c_s)$

$$\underline{\underline{S}} := D \cdot \underline{\underline{V_e}} = \begin{bmatrix} c_s^2 & -\varrho c_s & 0 & 0 \\ 0 & 0 & 1 & 0 \\ c_s^2 & \varrho v_x & 0 & -\varrho \\ c_s^2 & \varrho c_s & 0 & 0 \end{bmatrix}, \tag{5.22}$$

$$\underline{\underline{S}}^{-1} = \begin{bmatrix} 1/(2c_s^2) & 0 & 0 & 1/(2c_s^2) \\ -1/(2\varrho c_s) & 0 & 0 & 1/(2\varrho c_s) \\ 0 & 1 & 0 & 0 \\ -(v_x - c_s)/(2\varrho c_s) & 0 & -1/\varrho & -(v_x + c_s)/(2\varrho c_s) \end{bmatrix}, \tag{5.23}$$

and $\underline{\underline{\Lambda}}$ is the diagonal matrix of eigenvalues, namely the characteristic velocities λ_i:

$$\underline{\underline{\Lambda}} = \mathrm{diag}(v_x - c_s, v_x, v_x, v_x + c_s) =: \mathrm{diag}(\lambda_1, \lambda_2, \lambda_3, \lambda_4). \tag{5.24}$$

The corresponding wave amplitudes are given by

$$\underline{L} = \underline{\underline{\Lambda}} \cdot \underline{\underline{S}} \cdot \frac{\partial}{\partial x}\underline{U} = \begin{bmatrix} \lambda_1 \left(\frac{\partial p}{\partial x} - \varrho c_s \frac{\partial v_x}{\partial x}\right) \\ \lambda_2 \frac{\partial v_y}{\partial x} \\ \lambda_3 \left(c_s^2 \frac{\partial \varrho}{\partial x} + v_x \varrho \frac{\partial v_x}{\partial x} - \varrho \frac{\partial E}{\partial x}\right) \\ \lambda_4 \left(\frac{\partial p}{\partial x} + \varrho c_s \frac{\partial v_x}{\partial x}\right) \end{bmatrix}. \tag{5.25}$$

Izquierdo and Fueyo use implicitly an relation for an infinitesimal change in total Energy [28], corresponding to the total work on the control volume, without dwelling on this relationship:

$$d\left(\varrho \cdot E\right) = d\left(\frac{1}{2}\varrho v_x^2\right) + dp \equiv \frac{dJ}{dA\ dt}. \tag{5.26}$$

Assuming constant density ϱ during an infinitesimal time step, the following relations can be derived:

$$\frac{\partial E}{\partial t} = v_x \cdot \frac{\partial v_x}{\partial t} + \frac{1}{\varrho}\frac{\partial p}{\partial t}, \tag{5.27}$$

$$\frac{\partial E}{\partial x} = v_x \cdot \frac{\partial v_x}{\partial x} + \frac{1}{\varrho}\frac{\partial p}{\partial x}, \tag{5.28}$$

and with equation 5.28, the total Energy can be eliminated from L_3:

$$L_3 = \lambda_3 \left(c_s^2 \frac{\partial \varrho}{\partial x} - \frac{\partial p}{\partial x}\right). \tag{5.29}$$

With the LBM, the relation $p = c_s^2 \varrho$ holds and c_s is constant, resulting in $L_3 \equiv 0$.

In section 6.1, a linearized acoustic model is used leading to the same assumptions 5.27 and 5.28, also discussing the resulting error and a justification for assuming constant density.

Apparently, setting the wave amplitude L_4 for $\lambda_4 = v_x + c_s$ to zero results in a perfectly non-reflecting left boundary condition for inviscid flow and normal incoming pressure waves. This leads, except of a numerical error, to a perfect free field boundary condition for a perpendicular incoming sound pressure wave, as shown in section 5.2.2. For specifying proper boundary conditions, equations 5.18 can be rewritten for the primitive variables

$$\frac{\partial}{\partial t}\underline{U} + \underline{\underline{S}}^{-1} \cdot \underline{L} = 0. \tag{5.30}$$

Equation 5.27 and the wave amplitudes 5.25 lead to:

$$\frac{\partial \varrho}{\partial t} + \frac{1}{2c_s^2}(L_4 + L_1) = 0 \tag{5.31}$$

$$\frac{\partial p}{\partial t} + \frac{1}{2}(L_4 + L_1) = 0 \tag{5.32}$$

$$\frac{\partial v_x}{\partial t} + \frac{1}{2\varrho c_s}(L_4 - L_1) = 0 \tag{5.33}$$

$$\frac{\partial v_y}{\partial t} + L_2 = 0 \tag{5.34}$$

This leads to the condition for a Dirichlet velocity boundary condition $L_4 - L_1 \equiv 0$ or the condition $L_4 + L_1 \equiv 0$ for a Dirichlet pressure boundary condition. However, a perfectly non-reflecting boundary condition e.g. for a left boundary normal to $\underline{e}_x$ requires generally $L_4 = 0$

and $L_1 \neq 0$, which contradicts both of the Dirichlet conditions. This implies that a perfectly non-reflecting Dirichlet velocity or pressure boundary condition is generally not possible. On the contrary, the feedback of the boundary condition via pressure waves is necessary to install a desired state. The remedy by Poinsot and Lele [51] is to allow a distinct rate of reflection. This is modeled by a linear relaxation model, proposed by Rudy and Strikwerda [52]. Suppose L_i would be the wave amplitude of the incoming sound pressure wave. Then a penalty term is installed for the wave amplitude of the pressure wave directed into the domain,

$$L_i = K(\phi - \phi_b), \ \phi = [v_x \vee p] \tag{5.35}$$

for a Dirichlet velocity respectively pressure boundary condition with boundary state ϕ_b. The constant K was derived by Rudy and Strikwerda [52] in an involved Fourier analysis and results for most rapid decay in

$$K := \frac{\sigma(1 - \mathrm{Ma}^2)c_s}{L}, \tag{5.36}$$

where L marks the size of the domain and σ is a constant which has to be calculated iteratively by the non-analytical product log function $W(x) = W(x)e^{W(x)}$ (cf. Rudy and Strikwerda [52])

$$\sigma = W(e^{-1}) \approx 0.2784645428. \tag{5.37}$$

All other wave amplitudes have to be calculated, if possible, by a stable upstream finite difference, otherwise by exploiting equations 5.31 to 5.34 for the respective time derivative of the Dirichlet boundary value set to zero. Poinsot and Veynannte recommend $\sigma \equiv 0.58$ for the relaxation factor, based on field studies [50]. However, the penalty approach does in general not provide means to restrict the reflection to a predefined sound pressure level.

5.2.2 LODI Boundary Conditions for LBM in 1D

In this section, a LODI velocity inflow boundary condition is derived and applied to the test case of section 5.1.4. For one dimension holds $\frac{\partial v_y}{\partial t} \equiv 0$, resulting in $L_2 \equiv 0$. Due to the missing viscous shear force in 1D, there is no steady state pressure decay over the domain. Therefore the feedback of the boundary condition via the mentioned relaxation scheme is not necessary and the wave amplitude for sound pressure waves directing into the domain can be set directly to $L_4 \equiv 0$:

$$L_1 = (v_x - c_s)\left(c_s^2 \frac{\partial \varrho}{\partial x} - \varrho c_s \frac{\partial v_x}{\partial x}\right) \tag{5.38}$$

$$L_2 = L_4 \equiv 0 \tag{5.39}$$

This is equivalent to a LODI free field boundary condition. The spatial derivatives for L_1 can be modeled by one-sided upstream finite difference approximations of the same order as the LBM itself:

$$\frac{\partial \varrho}{\partial x} = \frac{1}{2\Delta x}(-3\varrho(x_b) + 4\varrho(x_b + \Delta x) - \varrho(x_b + 2\Delta x)) + O(\Delta x^2) \tag{5.40}$$

$$\frac{\partial v_x}{\partial x} = \frac{1}{2\Delta x}(-3v_x(x_b) + 4v_x(x_b + \Delta x) - v_x(x_b + 2\Delta x)) + O(\Delta x^2) \tag{5.41}$$

The boundary state is finally computed with equations 5.31 and 5.33 and in compliance to the error of the LBM by a forward Euler scheme:

$$\varrho^{(n)} = \varrho^{(n-1)} + \frac{\Delta t}{2c_s^2}(L_4 + L_1) + O(\Delta t^2) \tag{5.42}$$

$$v_x^{(n)} = v_x^{(n-1)} + \frac{\Delta t}{2\varrho c_s}(L_4 - L_1) + O(\Delta t^2) \tag{5.43}$$

The unknown distribution function on the boundary is set by solving for the first moment,

$$f_1 = f_2 + \varrho v_x. \tag{5.44}$$

As f_1 is overdetermined in the 1D case by the zeroth moment, equation 5.16 will result in an incorrect density. However, all distributions can be corrected by a new distribution function f':

$$f'_k = f_k + \frac{\varrho - \sum_i f_i}{3}. \tag{5.45}$$

It can be easily derived that the zeroth and first moment of f' comply with the desired boundary state of equations 5.42 and 5.43.

5.2.2.1 Discussion of the 1D Test Case

The derived boundary condition was applied to the 1D pressure wave test case of section 5.1.4. The Reynolds number was set to Re = 100 respectively. In the following, the results of the simulation, shown throughout figures 5.12 to 5.16, will be discussed. An example code is printed in appendix A.1.

Figures 5.12 and 5.13 display density and velocity on the domain for the specific time step $t = 500 \cdot \Delta t$, as shown in figures 5.8 and 5.10 for the filtering boundary conditions. The density deviates from the free field simulation in the region of the reflection $x \in [1, 300] \cdot \Delta x$ by 0.3 % of the geometrically damped wave amplitude near $x = 500$. The corresponding deviation of velocity amounts to 1.0 %.

In figures 5.14 to 5.16 the state of the boundary node set by the LODI condition is compared at $x_b = 0$ with the corresponding free field over time. The free field data was recorded in the same distance from the pressure peak, but in a ten time bigger domain, where no reflection from the boundary was interfering with the data. However, the initialization was identical.

Figure 5.14 and 5.15 illustrate that the LODI free field boundary condition is in agreement with the free field simulation. Figure 5.16 shows the relative error of the relevant unknown, the distribution function f_1, which is up to a 2.5% maximum for the specific case.

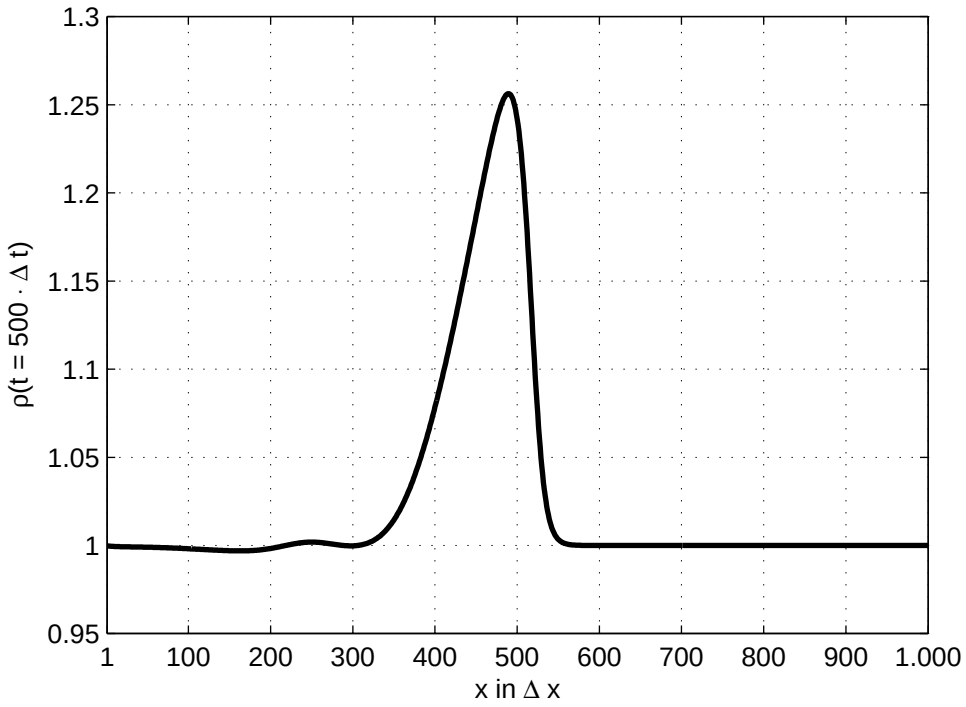

Figure 5.12: Reflection of pressure wave on left hand side, LODI boundary condition, for density

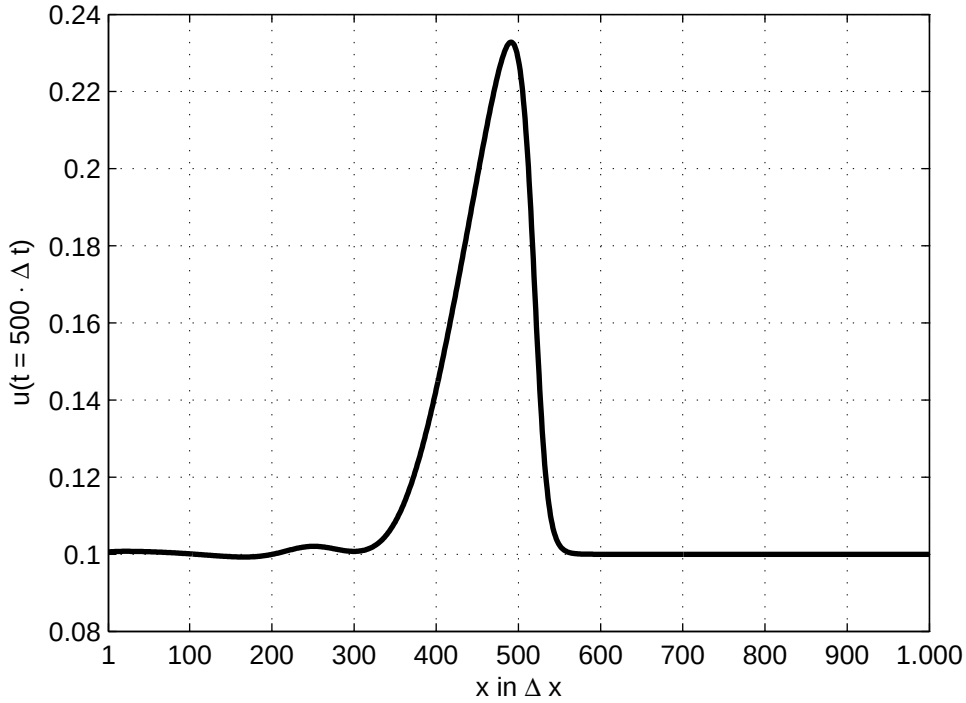

Figure 5.13: Reflection of pressure wave on left hand side, LODI boundary condition, for velocity

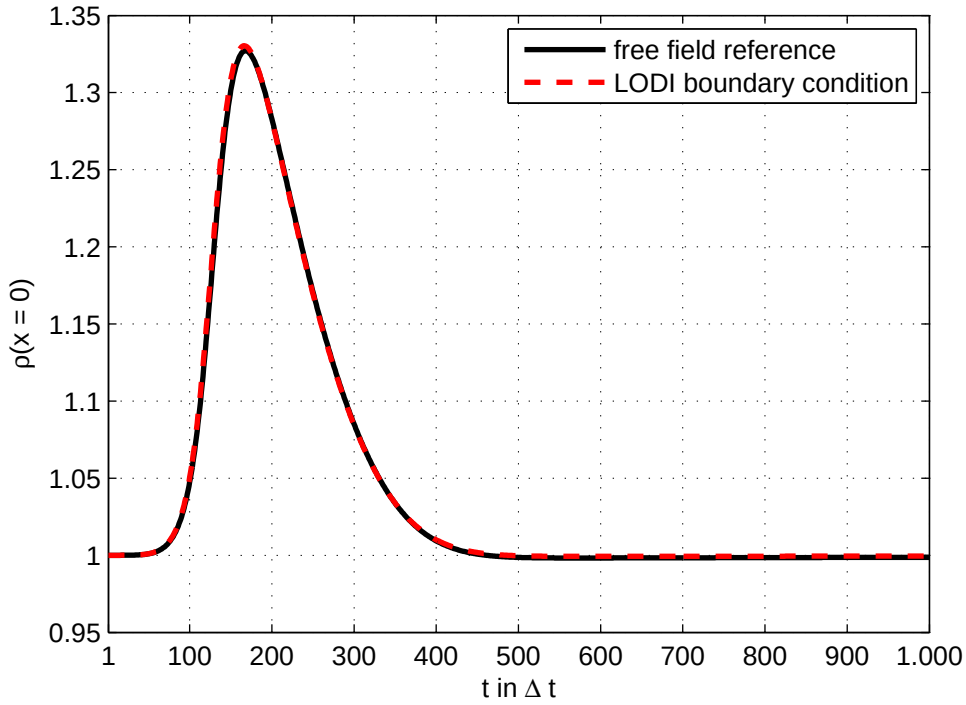

Figure 5.14: Density over time for left inflow LODI boundary with passing pressure wave

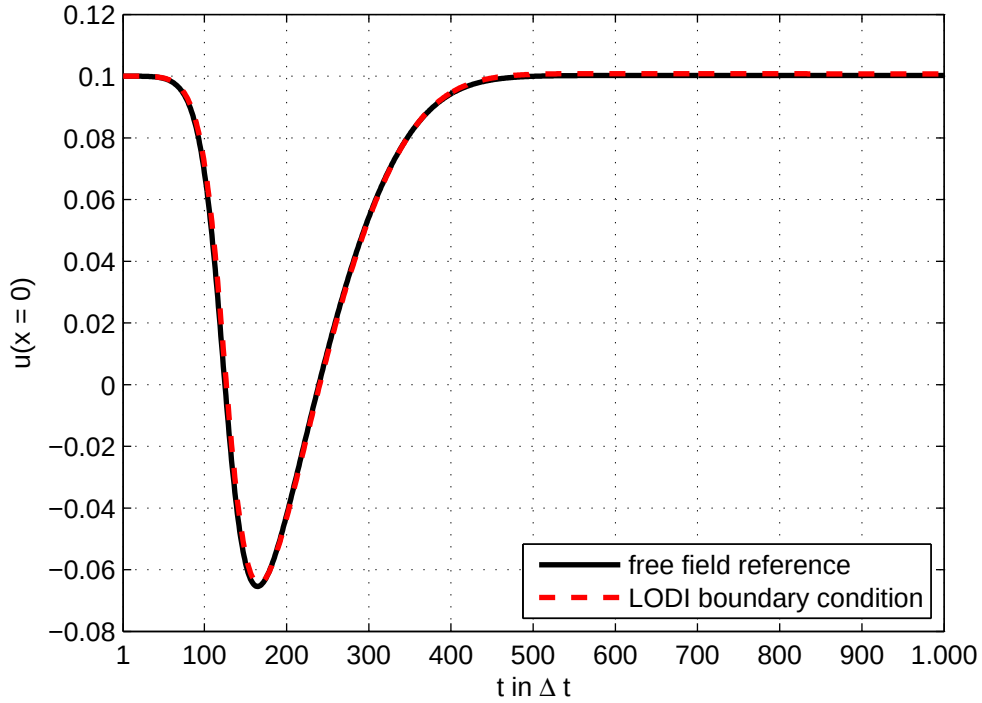

Figure 5.15: Velocity over time for left inflow LODI boundary with passing pressure wave

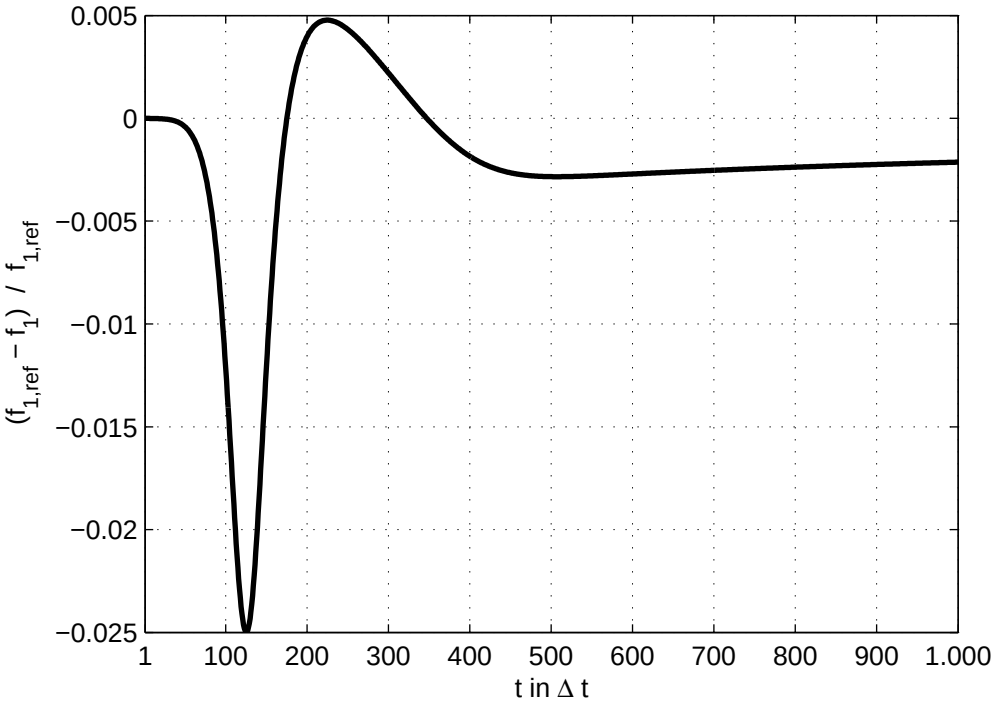

Figure 5.16: Relative error of f_1 for LODI boundary condition with passing pressure wave

5.2.3 LODI Boundary Conditions for LBM in 2D

5.2.3.1 Compressible LBM LODI Boundary Conditions

In this section, a LODI boundary condition for the two-dimensional LBM is set up for a left-hand side inflow boundary, normal direction $\underline{e}_x$. Other than the implementation of Izquierdo and Fueyo [28], the final state of the boundary is set directly on the grid node by non-equilibrium bounce-back, which Zou and He were already using in the derivation of their boundary conditions (cf. section 4.3). Therefore also the finite difference stencil is not conforming with the one used by Izquierdo and Fueyo. Apart from that, the boundary condition is designed to gain minimal reflection, hence to recover a free field. A pressure or velocity adaption will be not discussed in this context.

The requirement for the inflow is according to section 5.2.1 a vanishing wave amplitude L_4, resulting in the following setup of equations:

$$L_1 = (v_x - c_s)\left(c_s^2 \frac{\partial \varrho}{\partial x} - \varrho c_s \frac{\partial v_x}{\partial x}\right) \tag{5.46}$$

$$L_2 = v_x \frac{\partial v_y}{\partial x} \tag{5.47}$$

$$L_4 \equiv 0 \tag{5.48}$$

The three derivatives are each approximated by a finite difference stencil with an error of $O(\Delta x^2)$:

$$\frac{\partial \varrho}{\partial x} = \frac{1}{2\Delta x}\left(-3\varrho(x_b) + 4\varrho(x_b + \Delta x) - \varrho(x_b + 2\Delta x)\right) \tag{5.49}$$

$$\frac{\partial v_x}{\partial x} = \frac{1}{2\Delta x}\left(-3v_x(x_b) + 4v_x(x_b + \Delta x) - v_x(x_b + 2\Delta x)\right) \tag{5.50}$$

$$\frac{\partial v_y}{\partial x} = \frac{1}{2\Delta x}\left(-3v_y(x_b) + 4v_y(x_b + \Delta x) - v_y(x_b + 2\Delta x)\right) \tag{5.51}$$

The state of the boundary is computed by first order forward time integration applied on equations 5.31, 5.33 and 5.34:

$$\varrho^{(n)} = \varrho^{(n-1)} - \frac{\Delta t}{2c_s^2}(L_4^{(n-1)} + L_1^{(n-1)}) \tag{5.52}$$

$$v_x^{(n)} = v_x^{(n-1)} - \frac{\Delta t}{2\varrho c_s}(L_4^{(n-1)} - L_1^{(n-1)}) \tag{5.53}$$

$$v_y^{(n)} = v_y^{(n-1)} - \Delta t \cdot L_2^{(n-1)} \tag{5.54}$$

Finally, the three unknown distributions are set, as mentioned, by non-equilibrium bounce-back. This is basically equivalent by setting the unknown distribution by their equilibrium and copying the non-equilibrium from the opposite distribution:

$$f_1 = f_3 + \frac{2}{3}\varrho v_x \tag{5.55}$$
$$f_5 = f_7 + \frac{1}{6}\varrho(v_x + v_y) \tag{5.56}$$
$$f_8 = f_6 + \frac{1}{6}\varrho(v_x - \varrho v_y) \tag{5.57}$$

An example for the implementation can be found in appendix A.2.

5.2.3.2 Incompressible LBM LODI Boundary Conditions

For the incompressible LBM, the system of equations 5.18 has to be adapted according to the Chapman-Enskog derivation of mass and momentum conservation, as derived in equations 3.95 and 3.99. The energy equation is maintained, although for the pressure gradient the dynamic density is used. As a result, only the matrix A (cf. equation 5.20) has to be changed and turns into

$$\underline{\underline{A}} := \begin{bmatrix} 0 & \varrho_0 & 0 & 0 \\ c_s^2/\varrho_0 & 2v_x & 0 & 0 \\ 0 & 0 & v_x & 0 \\ c_s v_x/\varrho_0 & c_s^2 & 0 & v_x \end{bmatrix} \tag{5.58}$$

The eigendecomposition of A, as shown in section 5.2.1, leads to the following characteristic velocities λ_i:

$$\lambda_1 = v_x - \sqrt{v_x^2 + 4c_s^2}, \tag{5.59}$$
$$\lambda_2 = v_x, \tag{5.60}$$
$$\lambda_3 = v_x, \tag{5.61}$$
$$\lambda_4 = v_x + \sqrt{v_x^2 + 4c_s^2}. \tag{5.62}$$

Due to this fact, the formulation of the conservation of mass from the Chapman-Enskog procedure, equation 3.95, cannot be used. Rather an additional term is added, gaining a substitute for the equation 3.95,

$$\nabla \cdot \underline{v} + \frac{1}{\varrho_0}\frac{\partial}{\partial t}\varrho + \underbrace{\frac{\underline{v}}{\varrho_0}\nabla\varrho}_{\text{added}} = 0,$$

which results in an entry $A_{1,1} = v_x$. The divergence term on the left hand side of equation 3.99 is additionally neglected, so $A_{2,2} = 2v_x$ becomes $A_{2,2} = v_x$. This leads to the same characteristic velocities of equation 5.24. The characteristic amplitudes for the same free field formulation as in section 5.2.3.1 are:

$$L_1 = (v_x - c_s)\left(c_s^2 \frac{\partial \varrho}{\partial x} - \varrho_0 c_s \frac{\partial v_x}{\partial x}\right) \tag{5.63}$$

$$L_2 = v_x \frac{\partial v_y}{\partial x} \tag{5.64}$$

$$L_4 \equiv 0 \tag{5.65}$$

The three derivatives are approximated by the finite difference stencils of equations 5.49, 5.50 and 5.51. The forward time integration of equations 5.31, 5.33 and 5.34 leads to:

$$\varrho^{(n)} = \varrho^{(n-1)} - \frac{\Delta t}{2c_s^2}(L_4^{(n-1)} + L_1^{(n-1)}) \tag{5.66}$$

$$v_x^{(n)} = v_x^{(n-1)} - \frac{\Delta t}{2\varrho_0 c_s}(L_4^{(n-1)} - L_1^{(n-1)}) \tag{5.67}$$

$$v_y^{(n)} = v_y^{(n-1)} - \Delta t \cdot L_2^{(n-1)} \tag{5.68}$$

The three variables are set by non-equilibrium bounce-back of the incompressible LBM:

$$f_1 = f_3 + \frac{2}{3}\varrho_0 v_x \tag{5.69}$$

$$f_5 = f_7 + \frac{1}{6}\varrho_0 (v_x + v_y) \tag{5.70}$$

$$f_8 = f_6 + \frac{1}{6}\varrho_0 (v_x - v_y) \tag{5.71}$$

The corresponding implementation is demonstrated in section A.3.

5.2.4 2D Pressure Wave Test Case

For testing the two-dimensional non-reflecting boundary conditions, a pressure peak formed as 2D Gaussian bell curve is placed near the left boundary. The setup is sketched in figure 5.17: The simulation domain is square with an edge length of $l_x = l_y = 800 \cdot \Delta x$ (801 grid nodes). The pressure peak is placed at a distance of $p_x = 200 \cdot \Delta x$ from the left boundary and centered between the bottom and top at $p_y = 400 \cdot \Delta x$. With this setup, the simulation covers a varying impact angle of the pressure wave in a range of 0° to 60° relative to the normal vector of the left boundary.

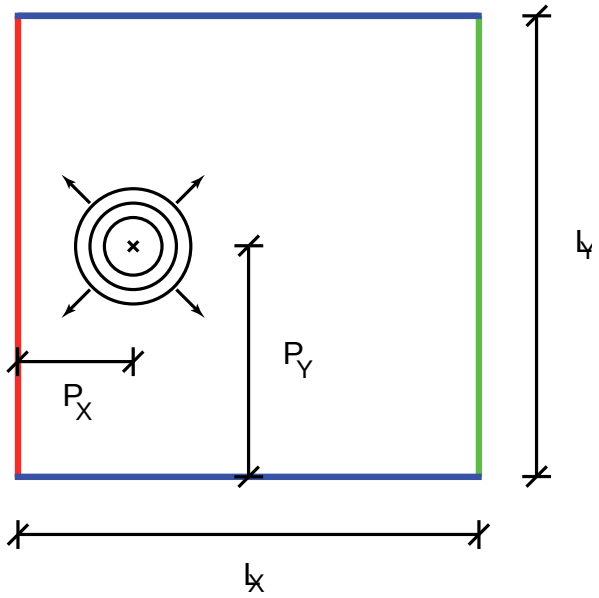

Figure 5.17: Setup, 2D pressure wave test case

On the left-hand side, marked in red, the boundary nodes implement the boundary condition to be tested. The right, marked in green, is realized by a Zou-He pressure boundary condition (cf. section 4.3) with a fixed density of $\varrho_0 = 1$. The top and bottom boundary nodes are bounce-back nodes (cf. section 4.2), so that there is a no-slip boundary half way between the bottom respectively top row and the next following inner row. This reduces the physical flow domain to

$$l_{y,p} = l_y - \Delta y \tag{5.72}$$

The density is initialized by setting the Gauss peak to:

$$\varrho(t=0,x,y) = \varrho_0 - \left[\varrho_{\max} - \varrho_0 \exp\left(-\frac{(x-p_x)^2 + (y-p_y)^2}{2 \cdot \left(\frac{l_y}{50}\right)^2}\right)\right] \tag{5.73}$$

$$\varrho_0 = 1 \tag{5.74}$$

$$\varrho_{\max} = 2 \tag{5.75}$$

Initially, the velocity in $\underline{e}_y$-direction is set to zero, $v_y = 0$. For the v_x velocity, two different initial conditions are used:

$$\text{Setup (a):} \quad v_x(t = 0, x, y) = 0 \tag{5.76}$$

$$\text{Setup (b):} \quad v_x(t = 0, x, y) = 4\frac{v_{\max}}{l_{y,p}^2} \cdot (y - \Delta y/2) \cdot (l_{y,p} - (y - \Delta y/2)) \tag{5.77}$$

The second one represents a parabolic duct flow covering the steady state while using the top/bottom no-slip boundary conditions with parabolic inflow velocity profile. This velocity setup is used, besides having a convective flow induced, to involve a shear force on the boundary. The distribution functions are initialized by the corresponding equilibrium distribution.

The viscosity of the simulation is in both cases such that the Reynolds number $Re = (L \cdot v_{\text{ref}} \cdot \varrho_0)/\nu = 100$ with a characteristic length $L = 195 \cdot \Delta x$, which resembles the object size of the simulation of section 7.4. For case (a), a maximum speed $v_{\text{ref}} = 0.1 \cdot c_0$ is set to maintain comparability with the subsequent simulations. For test case (b) the speed is set to $v_{\text{ref}} := v_{\max}$.

For comparing the simulation with non-reflecting boundary conditions to the corresponding free field, a reference simulation was set up with the same properties as above, but three times the domain length, as illustrated in figure 5.18. Only the data of the middle of the three sections, marked gray in figure 5.18, is evaluated. Reflections on the left and right boundary do not happen during the evaluated simulation time. The inflow is set statically to the velocity profile of equation 5.76 or 5.77 with a Zou-He velocity boundary condition, the outflow to the constant density $\varrho_0 = 1$ with the Zou-He pressure boundary condition (cf. section 4.3). The initial conditions are set consistently with the test setup according to equations 5.76 and 5.77.

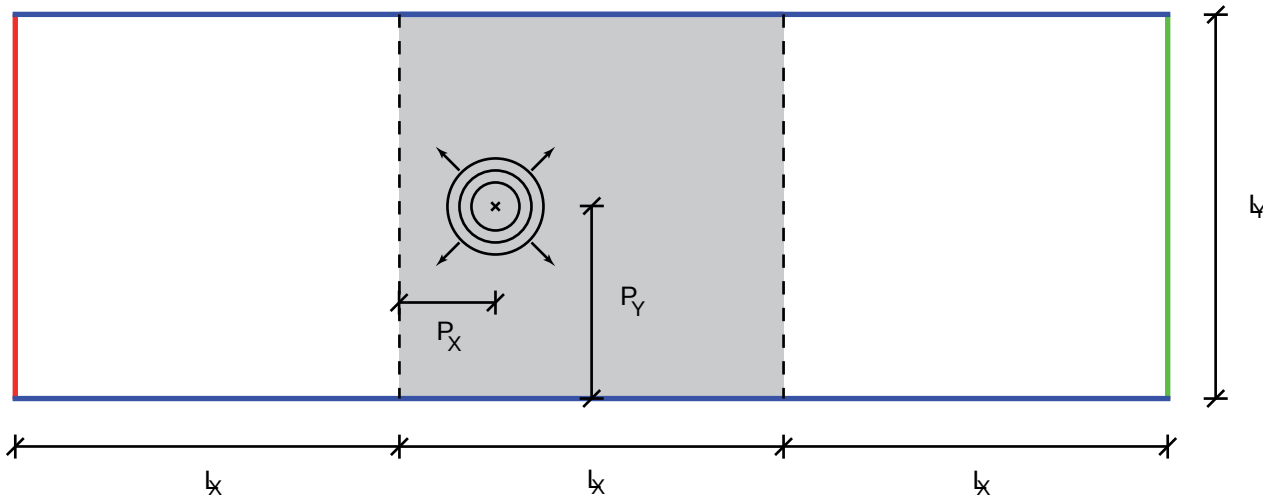

Figure 5.18: Free field reference for pressure wave test case

Figure 5.19 shows test case (a) and the reflection of the pressure peak at a Zou-He velocity boundary condition imposed on the left boundary for the compressible LBM. The colormap is scaled to the actual minimum and maximum density of each time step.

Figure 5.20 and 5.21 show the corresponding free field, for density and absolute velocity at time step $t = 700 \cdot \Delta t$.

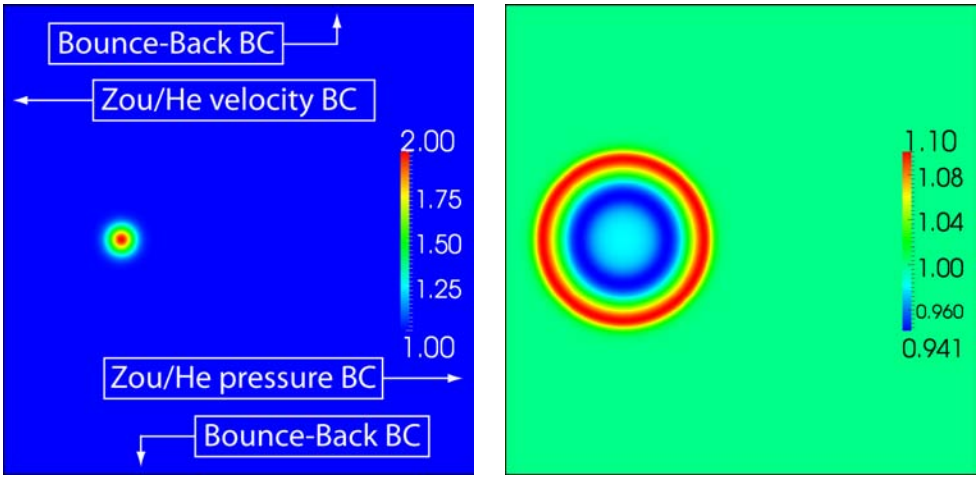

density at $t = 0$

density at $t = 200 \cdot \Delta t$

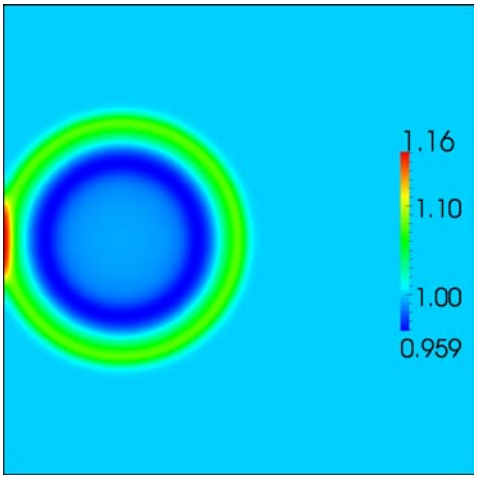

density at $t = 300 \cdot \Delta t$

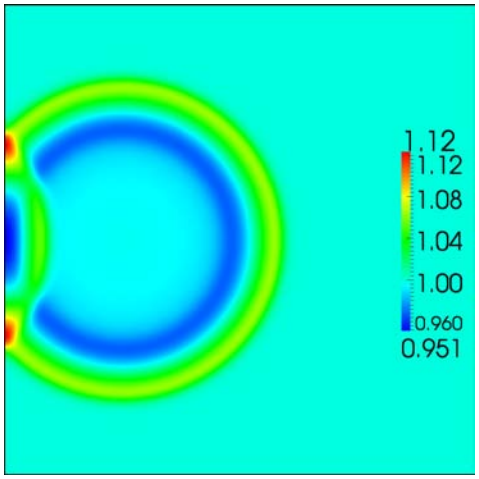

density at $t = 400 \cdot \Delta t$

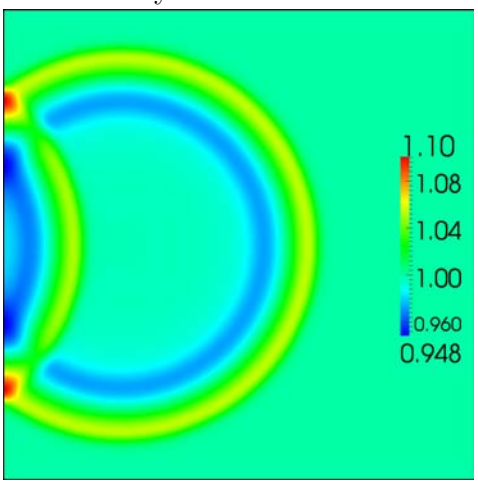

density at $t = 500 \cdot \Delta t$

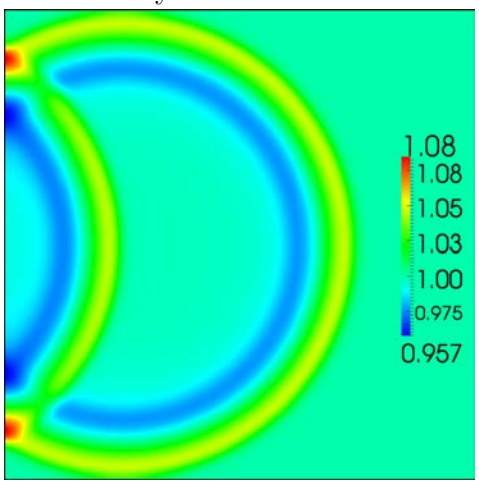

density at $t = 600 \cdot \Delta t$

Figure 5.19: Pressure peak evolving over time

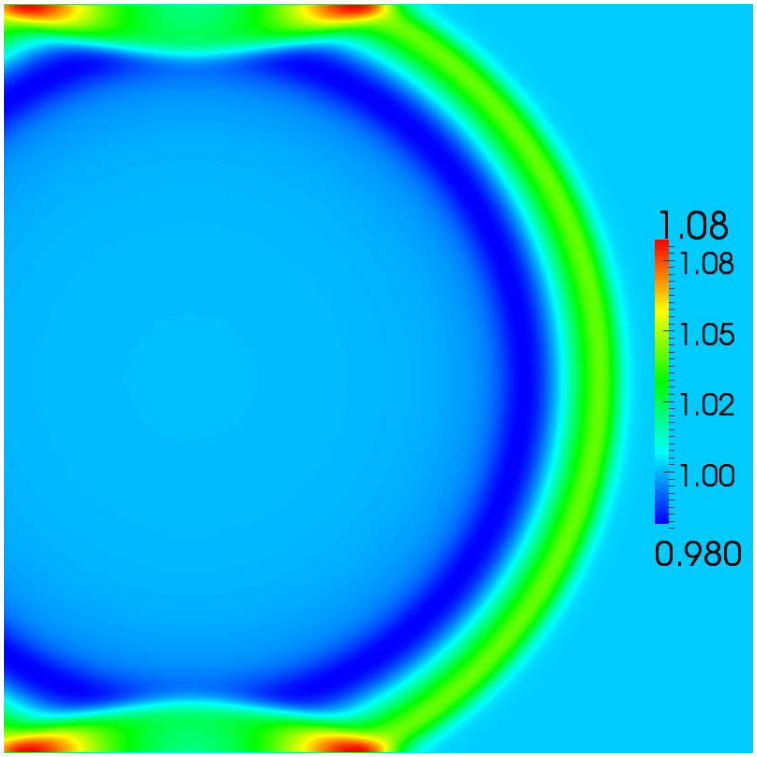

Figure 5.20: Free field of setup (a), density at $t = 700 \cdot \Delta t$

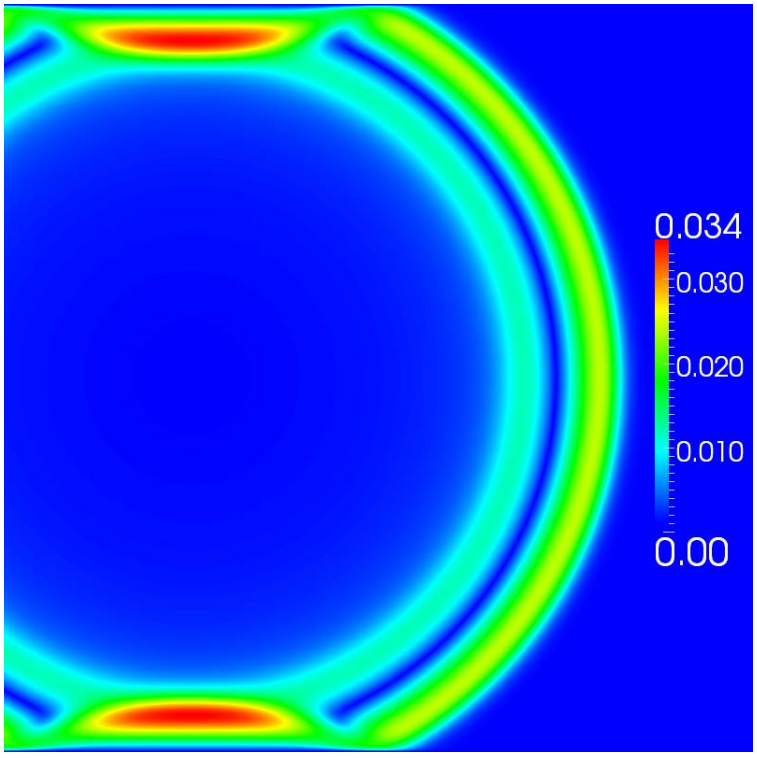

Figure 5.21: Free field of setup (a), absolute velocity at $t = 700 \cdot \Delta t$

5.2.5 2D Pressure Wave Test Case for LODI BCs

In this section, the results of the 2D pressure wave test case of section 5.2.4 are discussed for the LODI boundary condition of section 5.2.3. It will be shown that the LODI boundary condition has a reflection rate in dependence of the incident angle, and each test case includes a corresponding plot of the relative error in density, compared to the free field. The dashed line plotted in figure 5.22 marks the positions of sample points for this graph. As it represents the evolving pressure wave of the mirror source $(p_{x,mirror}, p_{y,mirror})$ with the radius r at the current time step, the reflection angle can be recovered at the position (x_s, y_s):

$$x_s = r * \mathrm{Re}\left(e^{(i\phi)}\right) + p_{x,mirror} \tag{5.78}$$

$$y_s = r * \mathrm{Im}\left(e^{(i\phi)}\right) + p_{y,mirror} \tag{5.79}$$

The sample points were taken in a range of 0° to 60° in steps of $\Delta\phi = 1°$. Intermediate grid values were computed by cubic interpolation.

5.2.5.1 Compressible LBM, Resting Fluid

First, the LODI free field boundary condition was tested for a resting initial fluid, as described in case (a) of section 5.2.4. The pressure peak evolves as in figure 5.19, except the reflection is suppressed on the left hand-side boundary. Figure 5.22 and 5.23 show the density and absolute velocity after 700 time steps. Figure 5.24 and 5.25 show the error compared to the corresponding free field simulation.

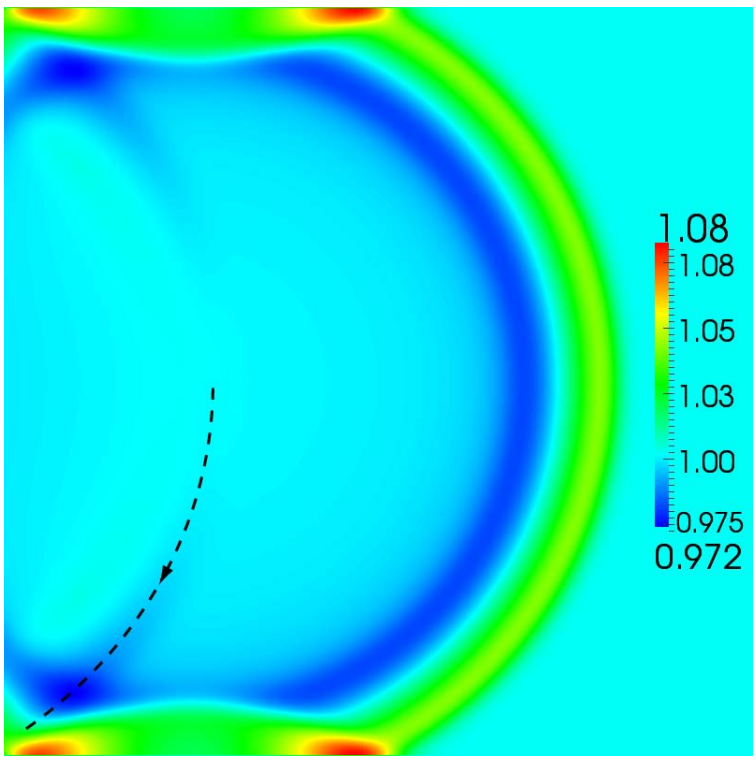

Figure 5.22: LODI free field BC, setup (a), density at $t = 700 \cdot \Delta t$. Line plotted along sample points as described in section 5.2.5

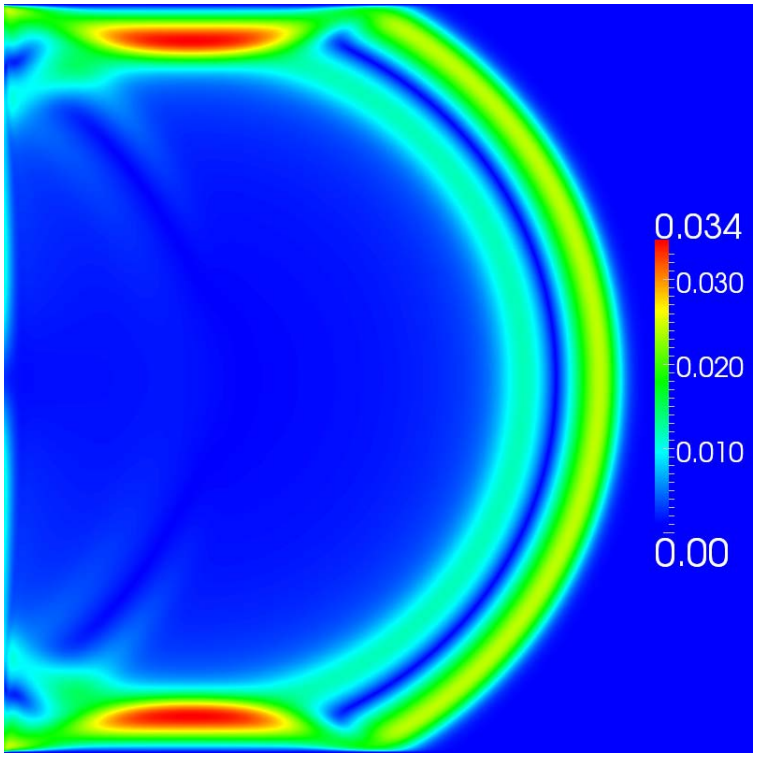

Figure 5.23: LODI free field BC, setup (a), absolute velocity at $t = 700 \cdot \Delta t$

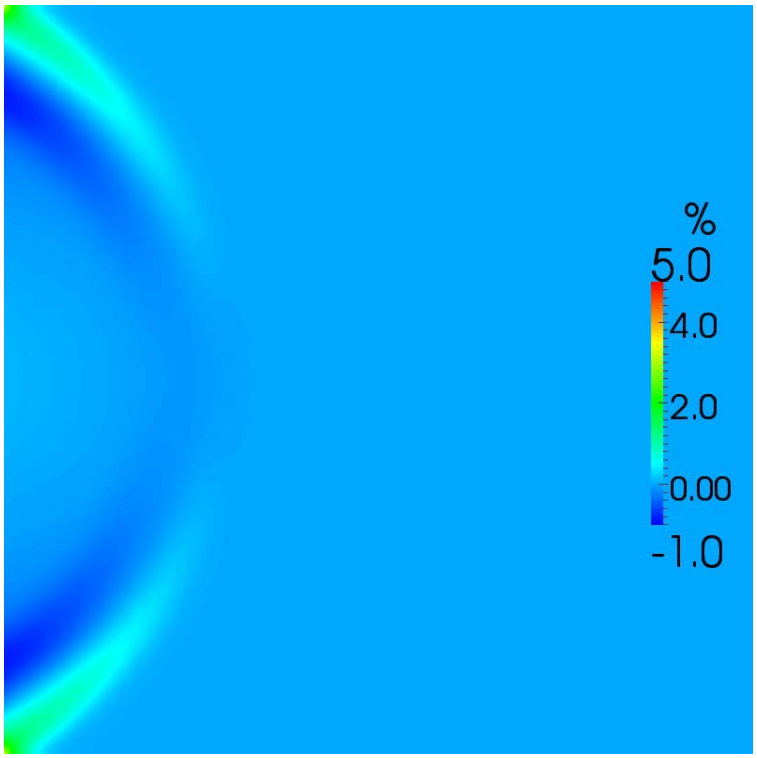

Figure 5.24: LODI free field BC, setup (a), relative density error in % at $t = 700 \cdot \Delta t$

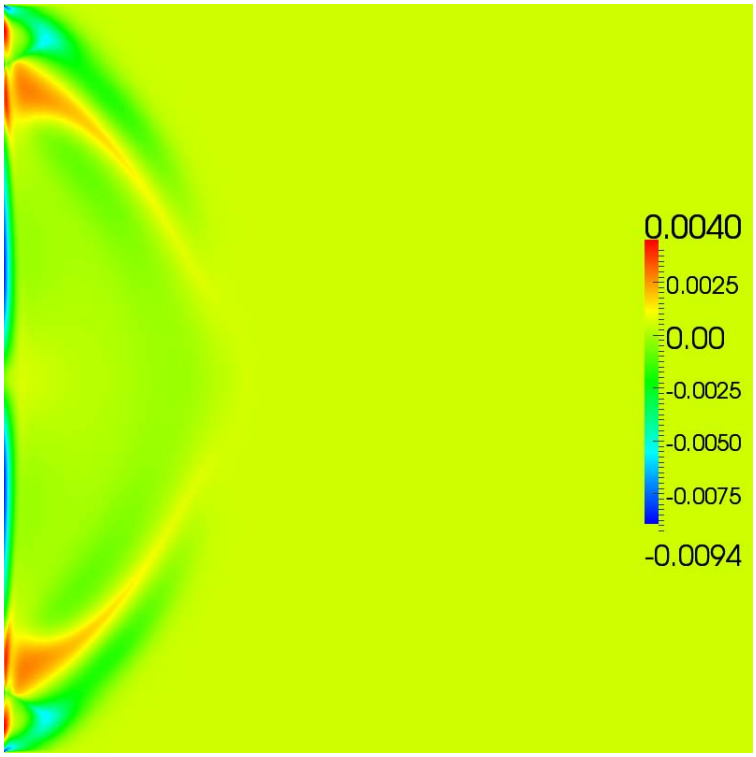

Figure 5.25: LODI free field BC, setup (a), absolute error of velocity error at $t = 700 \cdot \Delta t$

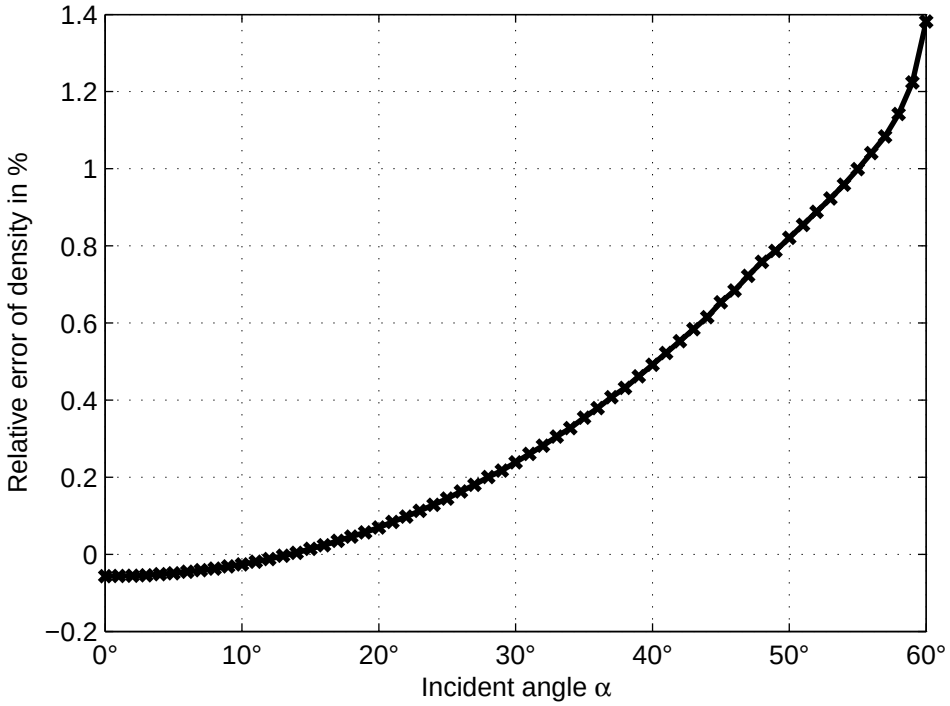

Figure 5.26: Reflection over incident angle

The characteristic angular dependence of the reflection for density can be seen in figure 5.26. The relative error ranges from 0% to 1.4%.

5.2.5.2 Compressible LBM, Parabolic Velocity Inflow Profile

Next, setup (b) of the test case of section 5.2.4 was simulated with the 2D LODI free field boundary condition on the left inflow boundary. The maximum inflow velocity was reduced to $v_{\max} = 0.03$ due to stability problems with the present implementation of the LODI boundary condition. The instability might be caused by the explicit forward time integration and occurred for a variety of ways to set the LODI state, including the use of the equilibrium distribution.

Figures 5.27 to 5.31 illustrate the results of the simulation, like in the previous section for time step $t = 700 \cdot \Delta t$. The maximum relative error in density is in the same range as for the hydrostatic case (a) of the previous section. The maximum error in absolute velocity, not considering the effects in the direct vicinity of the inflow boundary, equals 0.003, which is 10% of the maximum inflow velocity. The relative error in density in dependence on the incident angle, as described at the beginning of section 5.2.5, can be seen in figure 5.31. It ranges from 0% to 1.6%.

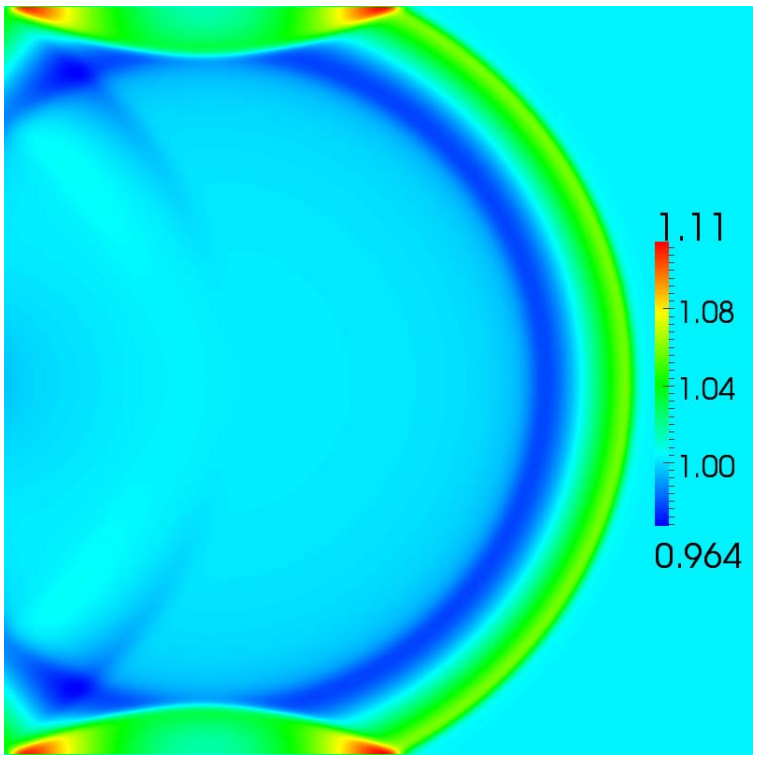

Figure 5.27: LODI free field BC, setup (b), density at $t = 700 \cdot \Delta t$

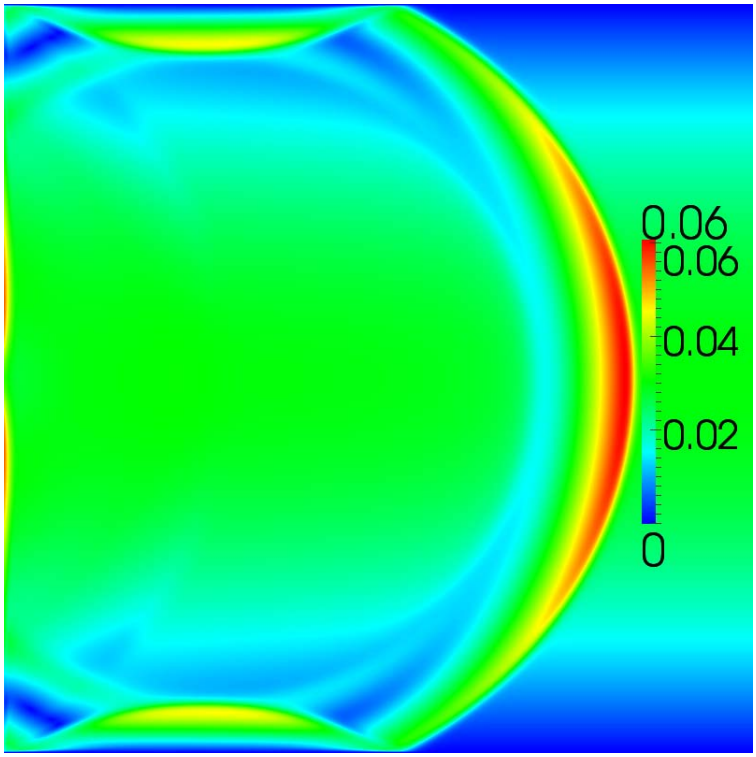

Figure 5.28: LODI free field BC, setup (b), absolute velocity at $t = 700 \cdot \Delta t$

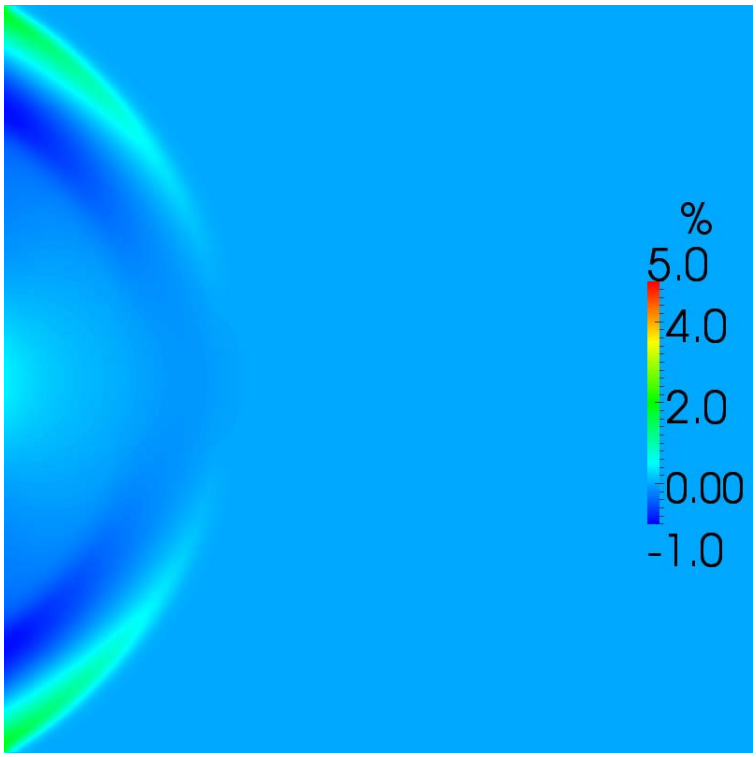

Figure 5.29: LODI free field BC, setup (b), relative density error in % at $t = 700 \cdot \Delta t$

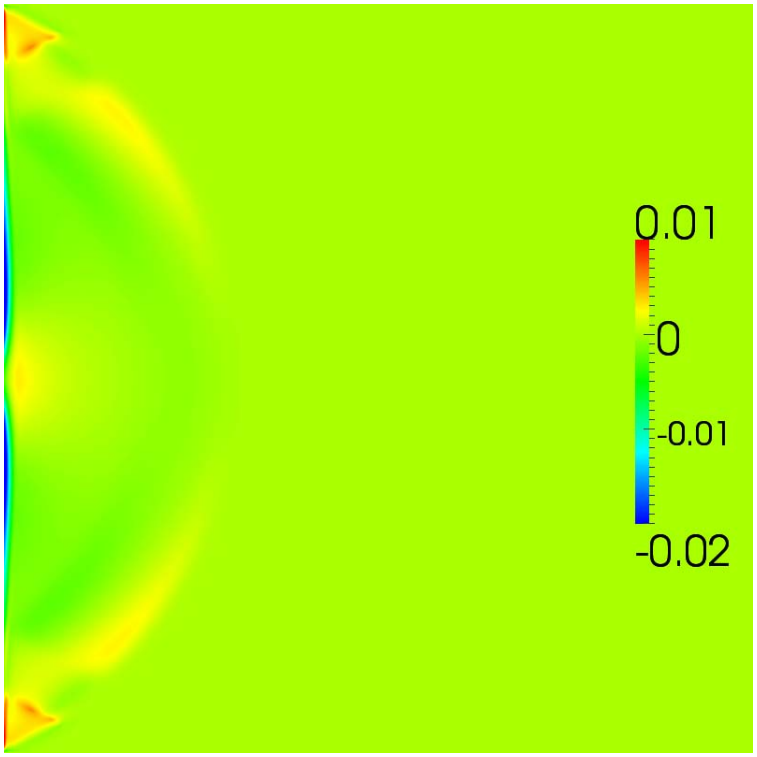

Figure 5.30: LODI free field BC, setup (b), absolute error of velocity error at $t = 700 \cdot \Delta t$

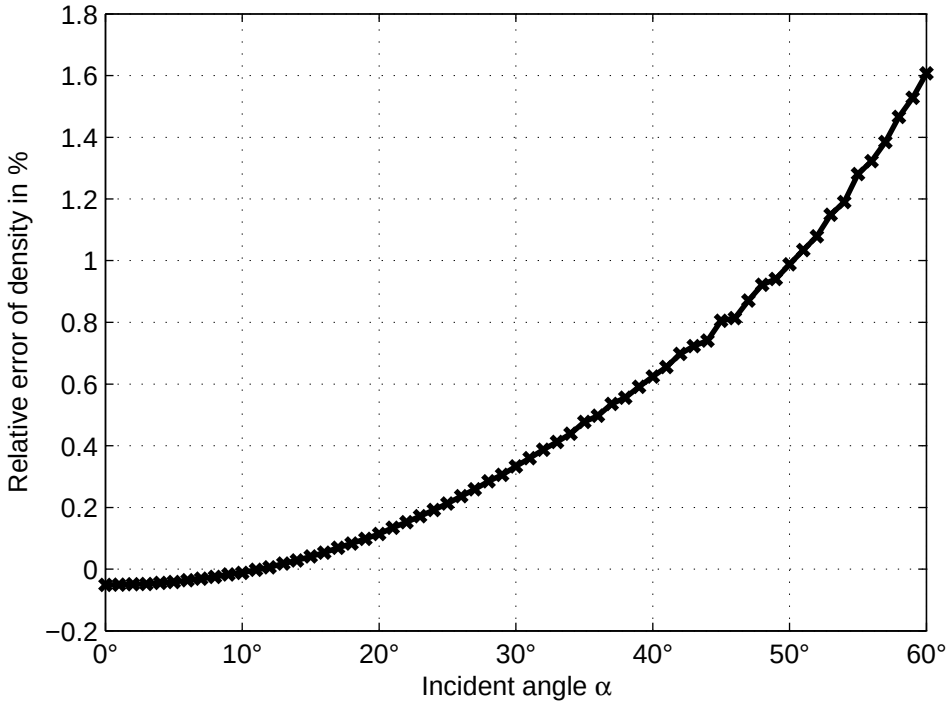

Figure 5.31: Reflection over incident angle, setup (b)

5.2.5.3 Incompressible LBM, Resting Fluid

For the incompressible LBM, the MRT model described in section 3.5.2 was used. The bulk viscosity was set to $\mu' = \frac{2}{3} \cdot \mu$. Figure 5.32 shows the density at time step $t = 700 \cdot \Delta t$, Figure 5.33 the corresponding velocity field. The relative error in density and the absolute velocity error, compared to the free field simulation, are shown in figure 5.34 and 5.35.

The significant relation of relative error in density over the incident angle (cf. introduction of section 5.2.5) can be found in figure 5.36. It can be seen that the error lies in a range of 0% to 1.4%, just as in the compressible case of section 5.2.5.1.

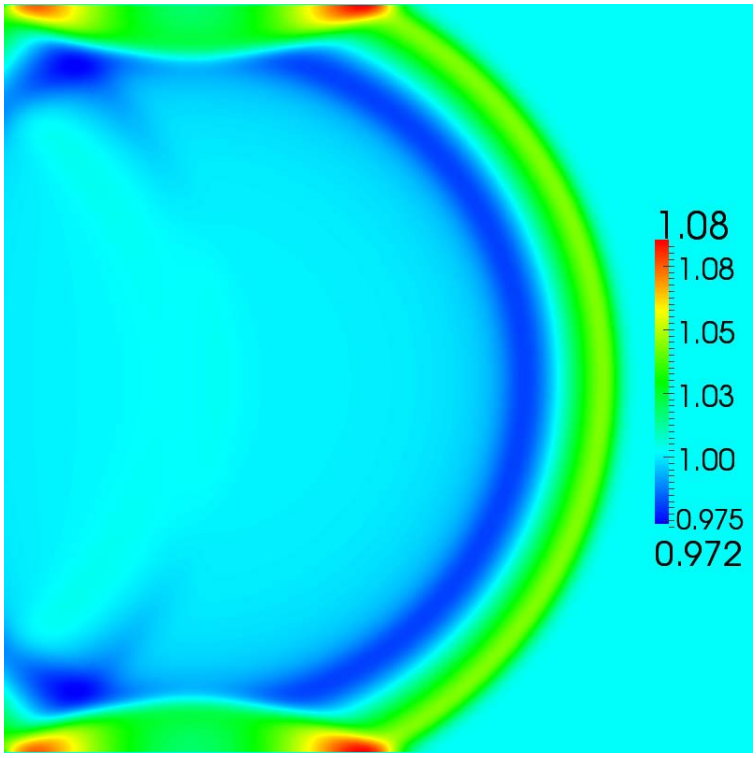

Figure 5.32: LODI free field BC, setup (a), density at $t = 700 \cdot \Delta t$

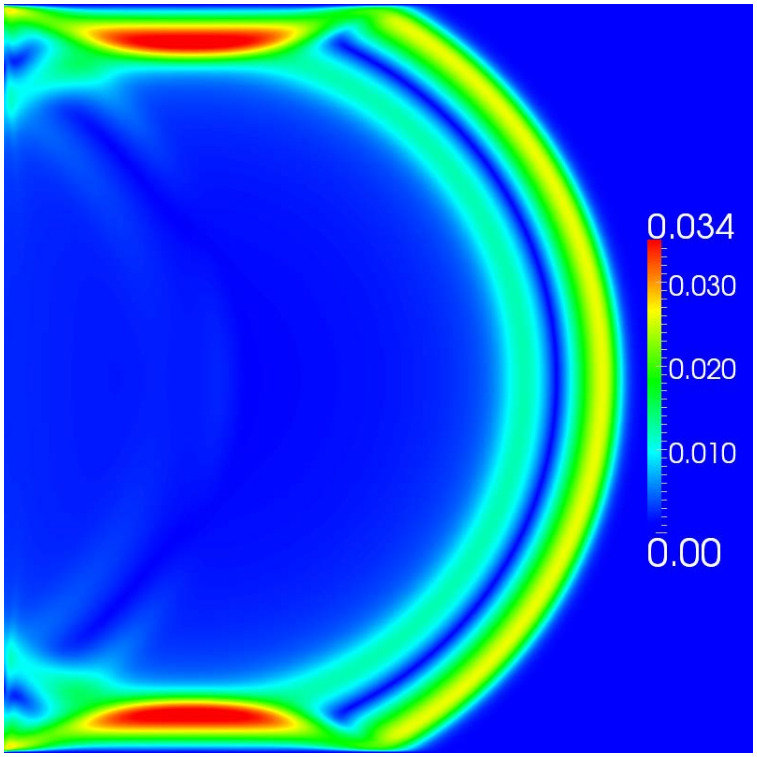

Figure 5.33: LODI free field BC, setup (a), absolute velocity at $t = 700 \cdot \Delta t$

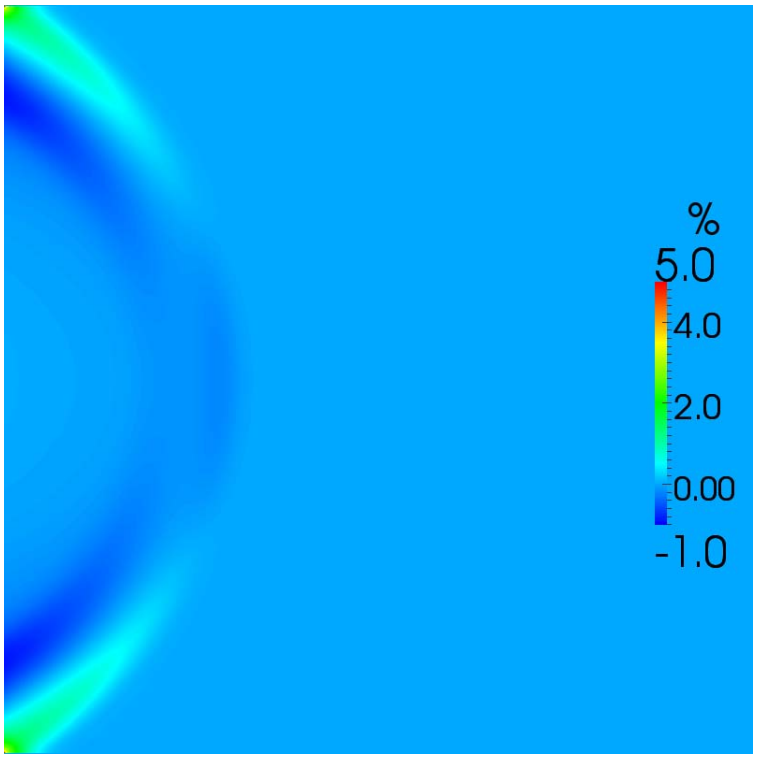

Figure 5.34: LODI free field BC, setup (a), relative density error in % at $t = 700 \cdot \Delta t$

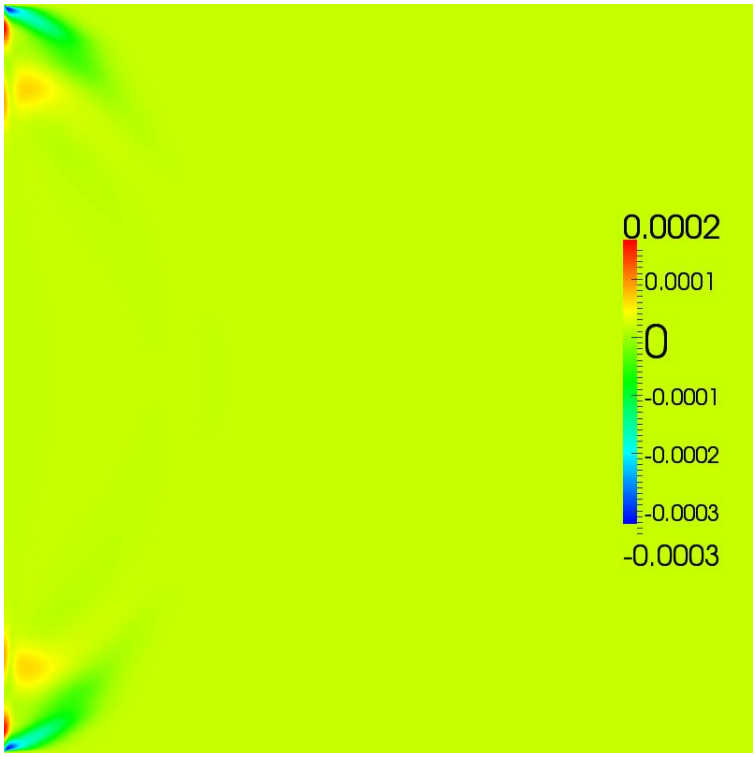

Figure 5.35: LODI free field BC, setup (a), absolute error of velocity error at $t = 700 \cdot \Delta t$

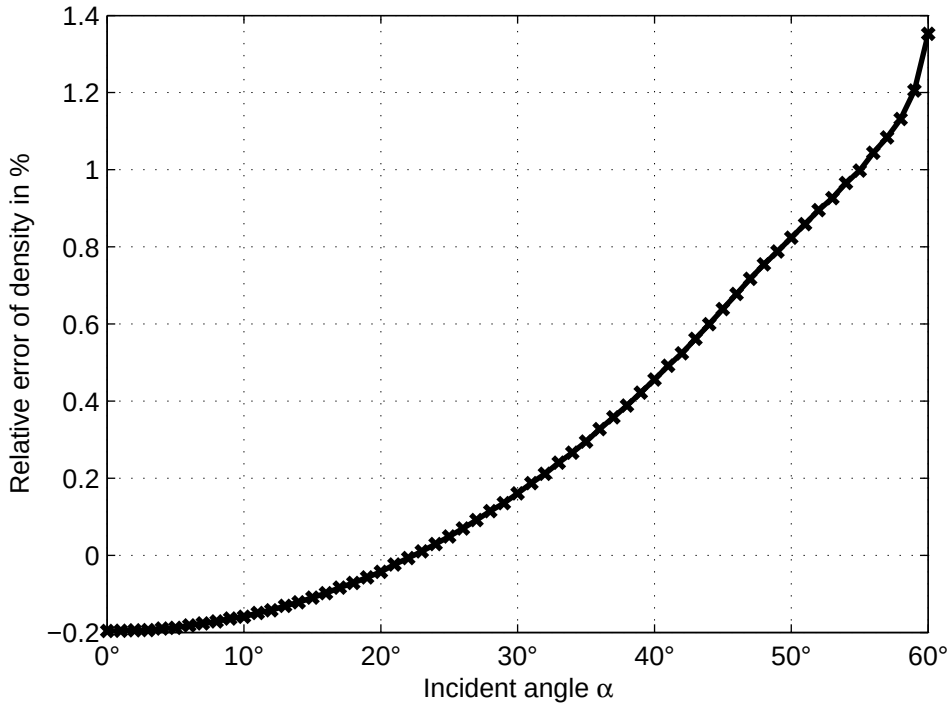

Figure 5.36: Reflection over incident angle

5.2.5.4 Incompressible LBM, Parabolic Velocity Inflow Profile

Finally, setup (b) was simulated with the incompressible LBM. The state of the flow field is shown in figure 5.37 and 5.38, the corresponding relative respectively absolute error in figure 5.39 and 5.40. The relative error in density, plotted over the expanding spherical wave maximum of the mirror source, ranges from 0% to 1.6%, just like in the compressible case in section 5.2.5.2.

In summary can be stated that the implemented LODI boundary condition shows in all cases tested a similar behavior. It is characterized by a distinct relation of the dependence of reflectance and angle of incidence, as seen in figure 5.24, 5.29, 5.34 and 5.39, respecitvely in figure 5.26, 5.31, 5.36 and 5.41. The reflected wave shows in relation to the free field simulation a maximum relative error between 1.4% and 1.6% for an incident angle of 60°, depending on the test case.

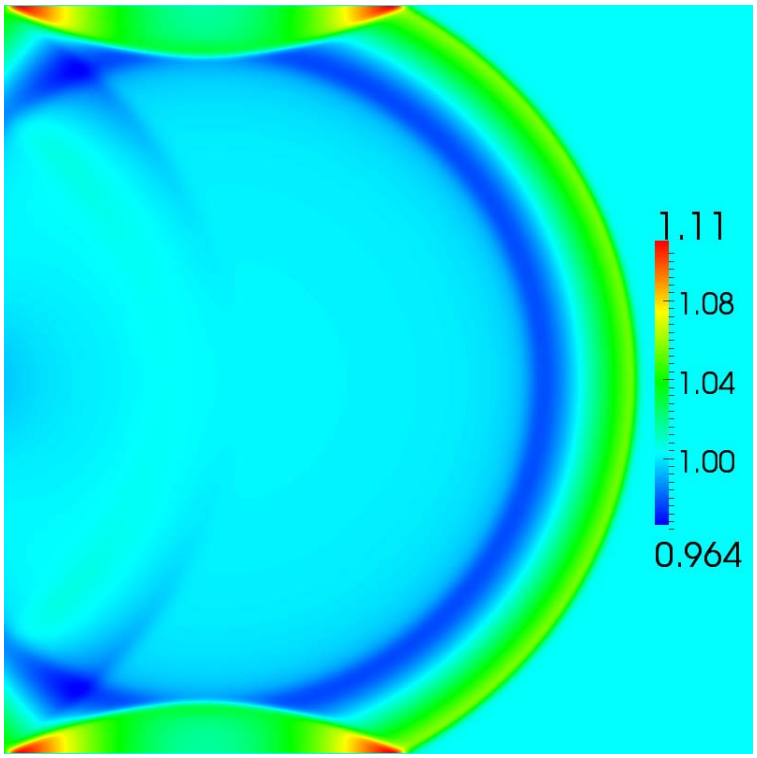

Figure 5.37: LODI free field BC, setup (b), density at $t = 700 \cdot \Delta t$

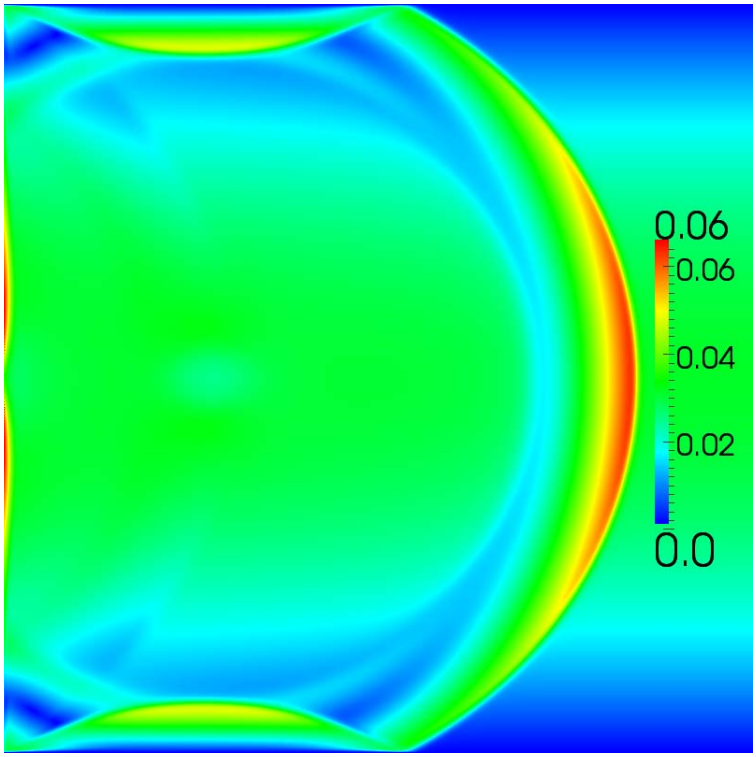

Figure 5.38: LODI free field BC, setup (b), absolute velocity at $t = 700 \cdot \Delta t$

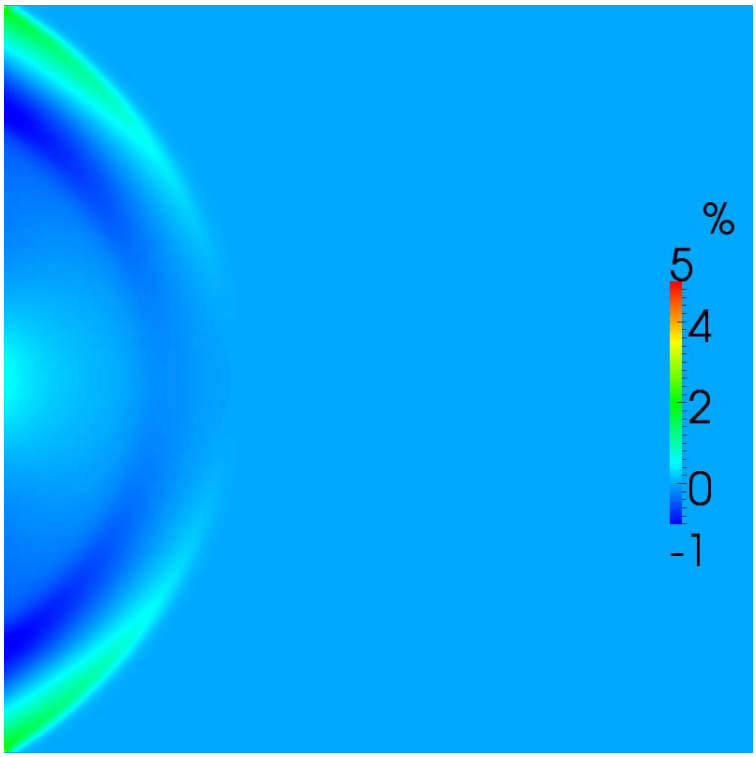

Figure 5.39: LODI free field BC, setup (b), relative density error in % at $t = 700 \cdot \Delta t$

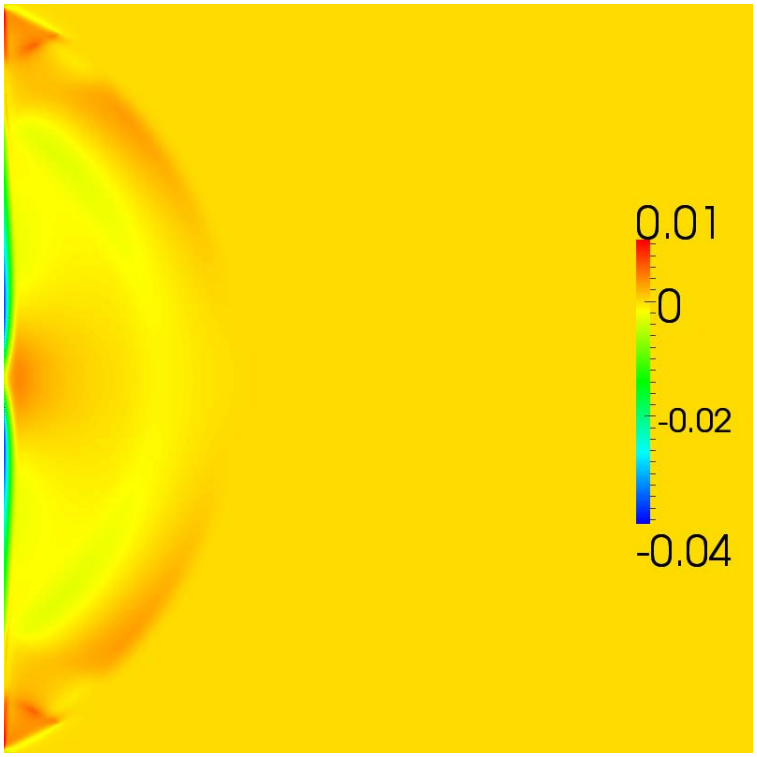

Figure 5.40: LODI free field BC, setup (b), absolute error of velocity error at $t = 700 \cdot \Delta t$

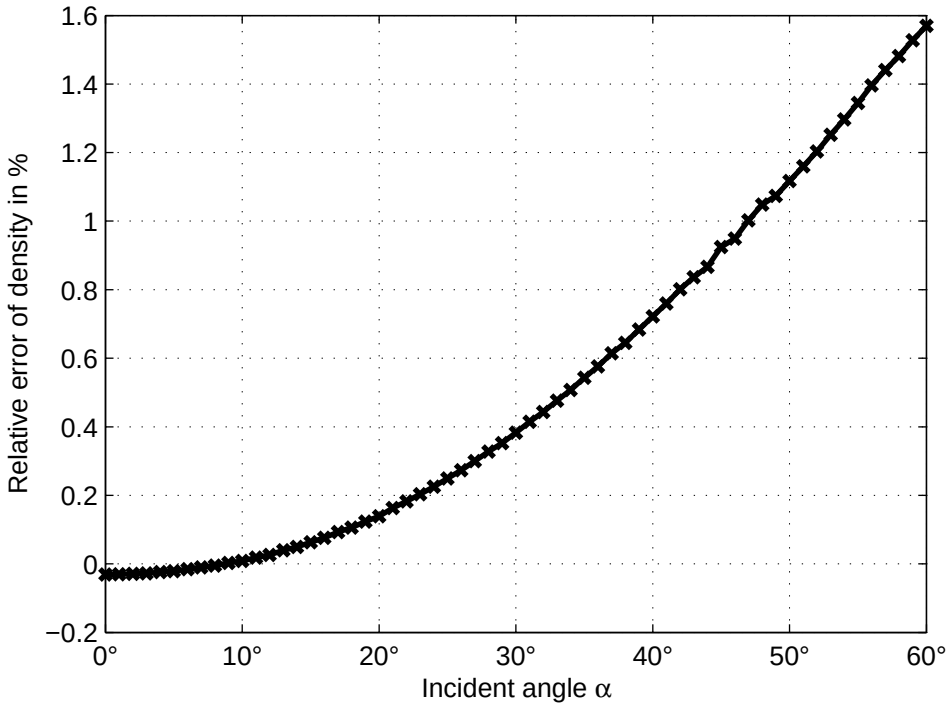

Figure 5.41: Reflection over incident angle

Chapter 6

Impedance Boundary Conditions

The intention of the boundary conditions presented in this chapter is to avoid reflections by adapting a specific impedance. There are several approaches with a similar intention. For example, this is subject to the widely known method of Perfectly Matched Layers (PML), introduced by Berenger in the context of the Maxwell equations [4]. This method was numerously adapted and also implemented in the field of classical Navier-Stokes methods (i.e. by Freund [16]). Tekitek et al. [55] introduce an implementation of PML for the Lattice Boltzmann Method. Although the basic objective is supposed to be the same, the boundary conditions derived below are entirely different.

6.1 Impedance Condition 1D

Instead of using conservation properties in differential form, as with the characteristic based LODI method in section 5.2, this can also be done in an integral formulation. As an advantage, the spatial derivatives, emerging in the differential formulation from Gauss's theorem, will vanish. This helps to overcome the most important disadvantage of the LODI boundary conditions and maintain strict locality. As a secondary effect, appropriate means will cancel the forward Euler time integration, resulting in an increase of numerical stability.

All considerations are based on the assumption that every change in pressure respectively density propagates with the speed of sound. An alternative approach would be to use high pass filtering (cf. chapter 5.1) at a boundary node on the density distributions facing outwards and sum the result to gain the overall sound density. As the unknown distributions all directing towards the inside of the domain (cf. page 36) should not be influenced by sound pressure waves, this consideration is valid. However, the infrasound part of the density change is not covered then. It is stressed that the restriction to a filter band has purely reasons of human perception.

The prerequisite of the distinct propagation speed leads to a slightly miscalculated pressure adaption in case of convected pressure changes, e.g. with turbulent outflow. However, this error seems to be negligible, as shown in chapter 7. A fixed pressure boundary condition on the other hand would always lead to a wrong pressure adaption in that case.

In this section, the basic principle of the impedance boundary condition is derived. It will be shown later that in a 2D or 3D case, the very same principle can be applied and merely has to be transformed to the appropriate direction of incidence of the sound pressure wave. The

LBM is especially well suited for the required transformation.

6.1.1 Impedance Condition for Compressible LBM

Suppose a pressure change enters a fixed control volume dV on the boundary. Its additional momentum at time step $t^{(n)} = \Delta t \cdot n$ inside the control volume with respect to the preceding time step equals:

$$\begin{aligned} dJ_{\mathrm{CV}}^{(n)} &= v^{(n)}\varrho^{(n)}dV' - v^{(n-1)}\varrho^{(n-1)}dV' - v^{(n-1)}d\varrho^{(n)}dV' = \\ &= v^{(n)}\varrho^{(n)}dV' - v^{(n-1)}\varrho^{(n)}dV'. \end{aligned} \tag{6.1}$$

The term of equation 6.1 referring to the change in density $d\varrho^{(n)} = \varrho^{(n)} - \varrho^{(n-1)}$ is related to pure convection of $d\varrho^{(n)}$ with the base velocity $v^{(n-1)}$. It is not part of the momentum flux of the pressure wave itself and therefore has to be subtracted.

Only a fraction dV' of the control volume dV is affected by the pressure wave. Considering the relative speed of sound $c_s \pm v^{(n-1)}$ for a pressure wave directing towards positive respectively negative e_x-direction, it is given by (Müller, [46]):

$$dV' = (c_s \pm v^{(n-1)}) \cdot dt \cdot dA. \tag{6.2}$$

With $dv^{(n)} = v^{(n)} - v^{(n-1)}$, the rate of momentum change per unit area therefore equals:

$$\frac{\partial J_{\mathrm{CV}}^{(n)}}{\partial A\ \partial t} = dv^{(n)} \cdot \varrho^{(n)} \cdot (c_s \pm v^{(n-1)}). \tag{6.3}$$

On the other hand, the momentum flux of an incoming sound pressure wave towards the control volume can be equally derived. As the change in density $d\varrho^{(n)}$ is supposed to be small compared to $\varrho^{(n-1)}$, the approximation for the wave front of a punctual source in distance r can be used (cf. Müller [47]):

$$dp^{(n)} = \frac{\varrho^{(n-1)}}{4\pi r}\frac{\partial Q(t_n - r/c_s)}{\partial t}. \tag{6.4}$$

In case of a sufficient distance r from the source, the volume flow Q can be set to:

$$dQ(t) = dv(t)\ dA. \tag{6.5}$$

For small time steps, the change in flow velocity can be approximated linearly in time:

$$dv(t) = \frac{v^{(n)} - v^{(n-1)}}{\Delta t} \cdot \left(t - t^{(n-1)}\right) + O(\Delta t) \quad \forall t \in \left[t^{(n-1)}, t^{(n)}\right]. \tag{6.6}$$

The error estimate is based on the assumption that the velocity increases or decreases monotonously. Equations 6.4, 6.5 and 6.6 justify that the pressure can be assumed to be constant during the same time step, as the time derivative of equation 6.6 is constant:

$$dp^{(n)} = \text{const.} \tag{6.7}$$

With the isothermal ideal gas law in case of the LBM,

$$d\varrho^{(n)} = \frac{c_s^2}{dp^{(n)}} = \text{const.}, \tag{6.8}$$

the density can also be assumed to be constant during one time step. The non-isotropic part of the momentum flux of a pressure change therefore results in

$$\frac{\partial J_c^{(n)}}{\partial A\ \partial t} = \int_{v^{(n-1)}}^{v^{(n)}} \underline{n} \cdot \varrho^{(n)} \cdot v\ dv = \frac{1}{2}\varrho^{(n)} \left[(v^{(n)})^2 - (v^{(n-1)})^2\right] \cdot \underline{n}, \tag{6.9}$$

with the incoming face orientation of the control volume $\underline{n} = \mp 1$. Together with the pressure term according to equation 2.25 as isotropic part of the momentum flux, this results in a total momentum flux of the sound pressure wave of

$$\frac{\partial J_{\text{flx}}^{(n)}}{\partial A\ \partial t} = \underline{n} \left(d\varrho^{(n)} c_s^2 + \frac{1}{2}\varrho^{(n)} \left[(v^{(n)})^2 - (v^{(n-1)})^2\right] \right). \tag{6.10}$$

This relation is equivalent to the assumption of Izquierdo and Fueyo in equation 5.26 and is the main reason for the almost identical level of error of both approaches.

To prevent reflection of the pressure wave, the rate of momentum change in the control volume and the incoming momentum flux have to balance to zero:

$$\frac{\partial J_{\text{CV}}^{(n)}}{\partial A\ \partial t} + \frac{\partial J_{\text{flx}}^{(n)}}{\partial A\ \partial t} \ = \ \mp d\varrho^{(n)} c_s^2 \mp \frac{1}{2}\varrho^{(n)} (dv^{(n)})^2 + dv^{(n)} \varrho^{(n)} c_s \ = \ 0 \tag{6.11}$$

The physically reasonable solution of equation 6.11 with $v^{(n)} = v^{(n-1)}$ for $\varrho^{(n)} = \varrho^{(n-1)}$ yields:

$$v^{(n)} = v^{(n-1)} \mp c_s \cdot \left(\sqrt{2 \cdot \frac{\varrho^{(n-1)}}{\varrho^{(n)}} - 1} - 1 \right). \tag{6.12}$$

The condition for non-reflection from equation 6.11 is therefore equivalent to setting the acoustic impedance z of the medium to

$$z^{(n)} = \frac{dp^{(n)}}{dv^{(n)}} = \frac{c_s^2 \cdot d\varrho^{(n)}}{v^{(n)} - v^{(n-1)}} = \mp \frac{c_s \cdot d\varrho^{(n)}}{\sqrt{2\frac{\varrho^{(n)} - d\varrho^{(n)}}{\varrho^{(n)}} - 1} - 1} = \mp \frac{c_s \cdot d\varrho^{(n)}}{\sqrt{1 - 2\frac{d\varrho^{(n)}}{\varrho^{(n)}}} - 1}. \tag{6.13}$$

In section 6.2 and 6.3, a second relation between density and velocity will be derived for the LBM. This allows for solving for both quantities. Finally, an arbitrary boundary condition can be used to fulfill the non-reflective condition of equation 6.11 by setting the flow velocity according to equation 6.12 in dependence of the incoming pressure change proportional to $d\varrho^{(n)}$.

6.1.2 Impedance Condition for Incompressible LBM

For the incompressible LBM model of section 3.5, the derivation of the principle of the impedance condition remains the same with adaptions regarding the altered first moment and equilibrium distribution. As the first moment recovers a constant density, $\varrho^{(n)}$ and $\varrho^{(n-1)}$ have to be set to ϱ_0 in equation 6.1. This results in a total momentum change, similar to equation 6.3, of

$$\frac{\partial J^{(n)}_{\text{CV, inc.}}}{\partial A\ \partial t} = dv^{(n)} \cdot \varrho_0 \cdot (c_s \pm v^{(n-1)}). \tag{6.14}$$

For the same reason, the momentum flux of equation 6.9 has to refer to a constant density:

$$\frac{\partial J^{(n)}_{c,\text{ inc.}}}{\partial A\ \partial t} = \frac{1}{2}\varrho_0 \left[(v^{(n)})^2 - (v^{(n-1)})^2\right] \cdot \underline{n}. \tag{6.15}$$

The pressure term of equation 6.10 however remains unchanged. Finally, the impedance condition of equation 6.11 changes to:

$$\mp d\varrho^{(n)} c_s^2 \mp \frac{1}{2}\varrho_0 (dv^{(n)})^2 + dv^{(n)} \varrho_0 c_s \ = \ 0. \tag{6.16}$$

The physically reasonable solution of this equation results in:

$$v^{(n)} = v^{(n-1)} \mp c_s \cdot \left(\sqrt{1 - 2 \cdot \frac{d\varrho^{(n)}}{\varrho_0}} - 1\right) \tag{6.17}$$

The acoustic impedance is set by the very same relation as shown in equation 6.13:

$$z^{(n)} = \frac{dp^{(n)}}{dv^{(n)}} = \mp \frac{c_s \cdot d\varrho^{(n)}}{\sqrt{1 - 2\frac{d\varrho^{(n)}}{\varrho_0}} - 1}. \tag{6.18}$$

6.1.3 Adaption Relative to Fixed Reference Level

In this section an error is deducted for an adaption of the impedance relative to a fixed initial reference level $v_0 := v^{(0)}$ and $\varrho_0 := \varrho^{(0)}$ instead of $v^{(n-1)}$ and $\varrho^{(n-1)}$ of the last time step while using equation 6.11. Let k be the index of an arbitrary time-step $0 < k < n$ and

$$\begin{aligned} d\varrho' &:= \sum_{i=k+1}^{n} d\varrho^{(i)}, \\ dv' &:= \sum_{i=k+1}^{n} dv^{(i)}. \end{aligned}$$

Suppose equation 6.11 was fulfilled for $d\varrho'$ and dv':

$$\mp d\varrho' c_s^2 \mp \frac{1}{2}\varrho^{(n)} dv'^2 + dv' \varrho^{(n)} c_s = 0 \tag{6.19}$$

Then the error of changing the reference level from $\varrho^{(k)}$, $v^{(k)}$ to $\varrho^{(k-1)}$, $v^{(k-1)}$,

$$\begin{aligned} &\mp(d\varrho' + d\varrho^{(k)})c_s^2 \mp \tfrac{1}{2}\varrho^{(n)}(dv' + dv^{(k)})^2 + (dv' + dv^{(k)})\varrho^{(n)} c_s = \\ &\quad dv^{(k)} \left(\mp \left(\tfrac{1}{2} d\varrho' dv^{(k)} + (\varrho^{(k)} + d\varrho')dv'\right) + d\varrho' c_s\right) =: err, \end{aligned} \tag{6.20}$$

results from equation 6.11. According to the linear dependence of dv on t assumed in section 6.1,

$$dv^{(n)} = \left(\frac{\partial}{\partial t} v^{(n)} - \frac{1}{2}\Delta t \frac{\partial^2}{\partial t^2} v^{(n)} + O(\Delta t^2)\right) \Delta t, \tag{6.21}$$

can be deduced: $dv^{(k)} = O(\Delta t)$. Suppose the multiplicand of equation 6.20 results in an error of at most

$$\mp \left(\frac{1}{2} d\varrho' dv^{(k)} + (\varrho^{(k)} + d\varrho')dv'\right) + d\varrho' c_s = O(\Delta t^2). \tag{6.22}$$

Under this assumption, a backward induction with equation 6.19 being true for $k = n - 1$ and $k \to k - 1$ results in:

$$(\varrho^{(n)} - \varrho_0)c_s^2 + \frac{1}{2}\varrho^{(n)}(v^{(n)} - v_0))^2 + (v^{(n)} - v_0))\varrho^{(n)} c_s + O(\Delta t^2) = 0. \tag{6.23}$$

This shows that solving equation 6.23 on the boundary results in an error of $O(\Delta t^2)$ and a total error of the simulation of $O(\Delta t)$ by addition of the partial errors. The numerical results of the simulations in section 6.2.2 and the appendix back this hypothesis as long as a formal prove of equation 6.22 is not available.

6.2 Impedance Boundary Conditions for LBM in 1D

6.2.1 Adaption Relative to Last Time Step

Below, an impedance boundary condition is derived for a left boundary and is applied to the 1D test case of section 5.1.4. With mass and momentum conservation for the compressible 1D LBM in lattice units,

$$\varrho = f_0 + f_1 + f_2, \tag{6.24}$$
$$\varrho v^{(n)} = f_1 - f_2, \tag{6.25}$$

density ϱ can be expressed in terms of the unknown velocity v,

$$\varrho = -\frac{f_0 + 2f_2}{v - 1}, \tag{6.26}$$

which, inserted into equation 6.11, leads to the solution

$$v^{(n)} = v^{(n-1)} - \left(c_s^2 \frac{\varrho^{(n-1)}}{\varrho_z} + c_s\right) + \sqrt{\left(c_s^2 \frac{\varrho^{(n-1)}}{\varrho_z} + c_s\right)^2 - 2c_s^2 \left(\frac{\varrho^{(n-1)}}{\varrho_z}\left(v^{(n-1)} - 1\right) + 1\right)}. \tag{6.27}$$

ϱ_z is hereby defined as

$$\varrho_z := f_0 + 2f_2. \tag{6.28}$$

The missing distribution function f_1 can easily be derived from equation 6.24 and 6.25:

$$f_1 = -\frac{f_0 v^{(n)} + f_2(1 + v^{(n)})}{1 - v^{(n)}}. \tag{6.29}$$

Equations 6.27, 6.28 and 6.29 can be implemented in a quite compact way (cf. appendix A.4). The results of the test case from section 5.1.4 are displayed below in figure 6.1 to 6.5, comparable to the free field simulation of figure 5.6 and 5.7 and the LODI implementation of figure 5.12 to 5.16.

In the test case, an initial pressure peak at $x = 100 \cdot \Delta x$ spreads to both sides. The left part is processed by the boundary condition of this section. The amount of reflection can be seen in figures 6.1 and 6.2 in the range $x \in [1, 300] \cdot \Delta x$ at time step $t = 500 \cdot \Delta t$. The density deviates from the free field simulation by 0.3 % of the geometrically damped wave amplitude near $x = 500 \cdot \Delta x$, the corresponding deviation of velocity is 0.9 %. This resembles almost exactly the 1D results of the LODI boundary condition (cf. section 5.2.2), although the underlying numerical scheme is different.

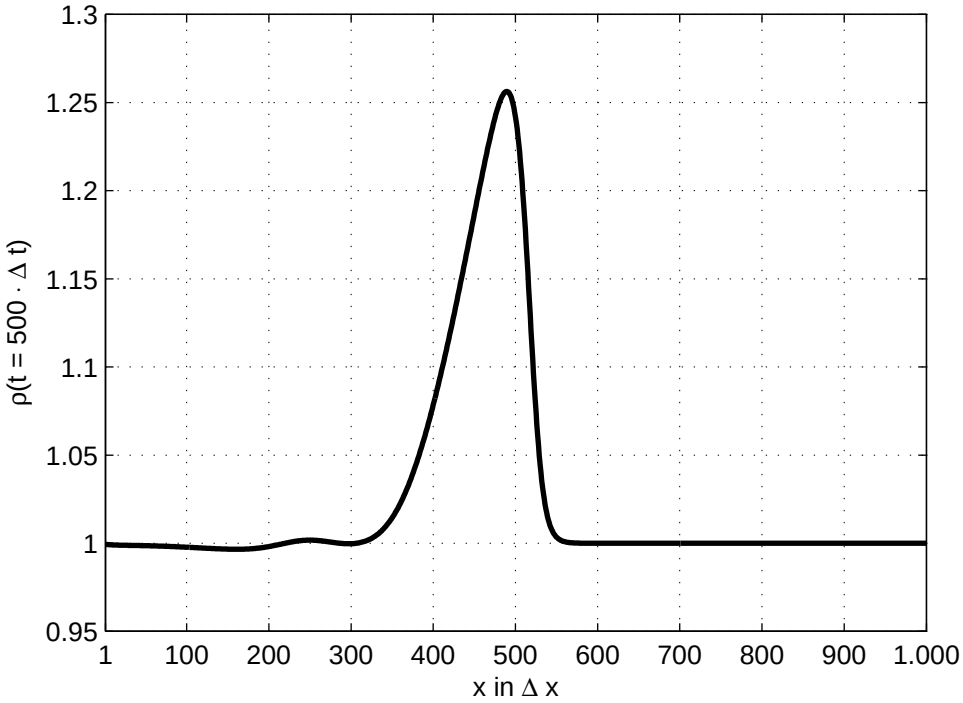

Figure 6.1: Reflection of pressure wave on left hand side boundary for density

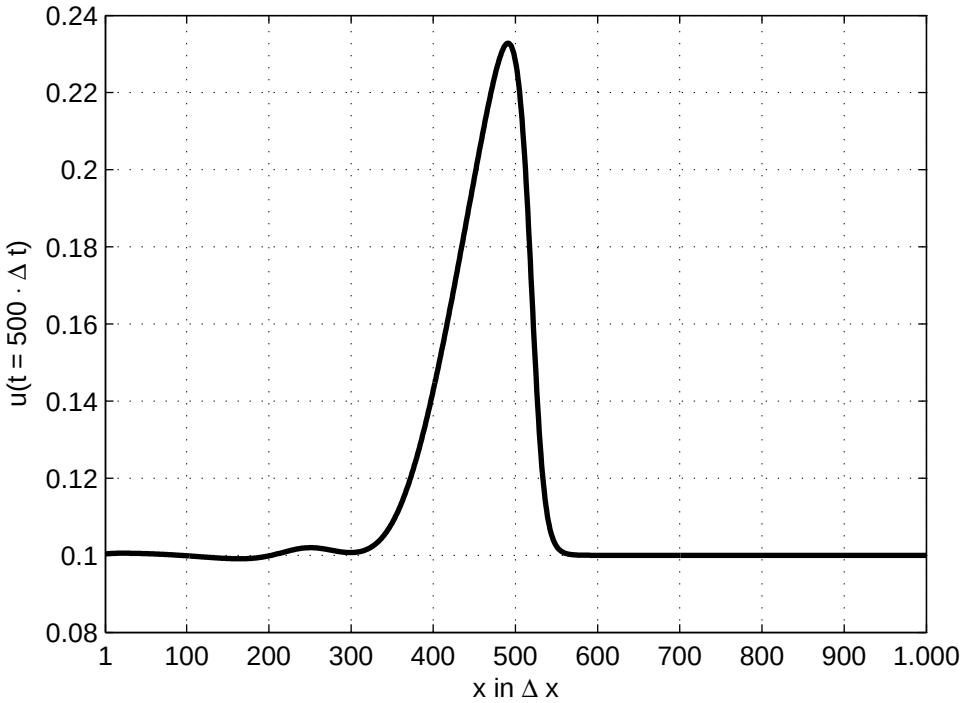

Figure 6.2: Reflection of pressure wave on left hand side boundary for velocity

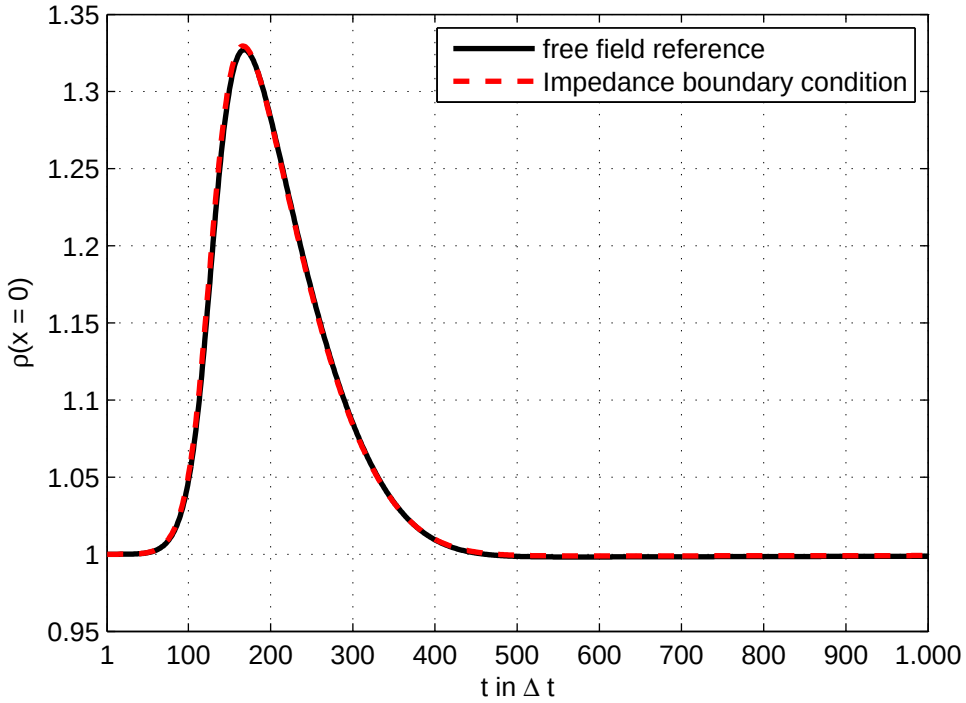

Figure 6.3: Density over time for left inflow impedance boundary with passing pressure wave

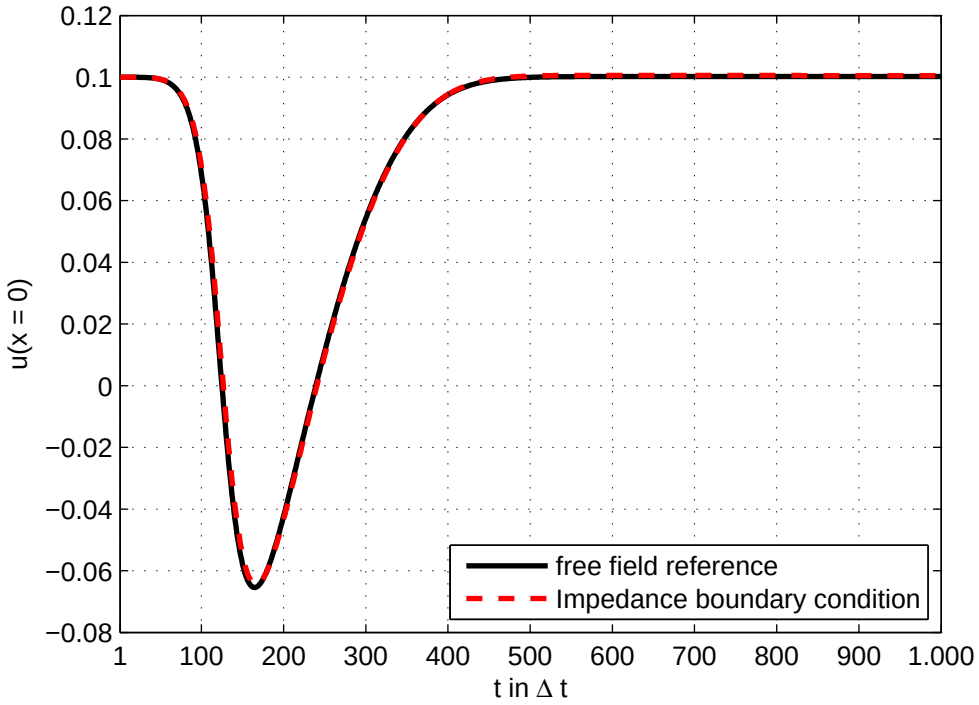

Figure 6.4: Velocity over time for left inflow impedance boundary with passing pressure wave

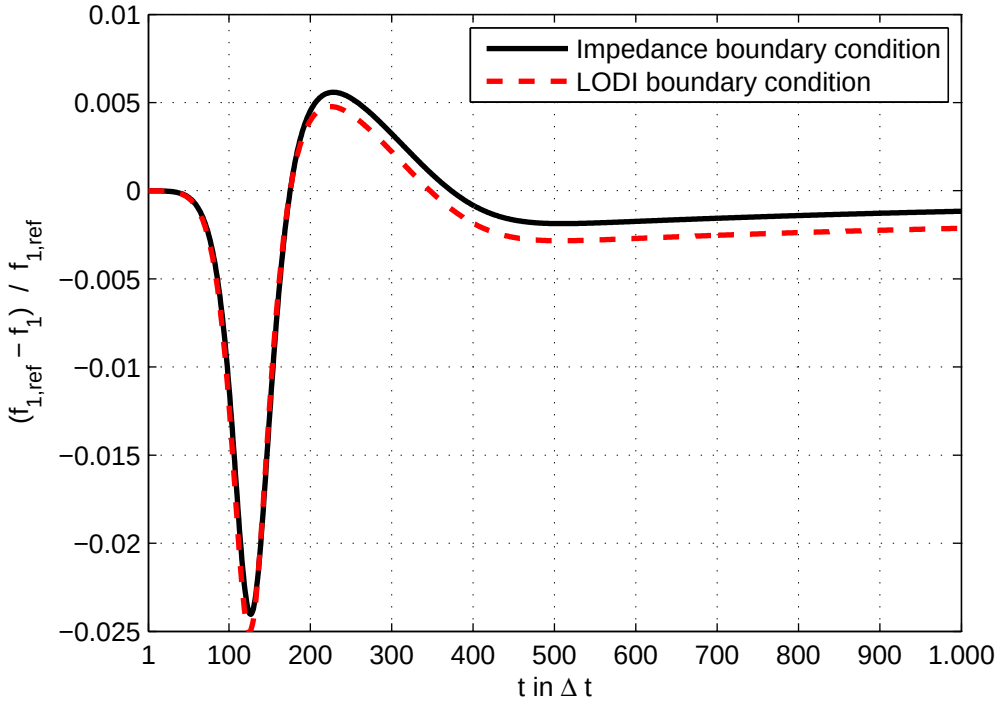

Figure 6.5: Relative error of f_1 compared to free field

Figure 6.3 and 6.4 compare the evolution of density and velocity at the location of the boundary condition over time with the corresponding free field, while the pressure peak passes by. The relative error for the essential density distribution f_1 is shown in figure 6.5. The maximum relative error in f_1 amounts to 2.4 %, once again in the range of the LODI boundary condition. In equation 6.6, a linear evolution of the particle velocity was assumed. Figure 6.5 illustrates that the error depends significantly on the curvature of the velocity profile. An extended approach taking into account the curvature could be an interesting subject to further research.

6.2.2 Adaption Relative to Fixed Reference Level

Next, the results of the test case of section 5.1.4 are discussed for an adaption of the impedance relative to a fixed reference level ϱ_0 and v_0, as derived in section 6.1.3. The only difference in derivation (cf. section 6.2.1) and implementation is a swap of $\varrho^{(n-1)}$ with ϱ_0 and $v^{(n-1)}$ with v_0. A code example can be found in the appendix A.5. The simulation recovers almost the same results as without fixed reference level. Therefore only the relative error of f_1 and the reflected amount of density will be compared.

In the plot of figure 6.6, it can be seen that the reflection level even reduces coincidentally for the specific case, evaluated as absolute deviation from the free field. The plot shows the corresponding density in the range $0 \leq x \leq 300 \cdot \Delta x$, the first third of the domain, where the reflection can be observed at time step $t = 500 \cdot \Delta t$. Figure 6.7 shows the error of f_1 relative to the free field simulation. Once again it lies with a maximum error of 2.2 % in the same range as the impedance boundary condition with adaption to the previous time step or the LODI boundary condition.

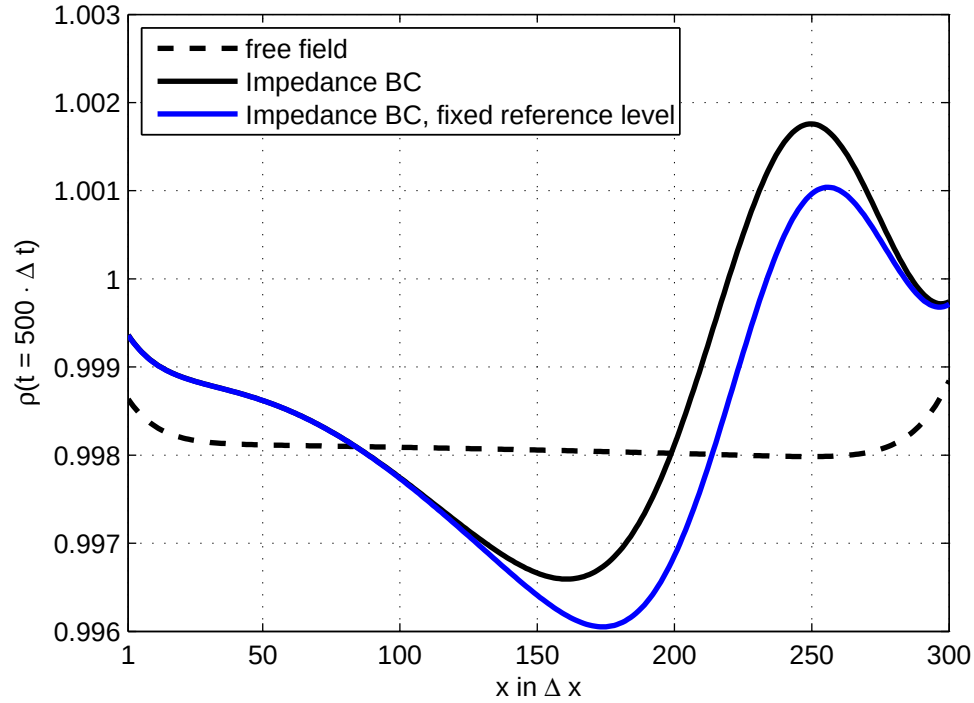

Figure 6.6: Reflection of pressure wave on left hand side for density

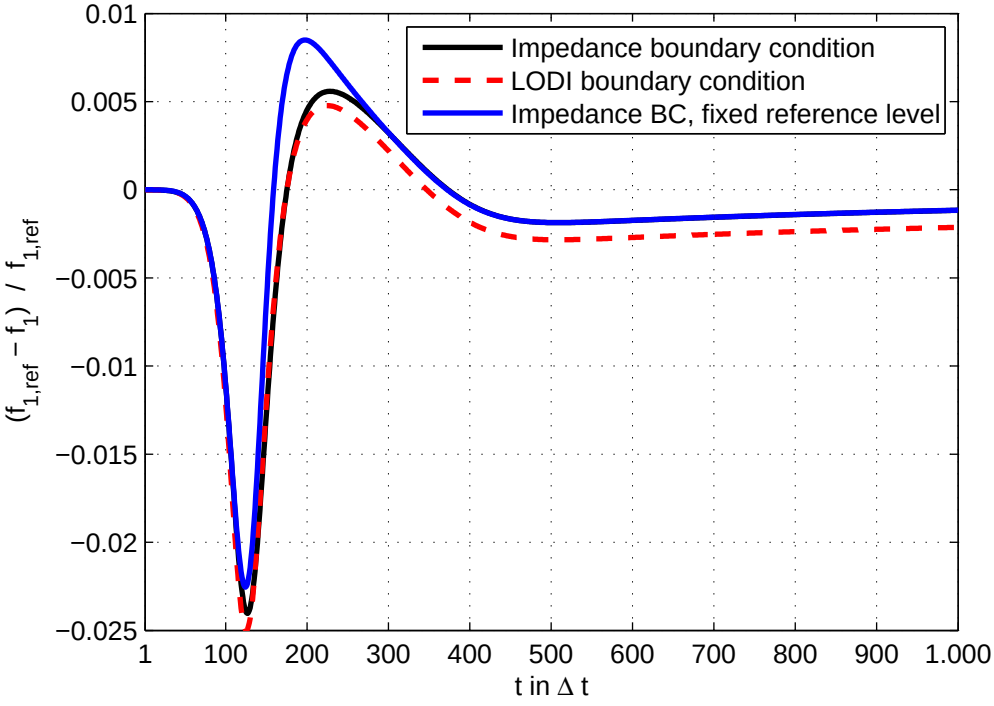

Figure 6.7: Relative error of f_1 during the pass of the pressure wave

6.2.3 Highly Viscous Flow

Eventually, the same simulation as in section 6.2.1 was conducted for a Reynolds number of $\mathrm{Re} = 10$, so viscosity was increased by a factor of 10. As seen in the derivation of section 6.1, neither shear nor volume viscosity was considered. In the one-dimensional case, the impact should come from the volume viscosity, which is significantly hight for the LBM ($\nu' = 2/3 \cdot \nu$, cf. section 3.4).

Figure 6.8 shows the density over the domain at time step $t = 800 \cdot \Delta t$, comparing a Dirichlet velocity boundary condition as described in section 5.1.4, the LODI free field boundary condition of section 5.2.2 and the impedance free field boundary condition of section 6.2.1. The maximum deviation of the density at the specific time step equals both for the LODI and impedance boundary condition 0.4 % of the free field density. However, as shown in figure 6.9, the relative error of the f_1 distribution lies with 8 % 3.6 times significantly higher than in the simulation with $\mathrm{Re} = 100$ (cf. figure 6.7).

At last, figure 6.10 shows the comparison of f_1 of the same simulation for a Reynolds number of $\mathrm{Re} = 1$, so viscosity was once more increased by one order of magnitude. With a relative error of 15.5 % for the impedance boundary condition, the error almost doubles, compared to the previous simulation with $\mathrm{Re} = 10$.

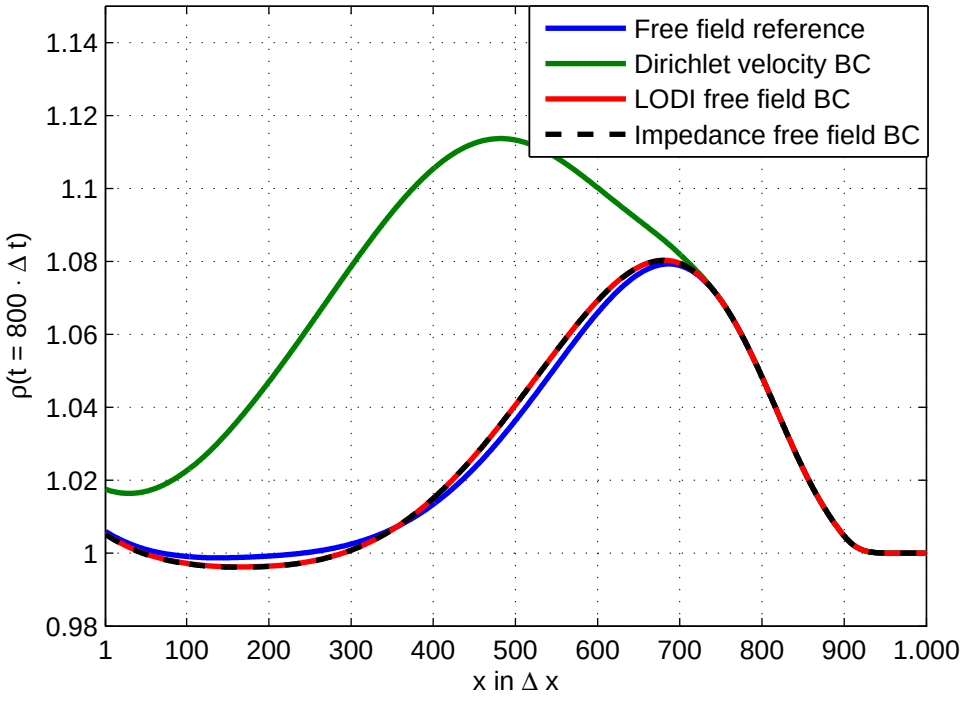

Figure 6.8: Reflection of pressure wave on left hand side for density, $\mathrm{Re} = 10$

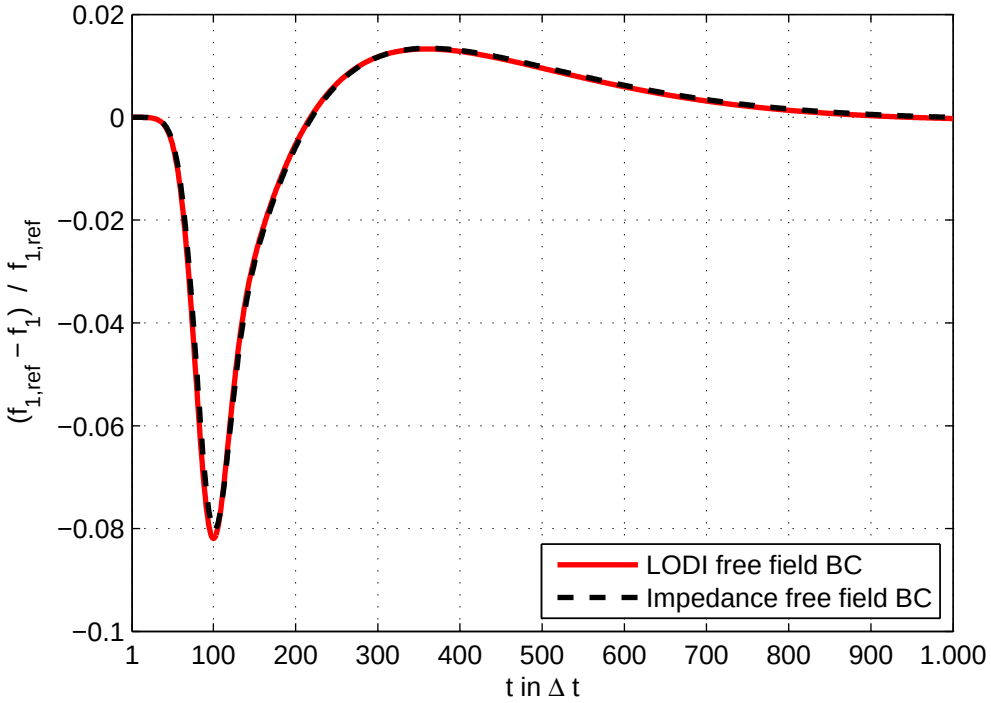

Figure 6.9: Relative error of f_1 during the pass of the pressure wave, Re = 10

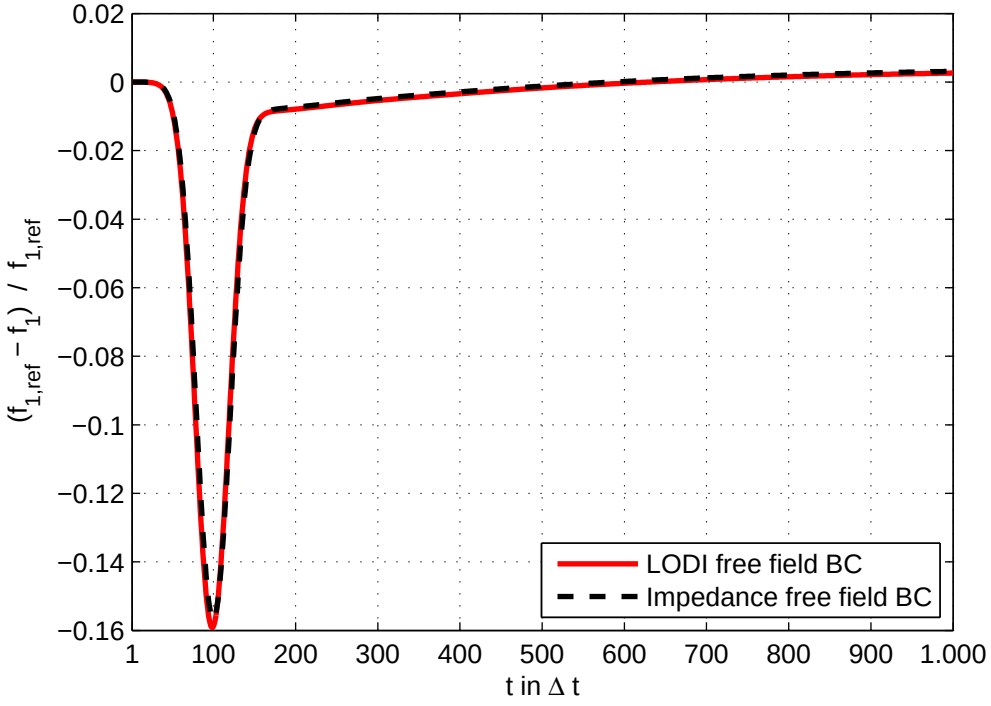

Figure 6.10: Relative error of f_1 during the pass of the pressure wave, Re = 1

6.3 Impedance Boundary Conditions for LBM in 2D

6.3.1 Adaption in Normal Direction for Compressible LBM

Similar as the 2D LODI boundary conditions of section 5.2.3, the assumption of a sound pressure wave incoming only in normal direction to the boundary can be made, resulting in a rather efficient implementation of the principle of section 6.1. This will be discussed in this section for the compressible Lattice Boltzmann method and, consistently to the previous chapter, for a left boundary.

Under the restrictive assumption of perpendicular incoming sound pressure waves, the condition for non-reflection of equation 6.11 can be directly adopted, choosing a plus sign for a left boundary:

$$\left(\varrho^{(n)} - \varrho^{(n-1)}\right) c_s^2 + \frac{1}{2}\varrho^{(n)} \left(v_x^{(n)} - v_x^{(n-1)}\right)^2 + \left(v_x^{(n)} - v_x^{(n-1)}\right) \varrho^{(n)} c_s \;=\; 0 \tag{6.30}$$

The density of the current time step $\varrho^{(n)}$ can be computed as a function of $v_x^{(n)}$ from mass and momentum conservation (the same approach being used by Zou and He [65]),

$$\varrho \;=\; \sum_i f_i, \tag{6.31}$$

$$v_x \cdot \varrho \;=\; \sum_i f_i \xi_{i,x}, \tag{6.32}$$

resulting in

$$\varrho^{(n)} = \left[\frac{f_0 + f_2 + f_4 + 2\left(f_3 + f_6 + f_7\right)}{1 - v_x}\right]^{(n)}. \tag{6.33}$$

Let ϱ_z be defined as:

$$\varrho_z := f_0 + f_2 + f_4 + 2\left(f_3 + f_6 + f_7\right). \tag{6.34}$$

Inserting equation 6.33 in equation 6.30 and solving for $v_x^{(n)}$ leads to an adapted velocity of

$$\begin{aligned} v_x^{(n)} \;=\; & v_x^{(n-1)} - \left(c_s^2 \frac{\varrho^{(n-1)}}{\varrho_z} + c_s\right) \\ & + \sqrt{\left(c_s^2 \frac{\varrho^{(n-1)}}{\varrho_z} + c_s\right)^2 - 2c_s^2 \left(\frac{\varrho^{(n-1)}}{\varrho_z}\left(v_x^{(n-1)} - 1\right) + 1\right)}. \end{aligned} \tag{6.35}$$

Once again, the physically reasonable solution with $v_x^{(n)} = v_x^{(n-1)}$ for $\varrho^{(n)} = \varrho^{(n-1)}$ was chosen. Instead of setting a zero $v_y^{(n)}$ velocity, this component is computed from the non-equilibrium bounce-back in vertical direction:

$$v_y^{(n)} = \frac{3}{2}\frac{f_2 - f_4}{\varrho^{(n)}} \tag{6.36}$$

The unknown distributions can now be set by an appropriate boundary condition, in the present case by using the compressible non-equilibrium bounce-back (cf. section 4.3.1):

$$f_1 = f_3 + \frac{2}{3}\varrho v_x \tag{6.37}$$

$$f_5 = f_7 + \frac{1}{6}\varrho(v_x + v_y) \tag{6.38}$$

$$f_8 = f_6 + \frac{1}{6}\varrho(v_x - v_y) \tag{6.39}$$

An example of code where the boundary condition has been implemented can be found in appendix A.6.

6.3.2 Adaption in Normal Direction, Compressible LBM, Fixed Reference Level

For adapting the impedance relative to a fixed reference level, e.g. $v_{x,0}$ and ϱ_0, rather than to the last time step, the corresponding velocity $v_x^{(n-1)}$ and density $\varrho^{(n-1)}$ have to be substituted by the fixed quantities, just like it is done in the 1D case of section 6.2.1. Equation 6.30 turns accordingly into

$$\left(\varrho^{(n)} - \varrho_0\right) c_s^2 + \frac{1}{2}\varrho^{(n)}\left(v_x^{(n)} - v_{x,0}\right)^2 + \left(v_x^{(n)} - v_{x,0}\right)\varrho^{(n)} c_s = 0. \tag{6.40}$$

The solution for the adapted velocity $v_x^{(n)}$ results therefore in:

$$v_x^{(n)} = v_{x,0} - \left(c_s^2\frac{\varrho_0}{\varrho_z} + c_s\right) + \sqrt{\left(c_s^2\frac{\varrho_0}{\varrho_z} + c_s\right)^2 - 2c_s^2\left(\frac{\varrho_0}{\varrho_z}\left(v_{x,0} - 1\right) + 1\right)}. \tag{6.41}$$

The respective density can still be computed by equation 6.33, the velocity in y-direction by equation 6.36. Finally, the unknown distribution functions are set by equations 6.37 to 6.39. An example for an implementation can be found in appendix A.7.

6.3.3 Isotropic Adaption for Compressible LBM

For a boundary condition adapting the impedance for an arbitrary direction of the incoming sound pressure wave, the 1D equation 6.11 can still be used, but dv has to be projected onto the corresponding direction of incidence. dv can be expressed by its absolute value and its corresponding sign:

$$\|dv\| = \sqrt{dv_x^2 + dv_y^2} = \sqrt{\left(v_x^{(n)} - v_x^{(n-1)}\right)^2 + \left(v_y^{(n)} - v_y^{(n-1)}\right)^2} \tag{6.42}$$

and

$$dv = \text{sign}(dv)\|dv\|. \tag{6.43}$$

Equation 6.11 adequately turns into

$$\begin{aligned} &\mp\left(\varrho^{(n)} - \varrho^{(n-1)}\right) c_s^2 \mp \tfrac{1}{2}\varrho^{(n)} \left[\left(v_x^{(n)} - v_x^{(n-1)}\right)^2 + \left(v_y^{(n)} - v_y^{(n-1)}\right)^2\right] + \\ &+ \text{sign}(dv) \cdot \sqrt{\left(v_x^{(n)} - v_x^{(n-1)}\right)^2 + \left(v_y^{(n)} - v_y^{(n-1)}\right)^2}\, \varrho^{(n)} c_s \;=\; 0. \end{aligned} \tag{6.44}$$

The problem of deciding the sign of dv can be reduced by consideration of symmetry. It will be shown that the sign(dv) can be determined by sign(dv_x).

Figure 6.11 shows without loss of generality for a left boundary, that a switch in sign for a tangential velocity dv_y does not change the orientation of dv. In the specific illustration can be seen that the orientation of the adaption dv is in any case contrary to the propagation of the sound pressure wave, which is always towards the boundary.

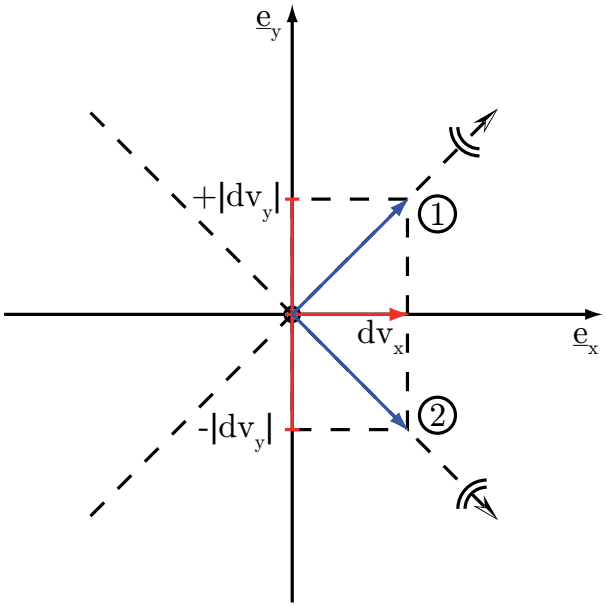

Figure 6.11: Symmetry of impedance condition for tangential propagation speed

However, as shown in figure 6.12, the orientation of a perpendicular velocity dv_x does affect the orientation of dv. Moreover, the orientation is exactly the same: sign(dv) = sign(dv_x).

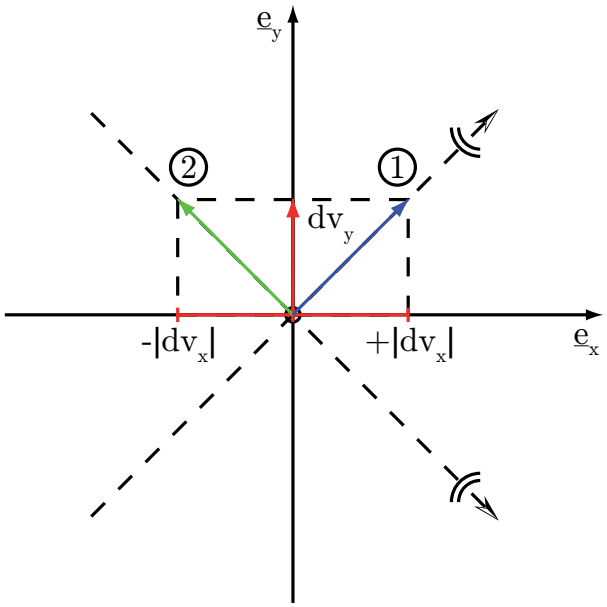

Figure 6.12: Antisymmetry of impedance condition for normal propagation speed

Consequently, the problem of equation 6.44 reduces to

$$I_c := \mp\left(\varrho^{(n)} - \varrho^{(n-1)}\right) c_s^2 \mp \tfrac{1}{2}\varrho^{(n)} \left[\left(v_x^{(n)} - v_x^{(n-1)}\right)^2 + \left(v_y^{(n)} - v_y^{(n-1)}\right)^2\right] + \\ + \operatorname{sign}(dv_x) \cdot \sqrt{\left(v_x^{(n)} - v_x^{(n-1)}\right)^2 + \left(v_y^{(n)} - v_y^{(n-1)}\right)^2}\, \varrho^{(n)} c_s \;=\; 0. \tag{6.45}$$

$\varrho^{(n)}$ is given by equation 6.33 (cf. section 6.3.1):

$$\varrho^{(n)} = \left[\frac{\varrho_z}{1 - v_x^{(n)}}\right]^{(n)} \tag{6.46}$$

with

$$\varrho_z := f_0 + f_2 + f_4 + 2\left(f_3 + f_6 + f_7\right), \tag{6.47}$$

$v_y^{(n)}$ is given by equation 6.36:

$$v_y^{(n)} = \frac{3}{2}\frac{f_2 - f_4}{\varrho^{(n)}} \tag{6.48}$$

It is stressed that the tangential velocities, in the specific case v_y, are depending explicitly on the density and therefore on v_x.

Theoretically, the methods of Cardano or Ferrari (cf. Bronstein and Semendjajew [7]) could be used to solve the quartic equation 6.45, excluding specific decision paths of the methods

by physical reasoning. However, for the complexity of the given problem, the solution even disregarding the dependency $\varrho^{(n)} = \varrho^{(n)}(v_x^{(n)})$ leads to several hundreds of partially very costly mathematical operations. The derivation of an analytical solution including equation 6.46 is even more complex. Therefore a compact iterative solution of the implicit problem was chosen, the Newton-Raphson algorithm:

$$v_{x,k+1} = v_{x,k} - \frac{I_c(v_{x,k})}{\frac{\partial I_c}{\partial v_x}(v_{x,k})} \tag{6.49}$$

The sign(dv_x) can be computed with equation 6.35: As the 1D approximation solves the problem for a perpendicular projection, the sign is the same as for the isotropic problem. The solution of the 1D problem is also used as start value for Newton's algorithm.

Finally ϱ is set according to equation 6.33, v_y according to equation 6.36 and the unknown distribution via non-equilibrium bounce-back, equations 6.37 to 6.39. An example for an implementation can be found in appendix A.8. The implementation for an adaption relative to a fixed reference level is shown in appendix A.9 and emerges from a mere substitution of $v_x^{(n-1)}$, $v_y^{(n-1)}$ and $\varrho^{(n-1)}$ by $v_{x,0}$, $v_{y,0}$ and ϱ_0 in equations 6.45 and 6.48.

6.3.4 Adaption in Normal Direction for Incompressible LBM

For the incompressible LBM model of section 3.5, the incompressible condition 6.16 has to be implemented, i.e. for a left boundary:

$$\left(\varrho^{(n)} - \varrho^{(n-1)}\right) c_s^2 + \frac{1}{2}\varrho_0^{(n)} \left(v_x^{(n)} - v_x^{(n-1)}\right)^2 + \left(v_x^{(n)} - v_x^{(n-1)}\right) \varrho_0^{(n)} c_s \;=\; 0 \tag{6.50}$$

Mass and momentum conservation result in:

$$\varrho \;=\; \sum_i f_i, \tag{6.51}$$

$$v_x \cdot \varrho_0 \;=\; \sum_i f_i \xi_{i,x}, \tag{6.52}$$

It is stressed that ϱ depicts the density deviation relative to a hydrostatic density and does not resemble the total density of the compressible model of section 6.1.1.

Equations 6.51 and 6.52 allow for expressing $\varrho^{(n)}$ as:

$$\varrho^{(n)} = \left[\varrho_z + v_x \varrho_0\right]^{(n)} \tag{6.53}$$

with

$$\varrho_z := f_0 + f_2 + f_4 + 2\left(f_3 + f_6 + f_7\right). \tag{6.54}$$

The solution of equations 6.50 and 6.53 results in:

$$v_x^{(n)} = v_x^{(n-1)} - \left(c_s^2 + c_s\right) + \sqrt{\left(c_s^2 + c_s\right)^2 + 2c_s^2\left(\frac{\varrho^{(n-1)}}{\varrho_0} - v_x^{(n-1)} - \frac{\varrho_z}{\varrho_0}\right)}. \tag{6.55}$$

Now v_y and the unknown density distributions can once again be set by using non-equilibrium bounce-back of the incompressible LBM:

$$v_y^{(n)} = \frac{3}{2}\frac{f_2 - f_4}{\varrho_0} \tag{6.56}$$

$$f_1 = f_3 + \frac{2}{3}\varrho_0 v_x \tag{6.57}$$

$$f_5 = f_7 + \frac{1}{6}\varrho_0(v_x + v_y) \tag{6.58}$$

$$f_8 = f_6 + \frac{1}{6}\varrho_0(v_x - v_y) \tag{6.59}$$

An example of an implementation can be found in appendix A.11.

6.3.5 Adaption in Normal Direction, Incompressible LBM, Fixed Reference Level

The adaption relative to a fixed reference level changes the implementation of the boundary conditions in the same way as for the compressible case in section 6.3.2. It merely covers the substitution of $\varrho^{(n-1)}$ by ϱ_0 and $v_x^{(n-1)}$ by $v_{x,0}$. Equation 6.55 simplifies to:

$$v_x^{(n)} = v_{x,0} - \left(c_s^2 + c_s\right) + \sqrt{\left(c_s^2 + c_s\right)^2 + 2c_s^2\left(1 - v_{x,0} - \frac{\varrho_z}{\varrho_0}\right)}. \tag{6.60}$$

Equations 6.56 to 6.59 remain unchanged. The corresponding code can be found in appendix A.12.

6.3.6 Isotropic Adaption for Incompressible LBM

The isotropic impedance boundary condition for the incompressible LBM of section 3.5 is derived in the same way as for the compressible model in section 6.3.3. The velocity along the direction of incidence of the sound pressure wave is again modeled by the absolute value and its sign, calculated from the perpendicular adaption:

$$dv = \operatorname{sign}(dv)\|dv\| = \operatorname{sign}(dv_x)\sqrt{\left(v_x^{(n)} - v_x^{(n-1)}\right)^2 + \left(v_y^{(n)} - v_y^{(n-1)}\right)^2}. \tag{6.61}$$

For a left boundary, the equation to solve results in (cf. equation 6.45):

$$I_i := \left(\varrho^{(n)} - \varrho^{(n-1)}\right) c_s^2 + \tfrac{1}{2}\varrho_0 \left[\left(v_x^{(n)} - v_x^{(n-1)}\right)^2 + \left(v_y^{(n)} - v_y^{(n-1)}\right)^2\right] + \\ + \operatorname{sign}(dv_x) \cdot \sqrt{\left(v_x^{(n)} - v_x^{(n-1)}\right)^2 + \left(v_y^{(n)} - v_y^{(n-1)}\right)^2}\varrho_0 c_s \;=\; 0. \tag{6.62}$$

A severe simplification arises from the fact that the tangential velocities, i.e. v_y in the specific case, do no longer depend on the density deviation ϱ, but only on the hydrostatic density. v_y is therefore not varying during the Newton-Raphson cycle and can simply be precomputed. With

$$\varrho^{(n)} = \left[\varrho_z + v_x \varrho_0\right]^{(n)} \tag{6.63}$$

and

$$\varrho_z := f_0 + f_2 + f_4 + 2\left(f_3 + f_6 + f_7\right), \tag{6.64}$$

equation 6.62 can be solved iteratively for $v_x^{(n)}$ with Newton's method:

$$v_{x,k+1} = v_{x,k} - \frac{I_i(v_{x,k})}{\frac{\partial I_i}{\partial v_x}(v_{x,k})}. \tag{6.65}$$

The initial value $v_{x,k=0}$ can be set by equation 6.55. After the iterative method as converged, $\varrho^{(n)}$ has to be set by equation 6.53 and the unknown distribution by equations 6.57 to 6.59. An example of an implementation is shown in appendix A.13, the corresponding example for a fixed reference level in appendix A.14.

6.4 2D Pressure Wave Test Case for Impedance BCs

For the evaluation of the impedance boundary condition, each of the boundary conditions of section 6.3 was applied on the 2D pressure wave test case of section 5.2.4. The corresponding implementation can be found in appendix A.6 to A.14. All boundary conditions were tested for setups (a) (resting fluid) and (b) (parabolic velocity profile, cf. section 5.2.4).

For each setup and variation of the boundary condition, the following results were included:

- Density field at time step $t = 700 \cdot \Delta t$
- Absolute velocity field at time step $t = 700 \cdot \Delta t$
- Relative density error in % at time step $t = 700 \cdot \Delta t$
- Absolute velocity error at time step $t = 700 \cdot \Delta t$
- Reflection over incident angle, worst case at time step $t = 700 \cdot \Delta t$ or $t = 770 \cdot \Delta t$ (cf. section 5.2.5)

As the main source of error is located for the isotropic boundary condition in the wake of the reflected wave, the reflection over the incident angle was plotted for those simulations 70 time steps later than for the perpendicular adapting boundary conditions. At this time step, the wake of the reflection progressed to the same position as described in section 5.2.5.

Due to the large amount of simulation results, the corresponding illustrations were shifted to the appendix B. In summary of the results shown there, the following conclusions can be made:

1. The impedance boundary conditions with perpendicular adaption show the same level of error as the LODI boundary conditions. This is exemplarily shown in figure 6.13, which compares the reflection over the incident angle of both implementations for compressible LBM and setup (a). The impedance boundary condition uses a fixed reference level.

2. Comparing the density and velocity field, figures 6.16 and 6.15 respectively figures 5.27 and 5.28 for LODI, it can be seen that the impedance boundary conditions do not suffer from instabilities at the inflow. As a key difference, the LODI implementation of section 5.2.3 relies on numerical time integration.

3. For the isotropic impedance boundary condition, the density and velocity field is exemplarily shown in figure 6.18 and 6.17 for the compressible LBM and the parabolic velocity profile of setup (b). Figure 6.14 and 6.19 compare the LODI boundary conditions of section 5.2.3 with the corresponding isotropic impedance boundary conditions with fixed reference level for setup (a). The data were taken from time step $t = 700 \cdot \Delta t$ and from the positions described in section 5.2.5. For the compressible as well as the incompressible LBM, an angle-dependent behavior of the isotropic impedance boundary conditions is no longer visible.

4. For the compressible and the incompressible LBM, the relative error to the free field solution lies for all simulations below 0.3% up to an incident angle of 50°, regarding the density field and taking also into account the error in the wake of the reflection. The increase at an angle of 60° is due to an interference with the bounce-back modeled corner of the domain.

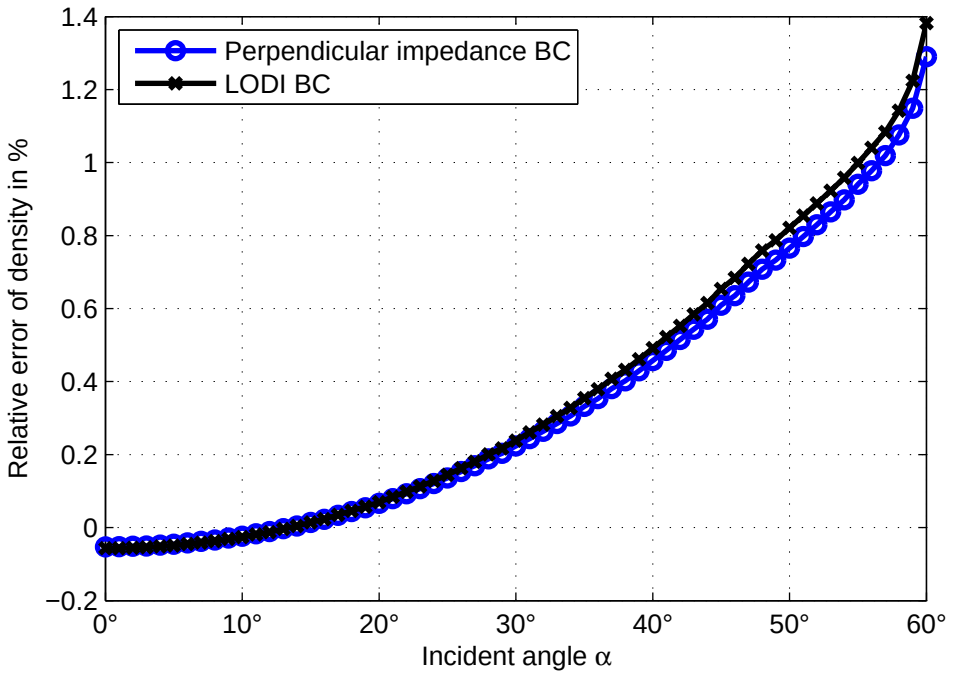

Figure 6.13: Reflection over incident angle, LODI and perpendicular impedance BC, compressible

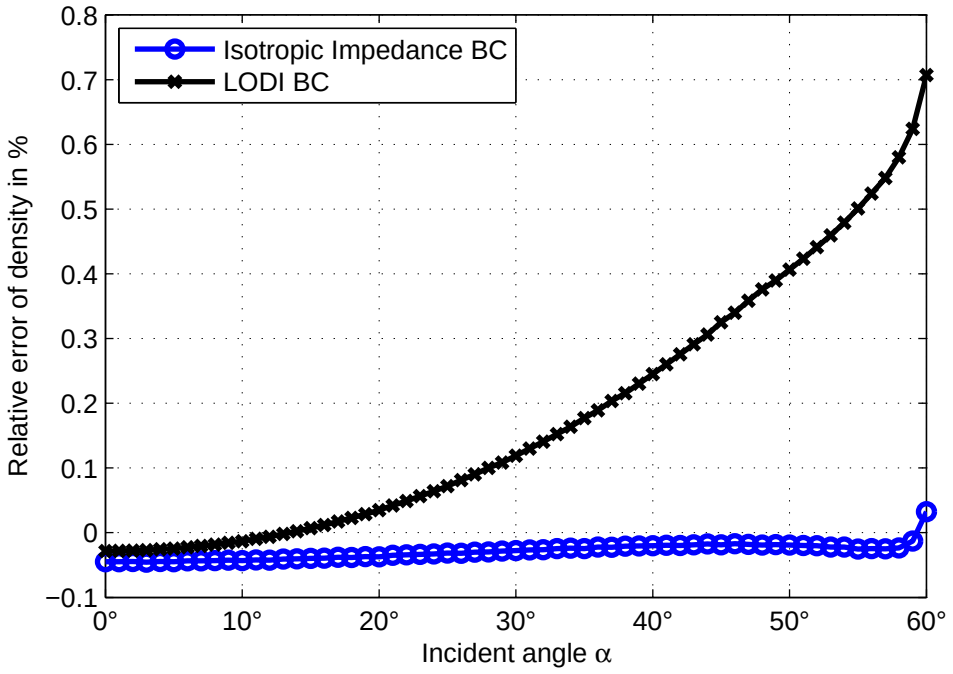

Figure 6.14: Reflection over incident angle, LODI and isotropic impedance BC, compressible

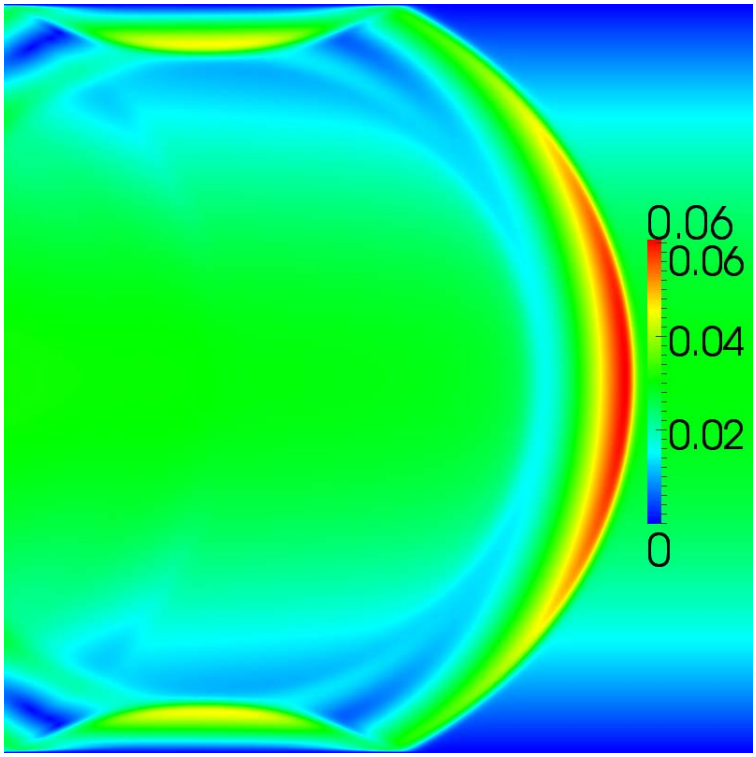

Figure 6.15: Perpendicular impedance free field BC, setup (b), absolute velocity at $t = 700 \cdot \Delta t$

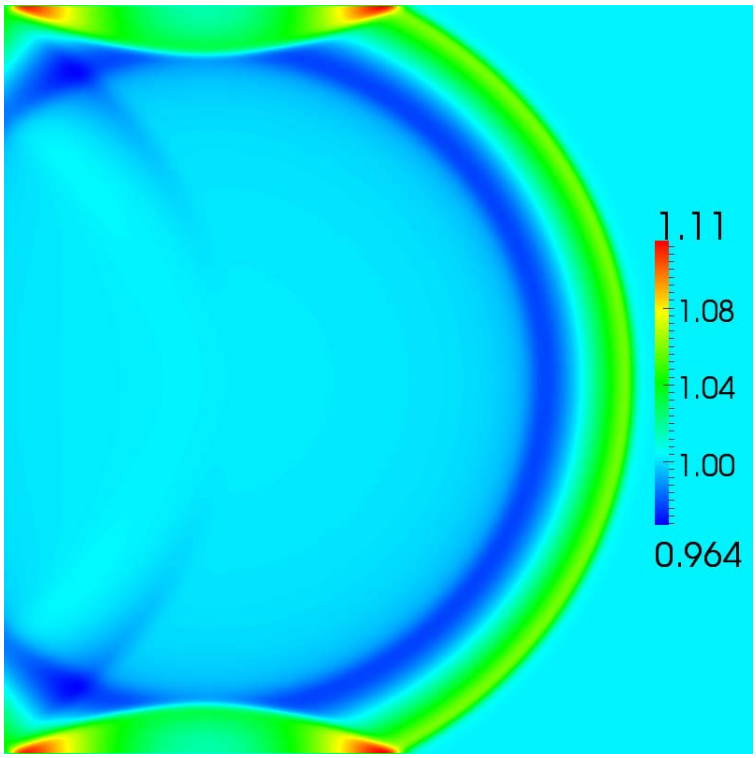

Figure 6.16: Perpendicular impedance free field BC, setup (b), density at $t = 700 \cdot \Delta t$

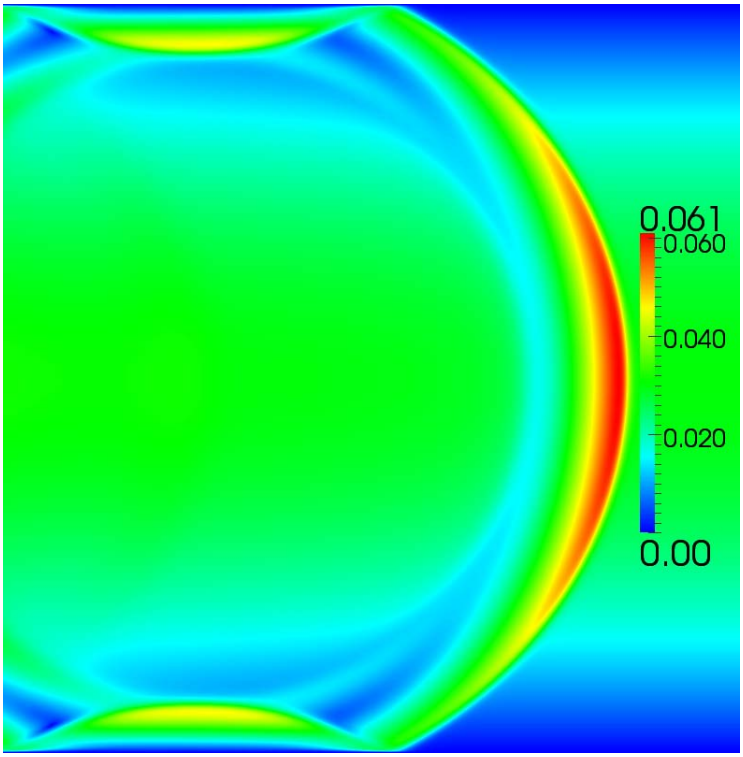

Figure 6.17: Isotropic impedance free field BC, setup (b), absolute velocity at $t = 700 \cdot \Delta t$

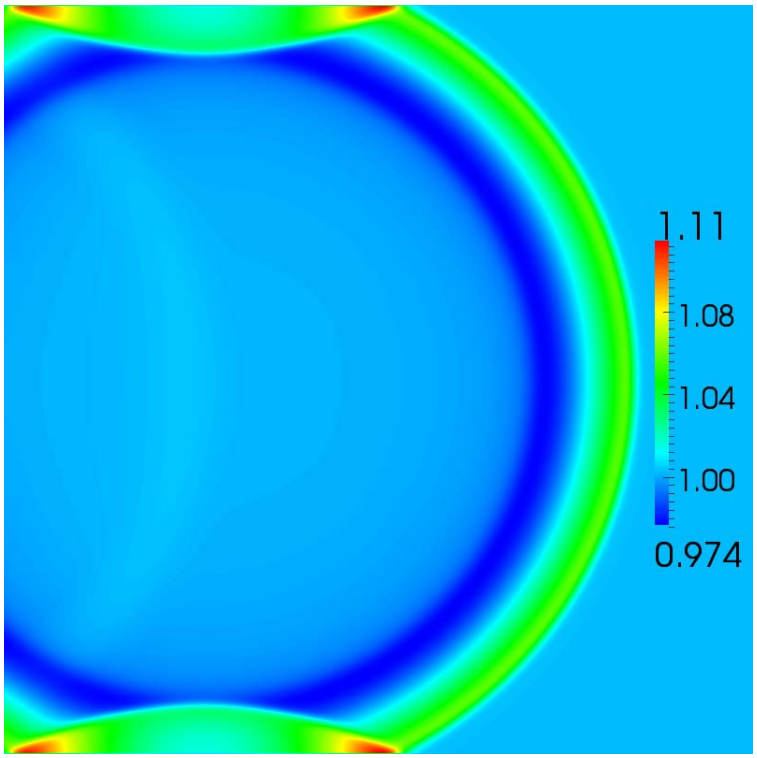

Figure 6.18: Isotropic impedance free field BC, setup (b), density at $t = 700 \cdot \Delta t$

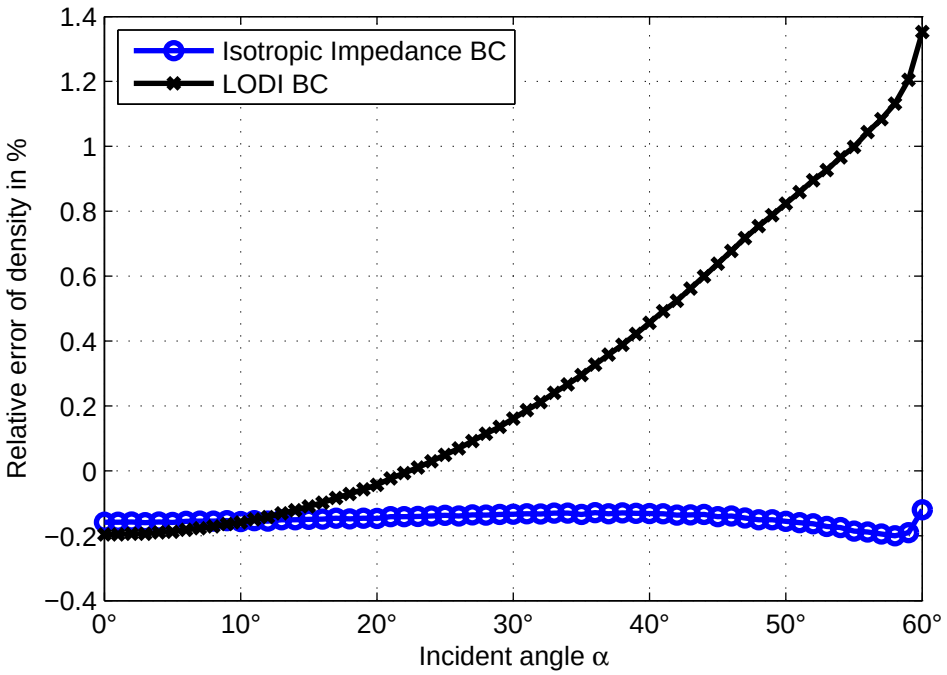

Figure 6.19: Reflection over incident angle, LODI and isotropic impedance BC, incompressible

6.5 Compensation of Non-Equilibrium Bounce-Back Error

As a matter of fact, calculating the tangential velocity by using equation 6.36 or 6.56 for non-equilibrium bounce-back results in an error of Δt per time step (cf. section 4.3.1). This error is not visible in all simulations described in appendix B due to the limited simulation time. Figure 6.20 shows the v_y velocity field for the compressible LBM simulation of the isotropic impedance free field boundary conditions, described in section 6.3.3. No irregularity can be observed at the inflow (parabolic velocity profile). Anyhow, the used scheme allows for resolving all pressure changes in the sufficient order of error.

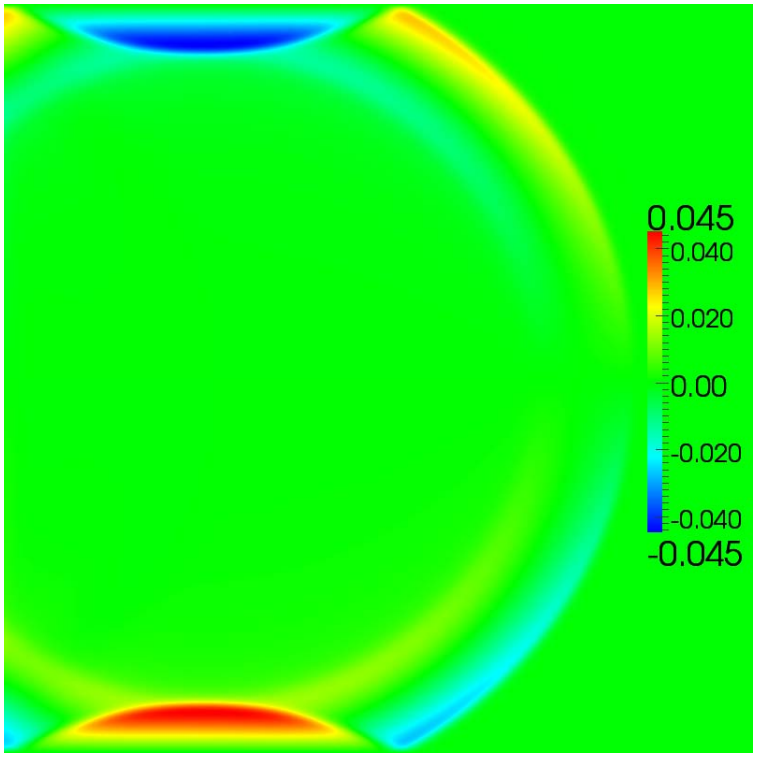

Figure 6.20: Isotropic impedance free field BC, setup (b), v_y velocity at $t = 700 \cdot \Delta t$

However, the situation changes when the error sums up over large simulation times and then emerges to be not negligible. This will be discussed in detail in section 7.4.2.1. The remedy chosen in this work is to relax the tangential velocity towards its initialization:

$$v_y^{(n+1)} = v_{y,0} \cdot (1 - \alpha) + v_y^{(n)} \cdot \alpha. \tag{6.66}$$

For the 2D pressure wave test case of section 6.4, a relaxation towards $v_{y,0} = 0$ is applied, which results in a mere multiplication of v_y with $\alpha \equiv 0.99$, reducing the specific tangential velocity by 1 % in each time step. Figure 6.21 shows the corresponding relative error in density of the simulation with setup (b), isotropic inflow boundary condition and relaxation scheme on the left hand side, compared with the anisotropic version. Although not fully isotropic, the error reduces by a factor of 4 compared to the perpendicular adaption in worst case, i.e. an

angle of 60°. Figure 6.22 shows a comparison with the unrelaxed isotropic boundary condition concerning the wake of the reflection. As it can clearly be seen, the error of the simulation with relaxation of the tangential velocity lies in the same range as in the unrelaxed case (not considering the boundary effect beyond an angel of 56°).

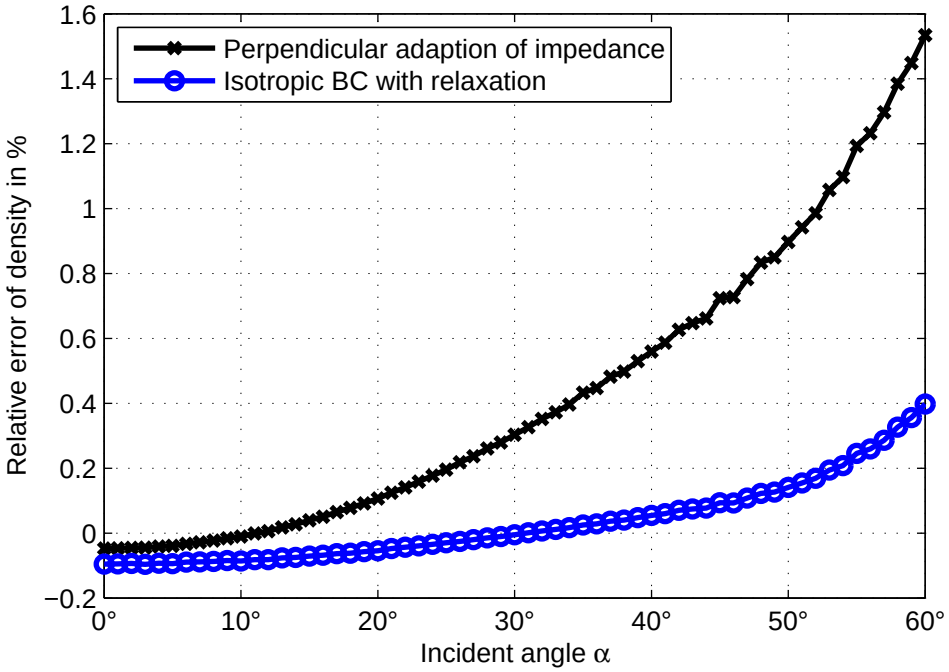

Figure 6.21: Reflection over incident angle at $t = 700 \cdot \Delta t$

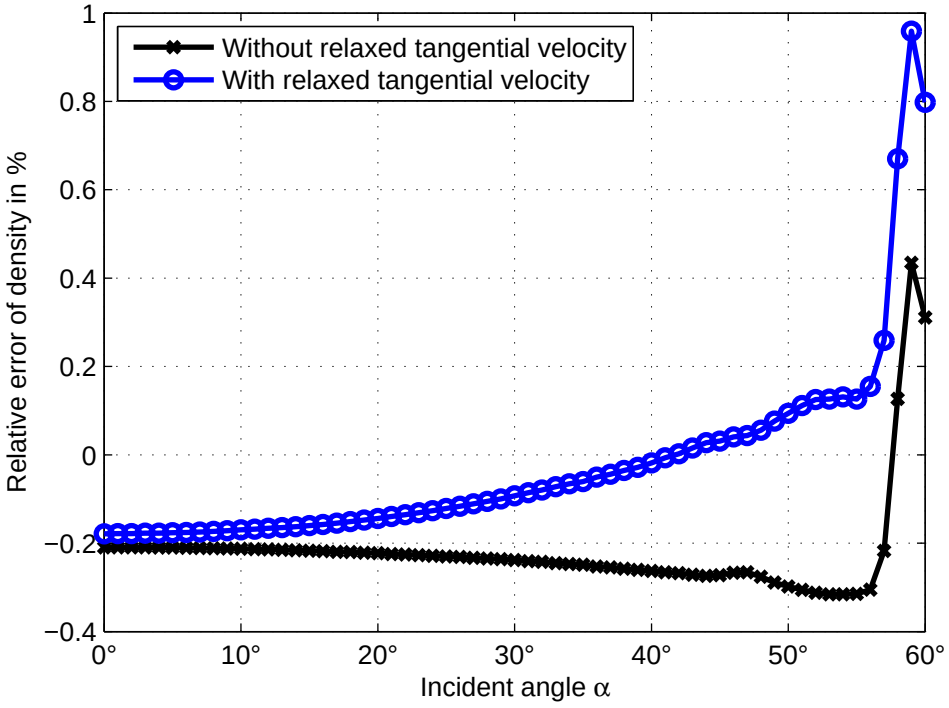

Figure 6.22: Isotropic BCs, reflection over incident angle at $t = 770 \cdot \Delta t$

Chapter 7

Boundary State Adaption for Impedance Boundary Conditions

In the preceding chapters, only non-reflecting boundary conditions representing a free field solution were discussed. The core of such a perfectly (not considering the numerical error) non-reflecting boundary condition is that the velocity will always depend on the incoming pressure change, respectively vice versa, for the differential as well as for the integral view on conservation properties for sound pressure waves (cf. the derivations of section 5.2 and 6.1). A non-reflecting boundary simply has to accommodate itself to the pressure wave, just as the values of a lattice point in the interior of the simulation domain would behave if a pressure wave was passing. If a certain value was fixed at a point in the middle of the domain, an error with the result of an emerging pressure wave would naturally occur. In conclusion, also on the boundary a non-reflecting condition is in contradiction to a fixed boundary state. Therefore a non-reflecting pressure or velocity boundary condition cannot be realized in a strict sense.

On the other hand, the state of the boundaries is usually to be specifically set over time, and it is essential to offer the option of tuning it towards desired values. The remedy is to allow the adaption with a certain rate: The extension by Poinsot and Lele [51] was a penalty factor (cf. section 5.2.1), setting a certain rate of reflection on purpose and so allowing for a gradually transition to the desired target state. However, the criterion for tuning this penalty factor is quantitatively hard to manage.

The approach used below for the boundary state adaption of the impedance boundary conditions allows to limit the level of reflection by a distinct pressure level value. The idea is to change the reference level to which the impedance is adapted. This is equivalent to increasing or decreasing the flux on the boundary to compensate the change of the state caused by the impedance adaption. The increase or decrease itself corresponds to a pressure wave feedback.

The deviation to the desired boundary state is not known in advance to the adaption of the impedance, as the free field state has first to be determined by the solution of the impedance condition, equation 6.11. After computing this intermediate state, it can be compared to the desired one. A maximum allowed boundary state adaption can be derived and then be applied. As this changes the reference level for the impedance adaption, the impedance condition has to be solved respectively again, however then with the simpler macroscopic relation. Finally, a fixed reference level has to be changed by the corresponding change in flux. As this will in most cases require additional memory, the adaption relative to the last time step might be most preferable.

In this chapter, both a velocity and a pressure boundary condition are derived for compressible and incompressible LBM, as an extension to the impedance boundary conditions of chapter 6. This is done for perpendicular adaption of the acoustic impedance. In the end, a benchmark problem is discussed to show the practical application.

7.1 Velocity Adaption

7.1.1 Compressible LBM

The velocity adaption can be applied, as already explained in the introduction to this chapter, after the velocity was computed from the solution of the impedance condition, i.e. equation 6.35 for perpendicular adaption. Let $v_{x,\mathrm{imp}}$ be the result of the impedance adaption. For the compressible LBM and a **left** boundary, the relation between density and velocity on the boundary is given by equation 6.33:

$$\varrho_{\mathrm{imp}} = \left[\frac{\varrho_z}{1 - v_{x,\mathrm{imp}}}\right] \tag{7.1}$$

with

$$\varrho_z := f_0 + f_2 + f_4 + 2\left(f_3 + f_6 + f_7\right). \tag{7.2}$$

This means that a change of the velocity $v_{x,\mathrm{imp}}$ to a new velocity $v_{x,\mathrm{new}}$ causes a change in density $d\varrho$ of:

$$\begin{aligned} d\varrho &= \varrho_{\mathrm{new}} - \varrho_{\mathrm{imp}} = \\ &= \frac{\varrho_z}{1 - v_{x,\mathrm{new}}} - \varrho_{\mathrm{imp}}. \end{aligned} \tag{7.3}$$

If the change in density was limited to

$$|d\varrho| \leq d\varrho_{\max}, \tag{7.4}$$

margins of a maximum and minimum permitted range $[v_{x,\min}, v_{x,\max}]$ can be derived for the velocity adaption $v_{x,\mathrm{new}}$ from equation 7.3:

$$v_{x,\min} = 1 - \frac{\varrho_z}{\varrho_{\mathrm{imp}} - d\varrho_{\max}}, \tag{7.5}$$

$$v_{x,\max} = 1 - \frac{\varrho_z}{\varrho_{\mathrm{imp}} + d\varrho_{\max}}. \tag{7.6}$$

Subsequently, $v_{x,\mathrm{new}}$ can be set either to the target value, if in range, or to the nearest value to the interval. As the reference level has changed, the impedance condition 6.11 has to be solved again, this time for the new density and with a known perpendicular velocity:

$$\varrho_{\mathrm{new}} = \frac{c_s^2 \cdot \varrho^{(n-1)}}{c_s^2 + \left(v_{x,\mathrm{new}} - v_x^{(n-1)}\right)\left(\frac{1}{2}\left(v_{x,\mathrm{new}} - v_x^{(n-1)}\right) + c_s\right)}, \tag{7.7}$$

respectively for the fixed reference level:

$$\varrho_{\mathrm{new}} = \frac{c_s^2 \cdot \varrho_0}{c_s^2 + \left(v_{x,\mathrm{new}} - v_{x,0}\right)\left(\frac{1}{2}\left(v_{x,\mathrm{new}} - v_{x,0}\right) + c_s\right)}. \tag{7.8}$$

In the present approach, the error resulting from the re-adaption will be corrected during the next time step. If using the fixed reference level, it has consequently to be changed as well:

$$\varrho_0^{n+1} = \varrho_0^n + \varrho_{\mathrm{new}} - \varrho_{\mathrm{imp}}^n, \tag{7.9}$$

$$v_{x,0}^{n+1} = v_{x,0}^n + v_{x,\mathrm{new}} - v_{x,\mathrm{imp}}^n. \tag{7.10}$$

v_y and the unknown distributions have to be set just like described in section 6.3.1, using the non-equilibrium bounce-back relation, equations 6.36 to 6.39. It is stressed that the use of this relation is not correct in a strict sense: The available known distributions correspond to the flux of the non-adapted state. However, the approach in this work is to let the error automatically be corrected during the subsequent time steps. A more advanced approach is subject to further research.

As an example, the velocity adaption was added to the impedance boundary condition of section 6.3.1. The implementation is appended in section A.16.

7.1.2 Incompressible LBM

For the incompressible model, equation 7.1 turns into:

$$\varrho_{\mathrm{imp}} = \varrho_z + \varrho_0 v_{x,\mathrm{imp}}. \tag{7.11}$$

With a limit

$$|d\varrho| \leq d\varrho_{\max}, \tag{7.12}$$

the range $[v_{x,\min}, v_{x,\max}]$ for maximum velocity adaption of $v_{x,\mathrm{new}}$ results in:

$$v_{x,\min} = v_{x,\mathrm{imp}} - \frac{d\varrho_{\max}}{\varrho_0}, \quad v_{x,\max} = v_{x,\mathrm{imp}} + \frac{d\varrho_{\max}}{\varrho_0}. \tag{7.13}$$

After adapting $v_{x,\mathrm{new}}$ within this interval, ϱ_{new} has to be set according to the solution of equation 6.50,

$$\varrho_{\mathrm{new}} = \varrho^{(n-1)} - \frac{\varrho_0 (v_{x,\mathrm{new}} - v_x^{(n-1)}) \left(\frac{1}{2} \left(v_{x,\mathrm{new}} - v_x^{(n-1)} \right) + c_s \right)}{c_s^2}, \tag{7.14}$$

respectively for the fixed reference level $v_{x,0}$ and ϱ_0:

$$\varrho_{\mathrm{new}} = \varrho_0 - \frac{\varrho_0 (v_{x,\mathrm{new}} - v_{x,0}) \left(\frac{1}{2} \left(v_{x,\mathrm{new}} - v_{x,0} \right) + c_s \right)}{c_s^2}. \tag{7.15}$$

A fixed reference level has to be redefined by equation 7.9 and 7.10, v_y and the distributions f_1, f_5 and f_8 are set by the non-equilibrium bounce-back equations.

7.2 Pressure Adaption

7.2.1 Compressible LBM

The pressure adaption works in the same way as the velocity adaption, merely the liming criteria can be applied immediately, as already formulated for the target value. Below, the adaption is performed for density rather than pressure, as both are linearly dependent by the isothermal ideal gas law $p = c_s^2 \cdot \varrho$. The description below refers to a **right** boundary with normal vector $-\underline{e}_x$.

After calculating the free field solution, the deviation of the resulting density ϱ_{imp} to its target value ϱ_{BC} is given by:

$$d\varrho = \varrho_{\mathrm{imp}} - \varrho_{\mathrm{BC}}. \tag{7.16}$$

For a maximum permitted change in density,

$$|d\varrho| \leq d\varrho_{\mathrm{max}}, \tag{7.17}$$

the pressure adapted density ϱ_{new} will be either one of the maximum interval bounds $\varrho_{\mathrm{imp}} \pm d\varrho_{\mathrm{max}}$ or directly the target density ϱ_{BC}, if it is within the interval. At last, the corresponding velocity $v_{x,\mathrm{new}}$ has to be recalculated, referring to the new reference density (cf. equation 6.12):

$$v_{x,\mathrm{new}} = v_x^{(n-1)} - c_s \cdot \left(\sqrt{2 \cdot \frac{\varrho^{(n-1)}}{\varrho_{\mathrm{new}}} - 1} - 1 \right), \tag{7.18}$$

respectively for the fixed reference level:

$$v_{x,\mathrm{new}} = v_{x,0} - c_s \cdot \left(\sqrt{2 \cdot \frac{\varrho_0}{\varrho_{\mathrm{new}}} - 1} - 1 \right). \tag{7.19}$$

The velocity in y-direction and the unknown density distributions are set with the non-equilibrium bounce-back equations. The fixed reference level has to be changed according to equation 7.9 and 7.10, if used as reference for the adaption.

7.2.2 Incompressible LBM

For the incompressible LBM, the derivation is almost identical to the previous section, merely the recalculation of $v_{x,\text{new}}$, equations 7.18 and 7.19, turn into:

$$v_{x,\text{new}} = v_x^{(n-1)} + c_s - \sqrt{c_s^2 + \frac{2c_s^2\left(\varrho^{(n-1)} - \varrho_{\text{new}}\right)}{\varrho_0}} \tag{7.20}$$

and

$$v_{x,\text{new}} = v_{x,0} + c_s - \sqrt{c_s^2 + 2c_s^2\left(1 - \frac{\varrho_{\text{new}}}{\varrho_0}\right)}. \tag{7.21}$$

7.3 Sound Pressure Level as Adaption Criteria

For aeroacoustic simulations, an appropriate measure might be a maximum reflected sound pressure level, which can easily be calculated on basis of the ideal gas law as (cf. Müller [47]):

$$\Delta L_{\max} = 20 \cdot \lg \frac{\Delta p}{p_{\text{ref}}} = 20 \cdot \lg \frac{\Delta \varrho}{\varrho_{\text{ref}}}. \tag{7.22}$$

$p_{\text{ref}} = 2 \cdot 10^{-5}$ Pa is the smallest perceivable pressure change for humans on basis of a hydrostatic pressure of $p_0 = 10^5$ Pa. Table 7.1 shows maximum sound pressure level changes with their corresponding maximum density changes for a hydrostatic density of $\varrho_0 = 1$, i.e. the non-dimensional case of an LBM simulation.

$\Delta L_{\max}$	$\Delta \varrho_{\max}$
1 dB	$2.2 \cdot 10^{-10}$
3 dB	$2.8 \cdot 10^{-10}$
10 dB	$6.2 \cdot 10^{-10}$
20 dB	$2.0 \cdot 10^{-9}$
40 dB	$2.0 \cdot 10^{-8}$
60 dB	$2.0 \cdot 10^{-7}$
80 dB	$2.0 \cdot 10^{-6}$
100 dB	$2.0 \cdot 10^{-5}$
120 dB	$2.0 \cdot 10^{-4}$

Table 7.1: Relation sound pressure level and density changes for $\varrho_0 = 1$

A density adaption of $\Delta\varrho = 0.1$ will consequently need about $4.5 \cdot 10^8$ time steps in simulation time if the reflection was limited to 1 dB. Even for a maximum reflection of 120 dB, the human threshold of pain, a simulation time of $500 \cdot \Delta t$ is needed.

In consequence, it is essential to strike a balance between level of reflection and convergence. For certain applications, it might even be better to re-model the problem for an acoustical free field, without boundary state adaption. The essence however is strictly of physical nature: It is theoretically not possible to have a non-reflecting boundary and a specific boundary state at the same time.

7.4 Benchmark: Flow around Cylinder

For evaluating a combination of free field and state adapted impedance boundary conditions, the laminar 2D-1 (steady) and 2D-2 (unsteady) benchmark defined by Schäfer and Turek [60] were used. The setup is displayed in figure 7.1. It models the flow around a cylinder in a rectangular domain. On the left hand-side, marked in red, a parabolic velocity profile is prescribed with an inlet velocity of

$$v_x(0, y, t) = \frac{4 v_{max} y (l_y - y)}{l_y^2}, \tag{7.23}$$

$$v_y(0, y, t) = 0. \tag{7.24}$$

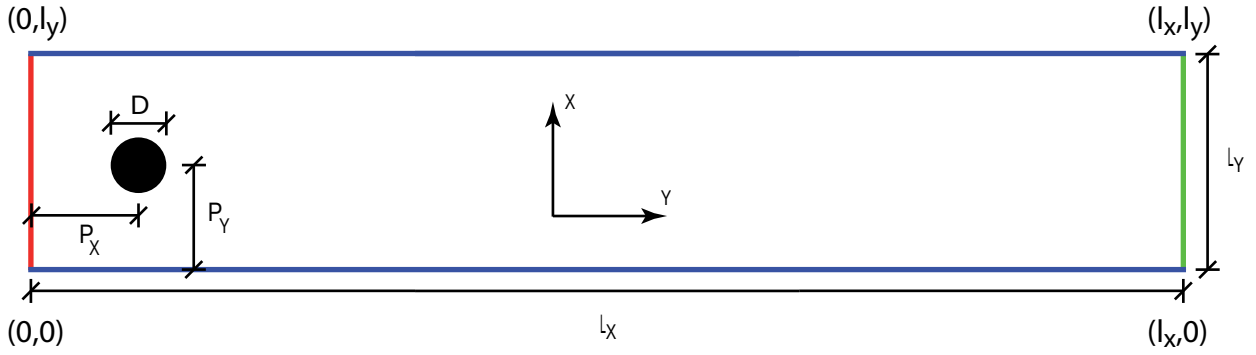

Figure 7.1: Setup of 2D benchmark

The bottom and top boundaries (in blue) are defined to have a zero velocity $v_x = v_y \equiv 0$. The outflow condition on the right hand side, marked in green, can be according to Schäfer and Turek "chosen by the user" [60]. For the steady benchmark, the Reynolds number is defined as $\mathrm{Re} := 20$, for the unsteady benchmark, $\mathrm{Re} := 100$. The Reynolds number with the kinematic viscosity ν,

$$\mathrm{Re} = \frac{\overline{v} D}{\nu}, \tag{7.25}$$

is hereby set by the average velocity $\overline{v}$,

$$\overline{v} = \frac{2}{3} v_{max}. \tag{7.26}$$

The diameter of the cylinder D represents the reference length of the simulation. The length of the domain equals $l_x = 22 \cdot D$, the height respectively $l_y = 4.1 \cdot D$. The position of the cylinder (obstacle with circular cross-section) is defined to be $p_x = p_y = 2 \cdot D$, with an origin of the coordinates at the lower left corner of the domain. This indicates a slight offset of the vertical position relative to the center of the domain.

In the benchmark simulations referred to below, the cylinder was generally modeled by first order simple bounce-back. The drag and lift forces F_D and F_L were computed by the first order momentum-exchange method, as described e.g. by Mei et al. [44]. For evaluation, the drag and lift coefficients c_D and c_L of the obstacle were computed by

$$c_D := \frac{2F_D}{\varrho\, \overline{v}^2 D}, \quad c_L := \frac{2F_L}{\varrho\, \overline{v}^2 D}. \tag{7.27}$$

For the unsteady benchmark, additionally the Strouhal number St was evaluated, which is defined as

$$\mathrm{St} := \frac{D}{\overline{v}\, T}, \tag{7.28}$$

with the period of separation T. For the simulations, three successively coarsened mesh levels were implemented with a number of grid nodes in x and y direction n_x and n_y, as listed in table 7.2. In the associated refinement strategy, attention was paid that the ratio of the diameter D and the domain height l_y corresponds as closely as possible to the proportions of the given benchmark geometry. For the time step, a diffusive scaling was conducted.

Level	n_x	n_y	D	v_{max}
h_3	420	79	19	0.0310
h_2	860	161	39	0.0151
h_1	1299	243	59	0.01

Table 7.2: Grid levels h_1, h_2 and h_3

The values marked below to be "reference" refer to the evaluation of the benchmark by Schäfer and Turek [60] "as suggested by the authors on the basis of the obtained solutions".

7.4.1 Results of Steady Benchmark

For the steady benchmark, the top and bottom no-slip boundaries were set by a velocity adapted impedance boundary condition with $v_x = v_y \equiv 0$ and a maximum reflection of $d\varrho_{\max} = 10^{-6}$. The inflow was set by a velocity adapted impedance boundary condition with velocities as defined by equation 7.23 and 7.24. The maximum reflection for the inflow boundary was set to $d\varrho_{\max} = 10^{-4}$ in order to get sufficient convergence for the velocity adaption. The outflow was modeled by a free field impedance boundary condition without boundary state adaption. All boundary conditions were using the **perpendicular adaption** of impedance, relative to the **preceding time step**. The tangential velocities on the boundaries were **explicitly set to zero** and not derived by the non-equilibrium bounce-back relation. This agrees consistently with the problem-specific situation.

The flow field was initialized with a uniform density of $\varrho_0(x, y, t = 0) \equiv 1$ and the velocity

$$v_x(x, y, t = 0) = \frac{4v_{max}y(l_y - y)}{l_y^2}, \tag{7.29}$$

$$v_y(x, y, t = 0) = 0. \tag{7.30}$$

The mesoscopic density distributions were set by the corresponding equilibrium distribution. Large initial velocity gradients in the vicinity of the obstacle result in significant pressure waves. This effect was intended, and a solution of the Poisson equation for the pressure field, like proposed by Mei et al. [43], was not done on purpose. Table 7.3 shows the results of the simulations. The prefix $\Delta_{\text{mid}}(h_i)$ marks the relative deviation of the specific value for grid level h_i to the midpoint of the reference range in relation to half of the reference range. For a general value Φ with a reference range from $\Phi_{\text{min, ref}}$ to $\Phi_{\text{max, ref}}$ and a mean value of

$$\overline{\Phi}_{\text{ref}} = \frac{\Phi_{\text{min, ref.}} + \Phi_{\text{max, ref.}}}{2}, \tag{7.31}$$

Δ_{mid} equals to

$$\Delta_{\text{mid}}(h_i)(\Phi) = \frac{|\Phi(h_i) - \overline{\Phi}_{\text{ref}}|}{\Phi_{\text{max, ref.}} - \overline{\Phi}_{\text{ref}}}. \tag{7.32}$$

For a value of $\Delta_{\text{mid}} \leq 1$ this would mean that the simulated result lies within the reference range given by Schäfer and Turek. It is stressed that Schäfer and Turek designate all reference ranges to be intervals for the particular "exact" solution [60], so the deviations are not equivalent to error levels.

	Compressible LBM		Incompressible LBM	
	c_D	c_L	c_D	c_L
Mid. Reference	5.5800	0.0107	5.5800	0.0107
Reference range	5.5700 - 5.5900	0.0104 - 0.0110	5.5700 - 5.5900	0.0104 - 0.0110
h_3	5.4780	0.0064	5.3157	0.0074
$\Delta_{\text{mid}}(h_3)$	10.2	14.3	26.4	11.0
h_2	5.4976	0.0086	5.4399	0.0088
$\Delta_{\text{mid}}(h_2)$	8.2	7.0	14.0	6.3
h_1	5.5078	0.0101	5.4725	0.0099
$\Delta_{\text{mid}}(h_1)$	7.2	2.0	10.8	2.7

Table 7.3: Results of the 2D-1 benchmark, Re = 20

Also a comparison was conducted with a conventional setup, implementing Zou-He velocity and pressure boundaries at the inflow respectively outflow and simple bounce-back boundary conditions at the top and bottom. For the Zou-He pressure boundary condition at the outflow, the density was uniformly set to $\varrho_0 \equiv 1$. Figure 7.2 shows the evolution of the density field over time, figure 7.3 the corresponding simulation with impedance boundary conditions, all for grid level h_1 and the compressible LBM model. The color scaling of each time step refers in both figures to the same range. The extinction of the spurious pressure waves on all boundaries can clearly be observed. Additionally, figure 7.4 and 7.5 illustrate the evolution of the drag and lift coefficients. For the specific case, the conventional approach takes 10.0 time steps longer to gain the steady state drag force within a relative error of 10 % and 4.9 time steps longer to gain it within a relative error of 1 %.

It is noted that a specific source of error emerges when implementing no-slip boundary conditions with a low maximum reflection level. It might happen that the normal boundary velocity then becomes significant as the boundary state adaption reacts too slowly, and a mass loss occurs on the boundary. Hence it is advisable to check the velocity and increase the reflectivity, if necessary: All incoming density changes smaller than $d\varrho_{\max}$ will not cause a change of the boundary velocity.

It is once again stressed that a strictly fixed no-slip boundary is physically not possible, as described in chapter 5 and 6: When a reflection is absorbed, the boundary will always cause a slight mass loss.

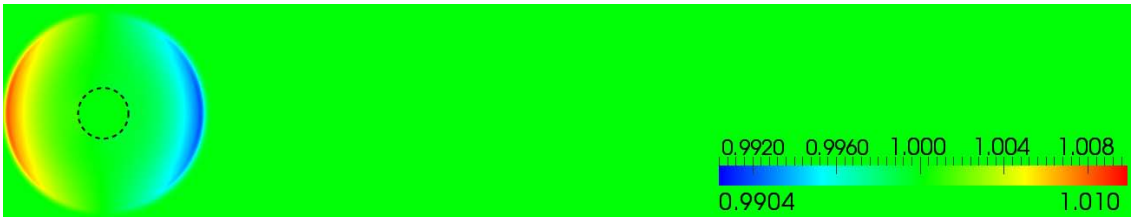

$t = 150 \cdot \Delta t$

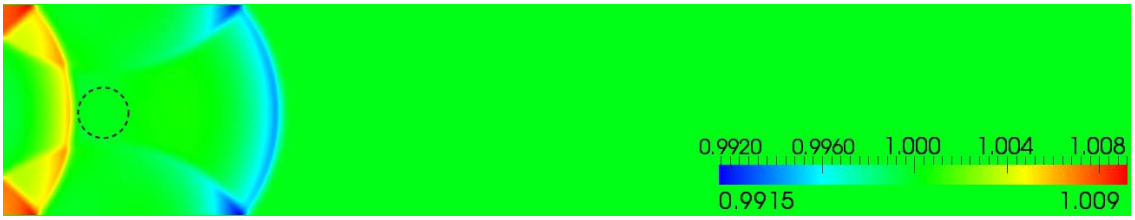

$t = 300 \cdot \Delta t$

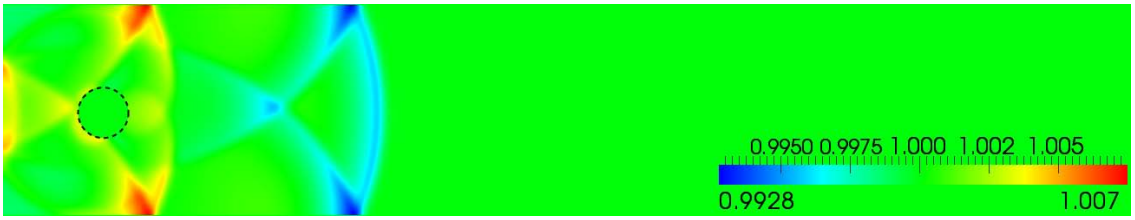

$t = 500 \cdot \Delta t$

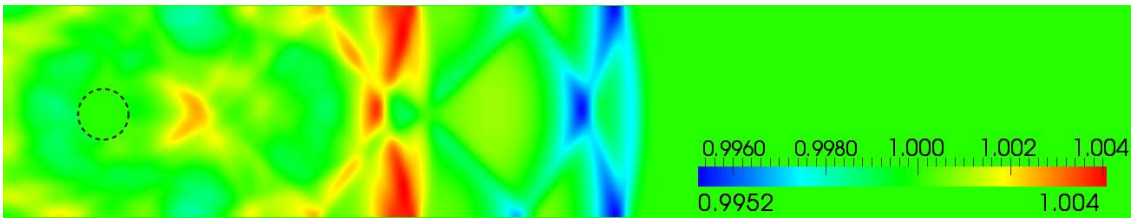

$t = 1000 \cdot \Delta t$

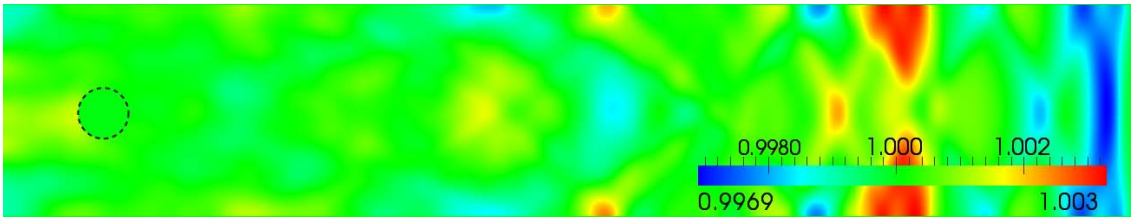

$t = 2000 \cdot \Delta t$

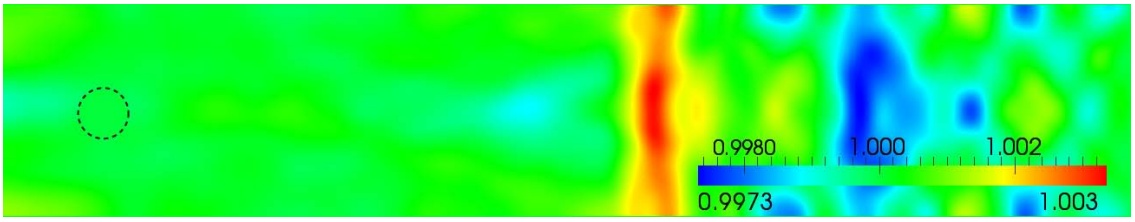

$t = 3000 \cdot \Delta t$

Figure 7.2: 2D-1 benchmark with conventional boundary conditions, density

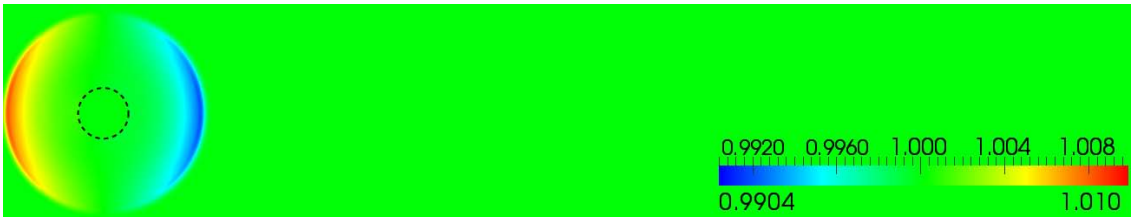

$t = 150 \cdot \Delta t$

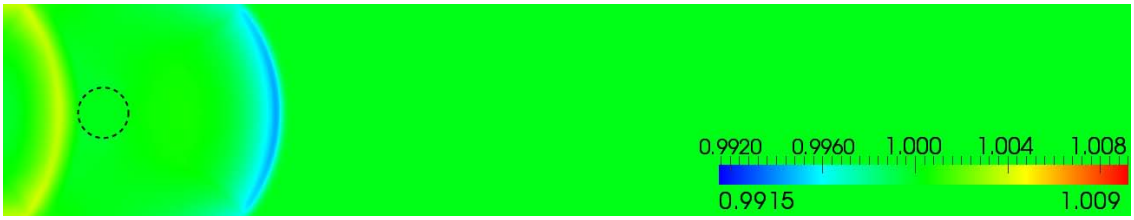

$t = 300 \cdot \Delta t$

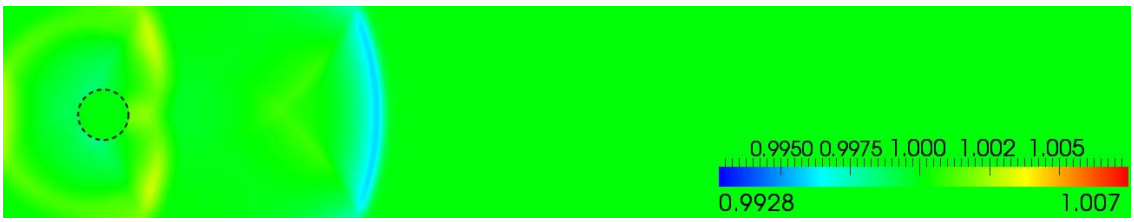

$t = 500 \cdot \Delta t$

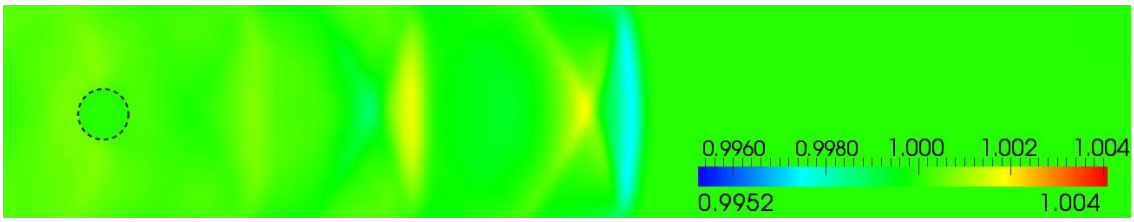

$t = 1000 \cdot \Delta t$

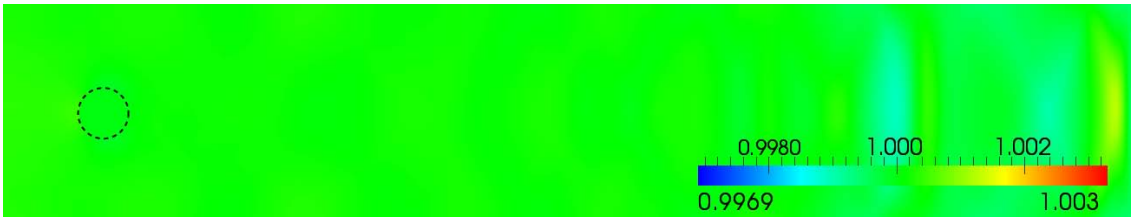

$t = 2000 \cdot \Delta t$

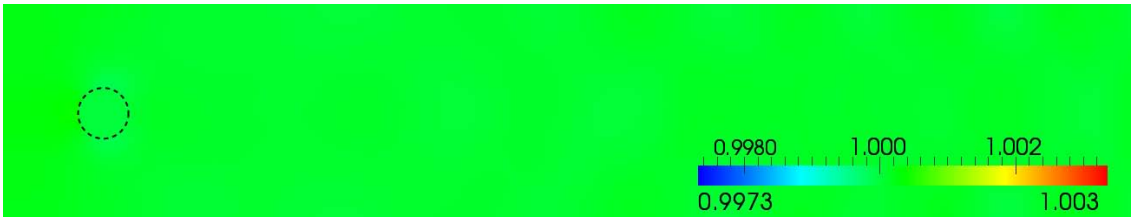

$t = 3000 \cdot \Delta t$

Figure 7.3: 2D-1 benchmark with impedance boundary conditions, density

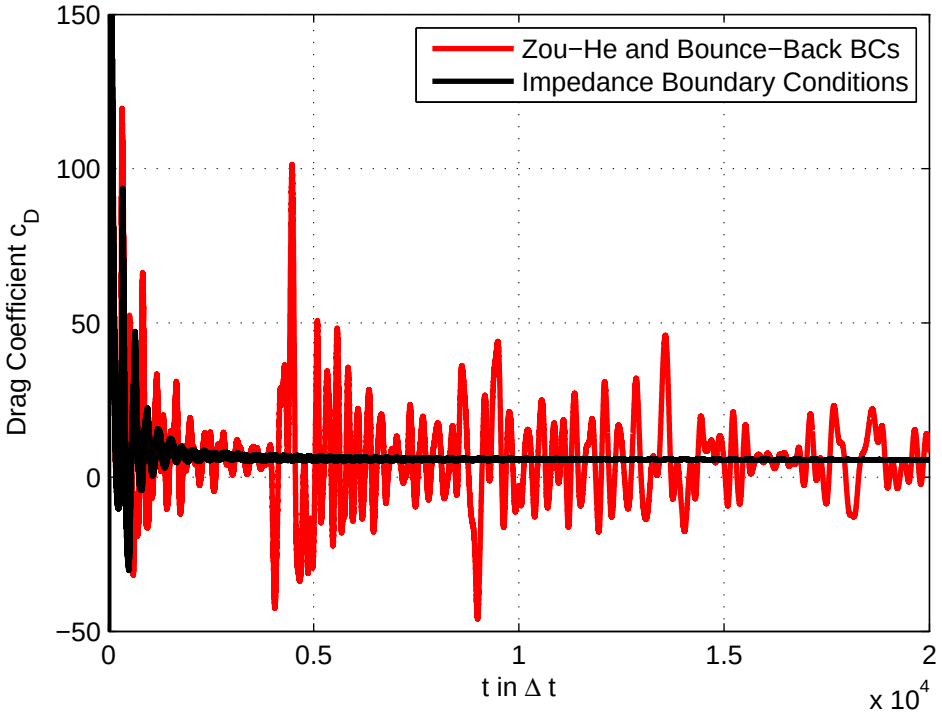

Figure 7.4: Drag coefficient during first 20,000 time steps

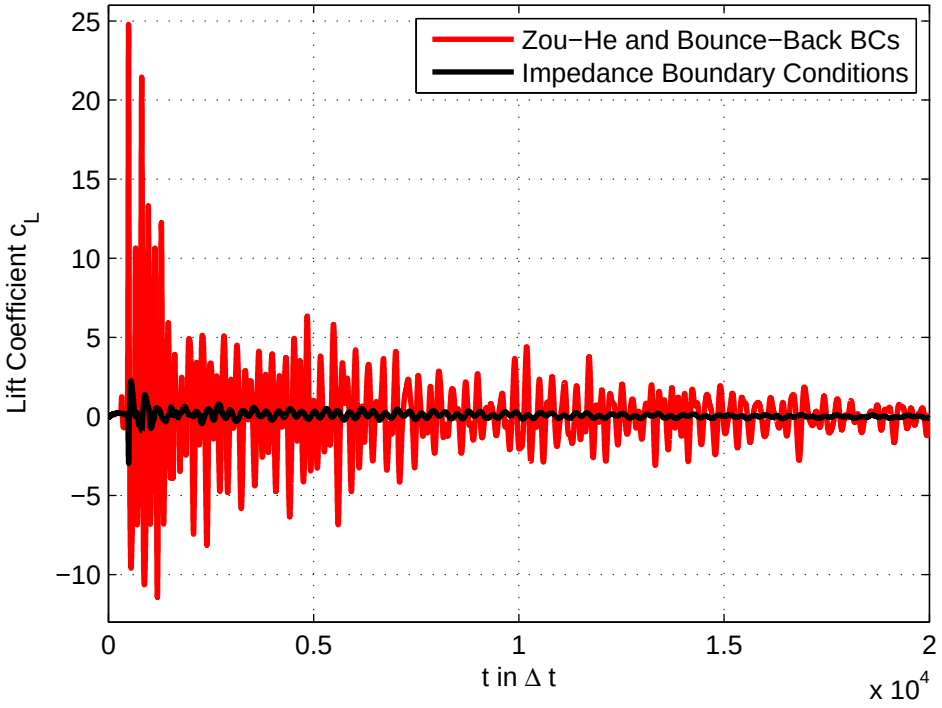

Figure 7.5: Lift coefficient during first 20,000 time steps

7.4.2 Results of Unsteady Benchmark

For the unsteady benchmark with Re = 100, basically the same boundary conditions were used as in section 7.4.1, but instead of the perpendicular adaption for the outflow, an isotropic free field impedance boundary condition was used (cf. appendix A.10 and A.15, but with relaxation factor for tangential velocity set to **rlx** $\equiv 1$). Again the flow field was initialized with $\varrho_0(x, y, t = 0) \equiv 1$ and velocities according to equation 7.29 and 7.30.

Table 7.4 shows the results of the simulation, both for the compressible and incompressible LBM model. The simulation time was set to $3 \cdot 10^5$ time-steps for grid levels h_3 and h_2. For level h_1, it was set to $6 \cdot 10^5$ time-steps in order to recover the settled state. The maximum for the drag and lift coefficients was taken from the last 3 periods, the Strouhal Number St was averaged over the last 7 periods. The prefix $\Delta_{\text{mid}}(h_i)$ marks the deviation of the specific value for grid level h_i to the midpoint of the reference range as defined by equation 7.32.

	Compressible LBM			Incompressible LBM		
	$c_{D,\max}$	$c_{L,\max}$	St	$c_{D,\max}$	$c_{L,\max}$	St
Mid. Reference	3.2300	1.0000	0.3000	3.2300	1.0000	0.3000
Reference range	3.2200 - 3.2400	0.9900 - 1.0100	0.2950 - 0.3050	3.2200 - 3.2400	0.9900 - 1.0100	0.2950 - 0.3050
h_3	3.4607	1.2249	0.3005	3.2164	1.0002	0.3046
$\Delta_{\text{mid}}(h_3)$	23.0	22.5	0.10	1.4	0.02	0.92
h_2	3.2917	1.0361	0.3028	3.2182	0.9851	0.3043
$\Delta_{\text{mid}}(h_2)$	6.2	3.6	0.56	1.2	1.5	0.86
h_1	3.2689	0.9819	0.3033	3.2346	0.9684	0.3042
$\Delta_{\text{mid}}(h_1)$	3.9	1.8	0.66	0.46	3.2	0.84

Table 7.4: Results of the 2D-2 benchmark, Re = 100

Once again a comparison with a conventional approach is shown, with the same setup as in section 7.4.1: Zou-He velocity and pressure boundaries at the inflow respectively outflow and simple bounce-back boundary conditions at the top and bottom. Figure 7.6 displays the density of the flow field for the conventional simulation for six different time steps, figure 7.7 the same data for the setup with impedance boundary conditions. Both simulations were done using the compressible LBM model. The selected plots refer to the same color scale.

The superposed spurious pressure waves from the initialization inhibit observing any evolution of vortices behind the cylinder in the conventional simulation. The non-reflecting impedance boundary conditions on all boundaries suppress interfering pressure waves, so the evolution can indeed be fully observed. Figure 7.8 shows a plot of the lift coefficients over time for the incompressible LBM model, which additionally illustrates the difference between both approaches.

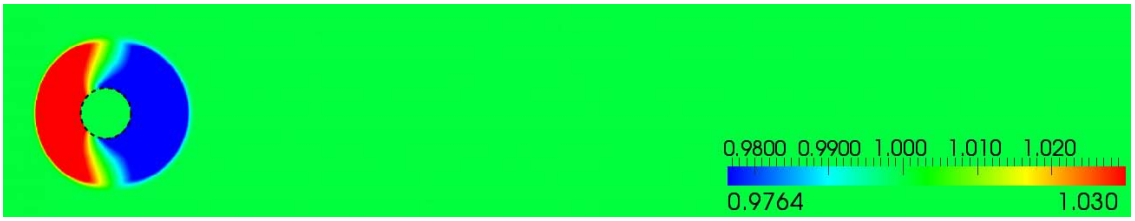

$t = 100 \cdot \Delta t$

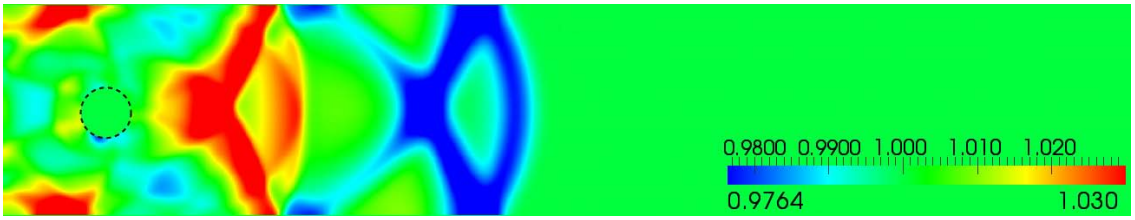

$t = 700 \cdot \Delta t$

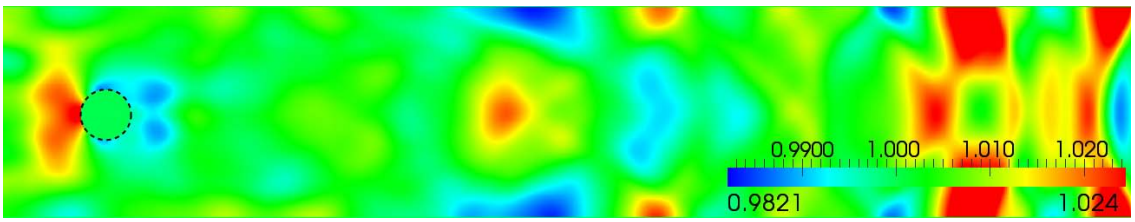

$t = 2000 \cdot \Delta t$

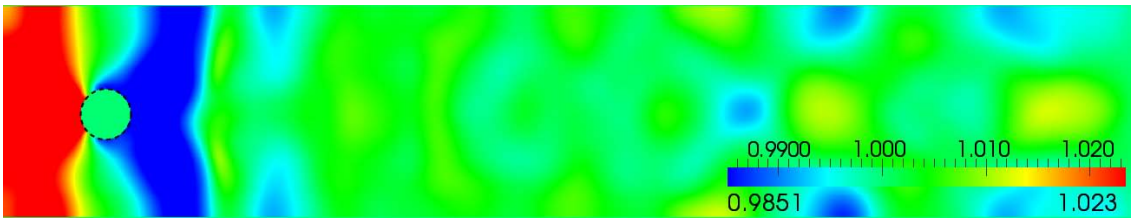

$t = 4600 \cdot \Delta t$

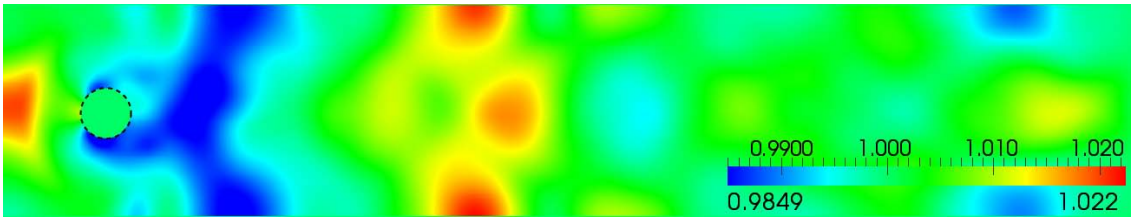

$t = 5400 \cdot \Delta t$

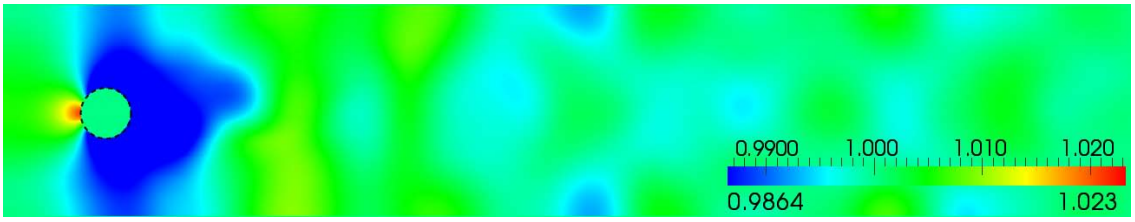

$t = 9000 \cdot \Delta t$

Figure 7.6: 2D-2 benchmark with conventional boundary conditions, density

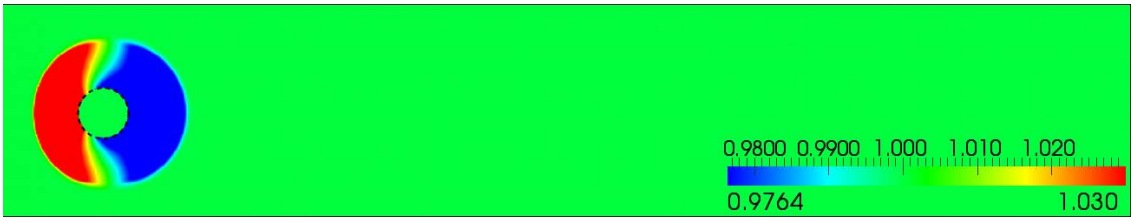

$t = 100 \cdot \Delta t$

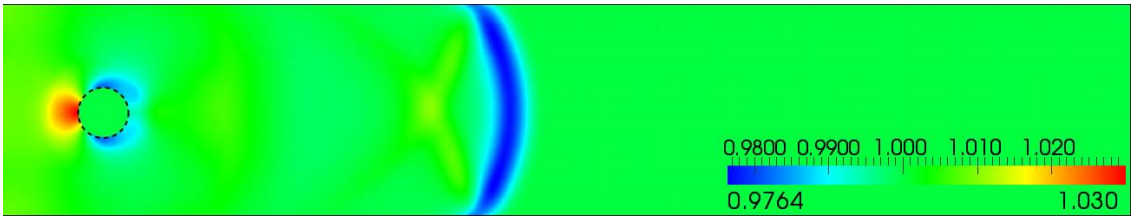

$t = 700 \cdot \Delta t$

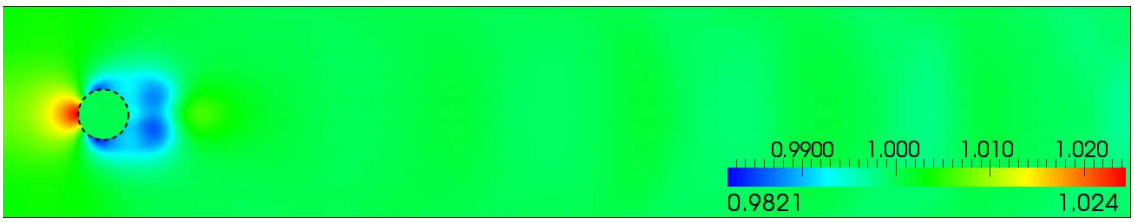

$t = 2000 \cdot \Delta t$

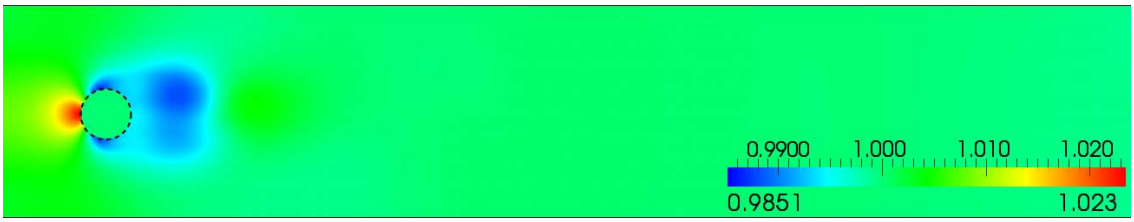

$t = 4600 \cdot \Delta t$

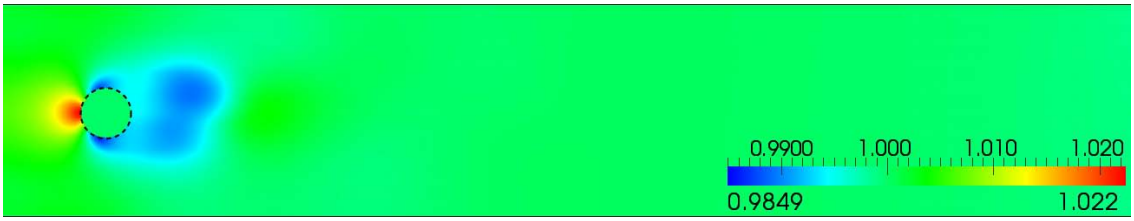

$t = 5400 \cdot \Delta t$

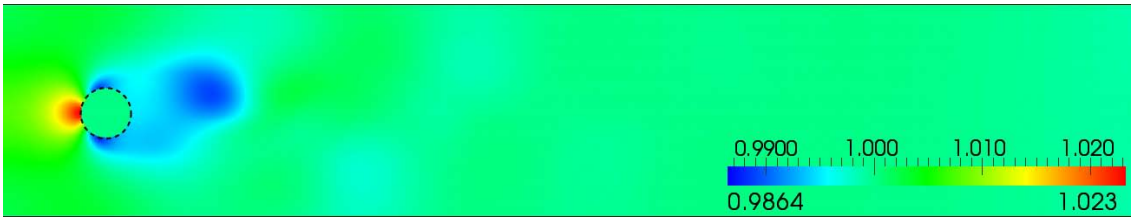

$t = 9000 \cdot \Delta t$

Figure 7.7: 2D-2 benchmark with impedance boundary conditions, density

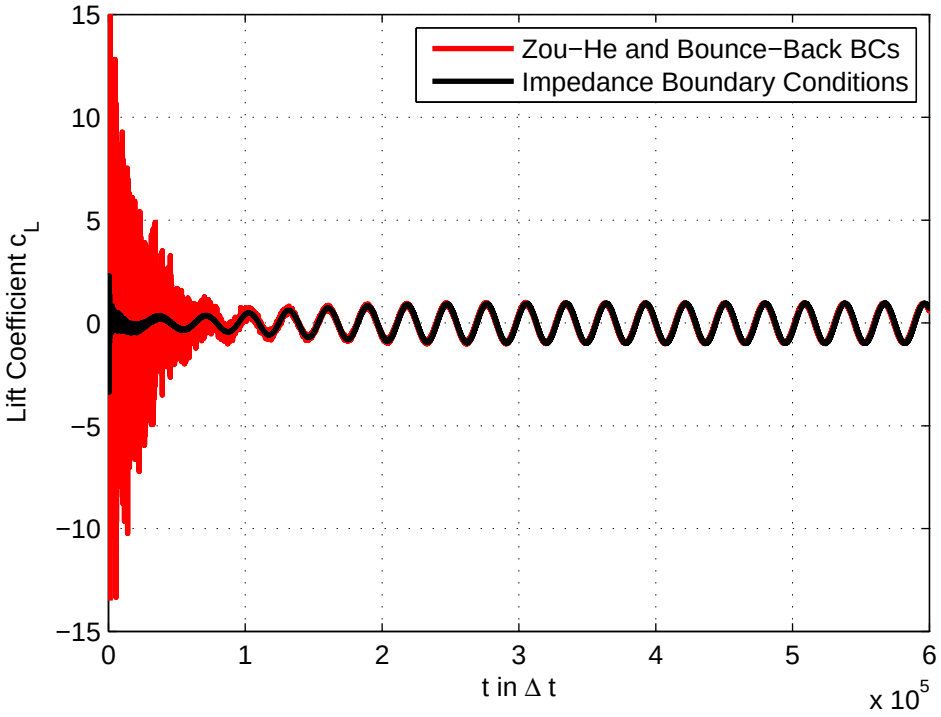

Figure 7.8: Lift coefficient over time for incompressible LBM simulations

7.4.2.1 Compensation of Non-Equilibrium Bounce-Back Error

As already addressed in section 6.5, the calculation of the tangential boundary velocity by utilizing the non-equilibrium bounce-back relation along a FDVM link is an approximation, which reads in case of D2Q9 and a boundary normal to $\underline{e}_x$ for the compressible LBM (cf. section 4.3.1)

$$v_y = \frac{3}{2}\frac{f_2 - f_4}{\varrho} + O(\Delta t) \tag{7.33}$$

and for the incompressible LBM

$$v_y = \frac{3}{2}\frac{f_2 - f_4}{\varrho_0} + O(\Delta t) \tag{7.34}$$

The transformation to a moment basis according to equations 3.89 (cf. section 3.4.2) shows that the distributions f_2 and f_4 directly depend on the velocity v_y, hence an error in v_y has a respective impact on both. Illustrated in figure 7.9 for the compressible LBM, the error sums up over time, until in the specific case it reaches a final level at time step $t = 20,000 \cdot \Delta t$, which amounts to the same order as the normal velocity.

The remedy chosen in this work is to exploit the knowledge about the average state of the tangential velocity, which is in the present case a tangential velocity of $\overline{v}_y \equiv 0$. Accordingly, in each time step the tangential velocity is relaxed towards its average state. The implementation for the simulation evaluated below is listed in appendix A.10 and decreases the velocity v_y by a factor of 0.01 each time step. By this means the impact of an approaching pressure wave is estimated with an additional error of only 1 %, but the diverging of the tangential velocity is effectively suppressed, as shown in figure 7.10 for the velocity after 20,000 time steps. The error of this procedure is also discussed in section 6.5.

Table 7.5 shows the results of the 2D-2 benchmark for compressible LBM and both the relaxed and unrelaxed version for the finest grid resolution. The results improve significantly.

	Compressible LBM		
	$c_{D,\max}$	$c_{L,\max}$	St
Mid. Reference	3.2300	1.0000	0.3000
Reference range	3.2200 - 3.2400	0.9900 - 1.0100	0.2950 - 0.3050
h_1 unrelaxed	3.2689	0.9819	0.3033
$\Delta_{\text{mid}}(h_1)$ unrelaxed	3.9	1.8	0.66
h_1 relaxed	3.2295	1.0017	0.3033
$\Delta_{\text{mid}}(h_1)$ relaxed	0.05	0.17	0.66

Table 7.5: Results of the 2D-2 benchmark with relaxation of v_y on the outflow

The implementation for incompressible LBM, as noted in appendix A.15, unfortunately suffers from wiggles, which form the origin of spurious pressure peaks deranging the pressure

field. Although the simulation can be carried out, it leads to erroneous results. The issue could not yet be treated sufficiently.

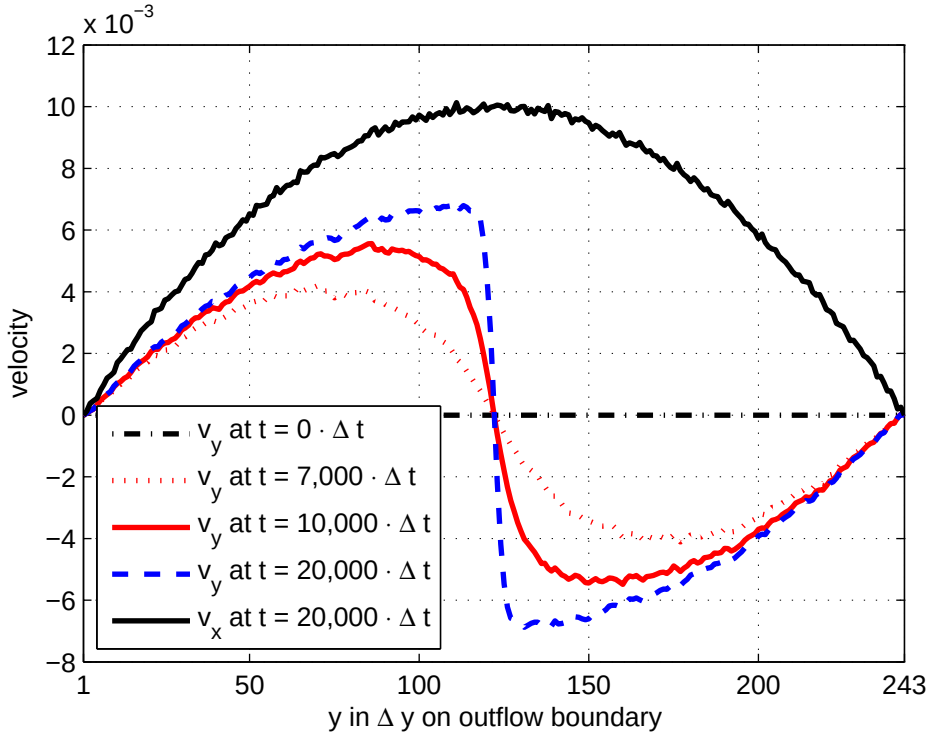

Figure 7.9: Evolution of tangential velocity on outflow boundary

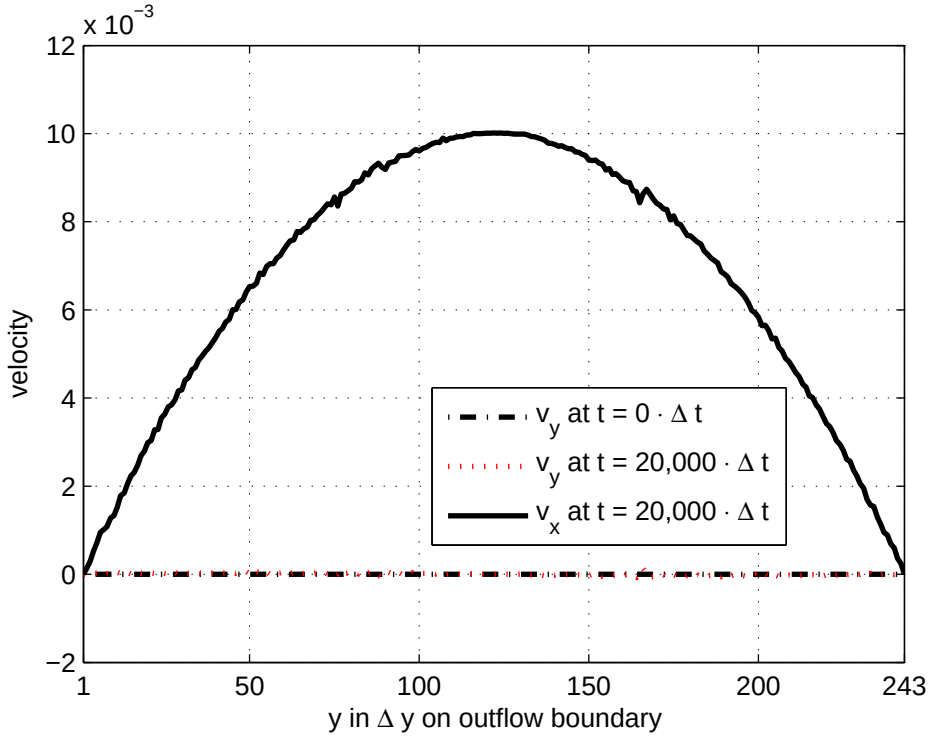

Figure 7.10: Tangential velocity on outflow boundary for relaxing scheme

Chapter 8

Impedance Boundary Conditions for LBM Shallow Water Model

In this chapter, the impedance boundary conditions of chapter 6 with the pressure adaption shown in chapter 7 are applied to a lattice Boltzmann shallow water model. Although the physical background is no longer strictly the same as in chapter 6, the equivalence of the underlying scheme allows for a transfer of the principle to the new application.

First, the shallow water model is introduced, followed by a description of the related state adapting impedance boundary condition. At last, the simulation of an open ended wave tank will illustrate the application.

The work below emerged from a collaboration with Christian Janßen, Hamburg University of Technology. The boundary conditions were implemented and simulated in the Efficient Lattice Boltzmann Environment (Elbe) for General Purpose Graphical Processing Unit (GPGPU) compute server [29].

8.1 Shallow Water Model for the LBM

As seen in chapter 3.4, the macroscopic behavior of the lattice Boltzmann scheme crucially depends on the choice of the equilibrium distribution. Zhou proposed a D2Q9 model [64], which recovers the Nonlinear Shallow Water (NSW) equations by setting a specific equilibrium distribution. The zeroth moment is interpreted as fluid height h:

$$h = \sum_i f_i, \tag{8.1}$$

$$h\underline{v} = \sum_i \underline{c} f_i. \tag{8.2}$$

The equilibrium is defined as

$$f_i^{(eq)}(h,\underline{v}) = \begin{cases} h - \frac{5}{6}\frac{gh^2}{c^2} - \frac{2}{3}\frac{h\underline{v}^2}{c^2} & \forall i = 0 \\ \frac{1}{6}\frac{gh^2}{c^2} + \frac{1}{3}\frac{h\left(\underline{v}\cdot\underline{\xi}_i\right)}{c^2} + \frac{1}{2}\frac{h\left(\underline{v}\cdot\underline{\xi}_i\right)^2}{c^4} - \frac{1}{6}\frac{h\underline{v}^2}{c^2} & \forall i \in \{1-4\} \\ \frac{1}{4}\left[\frac{1}{6}\frac{gh^2}{c^2} + \frac{1}{3}\frac{h\left(\underline{v}\cdot\underline{\xi}_i\right)}{c^2} + \frac{1}{2}\frac{h\left(\underline{v}\cdot\underline{\xi}_i\right)^2}{c^4} - \frac{1}{6}\frac{h\underline{v}^2}{c^2}\right] & \forall i \in \{5-8\} \end{cases}. \tag{8.3}$$

As a difference to the classical LBM, speed of sound is no longer constant, but depending on the waterline height:

$$c_s = \sqrt{hg}. \tag{8.4}$$

A specific characteristic of the model of Zhou is that it does not use non-dimensional quantities, but variables in specific SI units. This implies that not the unit propagation speed ξ is used, but the non-dimensional propagation speed c (cf. section 3.2.4), which varies with the scaling. The boundary conditions of chapter 6 have to be adapted accordingly.

Collision is done in the same way as for classical LBM, as seen from equation 3.23 and 3.87. The relaxation time is set by

$$\nu = \frac{c^2\ \Delta t}{6}\,(2\tau - 1) \tag{8.5}$$

with the kinematic viscosity $\nu = \mu/\varrho$. The Chapman-Enskog procedure finally leads to the macroscopic Nonlinear Shallow Water (NSW) equations (cf. Zhou [64]):

$$\frac{\partial}{\partial t}h \quad + \quad \nabla \cdot (h\underline{v}) = 0, \tag{8.6}$$

$$\frac{\partial}{\partial t}(h\underline{v}) \quad + \quad \nabla \cdot (h\underline{v} \otimes \underline{v}) = -\nabla\left(\frac{1}{2}gh^2\right) + \frac{\mu}{\varrho}\Delta(h\underline{v}) \tag{8.7}$$

with gravity acceleration g. External forces except gravity were not considered.

8.2 Impedance Boundary Condition

Below, the impedance boundary condition of section 6.3.1 with the boundary state adaption of chapter 7 is derived for the NSW model of Zhou. In equivalence to the compressible LBM, the impedance condition for the outflow in direction of $\underline{e}_x$ reads (cf. section 6.3):

$$-\left(h^{(n)}-h^{(n-1)}\right)c_s^2-\frac{1}{2}h^{(n)}\left(v_x^{(n)}-v_x^{(n-1)}\right)^2+\left(v_x^{(n)}-v_x^{(n-1)}\right)h^{(n)}c_s \;=\; 0. \tag{8.8}$$

The solution results in:

$$v_x^{(n)}=v_x^{(n-1)}-c_s\cdot\left(\sqrt{2\cdot\frac{h^{(n-1)}}{h^{(n)}}-1}-1\right). \tag{8.9}$$

Now equation 8.1 and equation 8.2 can be solved for $h^{(n)}$:

$$h^{(n)}=\frac{j_z}{c+v_x^{(n)}} \tag{8.10}$$

with

$$j_z:=\left[c\cdot(f_0+f_2+f_4+2\cdot(f_1+f_5+f_8))\right]^{(n)}. \tag{8.11}$$

Equation 8.10 inserted into equation 8.8 and solved for $v_x^{(n)}$ gains:

$$\begin{aligned} v_x^{(n)} \;=\; & v_x^{(n-1)}+\left(c_s^2\frac{h^{(n-1)}}{j_z}+c_s\right) \\ & -\sqrt{\left(c_s^2\frac{h^{(n-1)}}{j_z}+c_s\right)^2+2c_s^2\left(\frac{h^{(n-1)}}{j_z}\left(v_x^{(n-1)}+c\right)-1\right)}. \end{aligned} \tag{8.12}$$

Now the height can be computed according to equation 8.10. For the height adaption to a specific boundary value h_{BC}, the deviation $dh=h^{(n)}-h_{\mathrm{BC}}$ can be directly compared to a maximum adaption value $dh_{\max}$. After the adaption, v_x has to be reset according to equation 8.9. v_y can be set by the non-equilibrium bounce-back in tangential direction:

$$v_y=\frac{3}{2}\frac{c\,(f_2-f_4)}{h} \tag{8.13}$$

The unknown distributions are also set by using the non-equilibrium bounce-back rule:

$$f_3 \;=\; f_1-\frac{2h}{3c}v_x \tag{8.14}$$

$$f_7 \;=\; f_5-\frac{h}{6c}(v_x+v_y) \tag{8.15}$$

$$f_6 \;=\; f_8-\frac{h}{6c}(v_x-v_y) \tag{8.16}$$

An example code for the described boundary condition can be seen in appendix A.18.

8.3 Simulation and Results

As a test case, a wave tank simulation was chosen. The impedance boundary condition was applied to the outflow. The specific setup is intended to be used for simulation of periodic one-sided wave impact on the hull structure of a ship: The wave tank itself was 50 m in length and 12.5 m in width. The initial height of the waterline was 1 m. In the center of the wave tank, a column with a diameter of 2.5 m was placed. The resolution in space was set to $\Delta x = 0.098\ m$, the time step to $\Delta t = 0.0098\ s$, which results in a reference speed of $c = 10\ m/s$. On all solid boundaries, the two longitudinal sides, the bottom and the obstacle, bounce-back boundary conditions were applied. The value of the kinetic viscosity ν was set to water at a temperature of about $20°C$, $\nu_w = 10^{-6}\ m^2/s$.

At the beginning of the simulation, a first order piston wave maker (type KdV, cf. Guizien and Barthélemy [20]) on the left hand side produced a wave of height $h_w = 0.1\ m$ above the initial waterline.

The evolution of the wave can be seen in figure 8.1 and 8.2. The reflection of the wave was measured at time step $t = 400 \cdot \Delta t$ (cf. figure 8.2) at a distance of 37.5 m from the inflow. With a Zou and He type Dirichlet height boundary condition [65], the elevation was $h = 0.92444\ m$, a deviation of 7.6% from its reference level and in the same range as the original wave. The height for the impedance boundary condition with a maximum reflection level set to $dh_{\max} = 10^{-4}\ m$ amounted with $h = 0.99936\ m$ to a 0.06% deviation regarding the reference height.

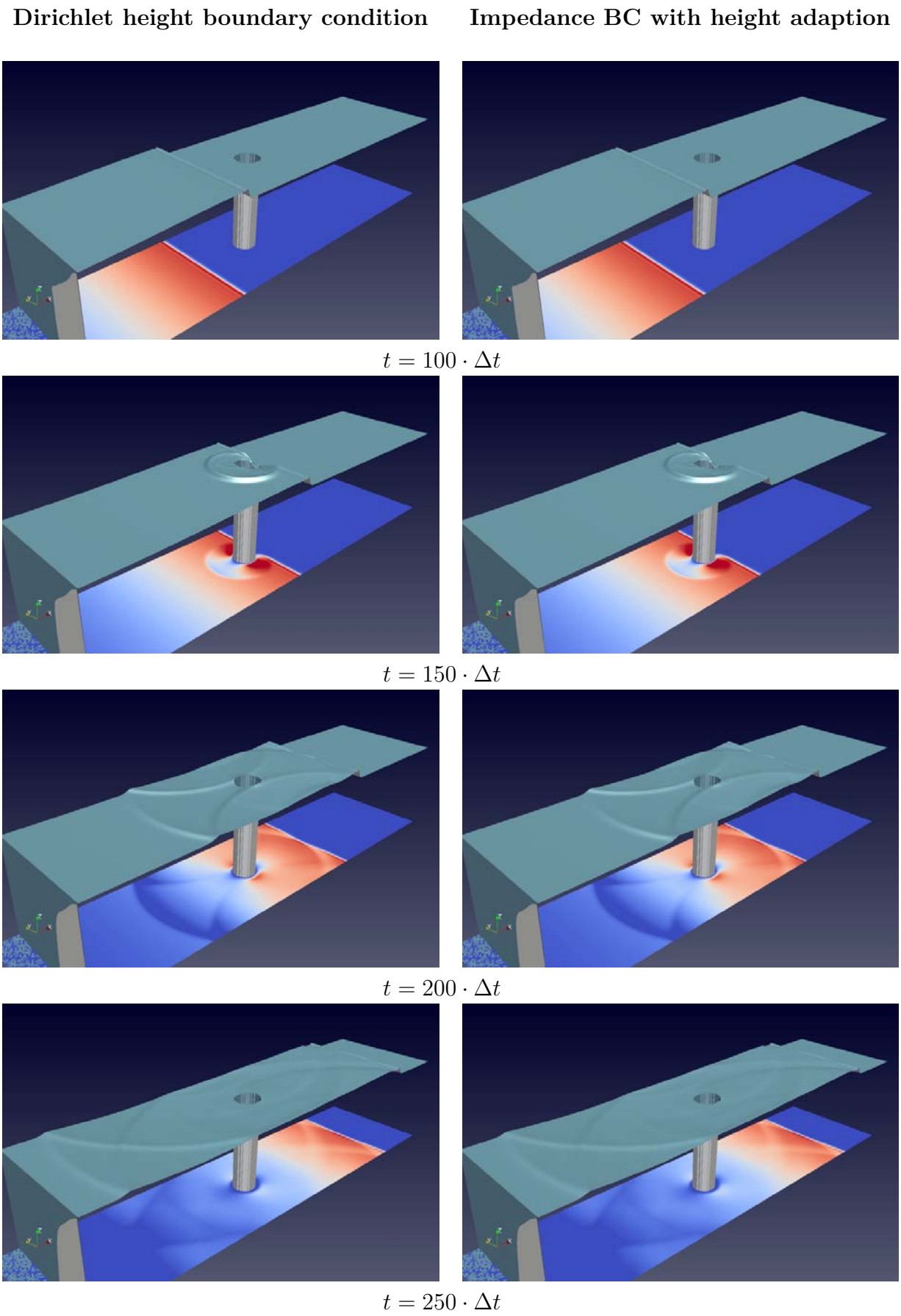

Figure 8.1: Wave tank simulation, color scale plot shows v_x velocity

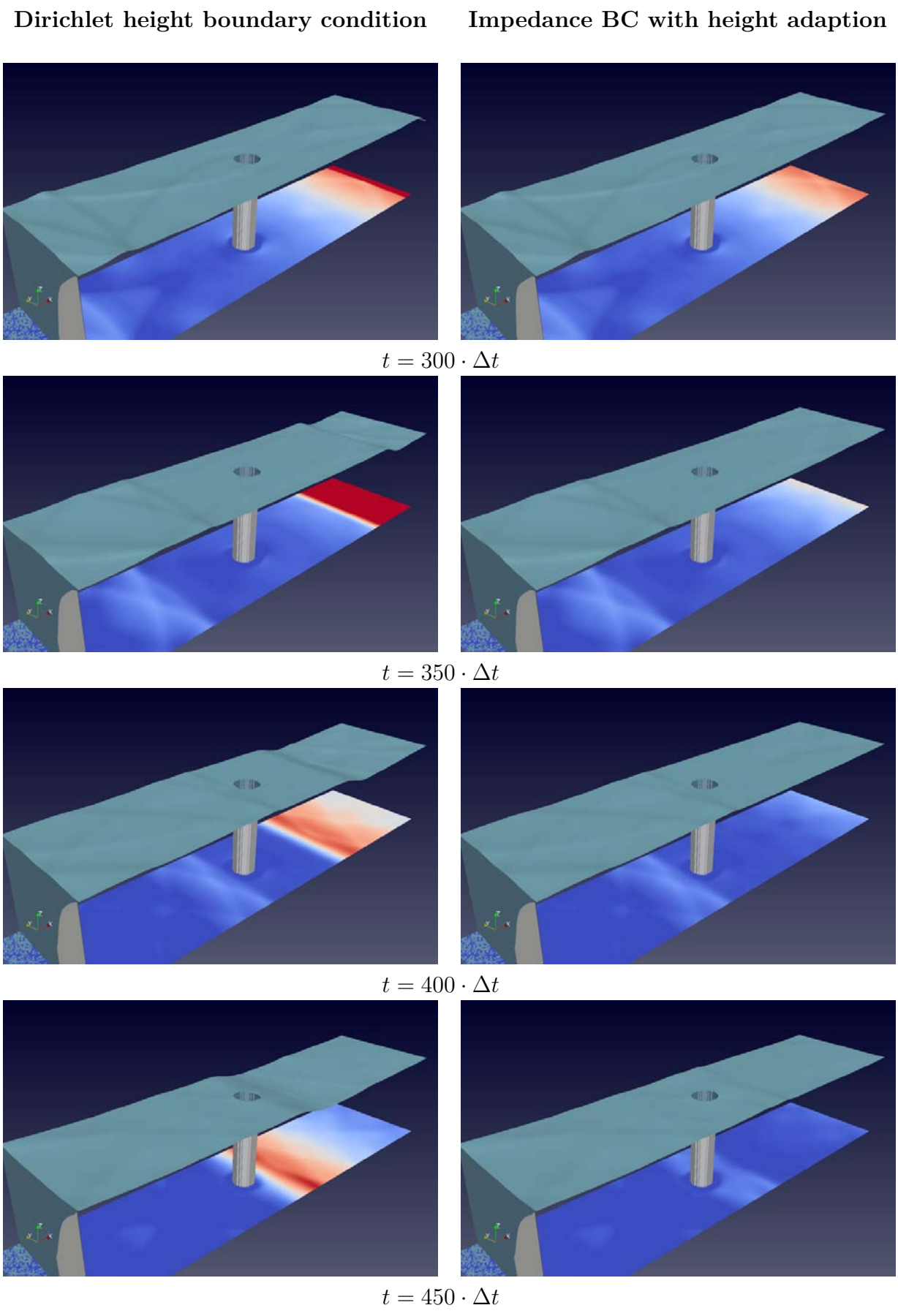

Figure 8.2: Wave tank simulation, color scale plot shows v_x velocity

Chapter 9

Conclusion and Outlook

The implementation of non-reflecting boundary conditions is always subject to a compromise. A problem with a free-field boundary condition can most exactly be approximated with minimal reflection, but a non-reflecting boundary condition with a constant boundary state is a contradiction in itself. Moreover, the simulation of a free field has to model the response of the outer area by suitable assumptions. The present work suggests to model an acoustic free field, i.e. to assume all pressure changes are propagating with the speed of sound. If the convection of pressure changes is of serious impact, one might better follow a different approach. Consequently, other disadvantages have to be accepted.

The approach of this work is based on the integral conservation of the momentum of sound pressure waves. This is equivalent to setting a specifically adapted acoustic impedance. The boundary conditions have a residual reflectivity which lies within the same range as those of characteristics based approaches. The key difference is that neither spatial nor time derivatives are required for their implementation. The time integration is based on an analytical model for the propagation of sound pressure waves, improving stability significantly compared to approaches using numerical integration. But first of all it allows for an implementation processing arbitrary directions of incoming pressure waves through the independence of spatial gradients. The implementation for suppression of perpendicular incoming pressure waves is based on an analytical solution of the underlying conditional equation. For the treatment of an arbitrary direction, an iterative method has been used.

Various aspects of the implementation have been elaborated, especially an extension for proper boundary state adaption. As a theoretical implication, this adaption results in a specific amount of reflection. Nevertheless, adverse effects can be limited based on a trade-off between convergence rate and reflectivity. A practical approach was shown to adjust the boundary conditions correspondingly.

All theoretical findings are supported by the results of several simulations. The boundary conditions were applied to an LBM model of the nonlinear shallow water equations, resulting in a significantly reduced amount of wave reflection.

However, there are a view open issues. Among the most important ones is the correct treatment of corners, respectively in three dimensions both for corners and edges. Up to now, this has been done by setting the additionally unknown distributions by an upstream interpolation of the state of neighboring nodes. This problem would be greatly simplified if a way was found to set the boundary condition not on a nodal basis, as it is done in this thesis, but in a link-wise manner, i.e. on basis of two opposing distribution directions. This would

also greatly simplify the programming complexity, since a single implementation could be used for various geometries. Another issue, not discussed at all in this thesis, is the implementation of inclined boundaries.

Further investigation concerning the linear approximation of the evolution of sound pressure in equation 6.6 on page 82 could be interesting. As it can be concluded from the simulation results, the linear model seems to have the main impact on the residual error of the approach. For the characteristic based method of section 5.2.1, a refined, e.g. quadratic model could also be an interesting approach: As seen from equation 5.26, the examined LBM implementation relies on the same relation.

As seen in section 6.3.3, an analytical solution of the underlying problem of the isotropic impedance boundary condition would result in a rather complex code. However, it is quite conceivable that the analysis of the significance of various terms of the conditional equation could result in an analytical approximation, which lies within the same range of error as the numerical method itself.

The boundary conditions were implemented in the context of the Lattice Boltzmann Method, but the basic physical principle is not restricted to the LBM. Eventually, an implementation of the approach could be attractive for classical Navier-Stokes based methods.

Appendix A

Code Examples

A.1 LODI Boundary Condition, 1D

The following code example is for a left hand side LODI boundary condition, as described in section 5.2.2.

```
csSq = c_s*c_s; // Constant: Speed of sound squared

drhodx = -0.5 * (3*lastRho[0] - 4.*lastRho[1] + lastRho[2]);
dvxdx  = -0.5 * (3*lastV[0]   - 4.*lastV[1]   + lastV[2]);

L1 = (lastV[0] - cs)*(csSq*drhodx - lastRho[0]*cs*dvxdx);

rho[0] = lastRho[0] - L1/(2*csSq);
v[0]   = lastV[0]   + L1/(2*cs*lastRho[0]);

f_1[0] = f_2[0] + rho[0]*v[0];

// Correct mass defect:
mD = f_0[0] + f_1[0] + f_2[0] - rho[0];
f_0[0] -= mD/3;
f_1[0] -= mD/3;
f_2[0] -= mD/3;
```

A.2 LODI Boundary Condition, 2D, Compressible LBM

The following code example is for a left hand side LODI free field boundary condition (face normal $\underline{e}_x$), as described in section 5.2.3.1. The implementation is for the compressible LB method.

```
// Constants:
c1o6     = 1/6;
c2o3     = 2/3;
cs       = 1/sqrt(3);
csSq     = 1/3;
c1oCsSq2 = 1.5;
c1o2cs   = 0.5*sqrt(3);

// Position at left boundary:
x = 0;

for_each node y {
  // Compute derivatives:
  drhodx = -0.5 * (3*lastRho[x][y] - 4*lastRho[x+1][y]
                   + lastRho[x+2][y]);
  dvdx   = -0.5 * (3*lastV_x[x][y] - 4*lastV_x[x+1][y]
                   + lastV_x[x+2][y]);
  dvdx   = -0.5 * (3*lastV_y[x][y] - 4*lastV_y[x+1][y]
                   + lastV_y[x+2][y]);

  // Compute wave amplitudes:
  L1 = (lastV_x[x][y] - cs) * (csSq*drhodx - lastRho[x][y]*cs*dvxdx);
  L2 =  lastV_x[x][y]*dvydx;

  // Compute solution of LODI equations:
  rho[y] = lastRho[x][y] - c1oCsSq2*L1;
  vx[y]  = lastV_x[x][y] + c1o2cs*L1/lastRho[x][y];
  vy[y]  = lastV_y[x][y] - L2;

  // Set unknown distributions by non-equilibrium bounce-back:
  f_1[y] = f_3[y] + c2o3*rho[y]*vx[y];
  f_5[y] = f_7[y] + c1o6*rho[y]*(vx[y] + vy[y]);
  f_8[y] = f_6[y] + c1o6*rho[y]*(vx[y] - vy[y]);
}
```

A.3 LODI Boundary Condition, 2D, Incompressible LBM

The following code example is for the incompressible LBM and a left hand side LODI free field boundary condition (face normal $\underline{e}_x$), as described in section 5.2.3.2. It is assumed that $\varrho_0 \equiv 1$.

```
// Constants:
c1o6       = 1/6;
c2o3       = 2/3;
cs         = 1/sqrt(3);
csSq       = 1/3;
c1oCsSq2   = 1.5;
c1o2csrho0 = 0.5*sqrt(3);

// Position at left boundary:
x = 0;

for_each node y {
  // Compute derivatives:
  drhodx = -0.5 * (3*lastRho[x][y] - 4*lastRho[x+1][y]
                   + lastRho[x+2][y]);
  dvxdx  = -0.5 * (3*lastV_x[x][y] - 4*lastV_x[x+1][y]
                   + lastV_x[x+2][y]);
  dvydx  = -0.5 * (3*lastV_y[x][y] - 4*lastV_y[x+1][y]
                   + lastV_y[x+2][y]);

  // Compute wave amplitudes:
  L1 = (lastV_x[x][y] - cs) * (csSq*drhodx - cs*dvxdx);
  L2 =  lastV_x[x][y]*dvydx;

  // Compute solution of LODI equations:
  rho[y] = lastRho[x][y] - c1oCsSq2*L1;
  vx[y]  = lastV_x[x][y] + c1o2csrho0*L1;
  vy[y]  = lastV_y[x][y] - L2;

  // Set unknown distributions by non-equilibrium bounce-back:
  f_1[y] = f_3[y] + c2o3*vx[y];
  f_5[y] = f_7[y] + c1o6*(vx[y] + vy[y]);
  f_8[y] = f_6[y] + c1o6*(vx[y] - vy[y]);
}
```

A.4 Impedance Boundary Condition, 1D

The following code example is for a left hand side impedance boundary condition, as described in section 6.2.

```
csSq = c_s*c_s; // Constant: Speed of sound squared

rhoZ = f_0[0] + 2*f_2[0];
rOrz = rho[0]/rhoZ;
tmp  = csSq*rOrz + c_s;

v[0] = v[0] - tmp + sqrt(tmp*tmp - 2*csSq*(rOrz*(v[0] - 1) + 1));

f_1[0] = (v[0]*f_0[0] + (1 + v[0])*f_2[0]) / (1 - v[0]);
rho    = f_0[0] + f_1[0] + f_2[0];
```

A.5 Impedance BC, Fixed Reference Level, 1D

The following code example is for a left hand side impedance boundary condition, as described in section 6.2, for a fixed reference level $\varrho 0$ and v_0 from initialization.

```
csSq = c_s*c_s; // Constant: Speed of sound squared

rhoZ = f_0[0] + 2*f_2[0];
rOrz = rho_0/rhoZ;
tmp  = csSq*rOrz + c_s;

v[0] = v_0 - tmp + sqrt(tmp*tmp - 2*csSq*(rOrz*(v_0 - 1) + 1));

f_1[0] = (v[0]*f_0[0] + (1 + v[0])*f_2[0]) / (1 - v[0]);
rho    = f_0[0] + f_1[0] + f_2[0];
```

A.6 Impedance BC, 2D, Compressible, Adaption in Normal Direction

This code example implements a left hand side impedance free field boundary condition (face normal $\underline{e}_x$) for the compressible LBM, as described in section 6.3.1.

```
// Constants:
c1o6 = 1/6;
c2o3 = 2/3;
cs   = 1/sqrt(3);
csSq = 1/3;

// Position at left boundary:
for_each node {
  // Compute solution of impedance condition:
  rhoZ     = f_0 + f_2 + f_4 + 2*(f_3 + f_6 + f_7);
  rhoOrhoZ = lastRho/rhoZ;
  temp     = cs + csSq*rhoOrhoZ;

  vx  = lastV_x - temp
        + sqrt(temp*temp - 2*csSq*(rhoOrhoZ*(lastV_x - 1) + 1));
  rho = rhoZ/(1 - vx);

  // Set y-velocity with non-equilibrium bounce-back:
  vy  = 1.5*(f_2 - f_4)/rho;

  // Set unknown distributions by non-equilibrium bounce-back:
  f_1 = f_3 + c2o3*rho*vx;
  f_5 = f_7 + c1o6*rho*(vx + vy);
  f_8 = f_6 + c1o6*rho*(vx - vy);
}
```

A.7 Impedance BC, 2D, Compressible, Adaption in Normal Direction, Fixed Reference Level

The code example is for a left hand side impedance free field boundary condition (face normal $\underline{e}_x$) with fixed reference level $v_{x,0}$ and ϱ_0, as described in section 6.3.2. ϱ_0 is supposed to be normalized to 1.

```
// Constants:
c1o6 = 1/6;
c2o3 = 2/3;
cs   = 1/sqrt(3);
csSq = 1/3;

// Position at left boundary:
for_each node y {
  // vx_0[y] and rho_0 are supposed to be
  // preset over whole simulation!

  // Compute solution of impedance condition:
  rhoZ      = f_0[y] + f_2[y] + f_4[y] + 2*(f_3[y] + f_6[y] + f_7[y]);
  rho0rhoZ = 1/rhoZ;
  temp      = cs + csSq*rho0rhoZ;

  vx[y]  = vx_0[y] - temp
         + sqrt(temp*temp - 2*csSq*(rho0rhoZ*(vx_0[y] - 1) + 1));
  rho[y] = rhoZ/(1 - vx[y]);

  // Set y-velocity with non-equilibrium bounce-back:
  vy[y]  = 1.5*(f_2[y] - f_4[y])/rho[y];

  // Set unknown distributions by non-equilibrium bounce-back:
  f_1[y] = f_3[y] + c2o3*rho[y]*vx[y];
  f_5[y] = f_7[y] + c1o6*rho[y]*(vx[y] + vy[y]);
  f_8[y] = f_6[y] + c1o6*rho[y]*(vx[y] - vy[y]);
}
```

A.8 Impedance BC, 2D, Compressible, Full Adaption

The following code example implements the isotropic impedance free field boundary condition of section 6.3.3 for the compressible LBM and a left hand side boundary.

```
// Constants:
c1o6 = 1/6;
c2o3 = 2/3;
cs   = 1/sqrt(3);
csSq = 1/3;

// Maximum number of iterations for Newton's method:
maxIter = 50;

// Position at left boundary:
for_each node {
  // Compute solution of 1D impedance condition:
  rhoZ     = f_0 + f_2 + f_4 + 2*(f_3 + f_6 + f_7);
  rhoZSq   = rhoZ*rhoZ;
  rhoOrhoZ = lastRho/rhoZ;
  temp     = cs + csSq*rhoOrhoZ;

  vx = lastV_x - temp
       + sqrt(temp*temp - 2*csSq*(rhoOrhoZ*(lastV_x - 1) + 1));

  // Full adaption of impedance ...
  temp    = 1.5*(f_2 - f_4);
  vyOldSq = lastV_y*lastV_y;
  lVxM1   = lastV_x - 1;

  // ... with Newton's method:
  for(iter = 0; iter < maxIter; iter++) {
      vxM1  = vx - 1;

      // Compute vy:
      vy  = -temp/rhoZ*vxM1;
      dvx = vx - lastV_x;
      dvy = vy - lastV_y;

      signdVx = sign(dvx); // Either +1 or -1
      dv_abs  = sqrt(dvx*dvx + dvy*dvy);

      c1 = rhoZSq*(  (csSq + 0.5*(lVxM1*lVxM1 - vxM1*vxM1 + vyOldSq
                     - vy*vy))*dv_abs
                   - (dvx*lVxM1 + lastV_y*dvy)*cs*signdVx  );

      if(abs(c1) < eps) break;

      c2 = vxM1*dv_abs*( vxM1*(temp*(0.5*vxM1*temp + lastV_y*rhoZ)
```

```
                                    + csSq*lastRho*rhoZ)
                            + (csSq + 0.5*(dvx*dvx + vyOldSq)
                            + signdVx*dv_abs*cs)*rhoZSq );

      dvx = c2/c1;
      vx += dvx;

      if(fabs(dvx) < eps) break;
  }

  rho = rhoZ/(1 - vx);

  // Set y-velocity with non-equilibrium bounce-back:
  vy  = temp/rho;

  // Set unknown distributions by non-equilibrium bounce-back:
  f_1 = f_3 + c2o3*rho*vx;
  f_5 = f_7 + c1o6*rho*(vx + vy);
  f_8 = f_6 + c1o6*rho*(vx - vy);
}
```

A.9 Impedance BC, 2D, Compressible, Full Adaption, Fixed Reference Level

This code example implements the same boundary condition like in the previous section, but for a fixed reference level ϱ_0 and $v_{x,0}$, with $\varrho_0 \equiv 1$.

```
// Constants:
c1o6 = 1/6;
c2o3 = 2/3;
cs   = 1/sqrt(3);
csSq = 1/3;

// Maximum number of iterations for Newton's method:
maxIter = 50;

// Position at left boundary:
for_each node y {
  // Compute solution of 1D impedance condition:
  rhoZ     = f_0[y] + f_2[y] + f_4[y] + 2*(f_3[y] + f_6[y] + f_7[y]);
  rhoZSq   = rhoZ*rhoZ;
  rhoOrhoZ = 1/rhoZ;
  temp     = cs + csSq*rhoOrhoZ;

  vx[y]  = vx_0[y] - temp
         + sqrt(temp*temp - 2*csSq*(rhoOrhoZ*(vx_0[y] - 1) + 1));

```

```
21    // Full adaption of impedance ...
22    temp  = 1.5*(f_2[y] - f_4[y]);
23    vy0Sq = vy_0[y]*vy_0[y];
24    lVxM1 = vx_0[y] - 1;
25
26    // ... with Newton's method:
27    for(iter = 0; iter < maxIter; iter++) {
28        vxM1  = vx[y] - 1;
29
30        // Compute vy:
31        vy[y] = -temp/rhoZ*vxM1;
32        dvx   = vx[y] - vx_0[y];
33        dvy   = vy[y] - vy_0[y];
34
35        signdVx = sign(dvx); // Either +1 or -1
36        dv_abs  = sqrt(dvx*dvx + dvy*dvy);
37
38        c1 = rhoZSq*(  (csSq + 0.5*(lVxM1*lVxM1 - vxM1*vxM1 + vy0Sq
39                        - vy[y]*vy[y]))*dv_abs
40                     - (dvx*lVxM1 + vy_0[y]*dvy)*cs*signdVx  );
41
42        if(abs(c1) < eps) break;
43
44        c2 = vxM1*dv_abs*(  vxM1*(temp*(0.5*vxM1*temp + vy_0[y]*rhoZ)
45                                  + csSq*rhoZ)
46                          + (csSq + 0.5*(dvx*dvx + vy0Sq)
47                                  + signdVx*dv_abs*cs)*rhoZSq  );
48
49        dvx = c2/c1;
50        vx[y] += dvx;
51
52        if(fabs(dvx) < eps) break;
53    }
54
55    rho[y] = rhoZ/(1 - vx[y]);
56
57    // Set y-velocity with non-equilibrium bounce-back:
58    vy[y]  = temp/rho[y];
59
60    // Set unknown distributions by non-equilibrium bounce-back:
61    f_1[y] = f_3[y] + c2o3*rho[y]*vx[y];
62    f_5[y] = f_7[y] + c1o6*rho[y]*(vx[y] + vy[y]);
63    f_8[y] = f_6[y] + c1o6*rho[y]*(vx[y] - vy[y]);
64 }
```

A.10 Impedance BC, 2D, Compressible, Full Adaption with Relaxation, Right Hand Side

The following code example implements the isotropic impedance free field boundary condition of section 6.3.3 for the compressible LBM and a right hand side boundary. The tangential velocity is relaxed by the factor "rlx" towards zero.

```
// Constants:
c1o6 = 1/6;
c2o3 = 2/3;
cs   = 1/sqrt(3);
csSq = 1/3;

// Maximum number of iterations for Newton's method:
maxIter = 50;

// Relaxation factor for tangential velocity (1 \%):
rlx = 0.99;

// Position at left boundary:
for_each node {
  // Compute solution of 1D impedance condition:
  rhoZ     = f_0 + f_2 + f_4 + 2*(f_1 + f_5 + f_8);
  rhoZSq   = rhoZ*rhoZ;
  rhoOrhoZ = lastRho/rhoZ;
  temp     = cs + csSq*rhoOrhoZ;

  vx = lastV_x + temp
       - sqrt(temp*temp + 2*csSq*(rhoOrhoZ*(lastV_x + 1) - 1));

  // Full adaption of impedance ...
  temp    = 1.5*(f_2 - f_4);
  vyOldSq = lastV_y*lastV_y;
  lVxP1   = lastV_x + 1;

  // ... with Newton's method:
  for(iter = 0; iter < maxIter; iter++) {
      vxP1 = vx + 1;

      // Compute vy:
      vy  = temp/rhoZ*vxP1;
      dvx = vx - lastV_x;
      dvy = vy - lastV_y;

      signdVx = sign(dvx); // Either +1 or -1
      dv_abs  = sqrt(dvx*dvx + dvy*dvy);

      c1 = rhoZSq*(  (csSq + 0.5*(lVxP1*lVxP1 - vxP1*vxP1 + vyOldSq
```

```
42                          - vy*vy))*dv_abs
43                        - (dvx*lVxP1 + lastV_y*dvy)*cs*signdVx   );
44
45        if(abs(c1) < eps) break;
46
47        c2 = vxP1*dv_abs*( vxP1*(temp*(0.5*vxP1*temp - lastV_y*rhoZ)
48                                 - csSq*lastRho*rhoZ)
49                           + (csSq + 0.5*(dvx*dvx + vyOldSq)
50                           - signdVx*dv_abs*cs)*rhoZSq );
51
52        dvx = c2/c1;
53        vx += dvx;
54
55        if(fabs(dvx) < eps) break;
56    }
57    rho = rhoZ/(1 + vx);
58
59
60    // Set y-velocity with non-equilibrium bounce-back and relax error:
61    vy  = rlx*temp/rho;
62
63    // Set unknown distributions by non-equilibrium bounce-back:
64    f_3 = f_1 - c2o3*rho*vx;
65    f_7 = f_5 - c1o6*rho*(vx + vy);
66    f_6 = f_8 - c1o6*rho*(vx - vy);
67 }
```

A.11 Impedance BC, 2D, Incompressible, Adaption in Normal Direction

This code example implements a left hand side impedance free field boundary condition (face normal $\underline{e}_x$) for the incompressible LBM, as described in section 6.3.4. It is assumed that $\varrho_0 \equiv 1$.

```
// Constants:
c1o6 = 1/6;
c2o3 = 2/3;
cs   = 1/sqrt(3);
csSq = 1/3;

// Position at left boundary:
for_each node {
  // Compute solution of impedance condition:
  rhoZ = f_0 + f_2 + f_4 + 2*(f_3 + f_6 + f_7);
  temp = csSq + cs;

  vx  = lastV_x - temp
        + sqrt(temp*temp + 2*csSq*(lastRho - lastV_x - rhoZ));
  rho = rhoZ + vx;

  // Set y-velocity with non-equilibrium bounce-back:
  vy  = 1.5*(f_2 - f_4);

  // Set unknown distributions by non-equilibrium bounce-back:
  f_1 = f_3 + c2o3*vx;
  f_5 = f_7 + c1o6*(vx + vy);
  f_8 = f_6 + c1o6*(vx - vy);
}
```

A.12 Impedance BC, 2D, Incompressible, Adaption in Normal Direction, Fixed Reference Level

The code example below is for a left hand side impedance free field boundary condition (face normal $\underline{e}_x$) with fixed reference level $v_{x,0}$ and ϱ_0, for the incompressible LBM, as described in section 6.3.5. It is assumed that $\varrho_0 \equiv 1$.

```
// Constants:
c1o6 = 1/6;
c2o3 = 2/3;
cs   = 1/sqrt(3);
csSq = 1/3;

// Position at left boundary:
for_each node {
  // vx_0[y] and rho_0 = 1 are supposed to be
  //preset over whole simulation!

  // Compute solution of impedance condition:
  rhoZ = f_0[y] + f_2[y] + f_4[y] + 2*(f_3[y] + f_6[y] + f_7[y]);
  temp = csSq + cs;

  vx[y]  = vx_0[y] - temp
           + sqrt(temp*temp + 2*csSq*(1 - vx_0[y] - rhoZ));
  rho[y] = rhoZ + vx[y];

  // Set y-velocity with non-equilibrium bounce-back:
  vy[y]  = 1.5*(f_2[y] - f_4[y]);

  // Set unknown distributions by non-equilibrium bounce-back:
  f_1[y] = f_3[y] + c2o3*vx[y];
  f_5[y] = f_7[y] + c1o6*(vx[y] + vy[y]);
  f_8[y] = f_6[y] + c1o6*(vx[y] - vy[y]);
}
```

A.13 Impedance BC, 2D, Incompressible, Full Adaption

The following code example implements the isotropic impedance free field boundary condition of section 6.3.6 for the incompressible LBM and a left hand side boundary. ϱ_0 is assumed to be $\varrho_0 \equiv 1$.

```
// Constants:
c1o6 = 1/6;
c2o3 = 2/3;
cs   = 1/sqrt(3);
csSq = 1/3;

// Maximum number of iterations for Newton's method:
maxIter = 50;

// Position at left boundary:
for_each node {

  // Compute solution of 1D impedance condition:
  rhoZ = f_0 + f_2 + f_4 + 2*(f_3 + f_6 + f_7);
  temp = csSq + cs;

  vx = lastV_x - temp
       + sqrt(temp*temp + 2*csSq*(lastRho - lastV_x - rhoZ));

  // Set y-velocity with non-equilibrium bounce-back:
  vy = 1.5*(f_2 - f_4);

  // Full adaption of impedance ...
  dvy = vy - lastV_y;
  dvySq = dvy*dvy;

  // ... with Newton's method:
  if(abs(dvy) > eps) {
    for(iter = 0; iter < maxIter; iter++) {
      dvx = vx - lastV_x;
      dv_abs = sqrt(dvx*dvx + dvySq);
      signdVx = sign(dvx); // Either +1 or -1

      c1 = -((dv_abs + signdVx*cs)*dvx + csSq*dv_abs);

      if(fabs(c1) < eps) break;

      c2 = ( csSq*(rhoZ + vx - lastRho)
           + dv_abs*(signdVx*cs + 0.5*dv_abs) )*dv_abs;

      dvx = c2/c1;
```

```
      vx += dvx;

      if(fabs(dvx) < eps) break;
    }
  }

  rho = rhoZ + vx;

  // Set unknown distributions by non-equilibrium bounce-back:
  f_1 = f_3 + c2o3*vx;
  f_5 = f_7 + c1o6*(vx + vy);
  f_8 = f_6 + c1o6*(vx - vy);
}
```

A.14 Impedance BC, 2D, Incompressible, Full Adaption, Fixed Reference Level

This code example implements the same boundary condition like in the previous section A.13, but for a fixed reference level ϱ_0 and $v_{x,0}$, with $\varrho_0 \equiv 1$, according to section 6.3.6.

```
// Constants:
c1o6 = 1/6;
c2o3 = 2/3;
cs   = 1/sqrt(3);
csSq = 1/3;

// Maximum number of iterations for Newton's method:
maxIter = 50;

// Position at left boundary:
for_each node y {

  // Compute solution of impedance condition:
  rhoZ = f_0[y] + f_2[y] + f_4[y] + 2*(f_3[y] + f_6[y] + f_7[y]);
  temp = csSq + cs;

  vx[y] = vx_0[y] - temp
          + sqrt(temp*temp + 2*csSq*(1 - vx_0[y] - rhoZ));

  // Set y-velocity with non-equilibrium bounce-back:
  vy[y] = 1.5*(f_2[y] - f_4[y]);

  // Full adaption of impedance ...
  dvy = vy[y] - vy_0[y];
  dvySq = dvy*dvy;

  // ... with Newton's method:
```

```
  if(abs(dvy) > eps) {
    for(iter = 0; iter < maxIter; iter++) {
      dvx = vx[y] - vx_0[y];
      dv_abs = sqrt(dvx*dvx + dvySq);
      signdVx = sign(dvx); // Either +1 or -1

      c1 = -((dv_abs + signdVx*cs)*dvx + csSq*dv_abs);

      if(fabs(c1) < eps) break;

      c2 = ( csSq*(rhoZ + vx[y] - drho0[y])
           + dv_abs*(signdVx*cs + 0.5*dv_abs) )*dv_abs;

      dvx = c2/c1;
      vx[y] += dvx;

      if(fabs(dvx) < eps) break;
    }
  }

  rho[y] = rhoZ + vx[y];

  // Set unknown distributions by non-equilibrium bounce-back:
  f_1[y] = f_3[y] + c2o3*vx[y];
  f_5[y] = f_7[y] + c1o6*(vx[y] + vy[y]);
  f_8[y] = f_6[y] + c1o6*(vx[y] - vy[y]);
}
```

A.15 Impedance BC, 2D, Incompressible, Full Adaption with Relaxation, Right Hand Side

The following code example implements the isotropic impedance free field boundary condition of section 6.3.6 for the incompressible LBM and a right hand side boundary. The tangential velocity is relaxed by the factor "rlx" towards zero. ϱ_0 is assumed to be $\varrho_0 \equiv 1$.

```
// Constants:
c1o6 = 1/6;
c2o3 = 2/3;
cs   = 1/sqrt(3);
csSq = 1/3;

// Maximum number of iterations for Newton's method:
maxIter = 50;

// Relaxation factor for tangential velocity (1 \%):
rlx = 0.99;

```

```
// Position at left boundary:
for_each node {

  // Compute solution of 1D impedance condition:
  rhoZ = f_0 + f_2 + f_4 + 2*(f_1 + f_5 + f_8);
  temp = csSq + cs;

  vx = lastV_x + temp
       - sqrt(temp*temp + 2*csSq*(lastRho + lastV_x - rhoZ));

  // Set y-velocity with non-equilibrium bounce-back:
  vy = 1.5*(f_2 - f_4);

  // Full adaption of impedance ...
  dvy = vy - lastV_y;
  dvySq = dvy*dvy;

  // ... with Newton's method:
  if(abs(dvy) > eps) {
    for(iter = 0; iter < maxIter; iter++) {
      dvx = vx - lastV_x;
      dv_abs = sqrt(dvx*dvx + dvySq);
      signdVx = sign(dvx); // Either +1 or -1

      c1 = -((dv_abs - signdVx*cs)*dvx - csSq*dv_abs);

      if(fabs(c1) < eps) break;

      c2 = ( csSq*(rhoZ - vx - lastRho)
            + dv_abs*(0.5*dv_abs - signdVx*cs) )*dv_abs;

      dvx = c2/c1;
      vx += dvx;

      if(fabs(dvx) < eps) break;
    }
  }

  rho = rhoZ - vx;

  // Relax error of vy-velocity:
  vy *= rlx;

  // Set unknown distributions by non-equilibrium bounce-back:
  f_3 = f_1 - c2o3*vx;
  f_7 = f_5 - c1o6*(vx + vy);
  f_6 = f_8 - c1o6*(vx - vy);
}
```

A.16 Impedance Velocity BC, 2D, Compressible

The code example is for a left hand side impedance **velocity** boundary condition (face normal $\underline{e}_x$) with fixed reference level $v_{x,0}$ and ϱ_0, as described in section 6.3.1 and 7.1.1. ϱ_0 is supposed to be normalized to 1.

```
// Constants:
c1o6 = 1/6;
c2o3 = 2/3;
cs   = 1/sqrt(3);
csSq = 1/3;

// Maximum reflected desity:
dRhoMax = 1e-4;

// Position at left boundary:
for_each node y {
  // vx_0[y] and rho_0 are to be preset over whole simulation!

  // Compute solution of impedance condition:
  rhoZ      = f_0[y] + f_2[y] + f_4[y] + 2*(f_3[y] + f_6[y] + f_7[y]);
  rho0OrhoZ = 1/rhoZ;
  temp      = cs + csSq*rho0OrhoZ;

  vx[y]  = vx_0[y] - temp
         + sqrt(temp*temp - 2*csSq*(rho0OrhoZ*(vx_0[y] - 1) + 1));
  rho    = rhoZ/(1 - vx[y]);

  // Maximum speed adaption:
  vLowerLimit = 1 - rhoZ/(rho - dRhoMax);
  vUpperLimit = 1 - rhoZ/(rho + dRhoMax);

  // Adapt speed:
  if      ( vx_0[y] > vUpperLimit ) vx[y] = vUpperLimit;
  else if( vx_0[y] < vLowerLimit ) vx[y] = vLowerLimit;
  else                             vx[y] = vx_0[y];

  // Solve impedance condition for new reference level:
  temp   = vx[y] - vx_0[y];
  rho[y] = csSq/(csSq + temp*(0.5*temp + cs));

  // Set y-velocity with non-equilibrium bounce-back:
  vy[y]  = 1.5*(f_2[y] - f_4[y])/rho[y];

  // Set unknown distributions by non-equilibrium bounce-back:
  f_1[y] = f_3[y] + c2o3*rho[y]*vx[y];
  f_5[y] = f_7[y] + c1o6*rho[y]*(vx[y] + vy[y]);
  f_8[y] = f_6[y] + c1o6*rho[y]*(vx[y] - vy[y]);
}
```

A.17 Impedance Pressure BC, 2D, Compressible

The code example is for a right hand side impedance **pressure** boundary condition (face normal $-\underline{e}_x$) with fixed reference level $v_{x,0}$ and ϱ_{BC}, as described in section 6.3.1 and 7.2.1.

```
// Constants:
c1o6 = 1/6;
c2o3 = 2/3;
cs   = 1/sqrt(3);
csSq = 1/3;

// Maximum reflected desity:
dRhoMax = 1e-4;

// Position at left boundary:
for_each node y {
  // vx_0[y] and rho_BC are to be preset over whole simulation!

  // Compute solution of impedance condition:
  rhoZ = f_0[y] + f_2[y] + f_4[y] + 2*(f_1[y] + f_5[y] + f_8[y]);
  rhoBCoRhoZ = rho_BC/rhoZ;
  temp       = cs + csSq*rhoBCoRhoZ;

  vx[y] = vx_0[y] + temp
        - sqrt(temp*temp + 2*csSq*(rhoBCoRhoZ*(vx_0[y] + 1) - 1));

  // Compute free field density:
  rho[y] = rhoZ/(1 + vx[y]);

  // Adapt density (resp. pressure):
  dRho = rho[y] - rho_BC;
  if      ( dRho >  dRhoMax ) rho[y] -= dRhoMax;
  else if( dRho < -dRhoMax ) rho[y] += dRhoMax;
  else                       rho[y]  = rho_BC;

  // Solve impedance condition for new reference level:
  temp   = 1/rho[y];
  vx[y]  = vx_0[y] - cs*(sqrt(2*rho0*temp - 1) - 1);

  // Set y-velocity with non-equilibrium bounce-back:
  vy[y]  = 1.5*(f_2[y] - f_4[y])*temp;

  // Set unknown distributions by non-equilibrium bounce-back:
  f_3[y] = f_1[y] - c2o3*rho[y]*vx[y];
  f_7[y] = f_5[y] - c1o6*rho[y]*(vx[y] + vy[y]);
  f_6[y] = f_8[y] - c1o6*rho[y]*(vx[y] - vy[y]);
}
```

A.18 Impedance BC for Nonlinear Shallow Water LBM

Below, the impedance boundary condition was implemented for the Nonlinear Shallow Water model as described in section 8.2. h_0 specifies the desired target waterline height value.

```
// Propagation velocity:
c = e;

// Constants:
c1o6c = 1/(6*c);
c2o3c = 2/(3*c);

// Speed of sound for abs(dh/h_0) << 1:
cs   = sqrt(h_0 * g);
csSq = cs*cs;

// Maximum reflected wave height:
dhMax = 1e-4;

// Position at right boundary:
for_each node {
  // Compute solution of impedance condition:
  j_z = c*(f_0 + f_2 + f_4 + 2*(f_1 + f_5 + f_8));
  h0j_z = h/j_z;

  temp = cs + csSq*h0j_z;
  vx += temp - sqrt(temp*temp + 2*csSq*((vx + c)*h0j_z - 1));

  // Compute free field height:
  h = j_z/(c + vx);

  // Height adaption:
  temp = h;
  dh = h - h_0;
  if      ( dh > dhMax  )   h -= dhMax;
  else if( dh < -dhMax )   h += dhMax;
  else                      h  = h_0;

  // Adapt velocity to new height:
  vx -= cs*(sqrt(2*temp/h - 1) - 1);

  // Compute y-velocity (set to zero to avoid long-term error):
  vy = 1.5*(f_2 - f_4)*c/h;

  // Set unknown distributions by non-equilibrium bounce-back:
  f_3 = f_1 - c2o3c*h*vx;
  f_7 = f_5 - c1o6c*h*(vx + vy);
  f_6 = f_8 - c1o6c*h*(vx - vy);
}
```

Appendix B

Results 2D Pressure Wave Test Case, Impedance BCs

B.1 Compressible LBM, Resting Fluid

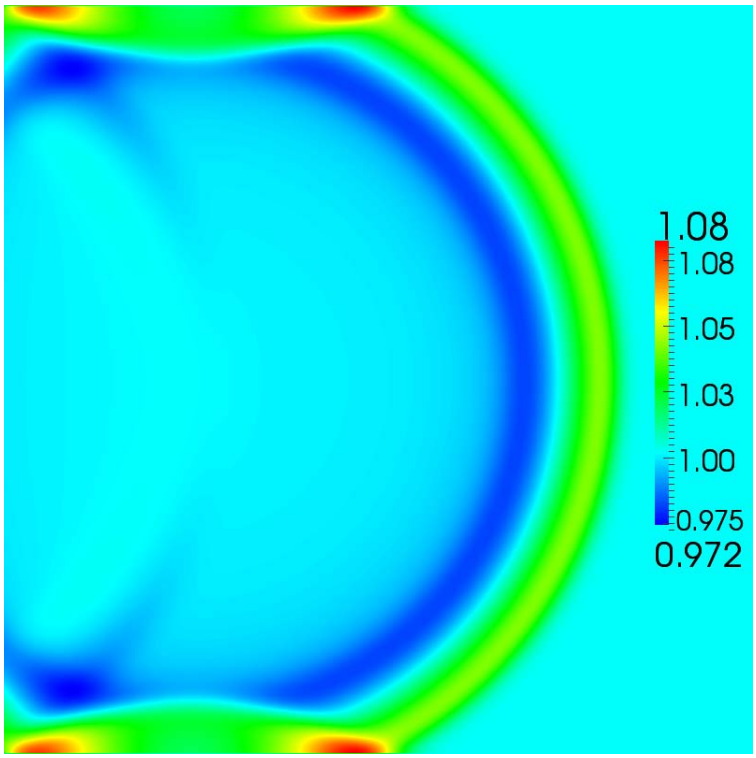

Figure B.1: Impedance free field BC, setup (a), density at $t = 700 \cdot \Delta t$

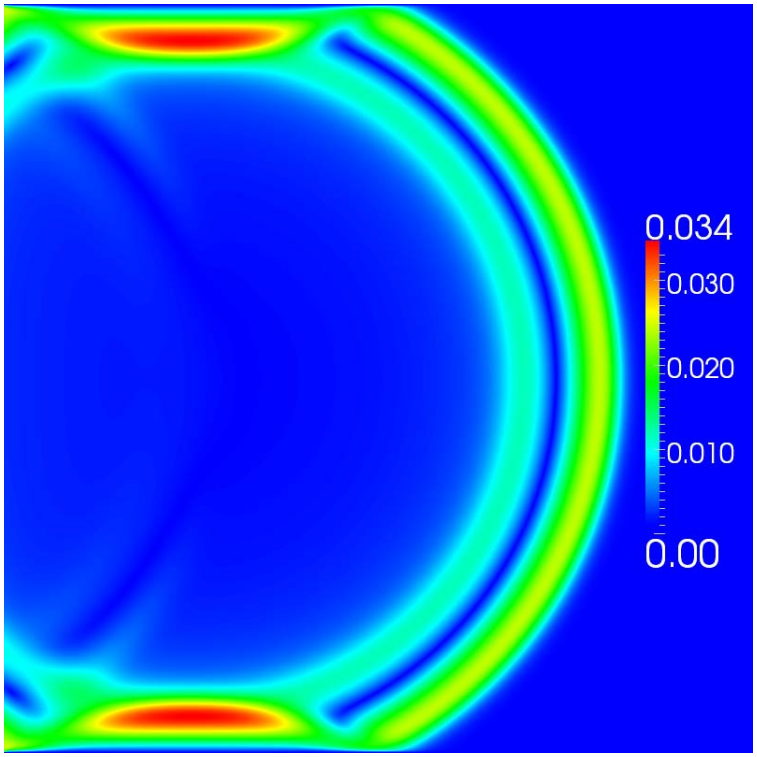

Figure B.2: Impedance free field BC, setup (a), absolute velocity at $t = 700 \cdot \Delta t$

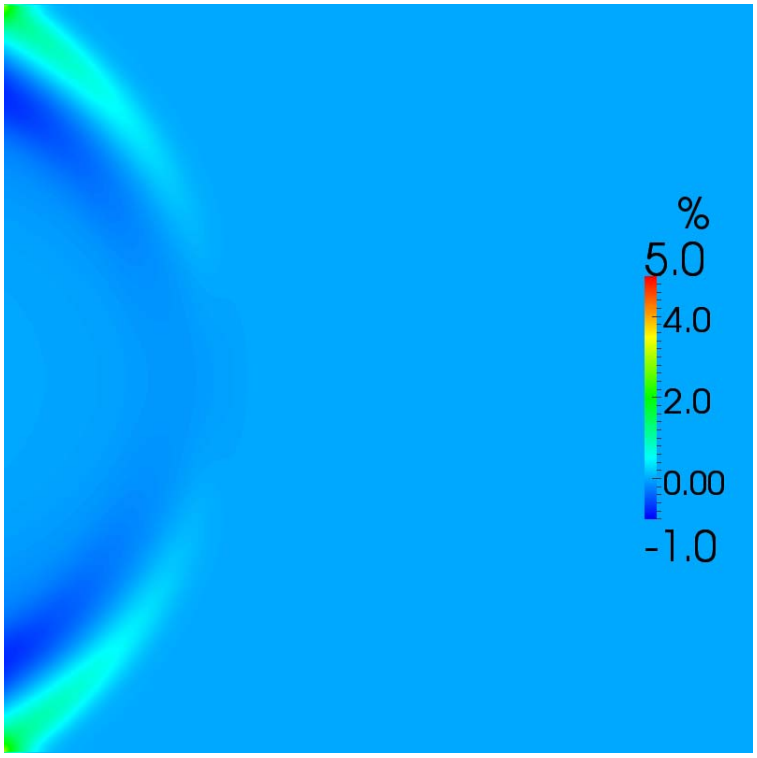

Figure B.3: Impedance free field BC, setup (a), relative density error in % at $t = 700 \cdot \Delta t$

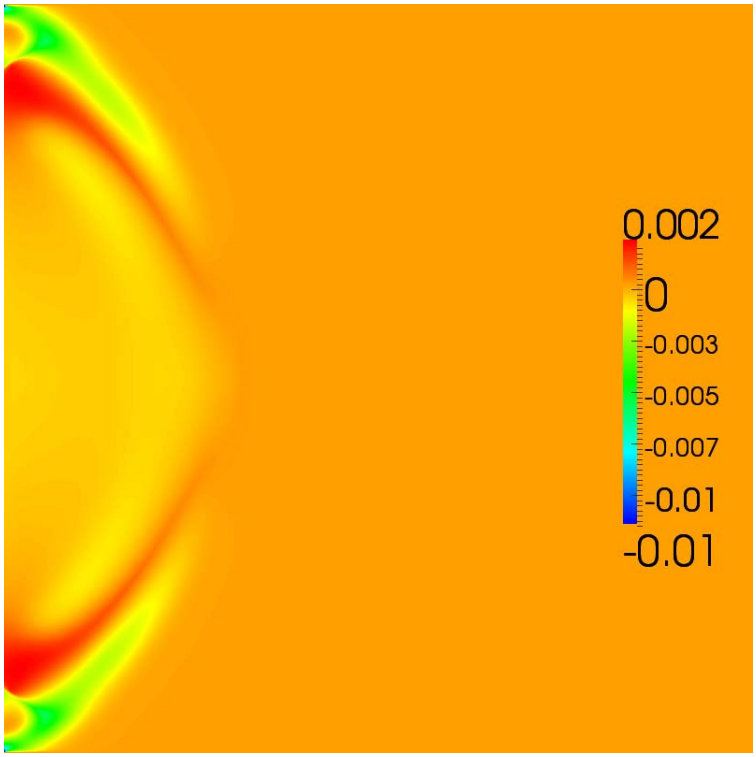

Figure B.4: Impedance free field BC, setup (a), absolute error of velocity error at $t = 700 \cdot \Delta t$

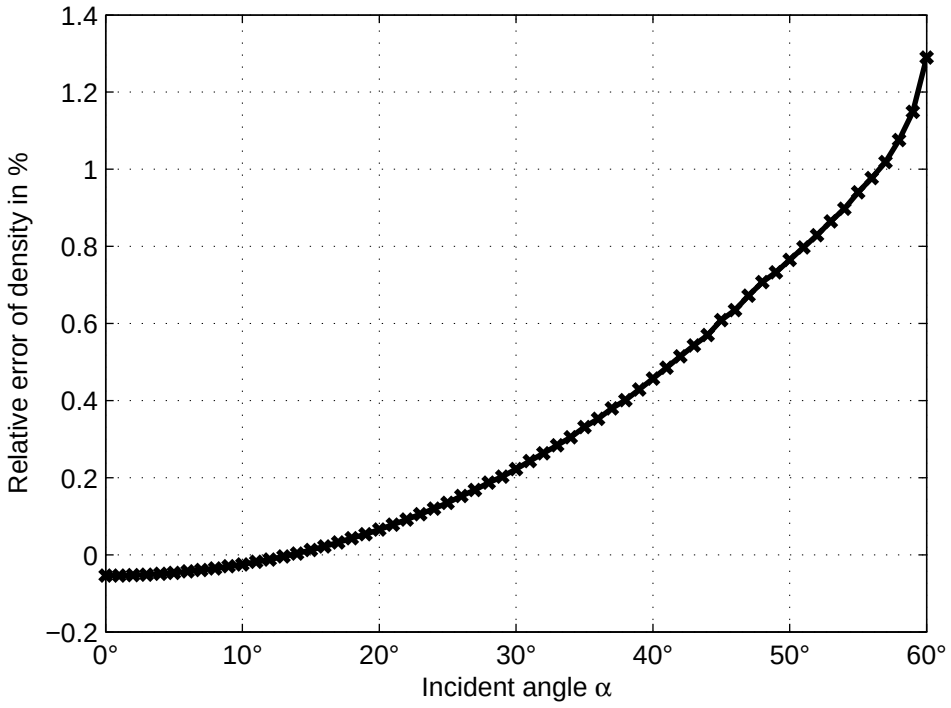

Figure B.5: Reflection over incident angle at $t = 700 \cdot \Delta t$

B.2 Compressible LBM, Parabolic Velocity Profile

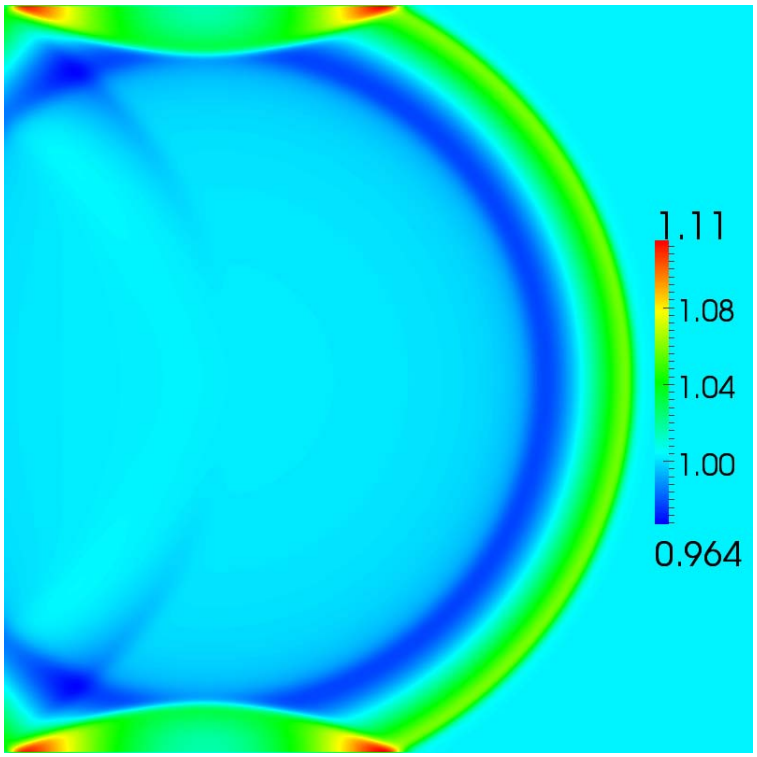

Figure B.6: Impedance free field BC, setup (b), density at $t = 700 \cdot \Delta t$

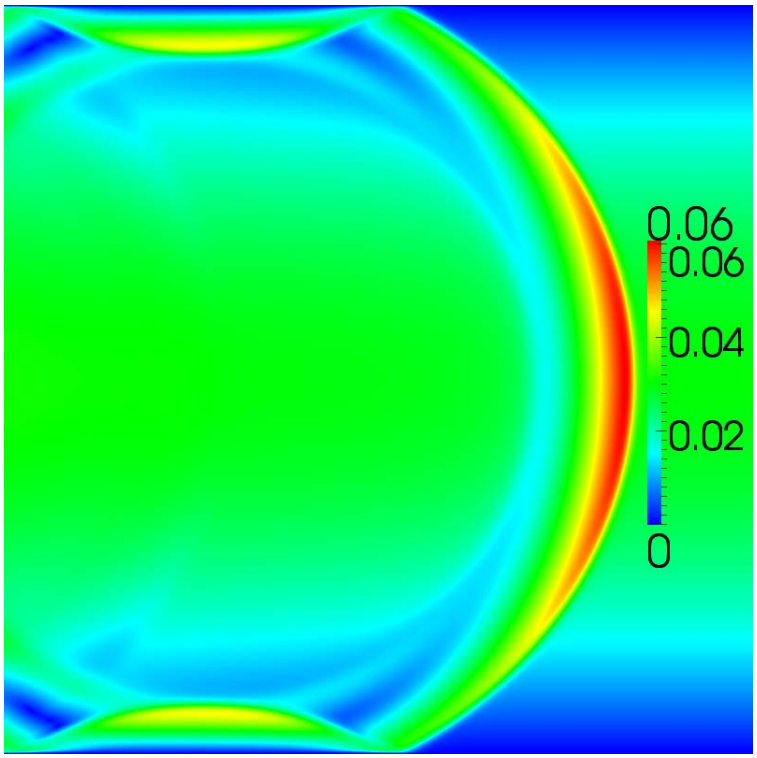

Figure B.7: Impedance free field BC, setup (b), absolute velocity at $t = 700 \cdot \Delta t$

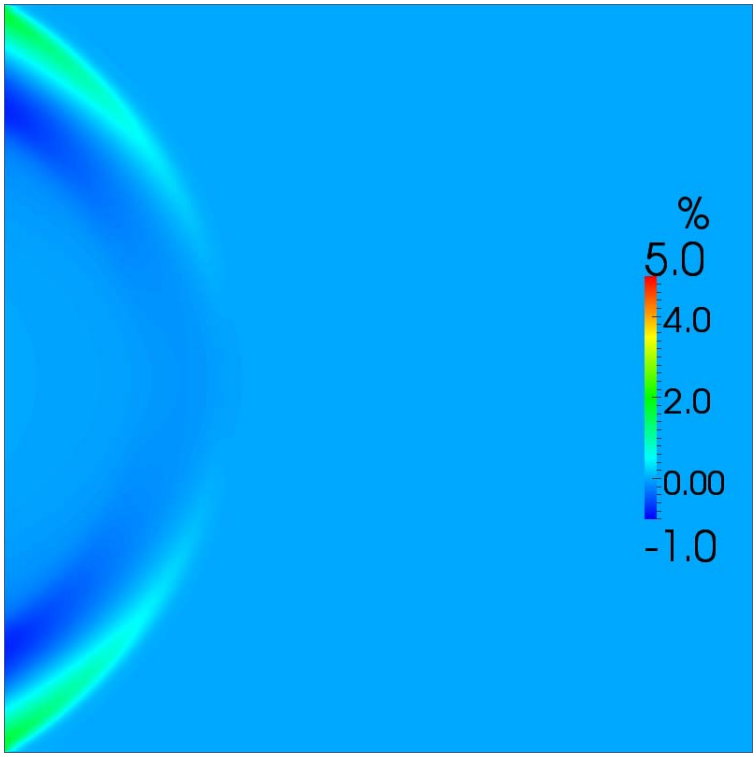

Figure B.8: Impedance free field BC, setup (b), relative density error in % at $t = 700 \cdot \Delta t$

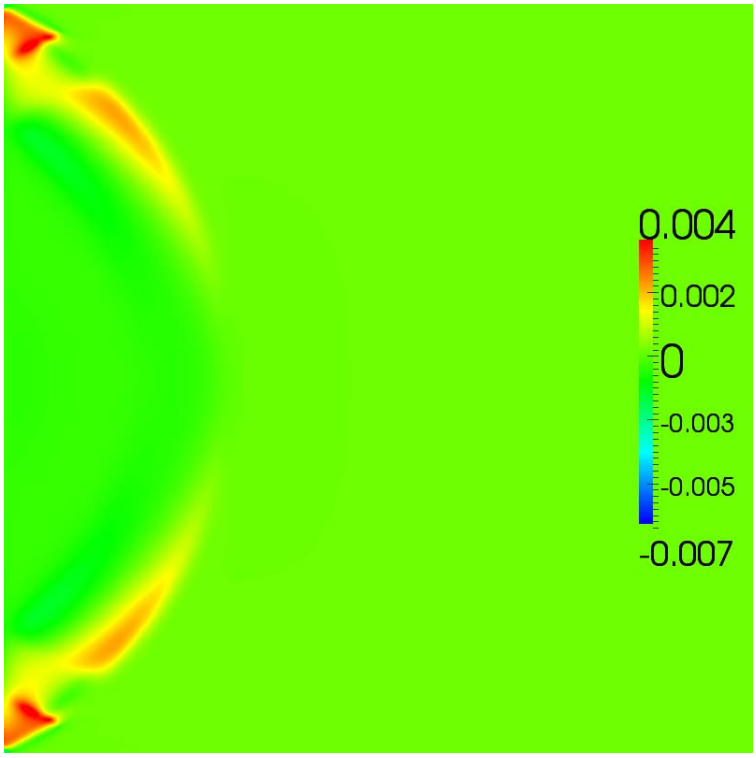

Figure B.9: Impedance free field BC, setup (b), absolute error of velocity error at $t = 700 \cdot \Delta t$

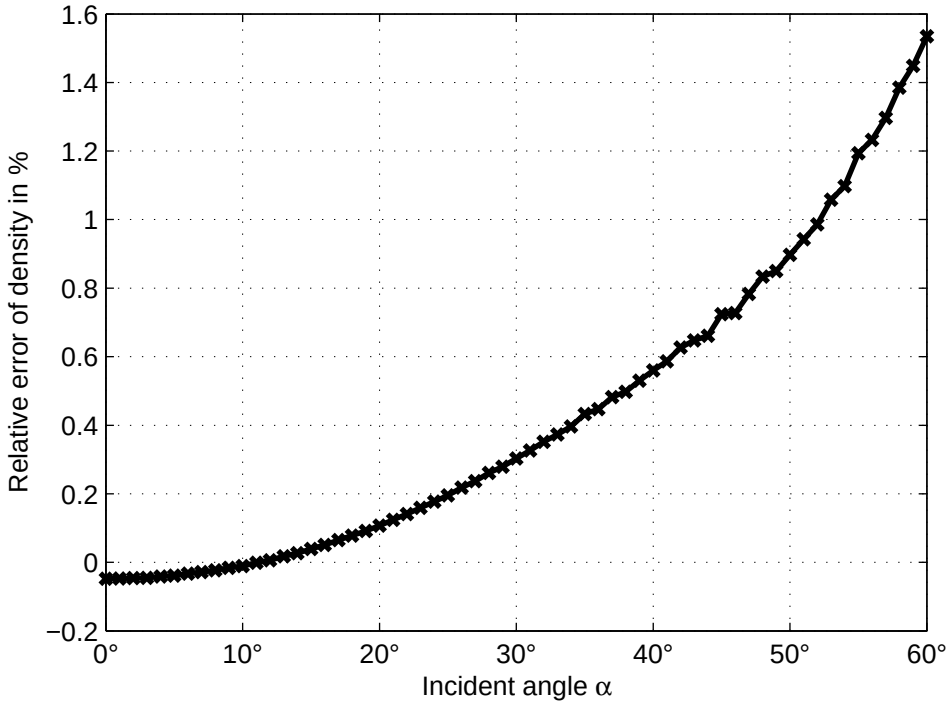

Figure B.10: Reflection over incident angle at $t = 700 \cdot \Delta t$

B.3 Compressible LBM, Fixed Reference Level, Resting Fluid

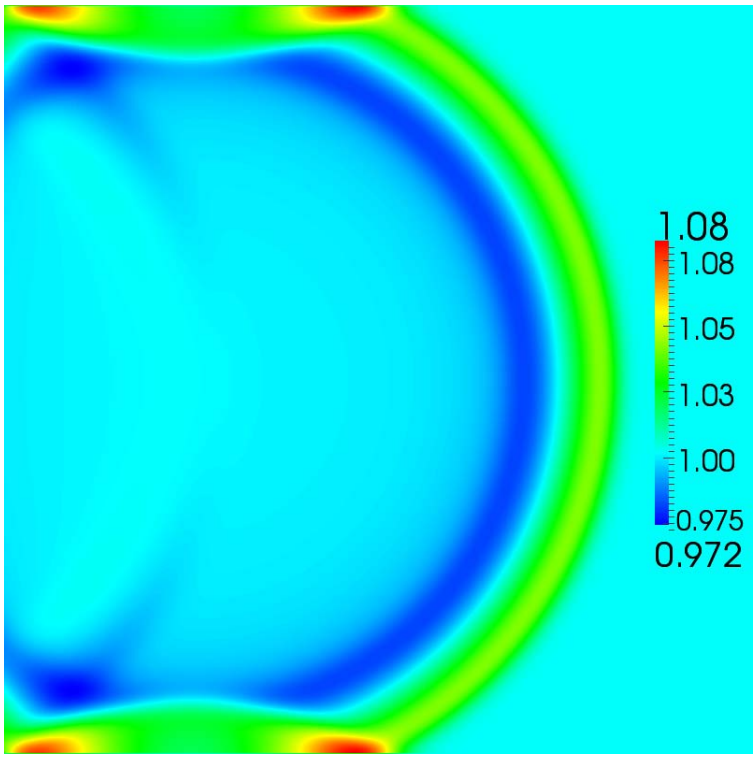

Figure B.11: Imp. fixed free field BC, setup (a), density at $t = 700 \cdot \Delta t$

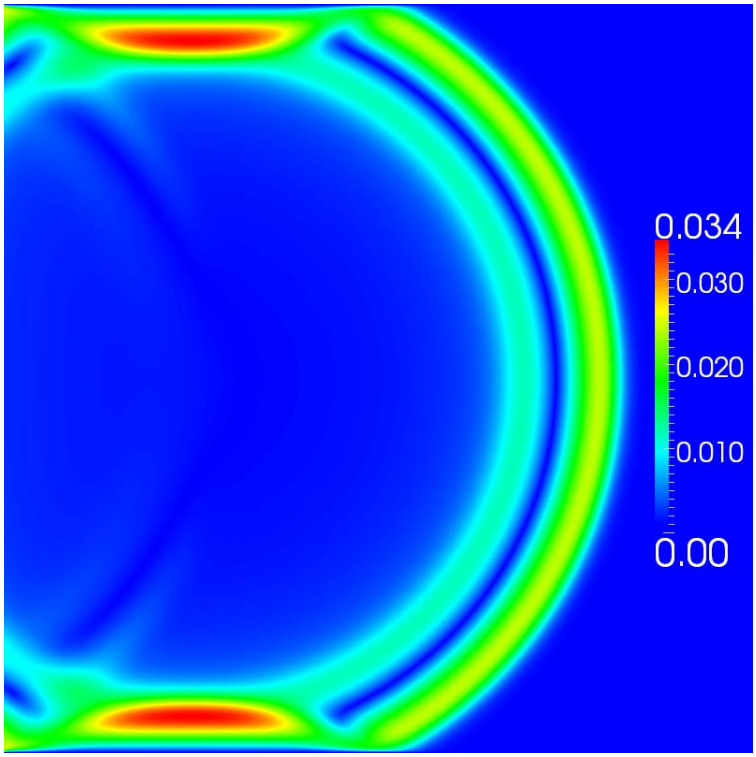

Figure B.12: Imp. fixed free field BC, setup (a), absolute velocity at $t = 700 \cdot \Delta t$

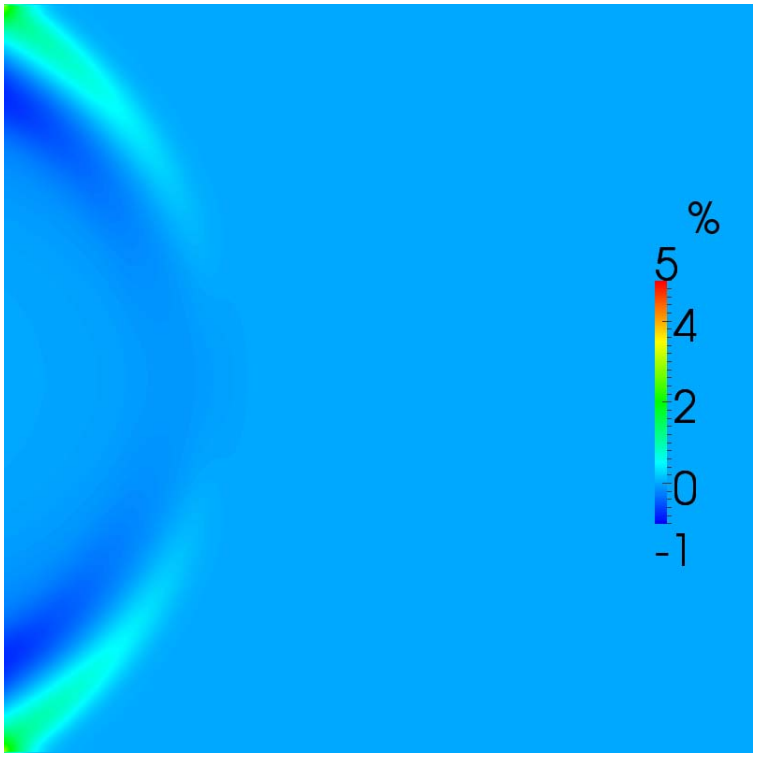

Figure B.13: Imp. fixed free field BC, setup (a), relative density error in % at $t = 700 \cdot \Delta t$

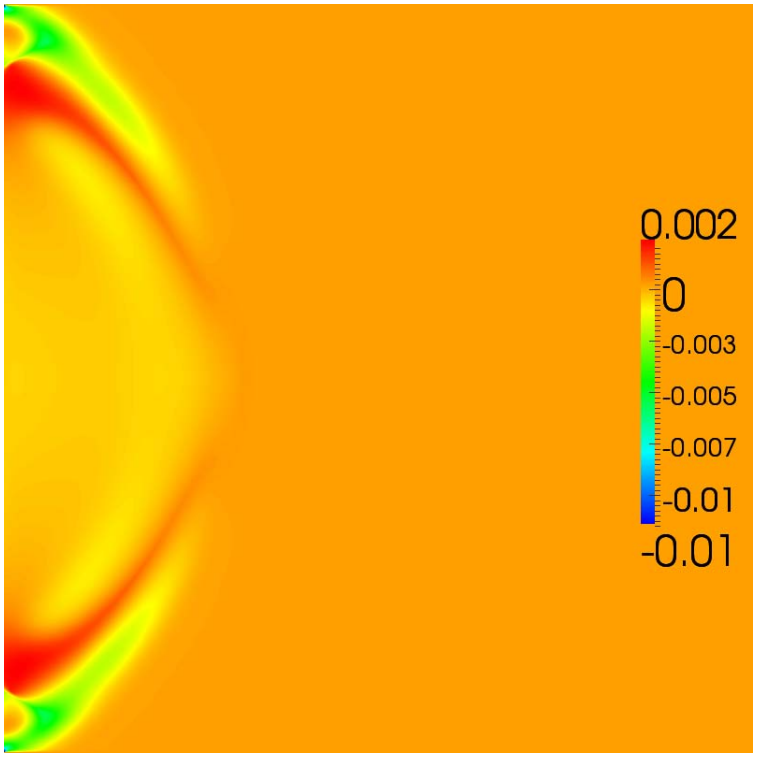

Figure B.14: Imp. fixed free field BC, setup (a), absolute error of velocity error at $t = 700 \cdot \Delta t$

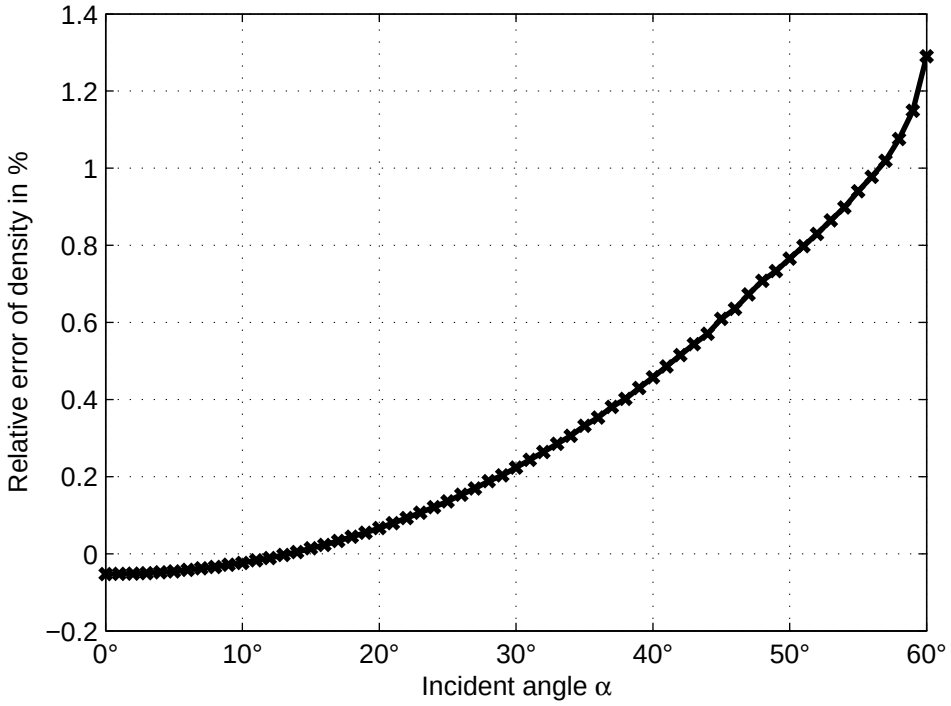

Figure B.15: Reflection over incident angle at $t = 700 \cdot \Delta t$

B.4 Compressible LBM, Fixed Reference Level, Parabolic Velocity Profile

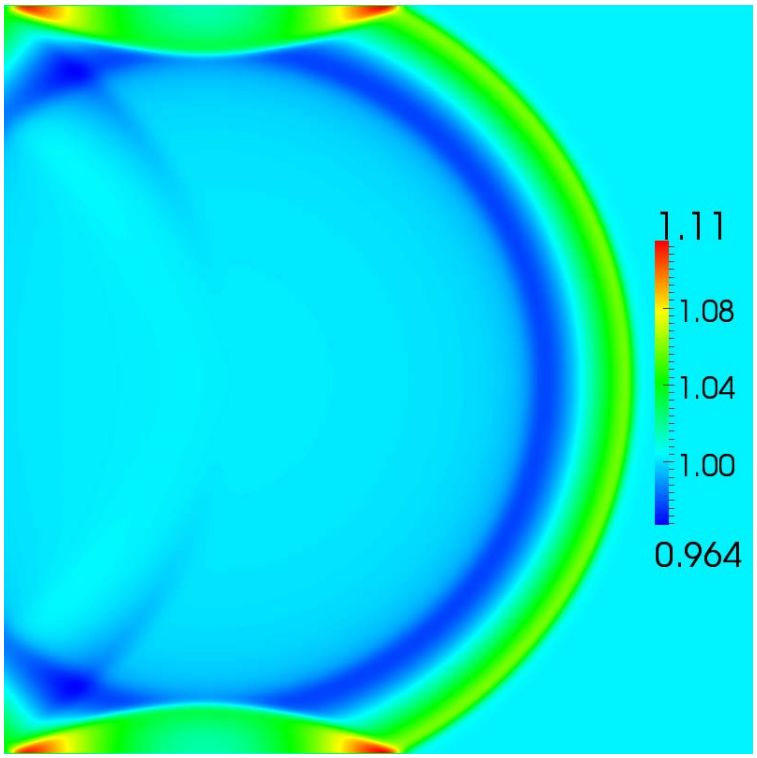

Figure B.16: Imp. fixed free field BC, setup (b), density at $t = 700 \cdot \Delta t$

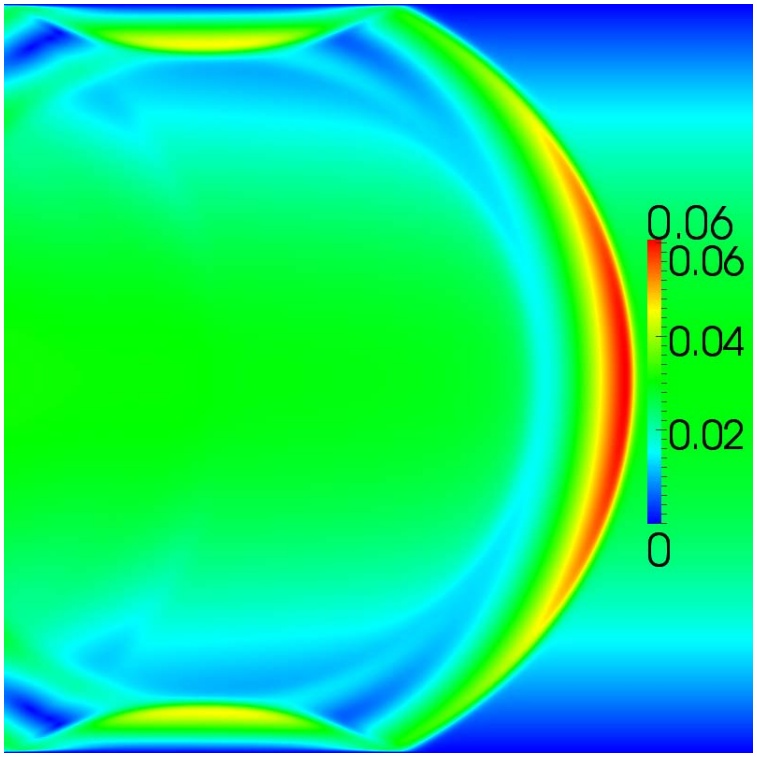

Figure B.17: Imp. fixed free field BC, setup (b), absolute velocity at $t = 700 \cdot \Delta t$

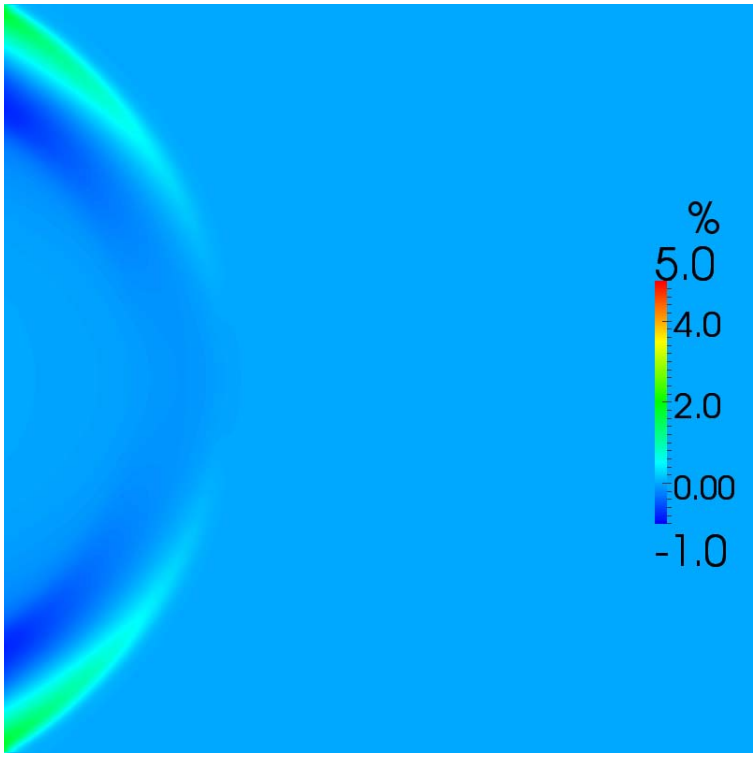

Figure B.18: Imp. fixed free field BC, setup (b), relative density error in % at $t = 700 \cdot \Delta t$

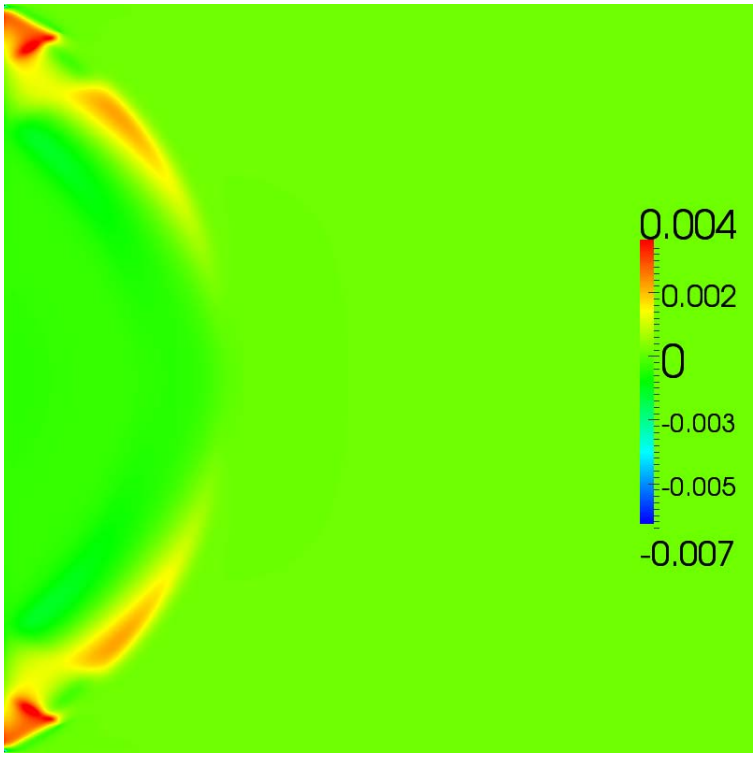

Figure B.19: Imp. fixed free field BC, setup (b), absolute error of velocity error at $t = 700 \cdot \Delta t$

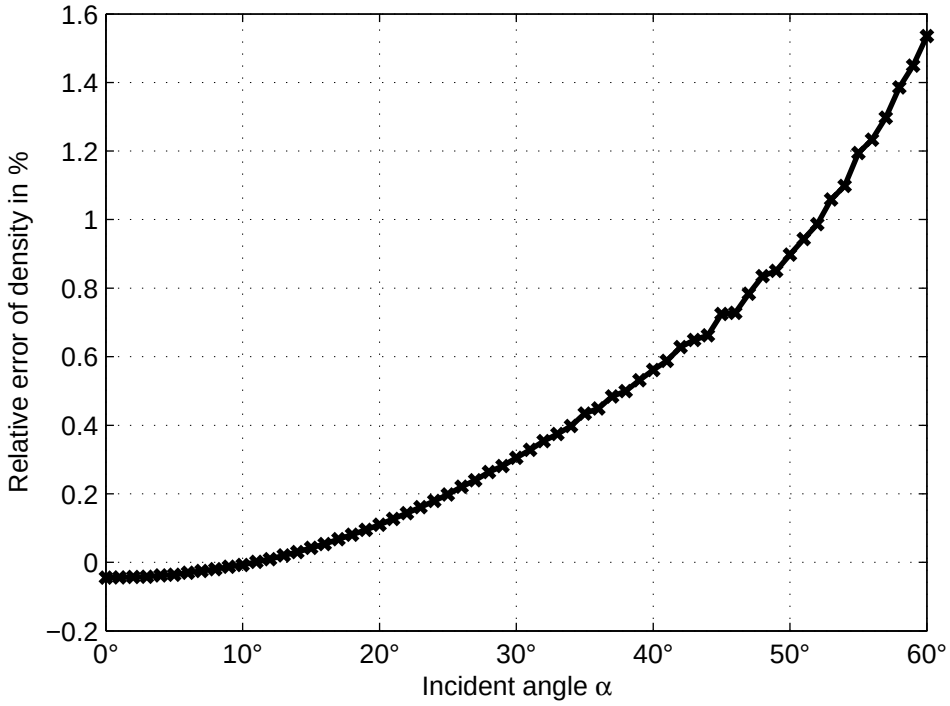

Figure B.20: Reflection over incident angle at $t = 700 \cdot \Delta t$

B.5 Incompressible LBM, Resting Fluid

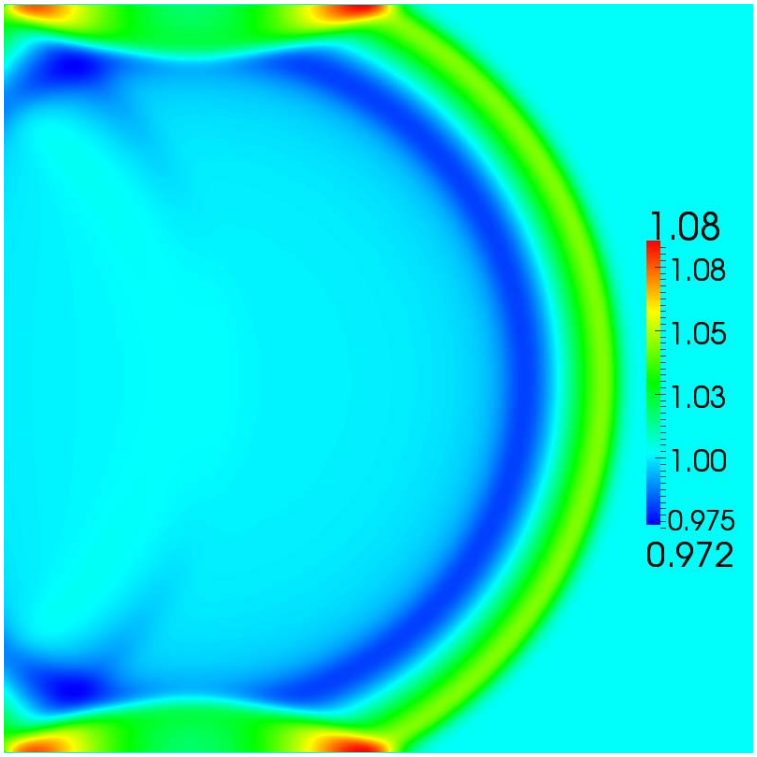

Figure B.21: Impedance free field BC, setup (a), density at $t = 700 \cdot \Delta t$

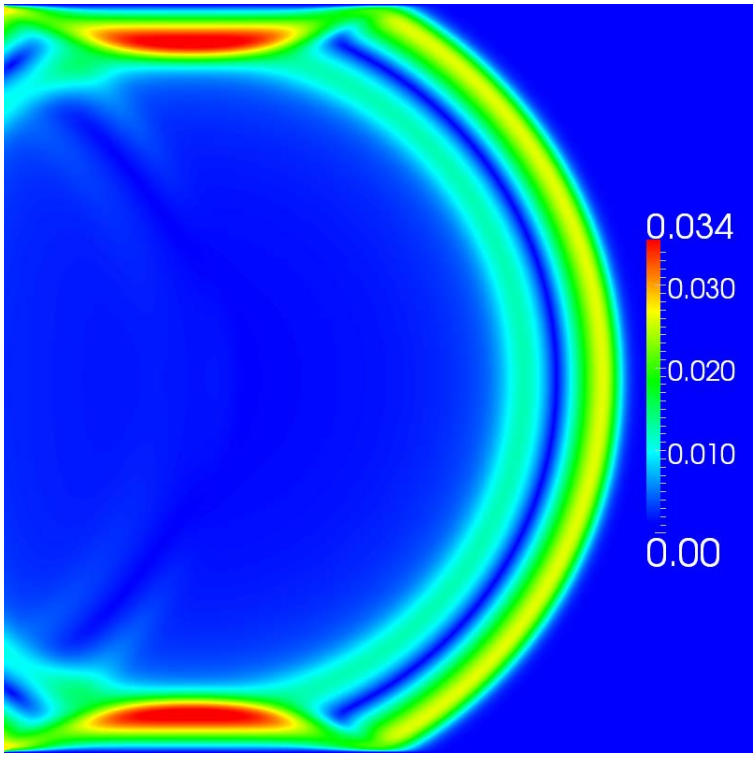

Figure B.22: Impedance free field BC, setup (a), absolute velocity at $t = 700 \cdot \Delta t$

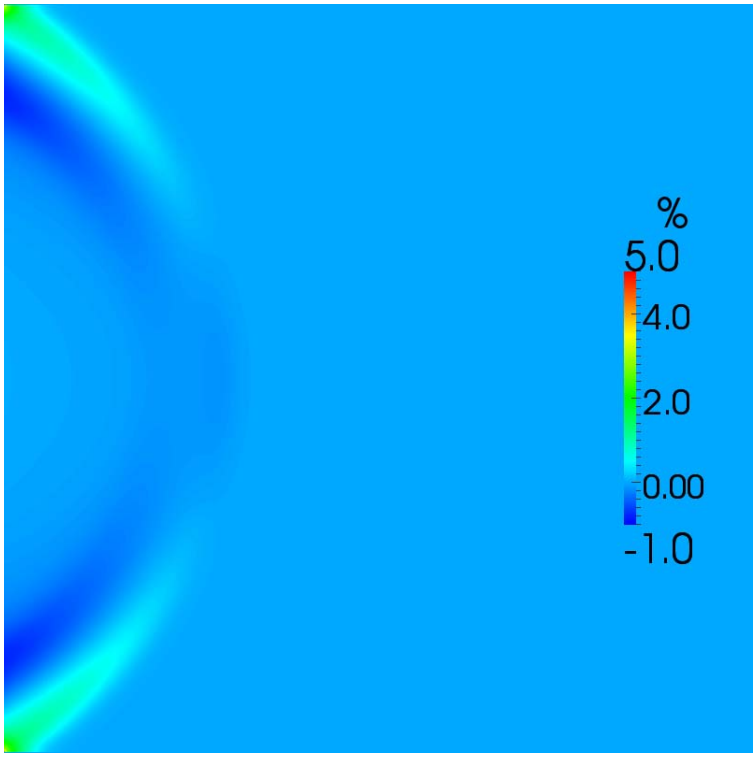

Figure B.23: Impedance free field BC, setup (a), relative density error in % at $t = 700 \cdot \Delta t$

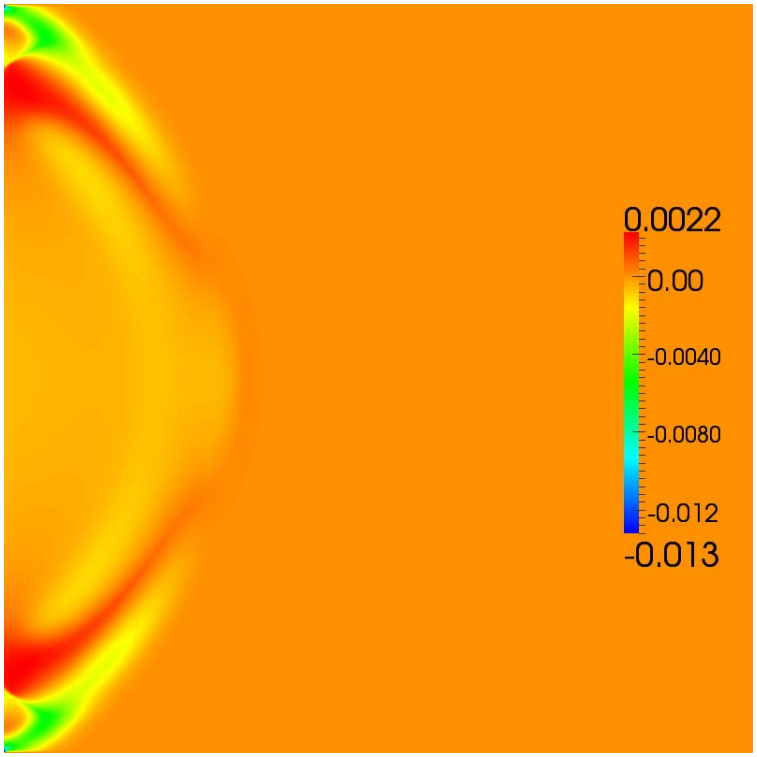

Figure B.24: Impedance free field BC, setup (a), absolute error of velocity error at $t = 700 \cdot \Delta t$

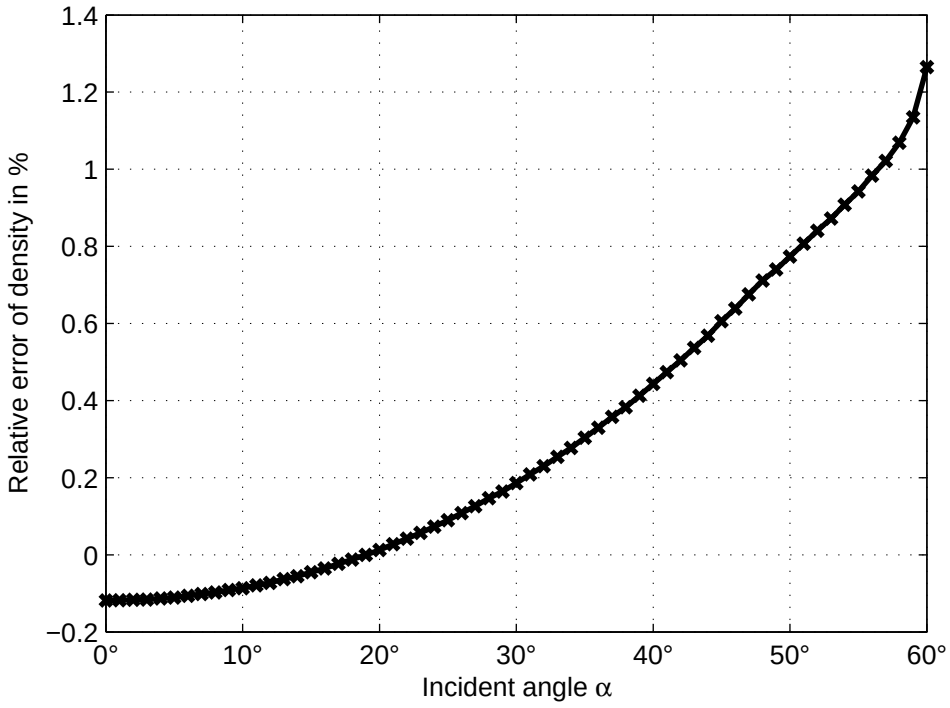

Figure B.25: Reflection over incident angle at $t = 700 \cdot \Delta t$

B.6 Incompressible LBM, Parabolic Velocity Profile

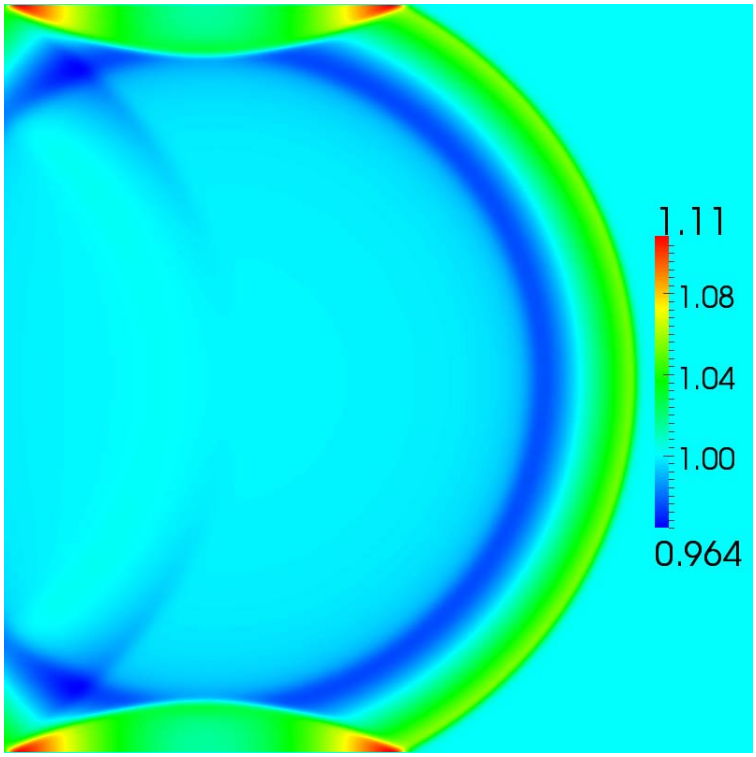

Figure B.26: Impedance free field BC, setup (b), density at $t = 700 \cdot \Delta t$

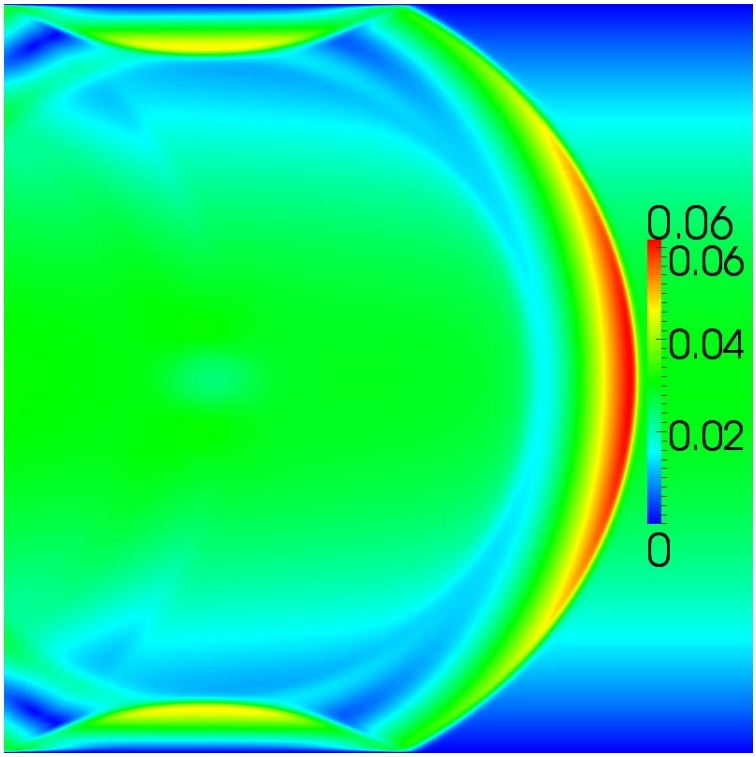

Figure B.27: Impedance free field BC, setup (b), absolute velocity at $t = 700 \cdot \Delta t$

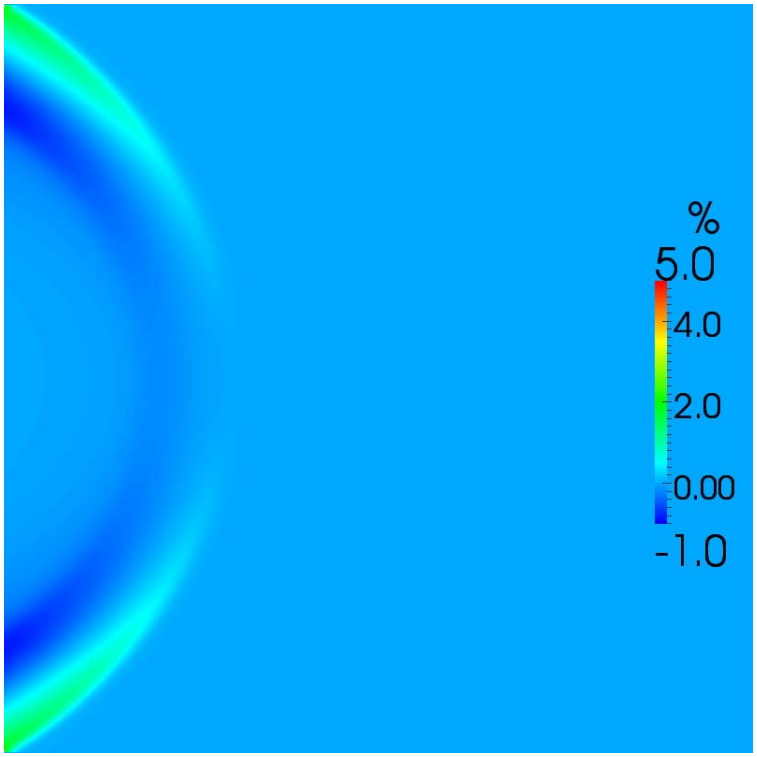

Figure B.28: Impedance free field BC, setup (b), relative density error in % at $t = 700 \cdot \Delta t$

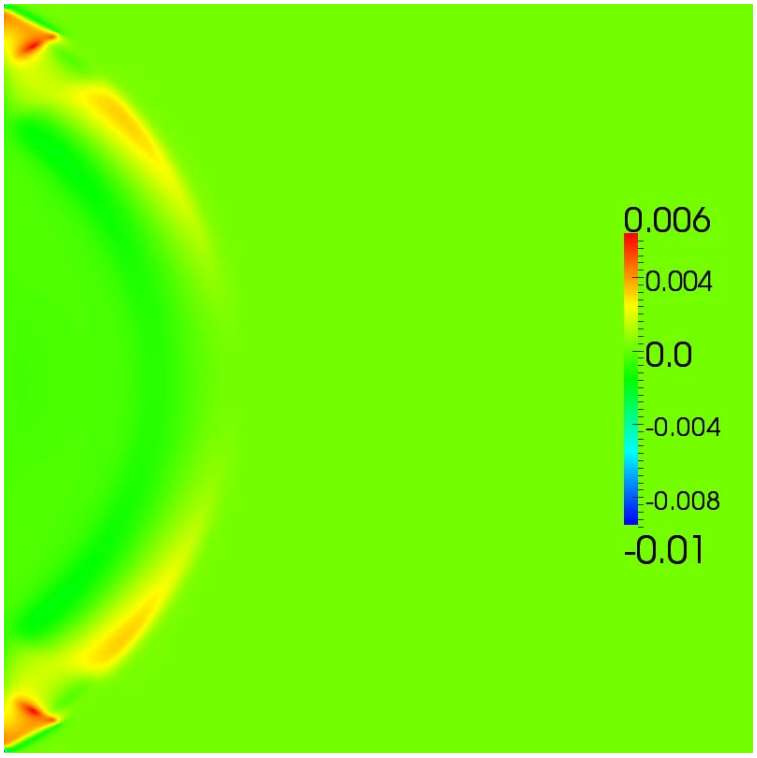

Figure B.29: Impedance free field BC, setup (b), absolute error of velocity error at $t = 700 \cdot \Delta t$

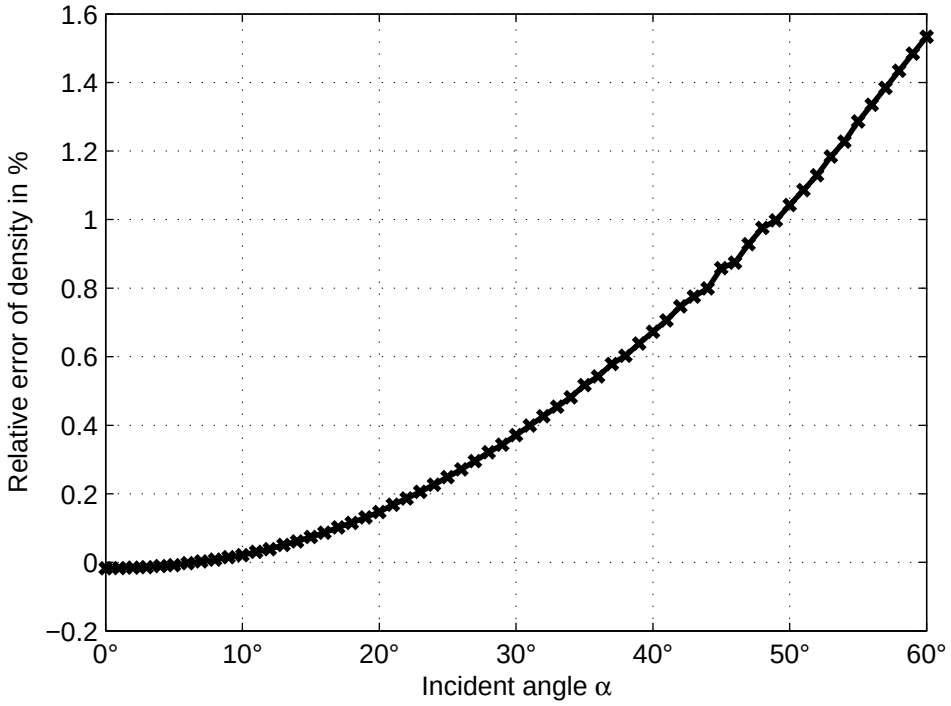

Figure B.30: Reflection over incident angle at $t = 700 \cdot \Delta t$

B.7 Incompressible LBM, Fixed Reference Level, Resting Fluid

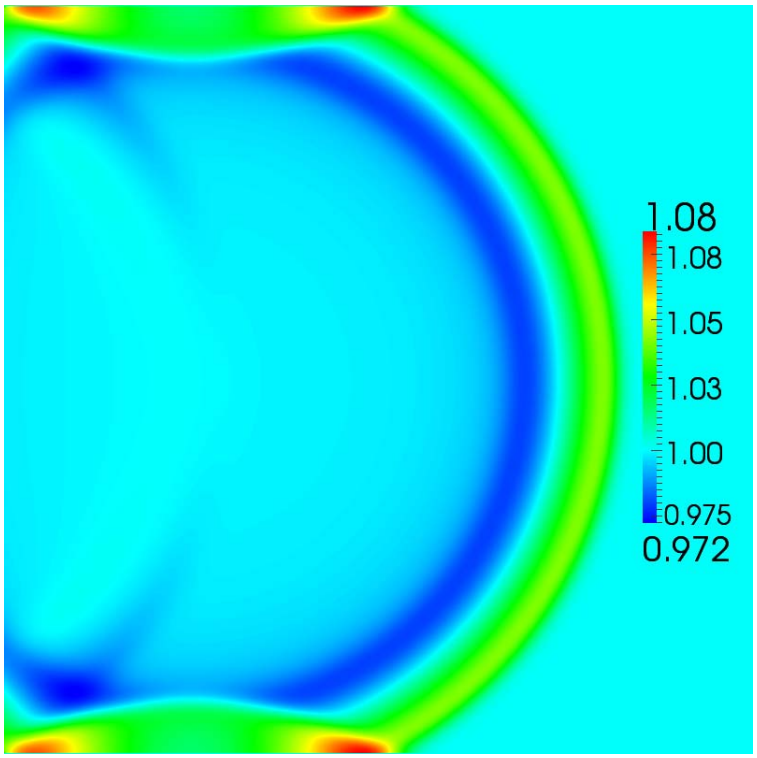

Figure B.31: Imp. fixed free field BC, setup (a), density at $t = 700 \cdot \Delta t$

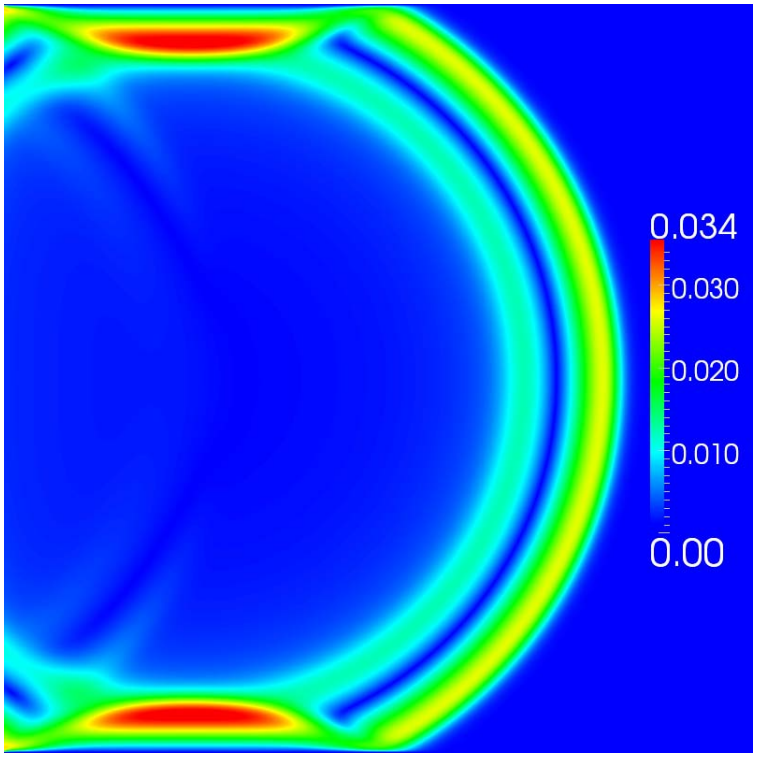

Figure B.32: Imp. fixed free field BC, setup (a), absolute velocity at $t = 700 \cdot \Delta t$

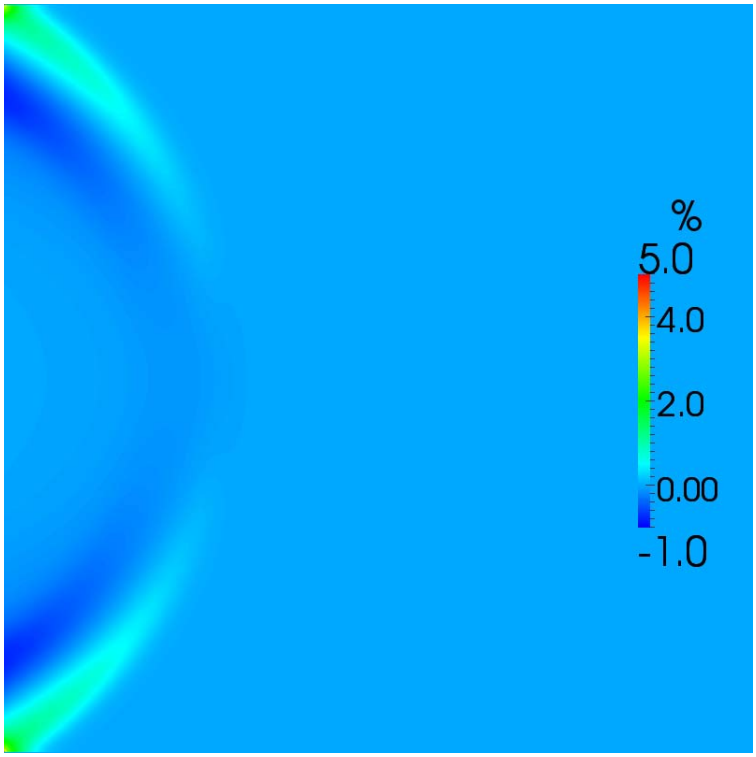

Figure B.33: Imp. fixed free field BC, setup (a), relative density error in % at $t = 700 \cdot \Delta t$

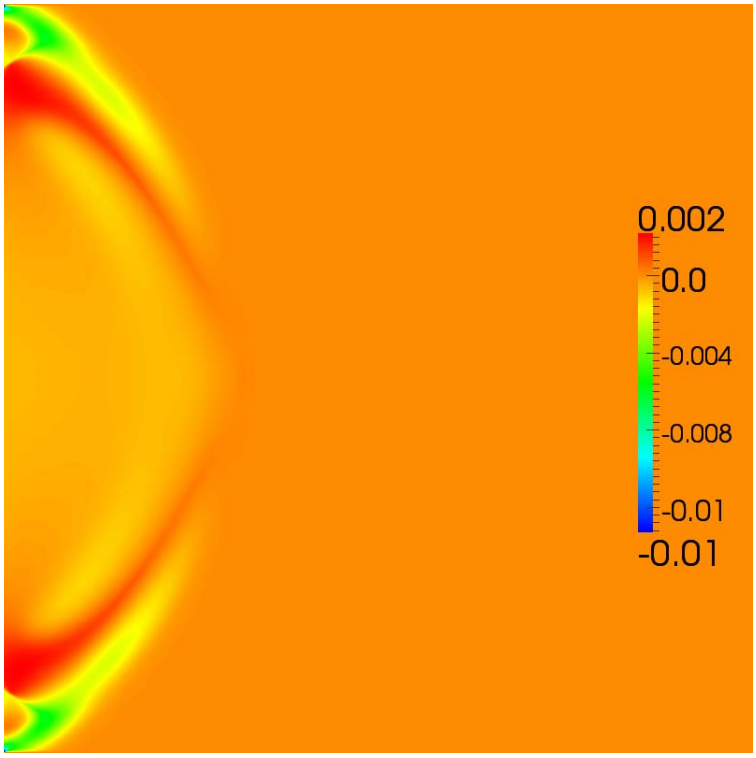

Figure B.34: Imp. fixed free field BC, setup (a), absolute error of velocity error at $t = 700 \cdot \Delta t$

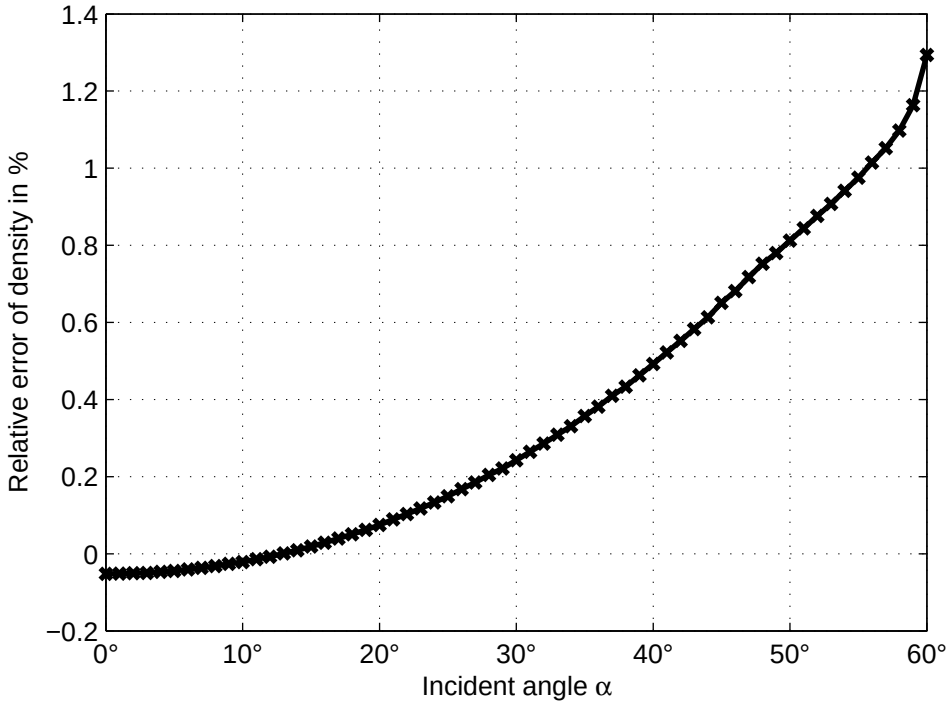

Figure B.35: Reflection over incident angle at $t = 700 \cdot \Delta t$v

B.8 Incompressible LBM, Fixed Reference Level, Parabolic Velocity Profile

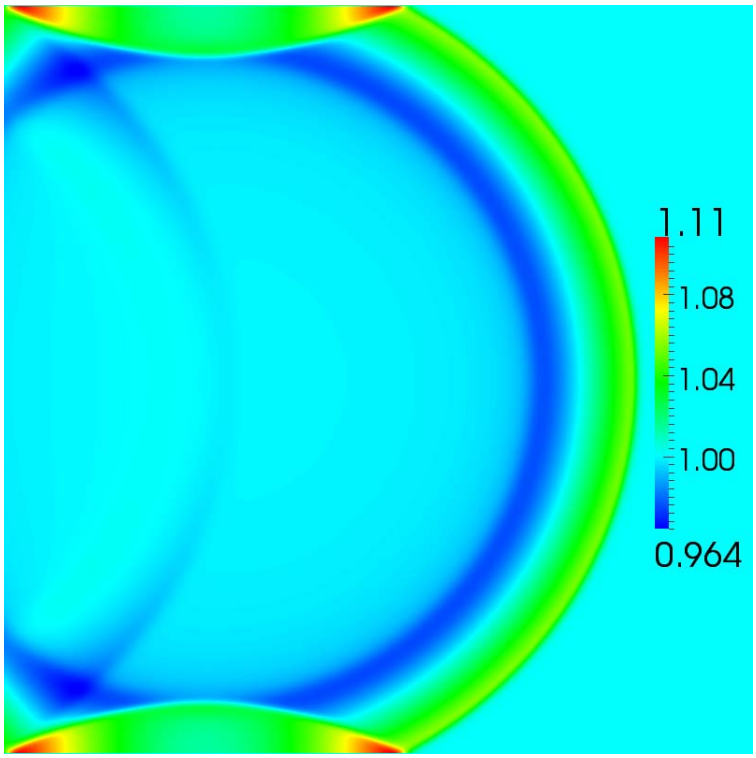

Figure B.36: Imp. fixed free field BC, setup (b), density at $t = 700 \cdot \Delta t$

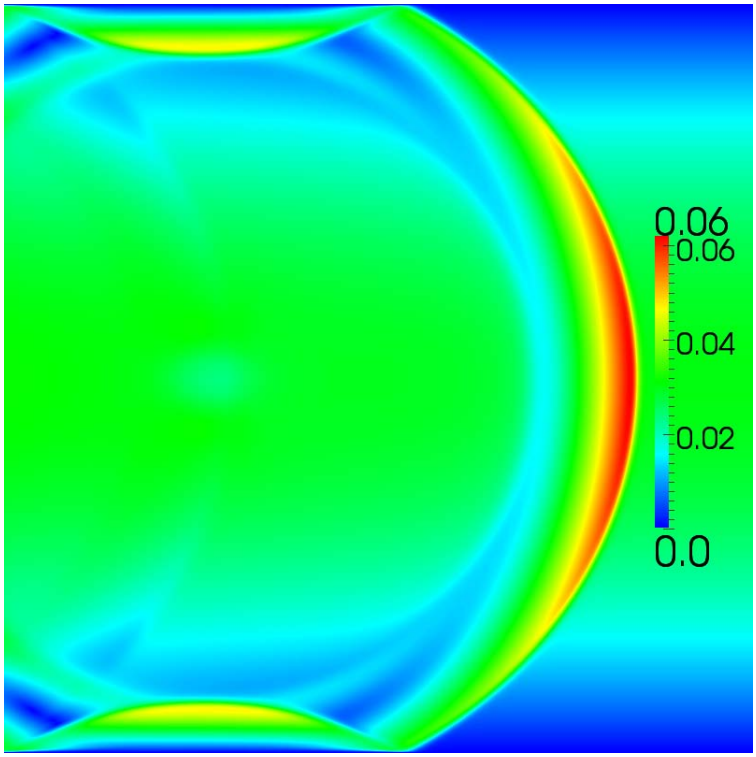

Figure B.37: Imp. fixed free field BC, setup (b), absolute velocity at $t = 700 \cdot \Delta t$

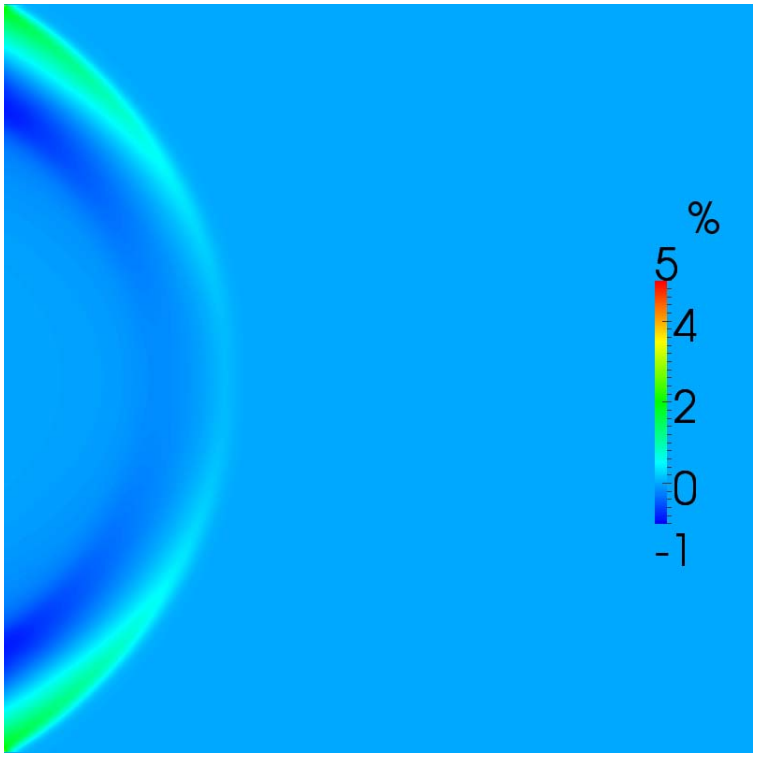

Figure B.38: Imp. fixed free field BC, setup (b), relative density error in % at $t = 700 \cdot \Delta t$

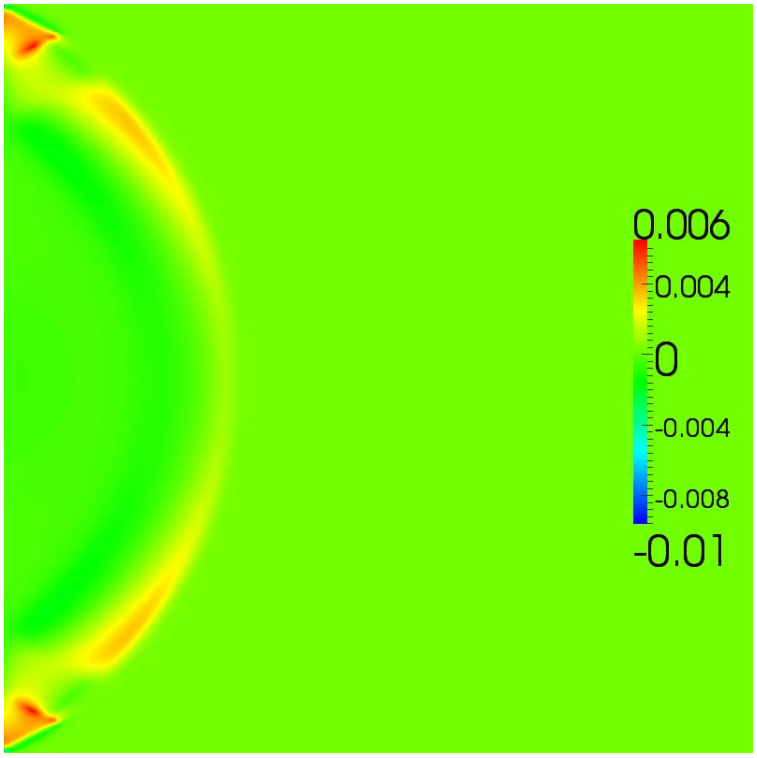

Figure B.39: Imp. fixed free field BC, setup (b), absolute error of velocity error at $t = 700 \cdot \Delta t$

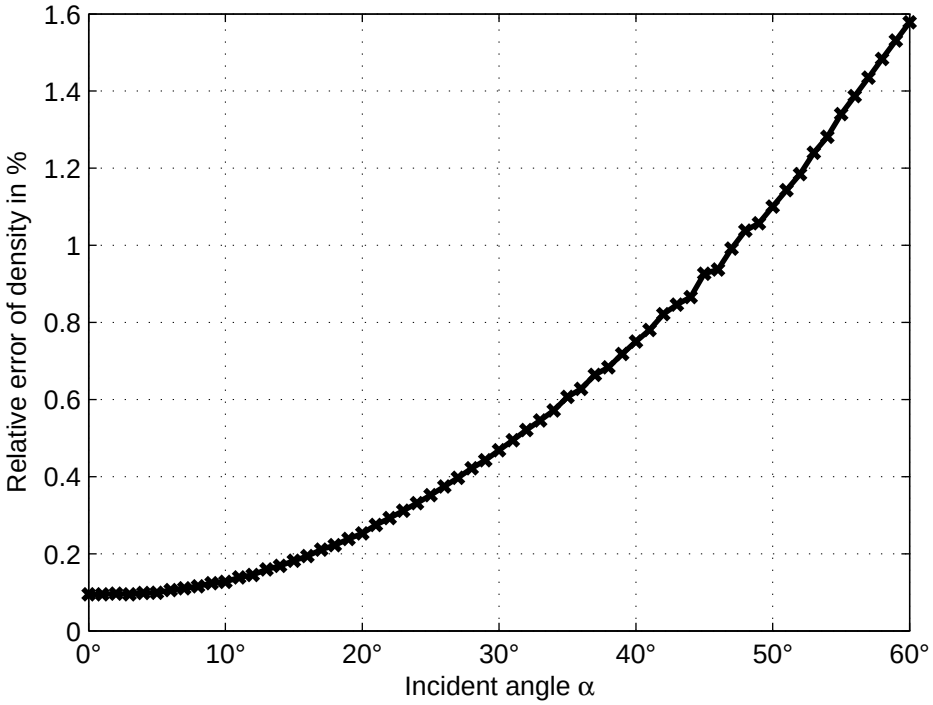

Figure B.40: Reflection over incident angle at $t = 700 \cdot \Delta t$

B.9 Compressible LBM, Full Adaption, Resting Fluid

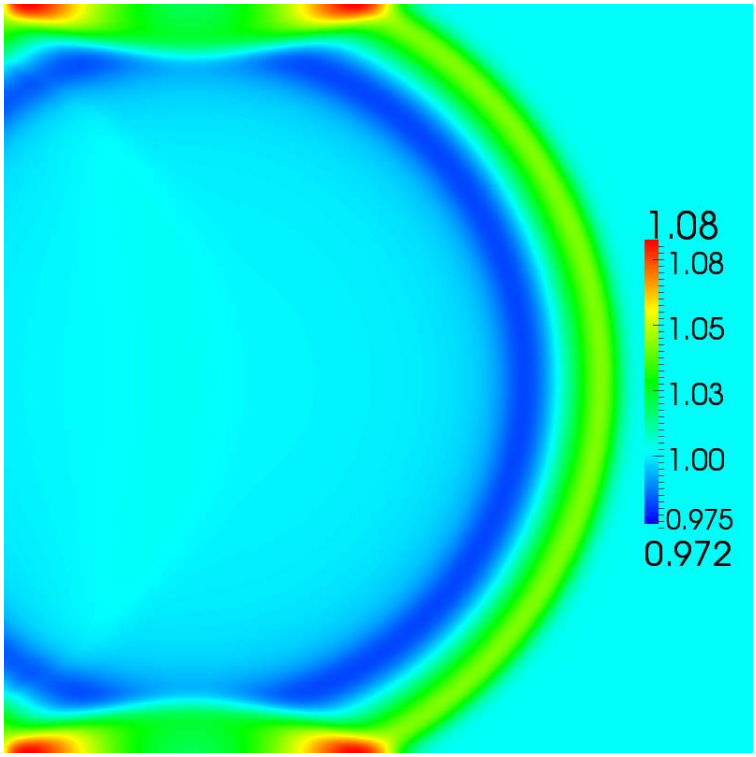

Figure B.41: Isotropic impedance free field BC, setup (a), density at $t = 700 \cdot \Delta t$

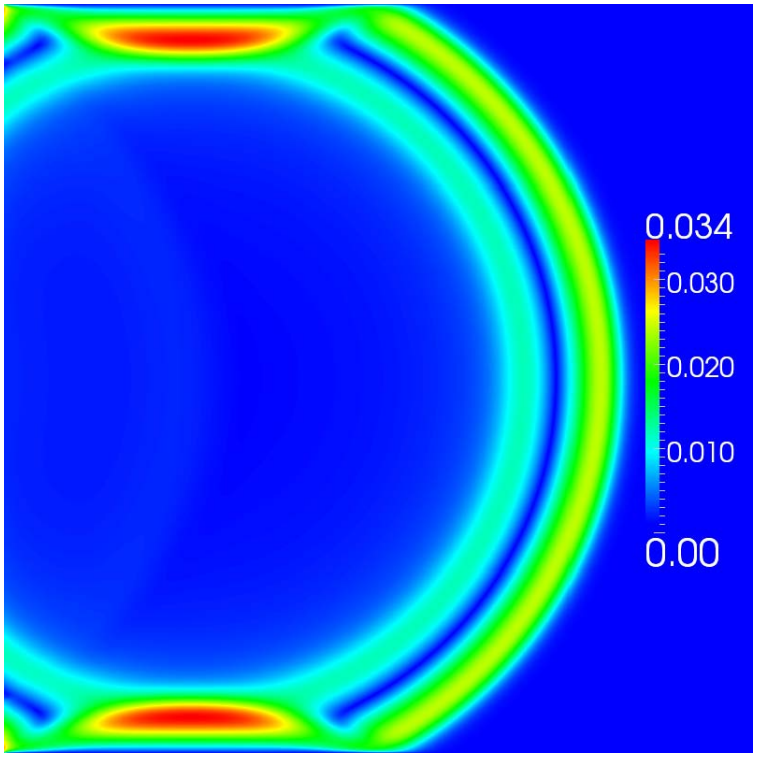

Figure B.42: Isotropic impedance free field BC, setup (a), absolute velocity at $t = 700 \cdot \Delta t$

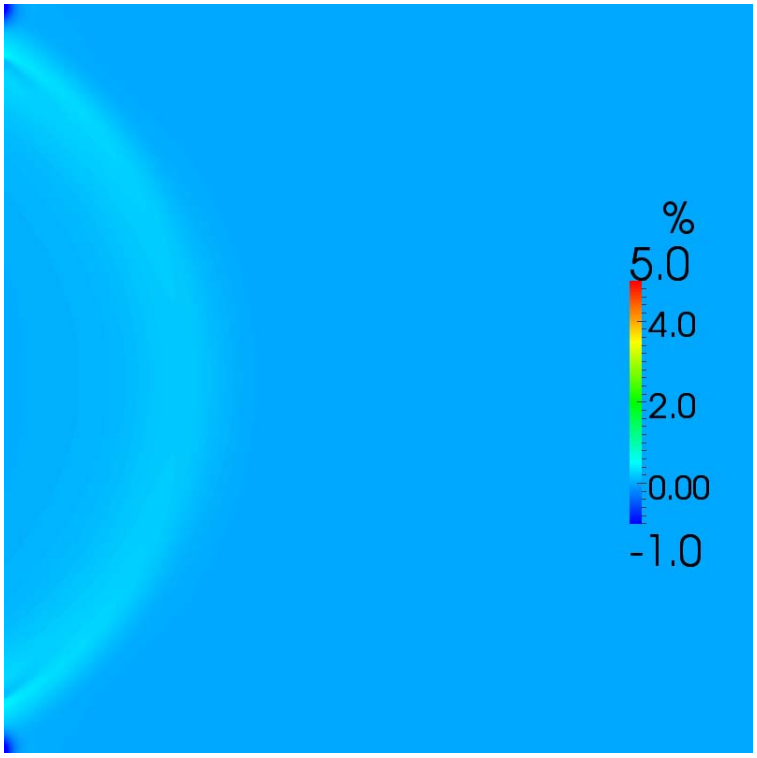

Figure B.43: Isotropic impedance free field BC, setup (a), relative density error in % at $t = 700 \cdot \Delta t$

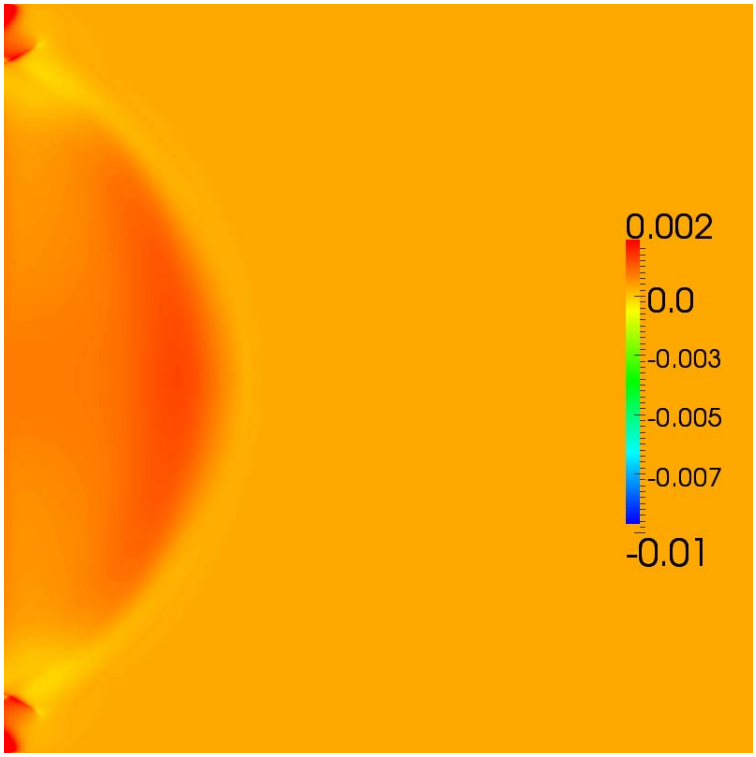

Figure B.44: Isotropic impedance free field BC, setup (a), absolute error of velocity error at $t = 700 \cdot \Delta t$

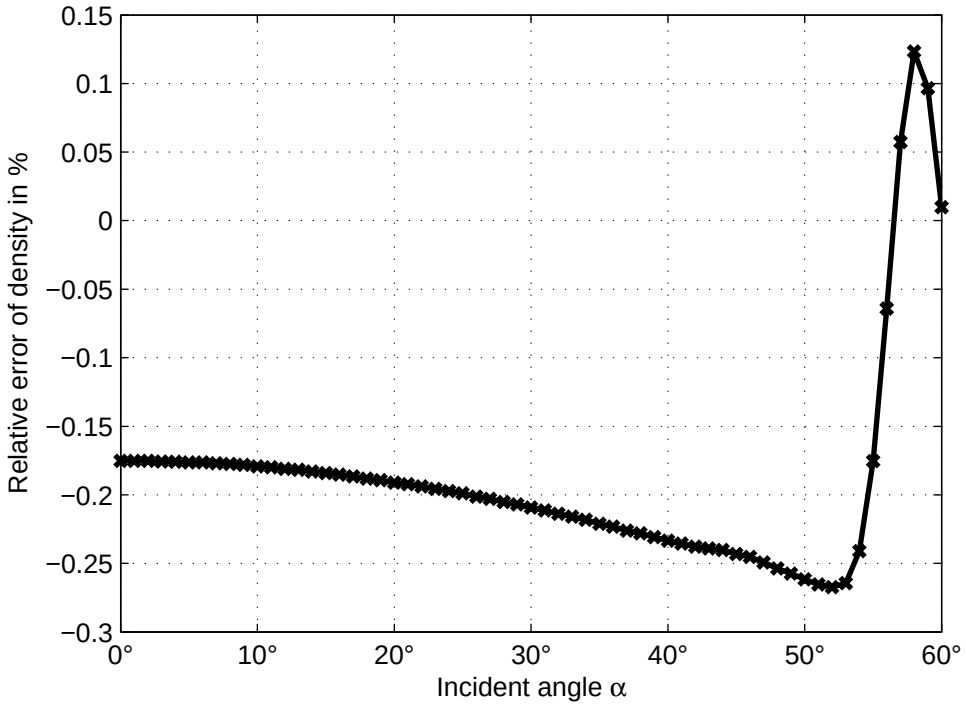

Figure B.45: Reflection over incident angle at $t = 770 \cdot \Delta t$

B.10 Compressible LBM, Full Adaption, Parabolic Velocity Profile

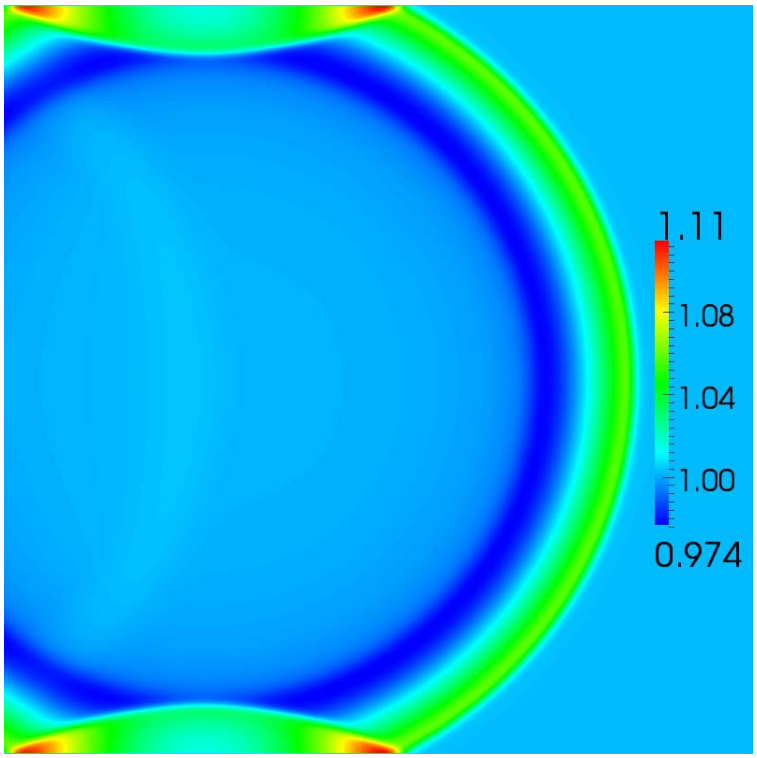

Figure B.46: Isotropic impedance free field BC, setup (b), density at $t = 700 \cdot \Delta t$

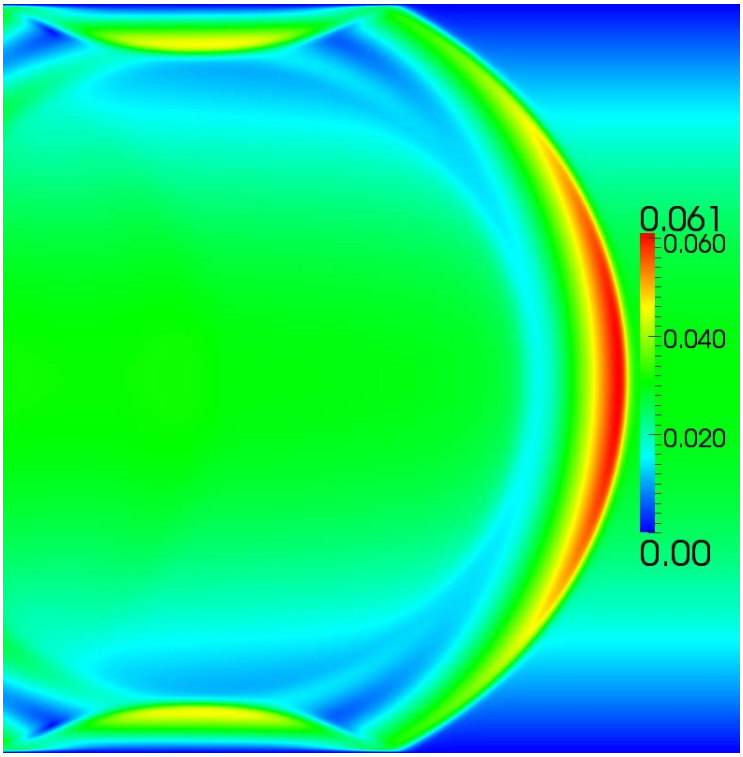

Figure B.47: Isotropic impedance free field BC, setup (b), absolute velocity at $t = 700 \cdot \Delta t$

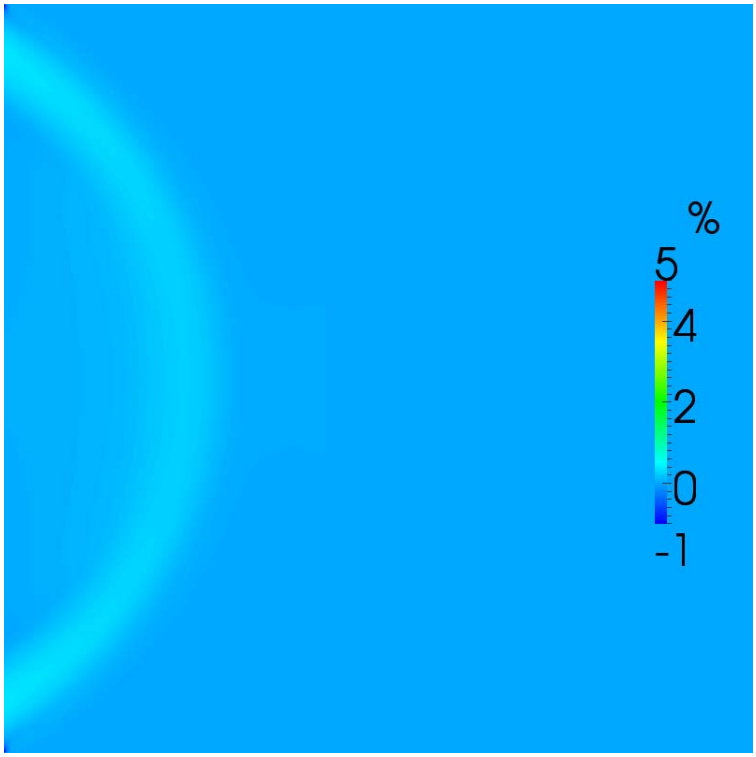

Figure B.48: Isotropic impedance free field BC, setup (b), relative density error in % at $t = 700 \cdot \Delta t$

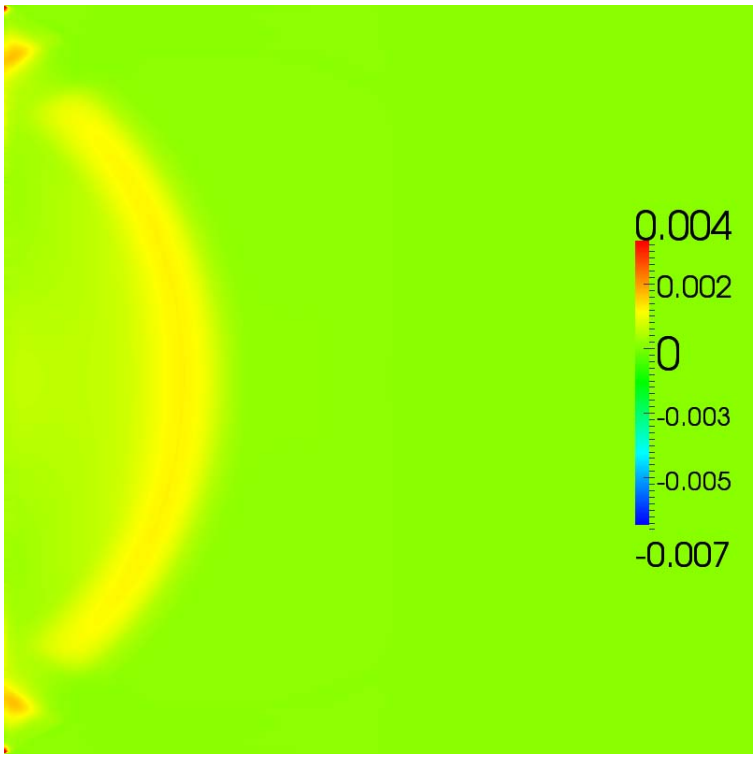

Figure B.49: Isotropic impedance free field BC, setup (b), absolute error of velocity error at $t = 700 \cdot \Delta t$

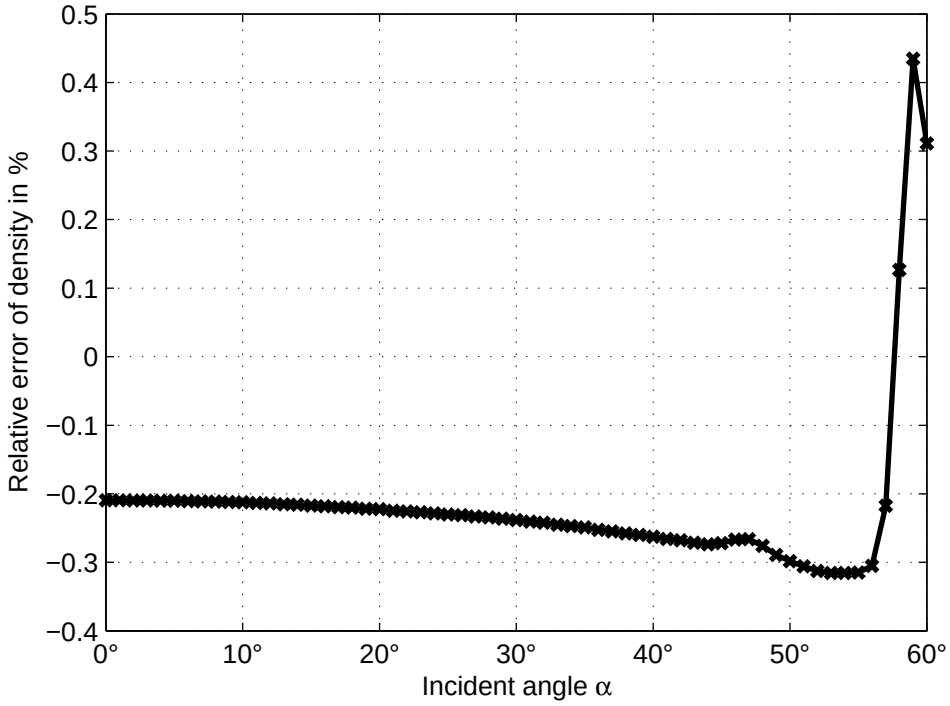

Figure B.50: Reflection over incident angle at $t = 770 \cdot \Delta t$

B.11 Compressible LBM, Full Adaption, Fixed Reference Level, Resting Fluid

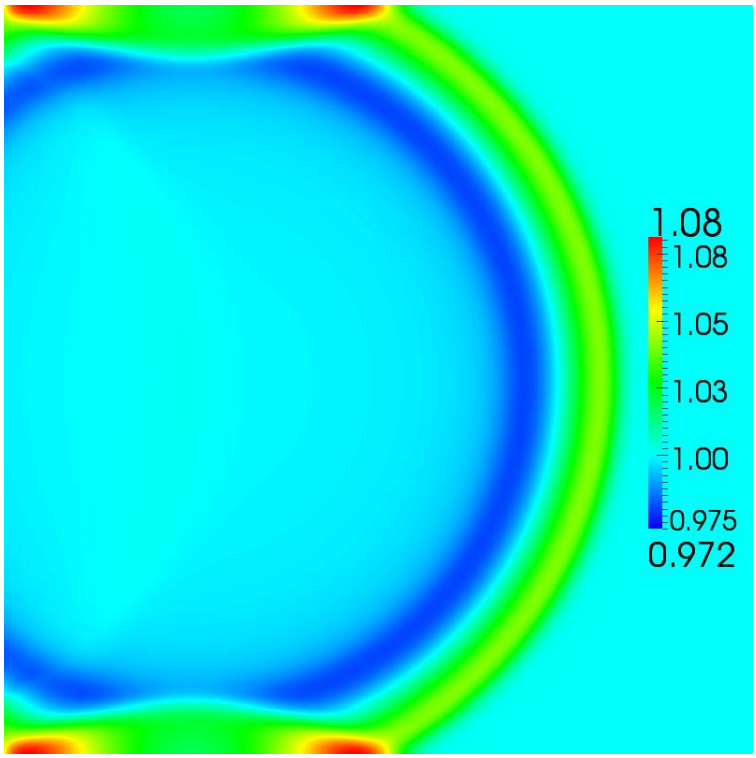

Figure B.51: Isotropic impedance free field BC, setup (a), density at $t = 700 \cdot \Delta t$

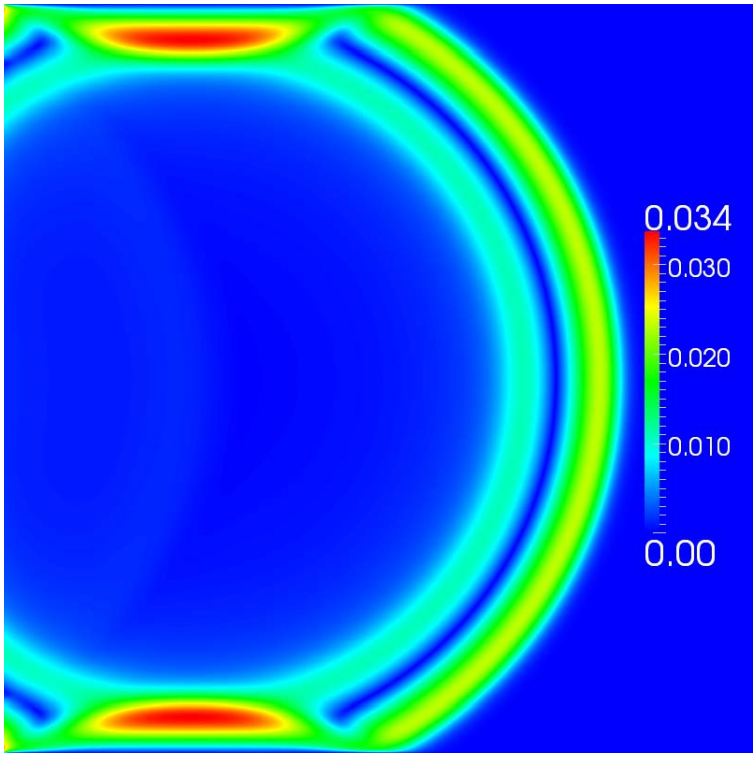

Figure B.52: Isotropic impedance free field BC, setup (a), absolute velocity at $t = 700 \cdot \Delta t$

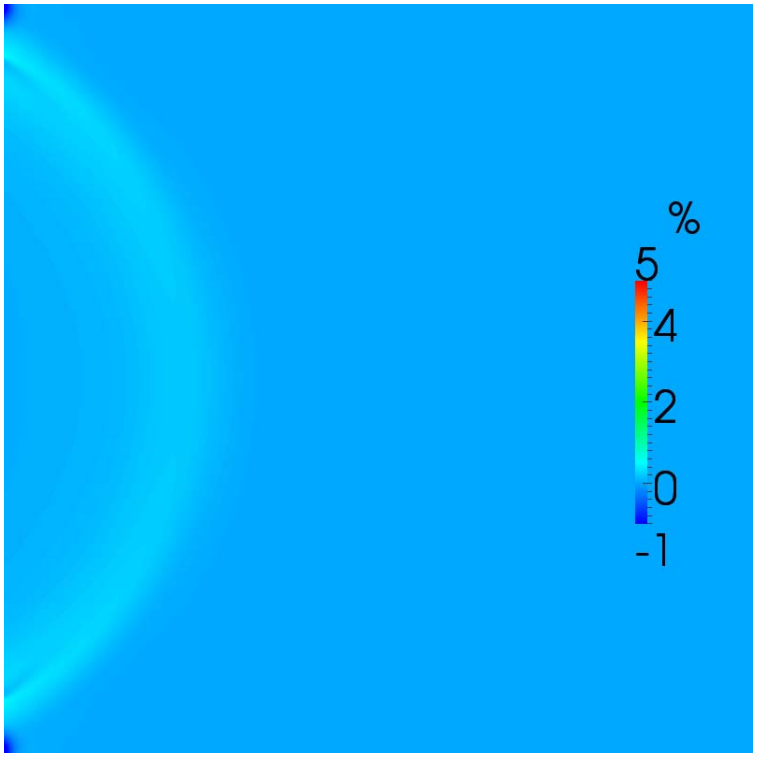

Figure B.53: Isotropic impedance free field BC, setup (a), relative density error in % at $t = 700 \cdot \Delta t$

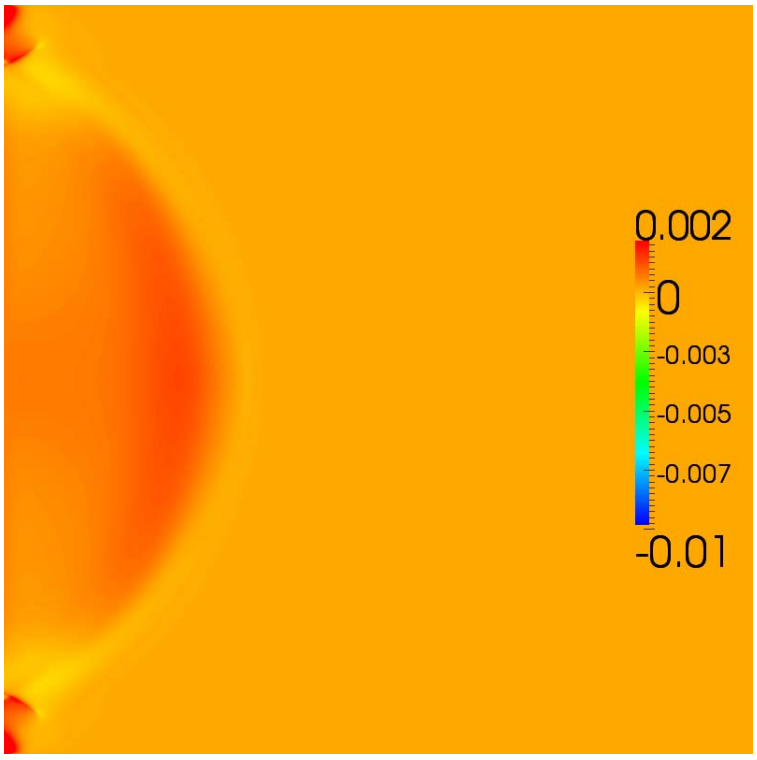

Figure B.54: Isotropic impedance free field BC, setup (a), absolute error of velocity error at $t = 700 \cdot \Delta t$

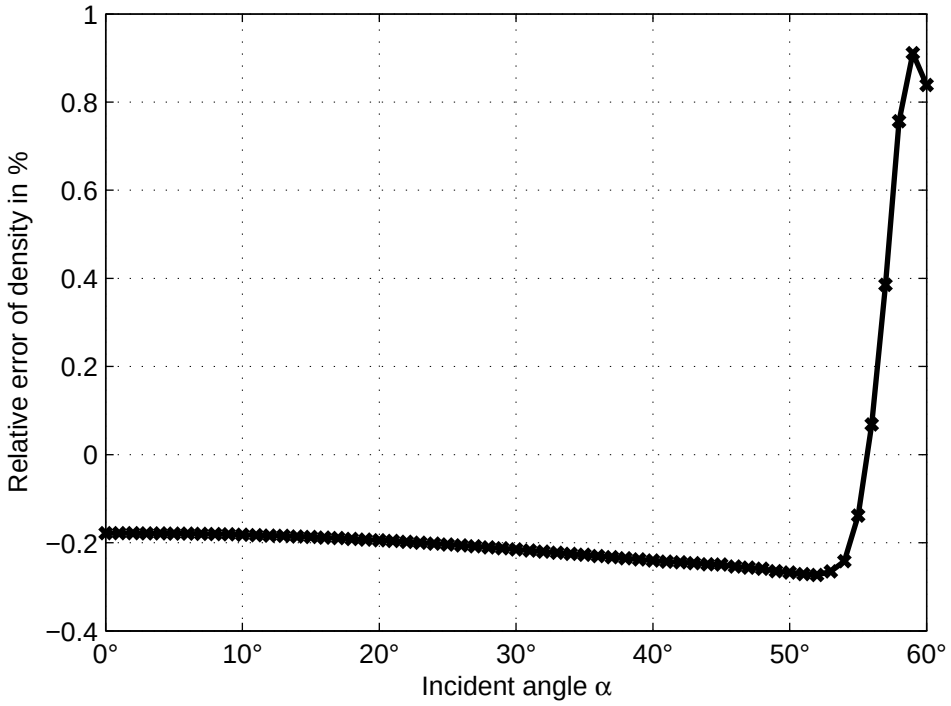

Figure B.55: Reflection over incident angle at $t = 770 \cdot \Delta t$

B.12 Compressible LBM, Full Adaption, Fixed Reference Level, Parabolic Velocity Profile

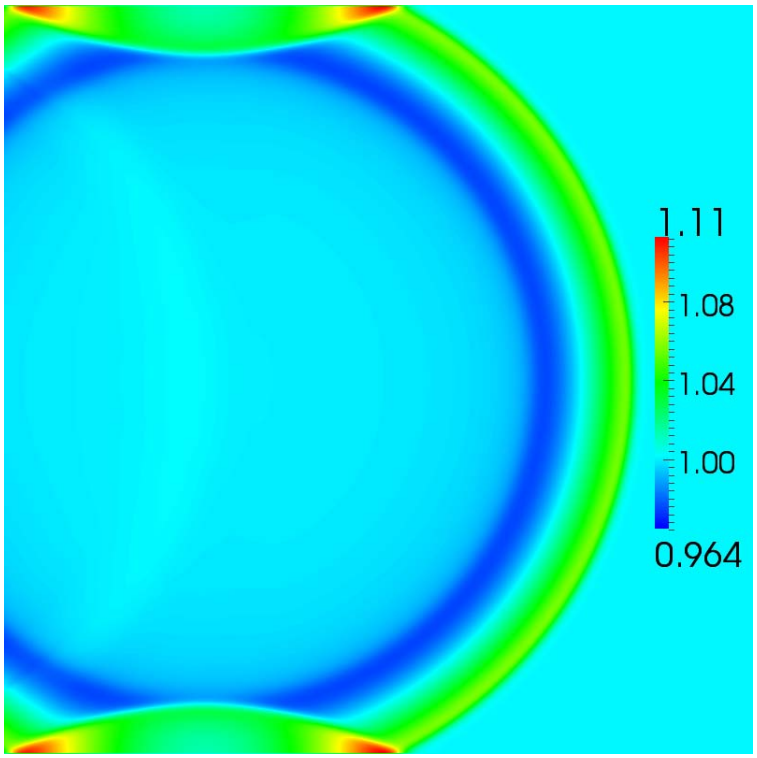

Figure B.56: Isotropic impedance free field BC, setup (b), density at $t = 700 \cdot \Delta t$

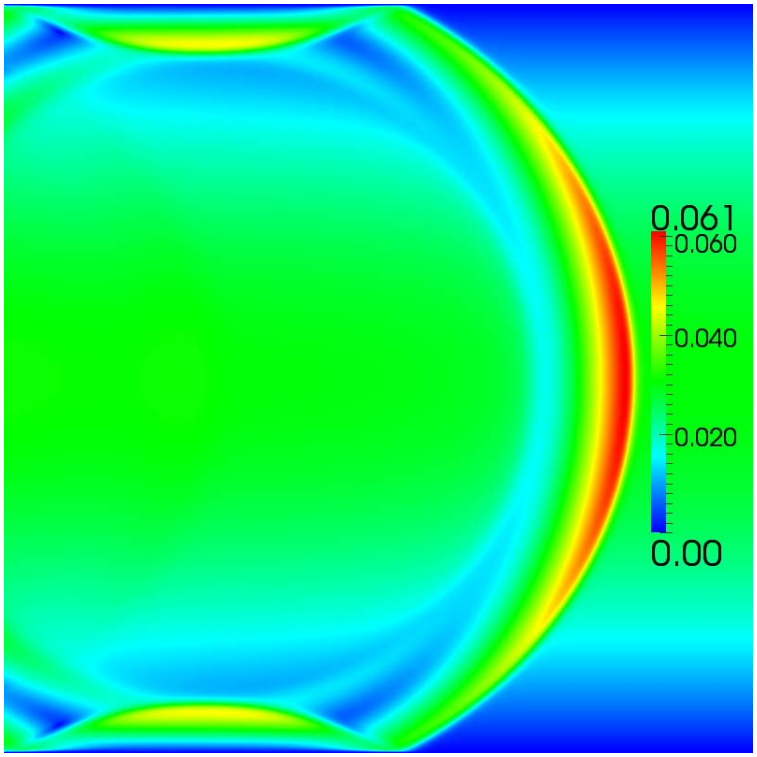

Figure B.57: Isotropic impedance free field BC, setup (b), absolute velocity at $t = 700 \cdot \Delta t$

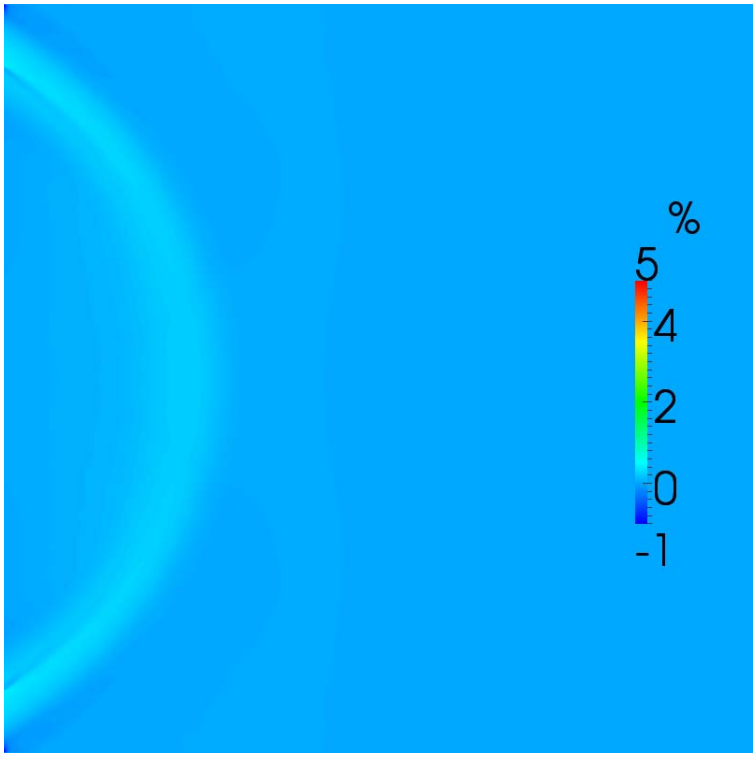

Figure B.58: Isotropic impedance free field BC, setup (b), relative density error in % at $t = 700 \cdot \Delta t$

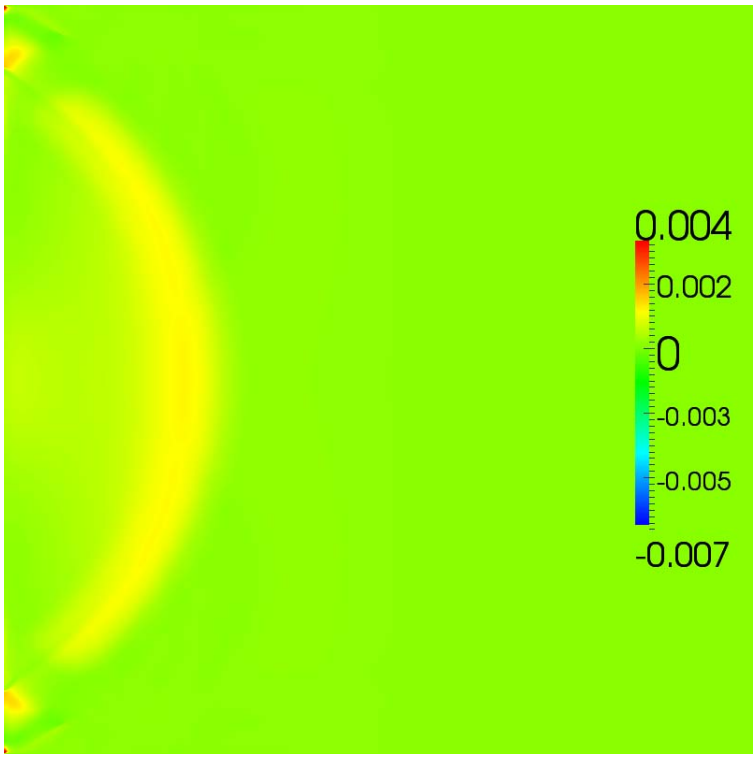

Figure B.59: Isotropic impedance free field BC, setup (b), absolute error of velocity error at $t = 700 \cdot \Delta t$

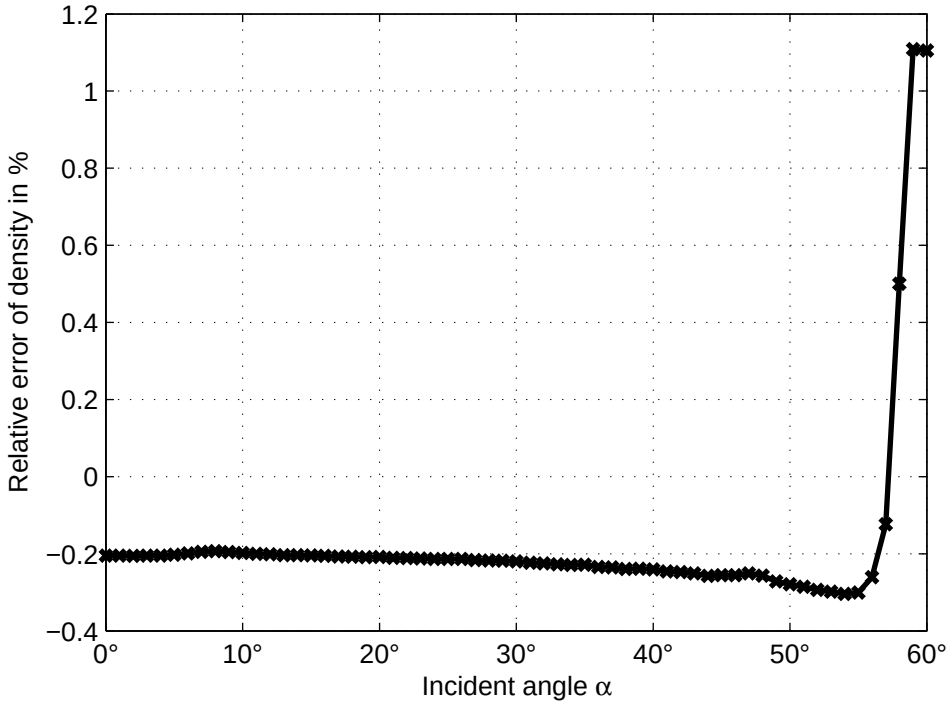

Figure B.60: Reflection over incident angle at $t = 770 \cdot \Delta t$

B.13 Incompressible LBM, Full Adaption, Resting Fluid

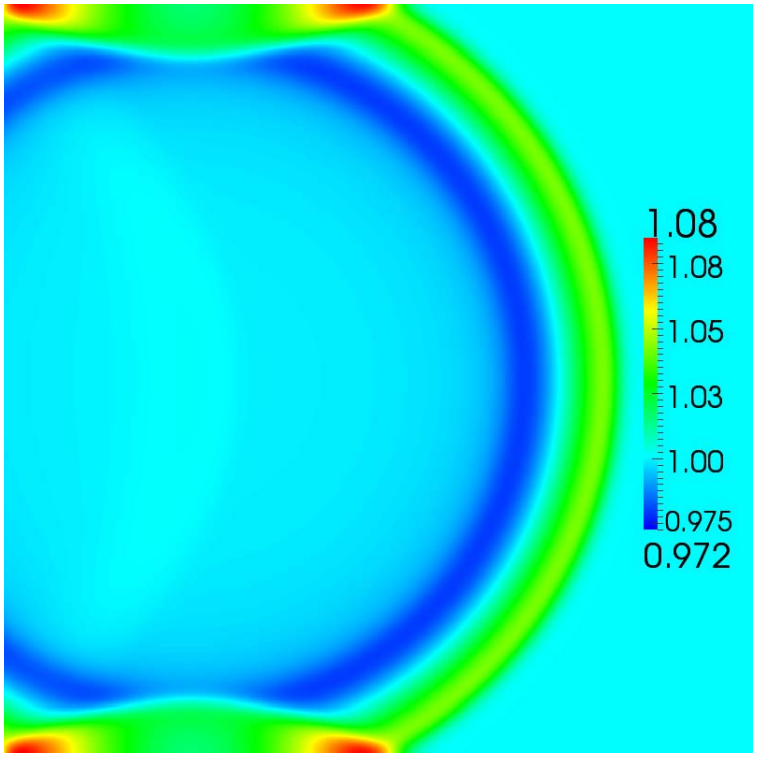

Figure B.61: Isotropic impedance free field BC, setup (a), density at $t = 700 \cdot \Delta t$

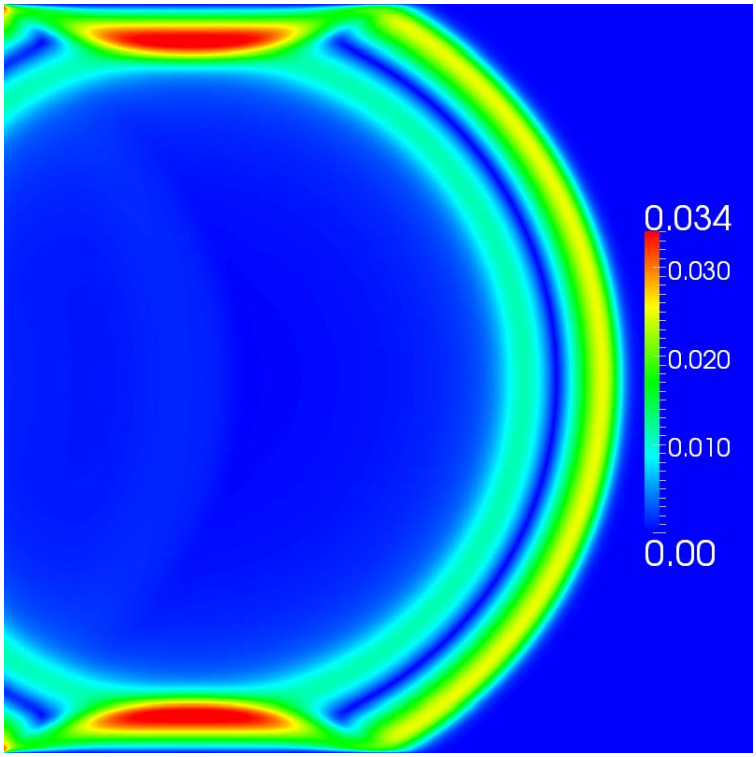

Figure B.62: Isotropic impedance free field BC, setup (a), absolute velocity at $t = 700 \cdot \Delta t$

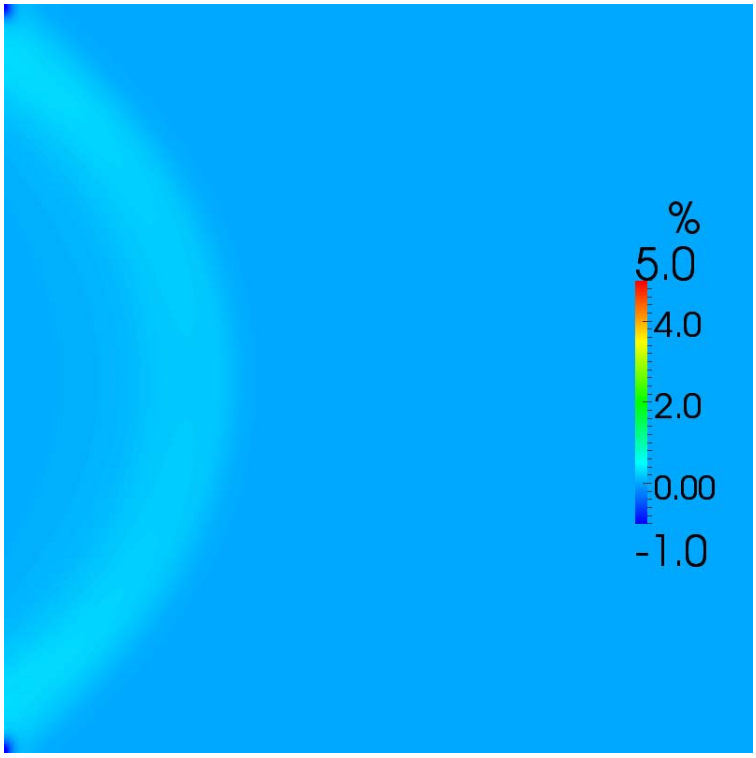

Figure B.63: Isotropic impedance free field BC, setup (a), relative density error in % at $t = 700 \cdot \Delta t$

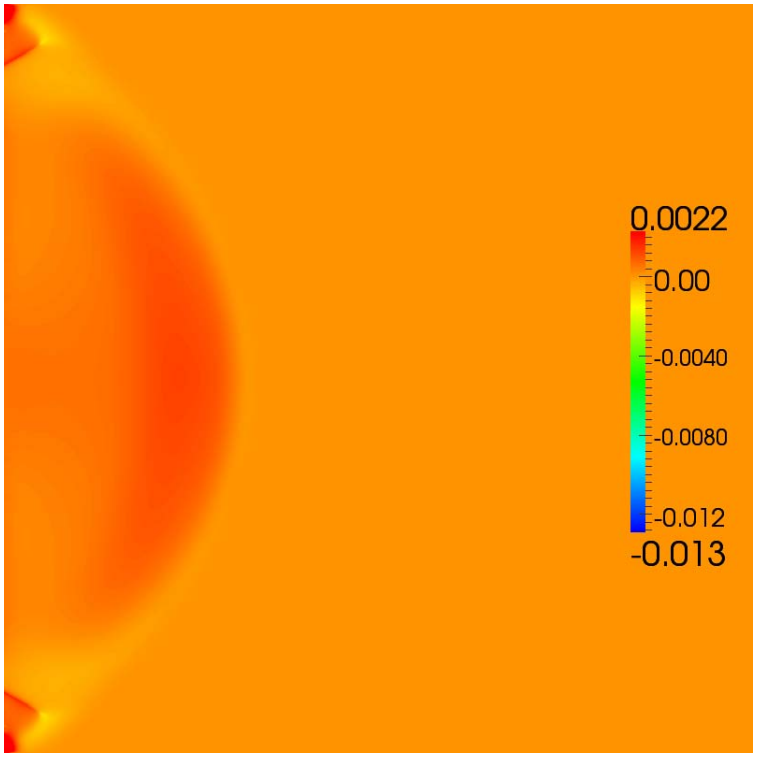

Figure B.64: Isotropic impedance free field BC, setup (a), absolute error of velocity error at $t = 700 \cdot \Delta t$

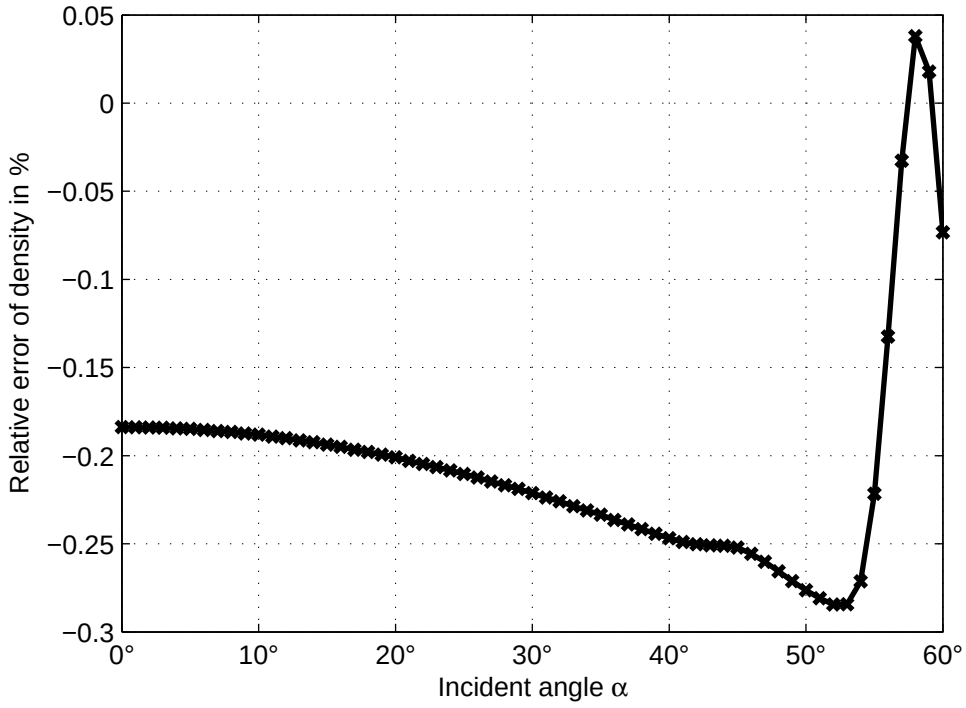

Figure B.65: Reflection over incident angle at $t = 770 \cdot \Delta t$

B.14 Incompressible LBM, Full Adaption, Parabolic Velocity Profile

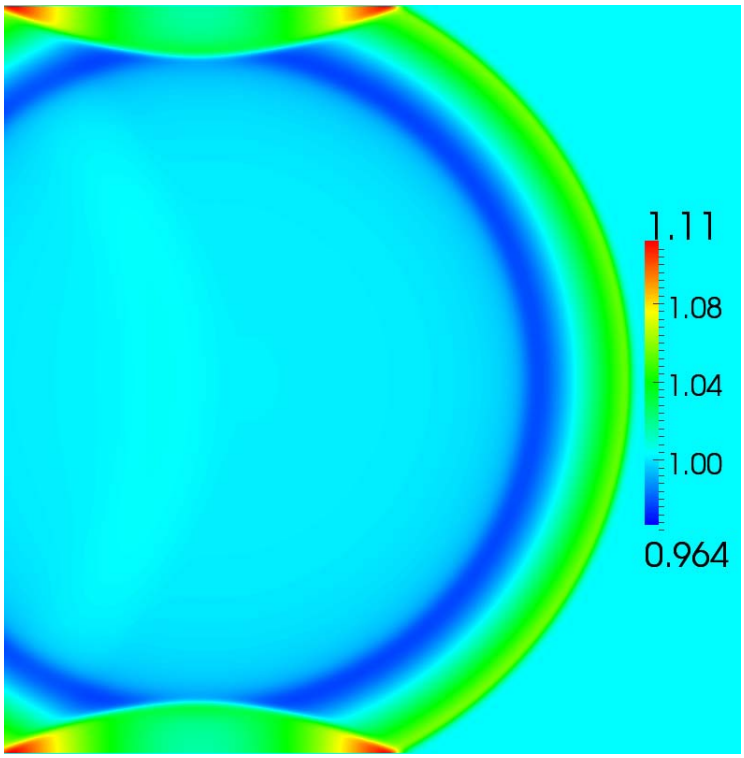

Figure B.66: Isotropic impedance free field BC, setup (b), density at $t = 700 \cdot \Delta t$

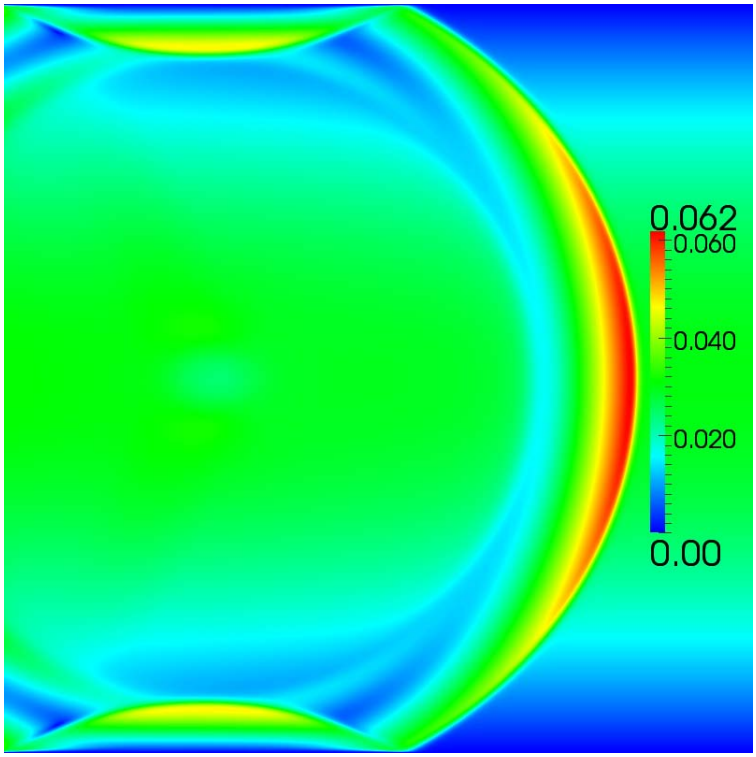

Figure B.67: Isotropic impedance free field BC, setup (b), absolute velocity at $t = 700 \cdot \Delta t$

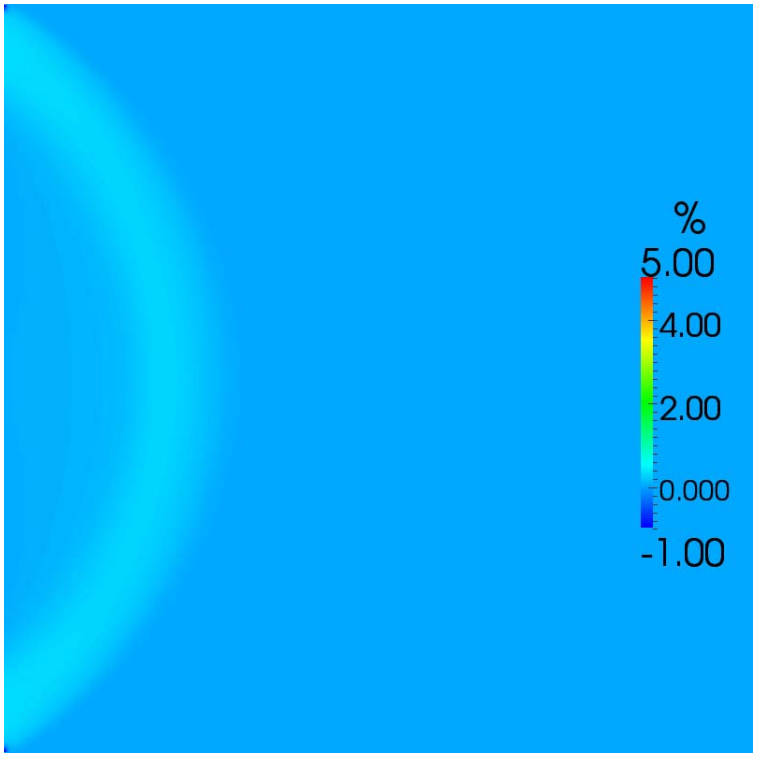

Figure B.68: Isotropic impedance free field BC, setup (b), relative density error in % at $t = 700 \cdot \Delta t$

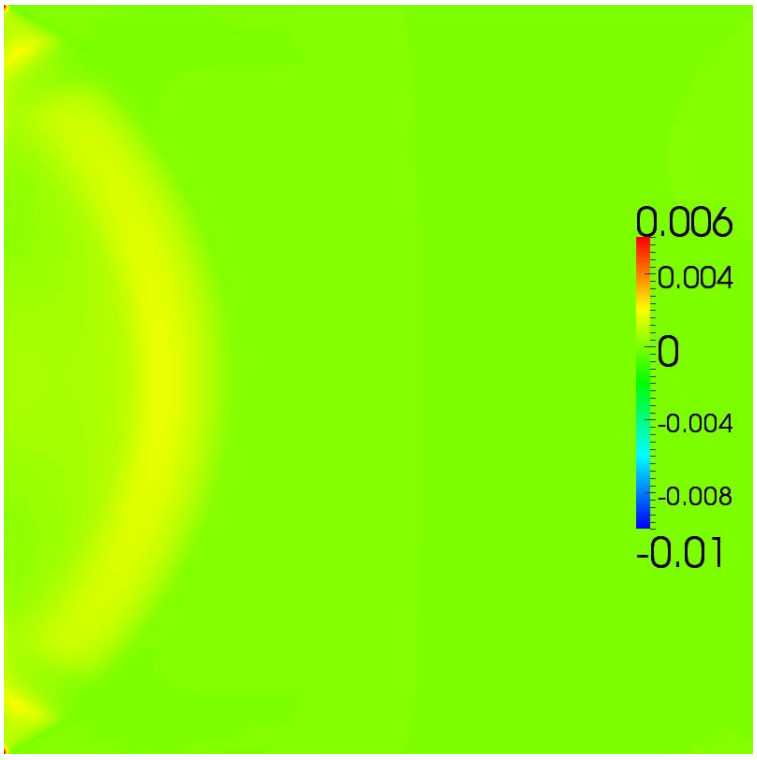

Figure B.69: Isotropic impedance free field BC, setup (b), absolute error of velocity error at $t = 700 \cdot \Delta t$

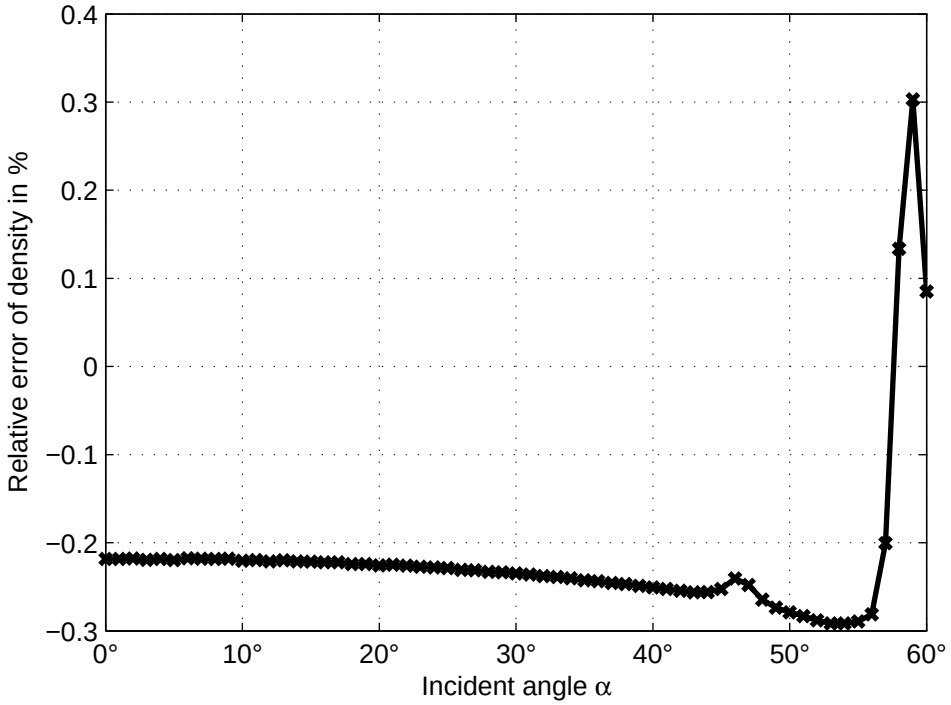

Figure B.70: Reflection over incident angle at $t = 770 \cdot \Delta t$

B.15 Incompressible LBM, Full Adaption, Fixed Reference Level, Resting Fluid

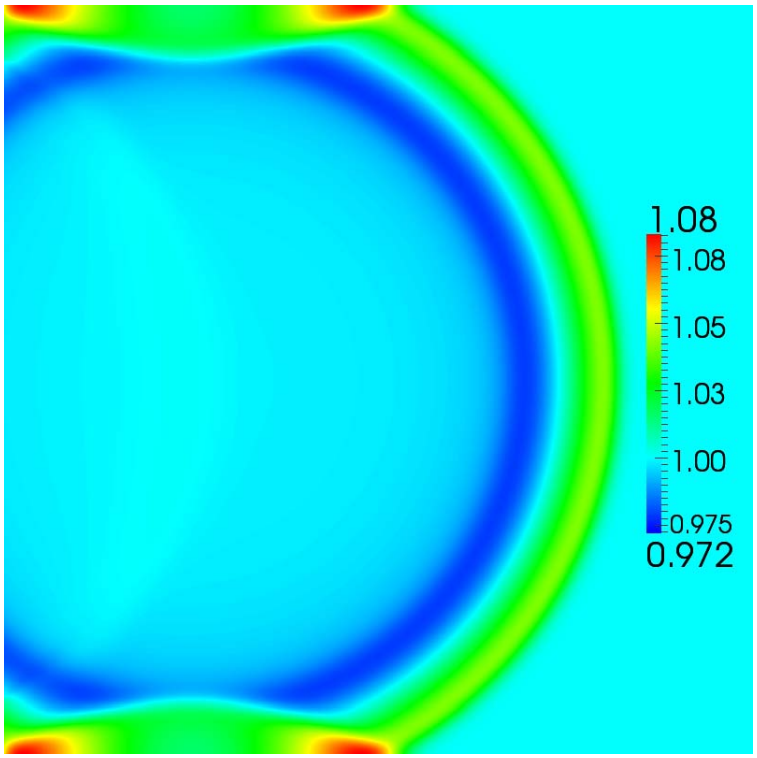

Figure B.71: Isotropic impedance free field BC, setup (a), density at $t = 700 \cdot \Delta t$

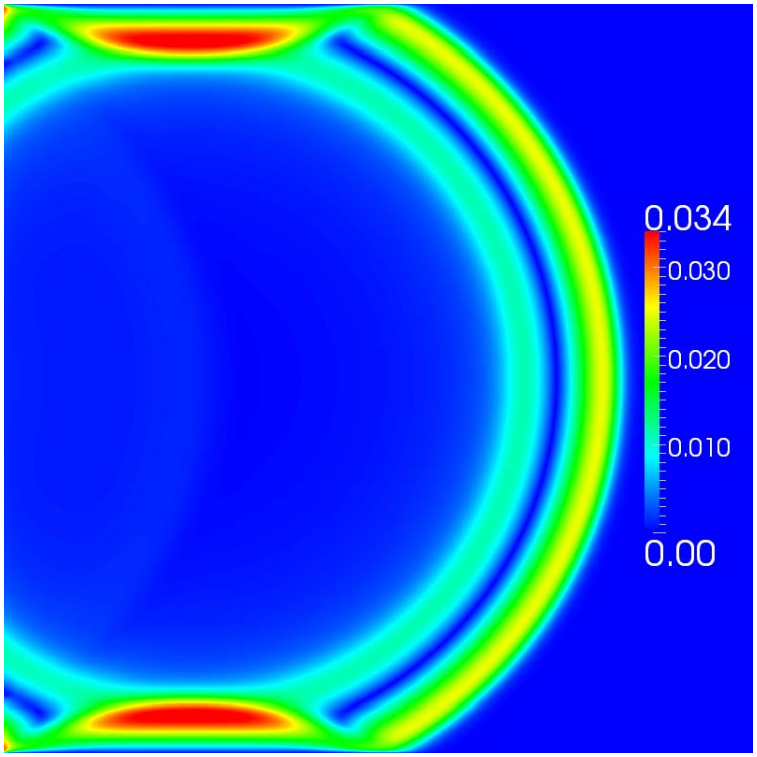

Figure B.72: Isotropic impedance free field BC, setup (a), absolute velocity at $t = 700 \cdot \Delta t$

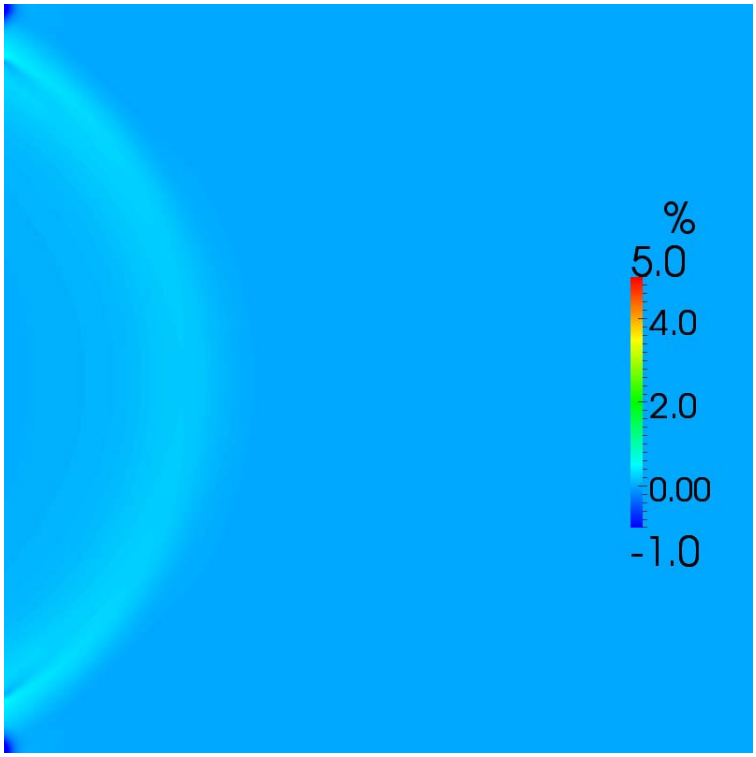

Figure B.73: Isotropic impedance free field BC, setup (a), relative density error in % at $t = 700 \cdot \Delta t$

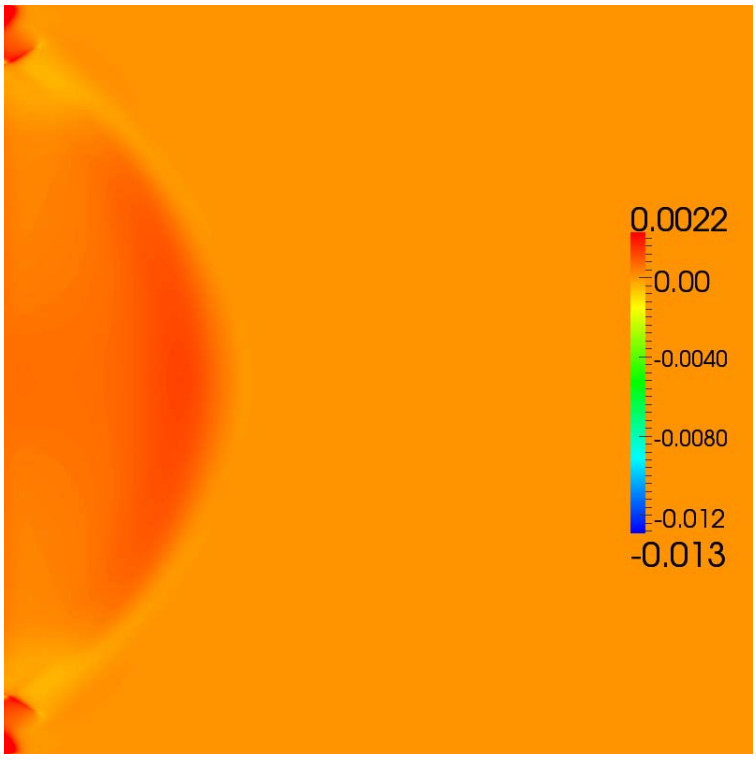

Figure B.74: Isotropic impedance free field BC, setup (a), absolute error of velocity error at $t = 700 \cdot \Delta t$

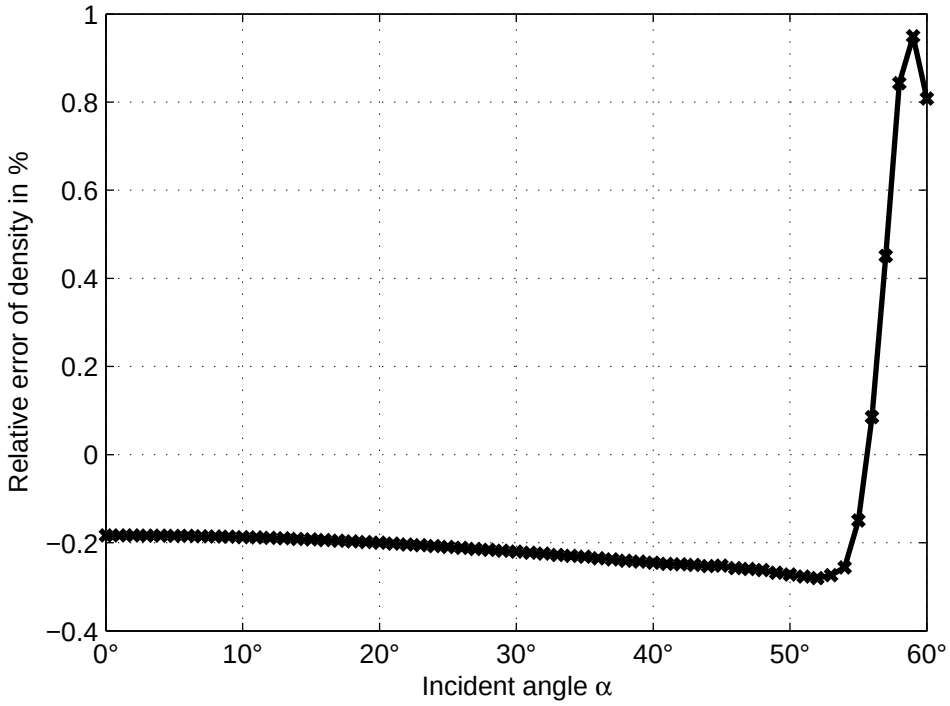

Figure B.75: Reflection over incident angle at $t = 770 \cdot \Delta t$

B.16 Incompressible LBM, Full Adaption, Fixed Reference Level, Parabolic Velocity Profile

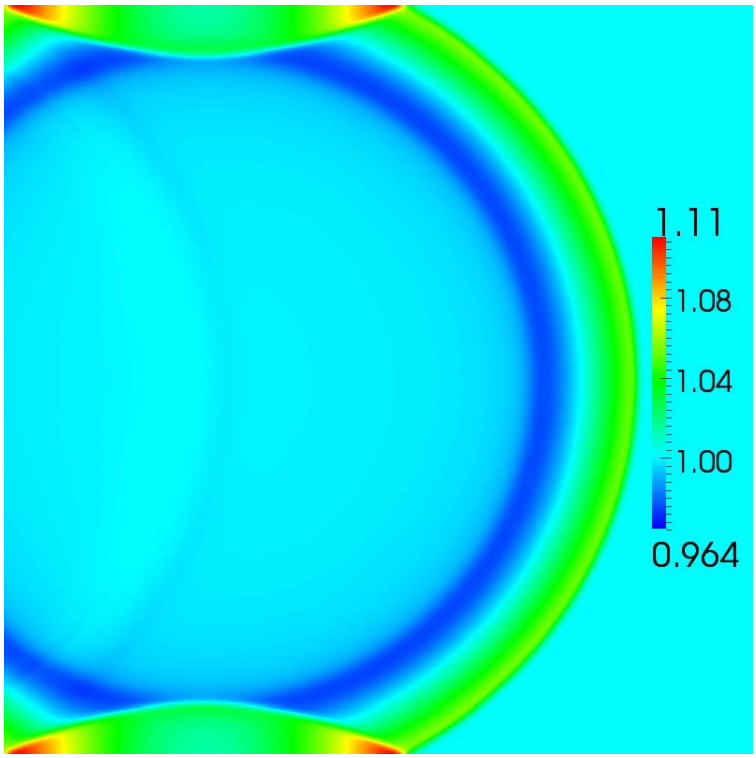

Figure B.76: Isotropic impedance free field BC, setup (b), density at $t = 700 \cdot \Delta t$

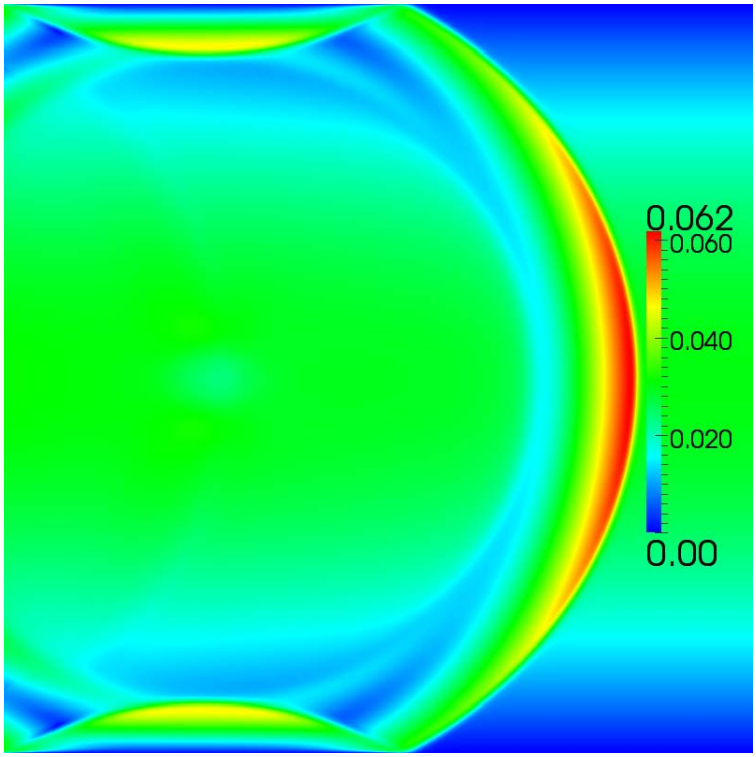

Figure B.77: Isotropic impedance free field BC, setup (b), absolute velocity at $t = 700 \cdot \Delta t$

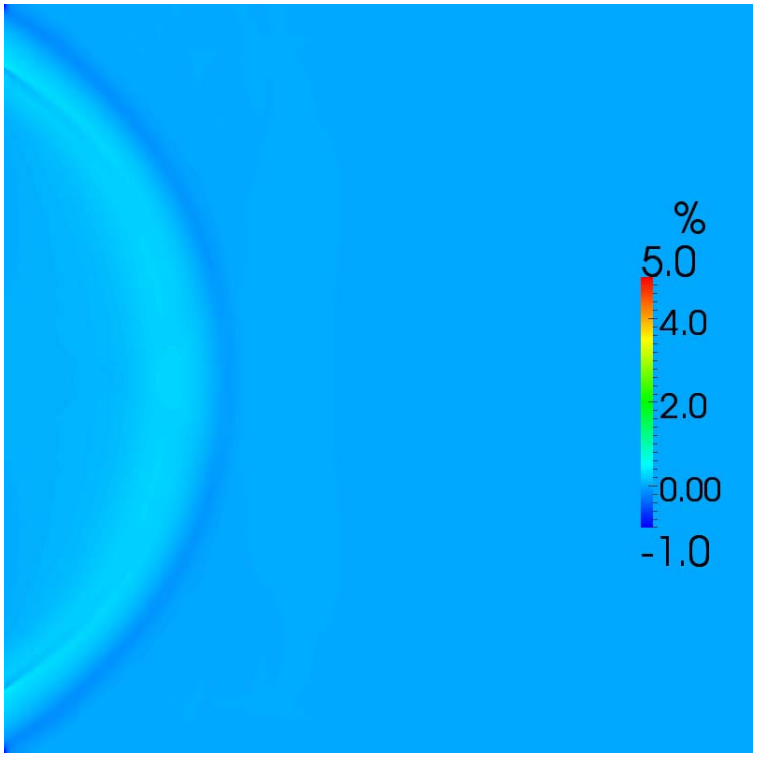

Figure B.78: Isotropic impedance free field BC, setup (b), relative density error in % at $t = 700 \cdot \Delta t$

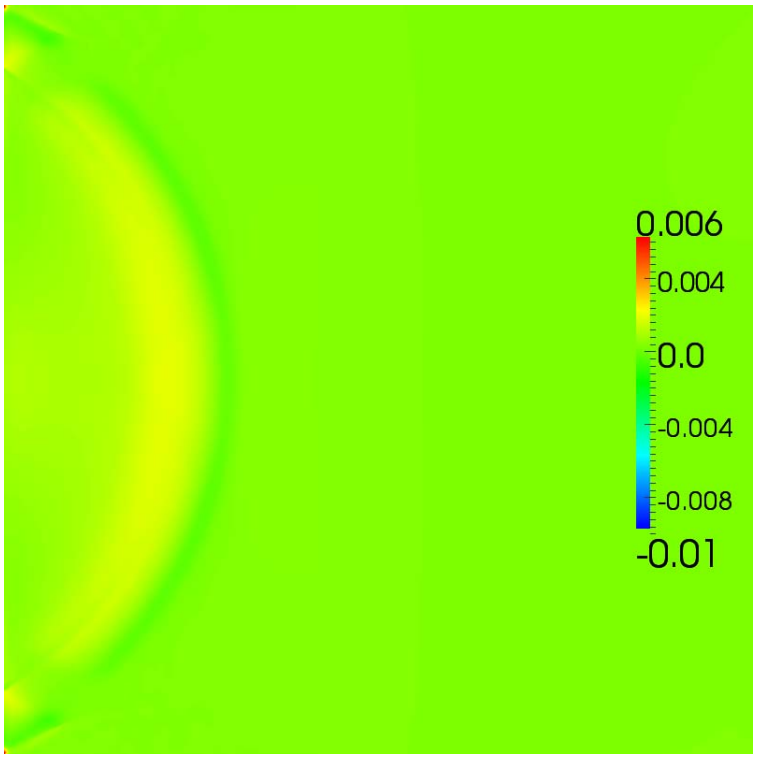

Figure B.79: Isotropic impedance free field BC, setup (b), absolute error of velocity error at $t = 700 \cdot \Delta t$

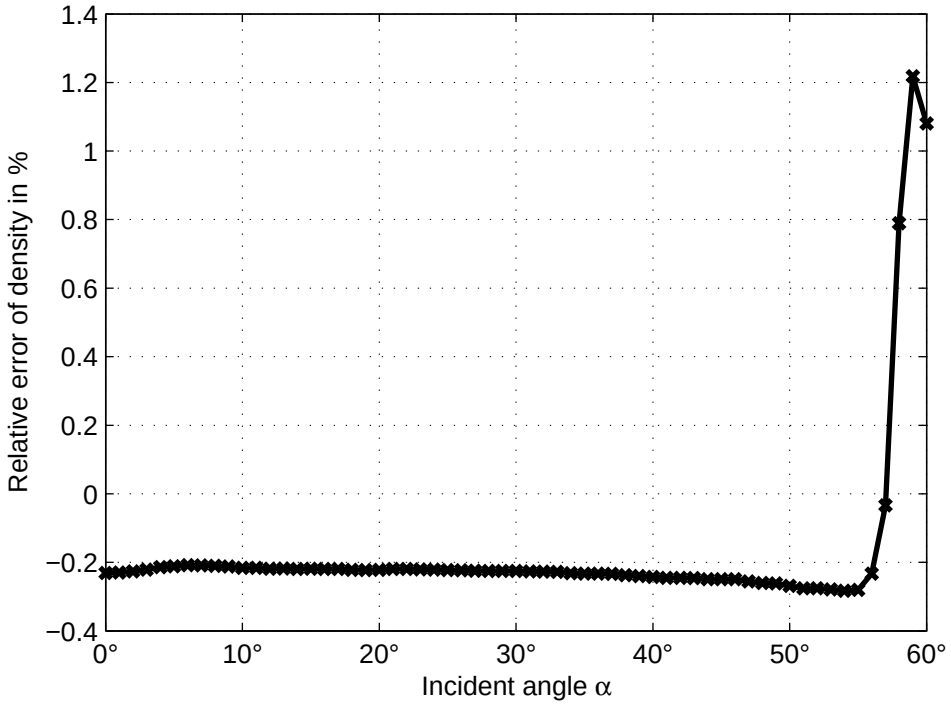

Figure B.80: Reflection over incident angle at $t = 770 \cdot \Delta t$

Bibliography

[1] Exa Corp. Website, 2012. http://www.exa.com.

[2] C. Bender and S. Orszag, Advanced Mathematical Methods for Scientists and Engineers, McGraw-Hill, 1978.

[3] S. Bennet, A Lattice Boltzmann Model for Diffusion of Binary Gas Mixtures, PhD thesis, Department of Engineering, University of Cambridge, 2010.

[4] J.-P. Berenger, A Perfectly Matched Layer for the Absorption of Electromagnetic Waves, Journal of Computational Physics, 114 (1994), pp. 185–200.

[5] P. Bhatnagar, E. Gross, and M. Krook, A model for collision processes in gases, Physical Review, 94 (1954), pp. 511–525.

[6] M. Bouzidi, M. Firdaouss, and P. Lallemand, Momentum transfer of a Boltzmann-Lattice fluid with boundaries, Physics of Fluids, 13 (2001), pp. 3452–3459.

[7] I. Bronstein and K. Semendjajew, Teubner-Taschenbuch der Mathematik, vol. 1, Verlag Harry Deutsch, 1996.

[8] E. Buckingham, On physically similar Systems; Illustrations of the Use of dimensional Equations", Physical Review, 4 (1914), pp. 345 – 376.

[9] S. Chapman and T. Cowling, The Mathematical Theory of Non-Uniform Gases, Cambridge University Press, New York, 1990.

[10] J. H. Chen, Numerical Boundary Conditions and Computational Modes, Journal of Computational Physics, 13 (1973), pp. 522–535.

[11] P. Dellar, An interpretation and derivation of the lattice Boltzmann method using Strang splitting, Computers & Mathematics with Applications, (2011).

[12] D. d'Humières and I. Ginzburg, Viscosity independent numerical errors for Lattice Boltzmann models: From recurrence equations to "magic" collision numbers, Computers & Mathematics with Applications, 58 (2009), pp. 823–840.

[13] D. d'Humières, I. Ginzburg, M. Krafczyk, P. Lallemand, and L. Luo, Multiple-relaxation-time lattice Boltzmann models in three dimensions, Philosophical Transactions: Mathematical, Physical and Engineering Sciences, 360 (2002), pp. 437–451.

[14] B. Engquist and A. Majda, Absorbing Boundary Conditions for the Numerical Simulation of Waves, Mathematics of Computation, 31 (1977), pp. 629–651.

[15] L. C. Evans, Partial Differential Equations, American Mathematical Society, 2010.

[16] J. B. Freund, Proposed Inflow/Outflow Boundary Conditions for Direct Computation of Aerodynamic Sound, Journal of the American Institute of Aeronautics and Astronautics, 35 (1997), pp. 740–742.

[17] M. Geier, private communication, 2011. IRMB, Technische Universität Braunschweig.

[18] S. Geller, Ein explizites Modell für die Fluid-Struktur-Interaktion basierend auf LBM und *p*-FEM, PhD thesis, Fakultät Architektur, Bauingenieurwesen und Umweltwissenschaften der Technischen Universität Carolo-Wilhelmina zu Braunschweig, 2010.

[19] I. Ginzbourg and P. M. Adler, Boundary flow condition analysis for the three-dimensional lattice Boltzmann model, Journal de Physique II France, 4 (1994), pp. 191–214.

[20] K. Guizien and E. Barthélemy, Accuracy of solitary wave generation by a piston wave maker, Journal of Hydraulic Research, 40 (2002), pp. 321–331.

[21] Z. Guo, B. Shi, and C. Zheng, A coupled lattice bgk model for the boussinesq equations, International Journal for Numerical Methods in Fluids, 39 (2002), p. 325–342.

[22] Z. Guo, C. Zheng, and B. Shi, Discrete lattice effects on the forcing term in the lattice Boltzmann method, Physical Review E, 65 (2002), p. 046308.

[23] D. Hänel, Molekulare Gasdynamik - Einführung in die kinetische Theorie der Gase und Lattice-Boltzmann-Methoden, Springer-Verlag, Berlin, Heidelberg, 2004.

[24] X. He and L.-S. Luo, Lattice Boltzmann model for the incompressible Navier-Stokes equation, Journal of Statistical Physics, 88 (1997), pp. 927–944.

[25] G. W. Hedstrom, Nonreflecting Boundary Conditions for Nonlinear Hyperbolic Systems, Journal of Computational Physics, 30 (1979), pp. 222 – 237.

[26] C. Hirsch, Numerical Computation of Internal & External Flows, Butterworth-Heinemann, Great Britan, 2007.

[27] S. Hou, Q. Zou, S. Chen, G. Doolen, and A. Cogley, Simulation of cavity flow by the lattice boltzmann method, Journal of Computational Physics, 118 (1994), pp. 329–347.

[28] S. Izquierdo and N. Fueyo, Characteristic nonreflecting boundary conditions for open boundaries in lattice boltzmann methods, Physical Review E, 78 (2008), pp. 1–7.

[29] C. Janssen, Elbe - Efficient Lattice Boltzmann Environment. Website, 2012. http://www.tuhh.de/fds/research/current-projects/elbe.html.

[30] M. Junk, A. Klar, and L. S. Luo, Asymptotic analysis of the lattice Boltzmann equation, Journal of Computational Physics, 210 (2005), p. 676.

[31] E. W. S. Kam, R. M. C. So, and R. C. K. Leung, Lattice Boltzmann Method Simulation of Aeroacoustics and Nonreflecting Boundary Conditions, Journal of the American Institute of Aeronautics and Astronautics, 45 (2007), pp. 1703–1712.

[32] G. Karniadakis and S. Sherwin, Spectral/hp Element Methods for Computational Fluid Dynamics, Oxford University Press, New York, 2005.

[33] D. Kim, H. Kim, M. Jhon, S. Vinay, and J. Buchanan, A Characteristic Non-Reflecting Boundary Treatment in Lattice Boltzmann Method, Chinese Physical Letters, 25 (2008), pp. 1964–1967.

[34] S. Kollmannsberger, S. Geller, A. Düster, J. Tölke, C. Sorger, M. Krafczyk, and E. Rank, Fixed-grid Fluid-Structure interaction in two dimensions based on a partitioned Lattice Boltzmann and p-FEM approach, International Journal for Numerical Methods in Engineering, 79 (2009), pp. 817–845.

[35] M. Krafczyk, Gitter-Boltzmann-Methoden: Von der Theorie zur Anwendung, postdoctoral thesis, Lehrstuhl für Bauinformatik, Fakultät für Bauingenieur- und Vermessungswesen, Technische Universität München, 2001.

[36] T. Kugelstadt, Op Amps for Everyone: Active Filter Design Techniques, vol. SLOA088, Texas Instruments, 2010.

[37] P. Lallemand and L. Luo, Theory of the lattice Boltzmann method: Dispersion, dissipation, isotropy, Galilean invariance, and stability, Physical Review E, 61 (2000), pp. 6546–6562.

[38] P. Lax, Weak solutions of nonlinear hyperbolic equations and their numerical computation, Communications on Pure and Applied Mathematics, 7 (1954), pp. 159–193.

[39] E. L. Lindman, "Free-Space" Boundary Conditions for the Time Dependent Wave Equation, Journal of Computational Physics, 18 (1975), pp. 66–78.

[40] J. Linxweiler, M. Krafczyk, and J. Tölke, Highly interactive computational steering for coupled 3d flow problems utilizing multiple gpus, Computing and Visualization in Science, (2011), pp. 1–16.

[41] L. Maheshwari and M. Anand, Analog Electronics, Motilal Books UK, 2005.

[42] G. McNamara, A. Guy R. McNamara, Garcia, and B. Alder, Stabilization of Thermal Lattice Boltzmann Models, Journal of Statistical Physics, 81 (1995), pp. 395–408.

[43] R. Mei, L. Luo, P. Lallemand, and D. d'Humières, Consistent Initial Conditions for LBE Simulations, Computers & Fluids, 35 (2006), pp. 855–862.

[44] R. Mei, D. Yu, W. Shyy, and L. Lou, Force evaluation in the lattice Boltzmann method involving curved geometry, Physical Review E, 65 (2002), p. 041203.

[45] G. Müller, Integral Transformation Methods, Lecture Notes, 2009. Chair of Structural Mechanics, Technische Universität München.

[46] G. Müller, private communication, 2010. Chair of Structural Mechanics, Technische Universität München.

[47] G. Müller and M. Möser, Handbook of Engineering Acoustics, Springer, 2012.

[48] B. Neuhierl, Strömungsakustik und Fluid-Struktur-Kopplung mit der Lattice-Boltzmann- und der Finite-Element-Methode, PhD thesis, Technische Universität München, 2008.

[49] X. B. Nie, X. Shan, and H. Chen, Lattice-Boltzmann/Finite-Difference Hybrid Simulation of Transonic Flow, in 47th AIAA Aerospace Sciences Meeting including The New Horizons Forum and Aerospace Exposition, Orlando, Florida, USA, 2009.

[50] T. Poinsot and D. Veynannte, Theoretical and Numerical Combustion, R.R. Edwards, 2. ed., 2005.

[51] T. J. Poinsot and S. K. Lele, Boundary Conditions for Direct Simulations of Compressible Viscous Flows, Journal of Computational Physics, 101 (1992), pp. 104–129.

[52] D. Rudy and J. Strikwerda, A Nonreflecting Outflow Boundary Condition for Subsonic Navier-Stokes Calculations, Journal of Computational Physics, 36 (1980), pp. 55–70.

[53] B. Shenoi, Introduction to Digital Signal Processing and Filter Design, John Wiley & Sons, 1. ed., 2005.

[54] S. Succi, The Lattice Boltzmann Equation for Fluid Dynamics and Beyond, Oxford University Press, Oxford, 2001.

[55] M. Tekitek, M. Bouzidi, F. Dubois, and P. Lallemand, Towards perfectly matching layers for lattice boltzmann equation, Computers & Mathematics with Applications, 58 (2009), pp. 903–913.

[56] K. W. Thompson, Time Dependent Boundary Conditions for Hyperbolic Systems, Journal of Computational Physics, 68 (1987), pp. 1–24.

[57] J. Tölke, Implementation of a Lattice Boltzmann kernel using the Compute Unified Device Architecture developed by nvidia, Computing and Visualization in Science, 13 (2008), pp. 29–39.

[58] J. Tölke, C. Baldwin, Y. Mu, N. Derzhi, Q. Fang, and A. Grader, Computer simulations of fluid flow in sediment, The Leading Edge, 29 (2010), pp. 68–74.

[59] J. Tölke and M. Krafczyk, Teraflop computing on a desktop pc with gpus for 3d cfd, Computational Fluid Dynamics, 22 (2008), pp. 443–456.

[60] S. Turek and M. Schäfer, Benchmark computations of laminar flow around cylinder, in Notes on Numerical Fluid Mechanics, E. H. Hirschel, ed., vol. 52, Vieweg-Verlag, 1996.

[61] P. Wenisch, C. van Treeck, A. Borrmann, E. Rank, and O. Wenisch, Computational steering on distributed systems: Indoor comfort simulations as a case study of interactive cfd on supercomputers, International Journal of Parallel, Emergent and Distributed Systems, 22 (2007), pp. 275–291.

[62] A. Wilde, Anwendung des Lattice-Boltzmann-Verfahrens zur Berechnung strömungsakustischer Probleme, PhD thesis, Technische Universität Dresden, 2006.

[63] P. Zeller, ed., Handbuch der Fahrzeugakustik, Vieweg and Teubner, 2009.

[64] J. Zhou, Lattice Boltzmann Methods for Shallow Water Flows, Springer, 2004.

[65] Q. Zou and X. He, On pressure and velocity boundary conditions for the lattice Boltzmann BGK model, Physics of Fluids, 9 (1997), pp. 1591–1598.